Istituto Universitario
di Studi Superiori

Università degli Studi
di Pavia

ROSE SCHOOL

European School for Advanced Studies

in Reduction of Seismic Risk

Bridge Isolation and Dissipation Devices:

state of the art review of seismic response and modelling
of modern seismic isolation and dissipation devices

A Dissertation Submitted in Partial Fulfilment of the Requirements for the Master Degree in
EARTHQUAKE ENGINEERING

by

Chiara Casarotti

Supervisors:

Dr. Rui Pinho, Prof. Gian Michele Calvi
University of Pavia and ROSE School

July 2004

The dissertation entitled “Bridge isolation and dissipation devices: state of the art review in bridge isolation, seismic response and modelling of bridge isolation and dissipation devices”, by Chiara Casarotti, has been approved in partial fulfilment of the requirements for the Master Degree in Earthquake Engineering.

Dr. Rui Pinho

Prof. Gian Michele Calvi

ABSTRACT

The basic principle of conventional earthquake-resistant design is to ensure an acceptable safety level while avoiding catastrophic failures and loss of life. When a structure does not collapse during a major earthquake, and the occupants can evacuate safely, it is considered that this structure has fulfilled its function even though it may never be functional again. Generally, this approach can be considered adequate for most types of structures. However for important structures, safer methods are required, while keeping economic factors in mind. For example, avoiding collapse is not sufficient for facilities that must remain functional immediately after an earthquake: hospitals, police stations, communication centers, strategically located bridges, and so on.

Over the last 20 years, a large amount of research has been conducted into developing innovative earthquake-resistant systems in order to raise the safety level while keeping construction costs reasonable. Most of these systems are intended to dissipate the seismic energy introduced into the structure by supplemental damping mechanisms and/or to isolate the main structural elements from receiving this energy through isolation systems.

Keywords: isolation, dissipation, bridge devices, bearings, dampers, isolators.

ACKNOWLEDGEMENTS

The author wishes to thank in particular Dr. Rui Pinho for all his guidance and support throughout the duration of the MSc program.

In addition, the author is grateful to Professor Gian Michele Calvi, who gave the opportunity of being part of the school and to all members of the Rose School at the University of Pavia for their friendly and precious assistance.

A particular thanks to all the students of the school, with whom I shared important moments of work and fun.

I specially thank Sandra, for her invaluable friendship, assistance and support in any single moment of the great time we shared.

TABLE OF CONTENTS

LIST OF FIGURES

LIST OF TABLES

1. INTRODUCTION

1.1 THE DEVELOPMENT OF ISOLATION CONCEPT IN SEIMIC DESIGN

A large number of countries extends in regions of seismic hazard, where earthquakes occur with varying severity and frequency. Progress in design and assessment methods of bridge structures traditionally followed major earthquakes, whenever the need of improving the safety level of engineering structures became evident.

Earthquakes design in the last decades passed through a complex, though relatively quick, process of development, and research endeavours for the mitigation of the seismic effects on structures witnessed the permanence of classical methodologies along with the birth of new ideas and new construction technologies, among which seismic isolation is relatively recent and evolving. The increasing acceptance of seismic isolation as a structural technique is shown by the number of retrofitted seismic isolation systems installed nowadays all over the world.

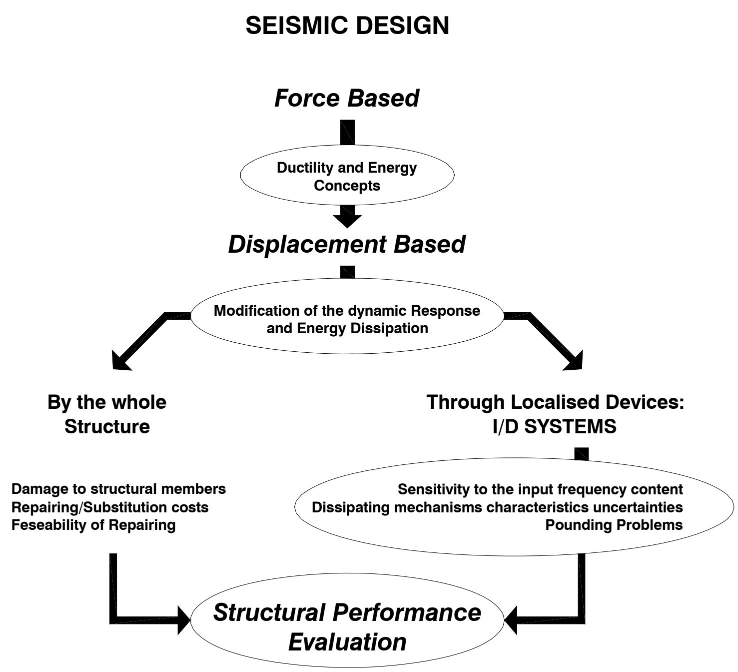

Fig. 1.1. Development of seismic design in the last decades

As schematically illustrated in (Fig. 1.1), due to historical and geographical reasons, bridges have been designed by reference to acceleration response spectra over the past 40 years, in such a way to remain elastic for a constant fraction of the gravity weight, applied as a uniform lateral force. The consequences of the elastic design approach in terms of damage and collapses of bridges are well known (Priestly *et al.*, 1996), due to the severe underestimations of seismic deflections, to the inadequate combinations of action patterns, to the neglecting of detailing allowing large inelastic deformation without significant strength degradation.

As in the 1950's and 1960's it was realized that structures survived levels of response accelerations apparently exceeding those corresponding to the ultimate strength, the concept of "ductility" began to be adopted, with the idea of attributing a structure of the capacity of deforming inelastically without significant strength loss, thus surviving high level earthquakes. It was understood that a general improvement of the structural response could be obtained by modifying the structural dynamic characteristics and dissipating the seismic energy during the event. Consequently, "capacity design principles" (also known as "failure-mode-control approach", Park and Pauley, 1975) were developed, based on the idea of assuring the structure a predetermined post elastic mechanism, in which selected ductile components are designed to withstand several cycles under reversed loading well beyond yield, the yield levels being chosen so that the forces transmitted to other members are limited to their elastic or low ductility range. These principles were applied more effectively as long as a number of displacement-based (some times referred to as performance-based) design methods were developed (e.g. fib Bulletin 25, 2003; Priestley and Calvi, 2003), with the scope of designing structures which would achieve, rather than be bounded by, a given performance limit state under a given seismic intensity, and essentially resulting in uniform-risk structures.

1.1.1 Seismic isolation conceptual design and conventional approach

Looking at the seismic problems through the lens of an energy approach (Fig. 2.2), it can be observed that the amount of earthquake energy filtered by the structure is in fact partly dissipated and partly transformed in demand on structural members, and specifically: (i) first, the transmission of the input energy to the structure is related to the proximity of the input frequency content to the structural dynamic characteristics, basically the mass and the stiffness (i.e. the period), (ii) then, the structural capability of reducing the seismic demand on members relies on the possibility of dissipating the absorbed energy.

The "failure-mode-control" approach relies on the effectiveness of selected sacrificial structural members ("plastic hinge zones"): the yielding in fact lengthens the fundamental period of the structure, and the hysteretic behaviour of the ductile components provides energy dissipation to damp the response motions. However, structural yielding is an inherently damaging mechanism and, even though the appropriate selection of the hinge locations and a careful detailing can ensure structural integrity, large deformations within the structure itself are required to withstand strong earthquake motions, possibly causing problems for components not intended to provide seismic resistance. Moreover, further problems occur in the detailing for the seismic design at a serviceability performance level and problems last concerning costs and feasibility of repairing after a major event.

In a different perspective, it was thought first to reduce substantially the transmission of the earthquake energy into the structure before damage occurs, and then to concentrate the energy dissipation in elements other then the structural members, i.e. in localised devices to be activated during the seismic event. In this sense, the concepts of period shift and energy dissipation by which seismic Isolation and Dissipation (I/D) Systems developed are similar to the conventional "failure-mode-control" approach, specifically: (i) the fundamental period of the fixed-based structure is much shorter than the isolated period, associated with very small participation factors of the higher modes, and (ii) energy dissipation is then obtained through Added Damping derived from yielding, viscous and/or friction dissipation. However, the conceptual background of the modern I/D Systems differs fundamentally from conventional seismic strategies in the philosophy of how the earthquake attack is withstood: in an isolated structure, the damage, i.e. the displacement and the dissipation, are localised in components specially designed and distinct from the structural members. The structure is designed to be protected, and the development of ductility, plasticization and dissipation, rely exclusively on the I/D system properties, which are calibrated on the desired level of structural response.

In bridges, where the scope is to protect relatively low-mass piers and their foundations, isolators and dissipators are more commonly placed between the top of the piers and the superstructure. The viscous damping and hysteretic properties of isolators are generally selected to maintain all components of the superstructure within the elastic range, or to require only limited ductile action. The bulk of the overall displacement of the structure can be concentrated in the isolator components, with relatively little deformation within the structure itself, which moves largely as a rigid body mounted on the isolation system.

1.1.2 Pros and cons of seismic isolation in the context of structural performance evaluation

Some advantages appear evident: first, the level of damage is more safely controlled and confined to generally well-replaceable spots; then, some kind of I/D system not only damp and reduce the action demand on the structure, but even limit physically the amount of force transmittable to the structure. However, design of tipycally isolated structures deserves in some case particular concern.

Practical isolation systems must trade off between the extent of force isolation and acceptable relative displacements across the isolation system during the earthquake motion. Acceptable displacements in conjunction with a large degree of force isolation can be obtained by providing damping, as well as flexibility in the isolator. In such a case, both the forces transmitted and the deformation within the structure are reduced, and the seismic design of the superstructure is considerably simplified, apart from the need for the service connections to accommodate the large displacements across the isolating layer. In addition, particular concern to the boundary condition of the structures is required, as the larger displacements resulting from the use of seismic isolation increase the possibility of pounding: collisions may occur between an abutment and a girder, adjacent girders of segmented bridges or between a girder and neighbouring structure due to their different phase vibrations.

As the required ground motions for structures have increased in intensity, the isolation systems have increased in complexity, with the trend toward very large isolators combined with large viscous dampers. However, combining large viscous dampers with isolators underscores the extreme difficulty of getting the level of damping intrinsic to a hysteretic isolator system above 20% equivalent viscous damping when the displacements become large. As a result, in the attempt to control through damping the large displacements induced by the cose-mandated motions, the use supplemental dampers is forced, but, unfortunately, the dampers themselves drive energy into higher modes, thus defeating the primary reason for using isolation: the effects of added damping on the structural response have to be carefully considered, because they can be possibly detrimental.

I/D devices also show some inherent problems: the properties of seismic isolation bearings, in fact, vary due to the effects of wear, ageing, temperature, history, nature of loading, etc. The concept of Property Modification Factors has been introduced by Constantinou *et al.* (1999) in order characterise the variability of the nominal properties of an isolator and understanding the consequences on the device and structural response.

A large variety of seismic isolation/dissipation devices have been developed all over the world. The most successful devices show simplicity and effectiveness of design, thus being reliable and economic to produce and install, and incorporating low maintenance. Different I/D technologies act differently on the structural performance, improving some response and possibly worsening others: only an appropriate combination of a number of factors allows understanding if the structural performance improves after the application of a specific I/D system, and which is the best technology to be employed. Among these factors, the absolute maximum acceleration is a measure of the force level induced into the system, of the damage potential to non-structural elements and of potential injury to the occupants, the maximum absorbed energy is a measure of potential structural damage, whilst the residual displacement is an indicator of the structural damage and of repair costs; in addition, one should consider the maximum displacement ductility over the total duration of the seismic input, the number and the typology of failed and/or yielded elements, the presence of soft-mechanisms, the ductility distribution and the risk of pounding.

As the whole thrust of seismic isolation is to shift the probable damage level from not repairable or repairable towards minor, and thereby to reduce the damage costs, the economic factors need also to be considered by an engineer wishing to decide whether a structure should incorporate seismic isolation: maintenance costs should be low for passive systems, though they may be higher for active seismic isolation, whilst the construction costs including seismic isolation usually vary by 5-10% from not isolated options. The design problem may be solved by means of a variety of possible structural forms and materials, with and without incorporating seismic isolation; the total costs and benefits of different solutions can be evaluated condidering the "value" of having the structure or its contents in a undamaged or with reduced damage after an earthquake. In many cases such additional benefits renders preferable the adoption of the seismic isolation option.

1.1.3 Dissertation objectives

The objective of present work is to provide a global overview of the historical and recent technologies for the reduction of the seismic demand on bridges: attention will focus on the theoretical background in which I/D systems developed, followed by an analytical presentation of each specific I/D technology. Each system features in fact peculiar characteristics, pros and cons that make it suitable to different design conditions and structural typologies, and improper for others. The majority of them has been currently tested through extensive analytical and experimental studies and structural implementation, whilst other are still in a phase of experimentation and research. The present work is intended to provide a tool for the structural engineer, making him capable of a critical comparison among various systems, of modeling and of designing them within general structural engineering software and of finally recommending the optimum solution for each particular situation of seismic design or retrofit project.

1.2 DISSERTATION OUTLINE

The second chapter presents the energy formulation of the seismic problem, in order to introduce the basic concepts of seismic isolation, the effects of damping on isolated structures. The property modification factors affecting the isolating/dissipating devices are discussed and the last part of the chapter presents a briefly review of the I/D devices, according to their hysteretic properties and to the different categories in which they are grouped.

The following chapters describe peculiarly the different I/D device typologies: Metallic and Friction Damper (Chapter 3), Viscous and Visco-elastic Dampers (Chapter 4), Self-centring Dampers (Chapter 5), Electro and Magnetorheological Dampers (Chapter 6), Elastomeric Isolators (Chapter 7), Sliding Devices (Chapter 8). The effectiveness and suitability of the devices to specific design situations is discussed, along with a description of the peculiar hysteretic behaviour and to the way of modeling each device. Preliminary design procedures are addressed.

2.BASIC ISSUES: SEISMIC DESIGN ISSUES, ENERGY CONCEPTS, FRICTION AND DISSIPATIVE MECHANISMS

2.1 BRIDGE CONSIDERATIONS

Buildings constitute structural typologies in series: the single subsystem is the storey, whose flexibility is ideally summed to the other ones to constitute the system flexibility; all the subsystems contribute to the unique base shear, but not through a direct sum of their contributions. Local mechanisms and quantities of interest are inter-storey drifts and shear profiles. Bridges are different structural typologies: basically, the single element is the pier or the bent, whose stiffness is added to the ones of the other piers, as they are in parallel; each subsystem has its own base shear, and they can be simply added to get the system base shear. The deformed shape of the superstructure and the pier base shears represent the local level quantities. A number of observations can be made in case of bridge structures:

- The inelastic mechanisms are ideally expected to be activated simultaneously at the base of many piers and the deformed shape is generally strongly affected by the stiffness characteristics of the deck (elastic part).
- The superstructure of the viaduct is often quite flexible in its own plane. Consequently, many modes can be excited during the response, depending on the instantaneous stiffness of the piers. The effects of higher modes are expected to be more important for irregular bridges, where they may be triggered at the level of the deck, and for isolated bridges, where they may be activated in the piers due to their relative freedom with respect to the deck.
- In the case of segmented multi-span bridges, the different bents may be treated as separate almost independent sub-systems, provided that the appropriate boundary conditions apply.
- Many observations and in general a lot of formulations of I/D system problems refer to the simple SDOF system of Fig. 2.1 (left): in the case of bridges, it has to be no longer regarded as the single story frame, but as a single bridge bent loaded in the transversal direction. This is important to be observed, as it allows extending to bridge analysis a lot of observations on the nature of the response of simple isolated systems originally formulated for buildings.

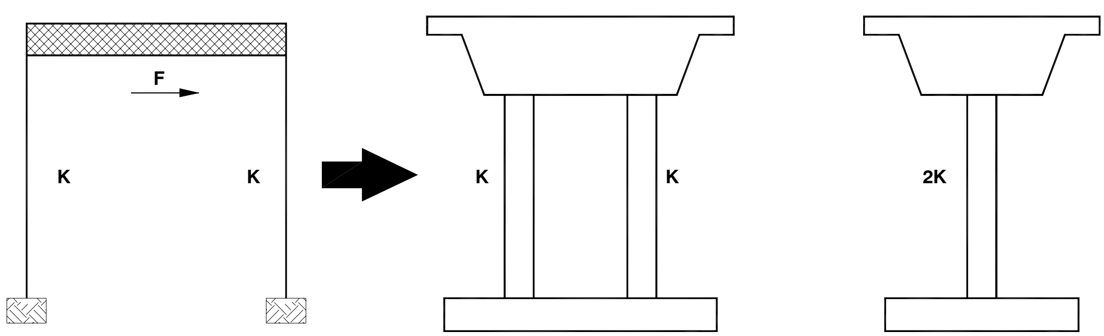

Fig. 2.1. SDOF model

2.2 ENERGY FORMULATION OF THE SEISMIC PROBLEM

From an energy point of view, the seismic problem can be regarded as a finite amount of energy being filtered by a structure. The energy balance approach evaluates the relative distribution of the absorbed input energy among the different kinds of internal structural energy. Considering a simple SDOF system (with dynamic characteristic m, c, k), the energy balance at any given time t is:

$$E_k(t) + E_d(t) + E_s(t) = E_I \tag{2.1}$$

$$\begin{aligned} E_k(t) + E_d(t) + E_s(t) &= \frac{1}{2} m\dot{x}(t)^2 + c\int_0^{x(t)} \dot{x}(t)dx + \int_0^{x(t)} F_s(t)dx \\ E_I &= -m\int_0^{x(t)} \ddot{x}_g(t)dx \end{aligned} \tag{2.2}$$

where $E_k(t)$ is the kinetic energy at time t, caused by the relative motion of the mass with respect to the base; *Ed(t)* is the energy dissipated by viscous damping up to time *t*; *Es(t)* is strain at time t, partly recoverable as elastic strain energy and partly and dissipated as hysteretic energy; $E_I(t)$ is the input energy introduced into the system; *Fs(t)* is the restoring force of the system.

It is worth to notice that the input energy contribution is integrated through the relative displacement x of the structure, meaning that the energy induced in the structure is not only dependent on the characteristics of the ground motion, but also of the structure, as it acts as a filter. The way in which the input energy is dissipated by the structure is a measure of the occurred damage and/or of the effectiveness of a specific I/D system. The installation of an isolation technology influences the amount of energy introduced into the structure, whilst the introduction of dissipating devices has an important effect on the distribution of energy, generally resulting in reduced structural damage (unrecoverable strain energy). Common engineering softwares allows to control the energy distribution of a structure subjected to nonlinear dynamic analyses.

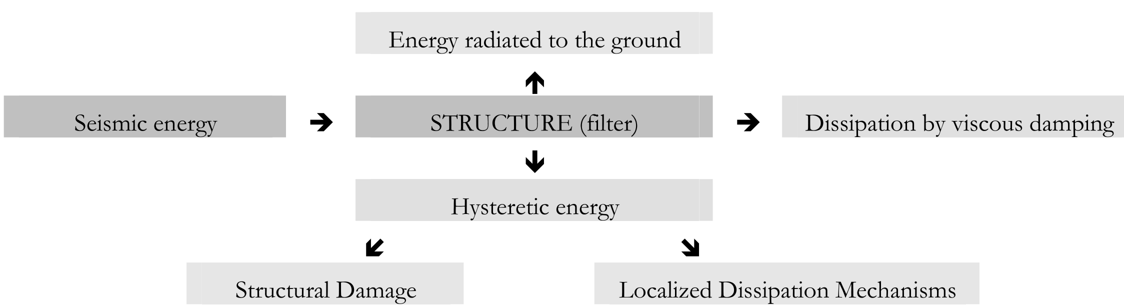

Fig. 2.2. Energy distribution at the end of an earthquake.

2.3 BASE CONCEPTS AND LINEAR THEORY OF SEISMIC ISOLATION

The linear theory of seismic isolation, given in details by Kelly (1996, 1999), is based on a two d.o.f. structural model, as shown in Fig. 2.3. The mass m represents the superstructure and m_b the base mass above the isolation system. The stiffness and damping of the structure and of the isolation system are represented by k_s, c_s, k_b and c_b respectively. u_s, u_b and u_g are the absolute displacements of the two masses and of the ground, while relative displacements in equation (2.3) represent respectively the isolation system displacement and the interstorey drift. The basic equations of motion of the two-degree-of-freedom model are given in equation (2.4), where M is the total mass.

$$v_b = u_b - u_g \quad ; \quad v_s = u_s - u_b \tag{2.3}$$

$$\begin{bmatrix} M & m \\ m & m \end{bmatrix} \begin{Bmatrix} \ddot{v}_b \\ \ddot{v}_s \end{Bmatrix} + \begin{bmatrix} c_b & 0 \\ 0 & c_s \end{bmatrix} \begin{Bmatrix} \dot{v}_b \\ \dot{v}_s \end{Bmatrix} + \begin{bmatrix} k_b & 0 \\ 0 & k_s \end{bmatrix} \begin{Bmatrix} v_b \\ v_s \end{Bmatrix} = \begin{bmatrix} M & m \\ m & m \end{bmatrix} \begin{Bmatrix} 1 \\ 0 \end{Bmatrix} \ddot{u}_g$$

or

$$\mathbf{M}\ddot{\mathbf{v}} + \mathbf{C}\dot{\mathbf{v}} + \mathbf{K}\mathbf{v} = \mathbf{M}r\ddot{u}_g \tag{2.4}$$

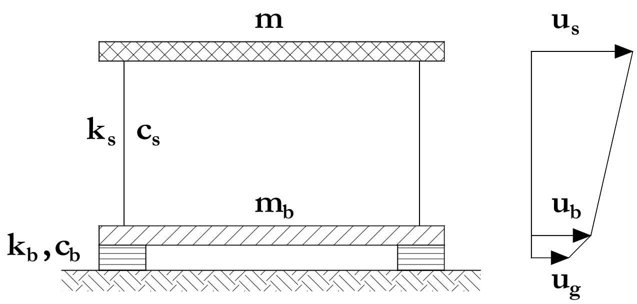

Fig. 2.3. Parameters of 2DOF isolated system

The nominal frequencies and damping ratios of the system are obtained as follows:

$$\omega_s = \sqrt{(k_s / m)} >> \omega_b = \sqrt{(k_b / M)} \tag{2.5}$$

$$\varepsilon = (\omega_s / \omega_b)^2 \tag{2.6}$$

$$\xi_s = \frac{c_s}{2m\omega_s} \quad ; \quad \xi_b = \frac{c_b}{2M\omega_b} \tag{2.7}$$

ε is assumed to be in the range of $0\text{-}10^{-2}$. The solution of the (2.4) leads to the characteristic system frequencies in equations (2.8), approximated by the (2.9), where the mass ratio γ is defined as m/M:

$$\begin{aligned} \omega_1^2 &= \frac{1}{2(1-\gamma)} \left\{ \omega_b^2 + \omega_s^2 - \left[(\omega_b^2 - \omega_s^2)^2 + 4\gamma\omega_b^2\omega_s^2 \right]^{1/2} \right\} \\ \omega_2^2 &= \frac{1}{2(1-\gamma)} \left\{ \omega_b^2 + \omega_s^2 + \left[(\omega_b^2 - \omega_s^2)^2 + 4\gamma\omega_b^2\omega_s^2 \right]^{1/2} \right\} \end{aligned} \tag{2.8}$$

$$\begin{aligned} \omega_1^2 &= \omega_b^2 (1 - \gamma\varepsilon) \\ \omega_2^2 &= \frac{\omega_s^2}{1-\gamma} (1 + \gamma\varepsilon) \end{aligned} \tag{2.9}$$

The equations (2.10) to (2.12) display respectively the classical modes of the combined system, shown in Fig. 2.4, the modal masses and the modal participation factors:

$$\underline{\phi}^{1T} = \{1, \varepsilon\}$$
$$\underline{\phi}^{2T} = \left\{1, -\frac{1}{\gamma}\left[1-(1-\gamma)\varepsilon\right]\right\} \qquad (2.10)$$

$$M_1 = M(1-2\gamma\varepsilon)$$
$$M_2 = M\frac{(1-\gamma)\left[1-2(1-\gamma)\varepsilon\right]}{\gamma} \qquad (2.11)$$

$$\Gamma_1 = 1-\gamma\varepsilon$$
$$\Gamma_2 = \gamma\varepsilon \qquad (2.12)$$

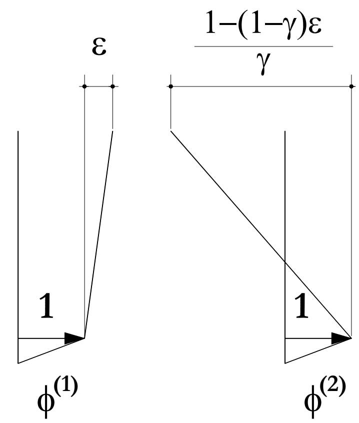

Fig. 2.4. Classical modes of the combined system

The found results reveal the basic concepts on which an isolation system relies: the participation factor of the second mode, responsible for the structural deformation, is in the order of magnitude of ε, and if the two frequencies are well separated it may be very small. Then, the second mode is shifted far from the typical range of strong motion frequencies. Since the participation factor of the second mode is very small, it is also almost orthogonal to the earthquake input: this means that in any case the input energy associated to the second mode structural frequency will not be inferred to the structure; the effectiveness of an isolation system consists in fact in deflecting energy through its othogonality property rather than in absorbing it.

Energy absorption is however another component of the isolation system. The modal damping ratios depend on the structural and the isolators dampings: when they can be treated separately, and the energy dissipation can be described just by linear viscous damping, simple relationships are found:

$$\beta_1 = \beta_b\left(1-\frac{3}{2}\gamma\varepsilon\right)$$
$$\beta_2 = \frac{\beta_s + \gamma\beta_b\varepsilon^{1/2}}{(1-\gamma)^{1/2}}\left(1-\frac{\gamma\varepsilon}{2}\right) \qquad (2.13)$$

A natural rubber isolation system may provide a degree of damping in the range of 5 to 20% of critical, and the structure generally of 2%: the common assumption of a structural damping of 5% of critical implies the occurring of some degree of damage to have occurred, that is avoided in isolated structures.

The second equation of (2.13) shows that the structural damping is increased by the bearing damping, whose contribution might be significant in case of a β_s very small: high damping in the rubber bearings can contribute significantly to the structural mode.

2.3.1 Effects of damping on the response of seismic isolated structures

Results so far obtained assume that the damping in the system is light enough to allow retaining the orthogonality of the modes. In most structural applications the damping is assumed small enough that the effect of the coupling terms in the equations of motion are negligible and the solution can be obtained from the uncoupled modal equations of motions. In the case of seismic isolation, this leads to very simple results for base displacement, base shear, and interstorey drift, and these simple results formed the basis of the earlier design approaches as exemplified by the 1986 SEAONC Yellow Book.

Recent moderate or large magnitude earthquakes in urban areas have led to significantly increase the current code requirements in many countries. The codes governing the design of seismically isolated structures have always been more conservative than those for conventional structures, and these codes are now so conservative that the benefit of seismic isolation - that it provides functionality (elastic response) for large ground motion at an affordable cost - may be jeopardized. In many recent isolated structures, the code requirements are so conservative that the designers employ additional viscous dampers in an attempt to control the large design displacements, thus achieving damping factors for the isolation system in the order of 50% of critical: at such levels of damping the equations cannot remain uncoupled and a complex modal analysis should be used, loosing the physical insight that led to the simple results of the uncoupled solution. Kelly (1999) studied the effect of high levels of damping in the isolation system. He found that the addition of dampers, while controlling the isolator displacement, has the counter effect of increasing the interstorey drift and floor accelerations. For a constant velocity design spectrum the accelerations generated by the coupling terms become the dominant term. It is not widely appreciated that in base-isolated structures the higher modes, which carry both the floor accelerations and the interstorey drift, are almost orthogonal to the base shear, so that a low base shear is not a guarantee of an effective isolation system. In this respect the effort to improve the performance of the system by adding damping has to be carefully evaluated.

Moreover, identifying a Maximum Credible Earthquake level with a very large and very rare event for design of the isolators raises the possibility that in the more probable, lower-level earthquake, the isolation system will be too stiff and too heavily damped to be moved. The solutions of how to control displacements for large input level earthquakes while maintaining good performance for low-to-moderate input level earthquakes are several, but mainly reduce to designing a system that is very stiff at low input shaking, softens with increasing input reaching a minimum and then stiffens again at higher levels of input. With frictional systems such as the FPS, this can be achieved by gradually increasing the curvature of the disc at radii larger than a given threshold displacement and increasing the surface roughness, whilst in case of elastomeric isolators increased stiffness and damping are associated with the strain-induced crystallization that occurs in the elastomer at strains around 150 to 200 per cent shear strain (depending on the compound). In each case, it is suggested to design an isolation system that provides isolation functionality at the design level and displacement control for extreme events.

2.3.2 Near field effects on the response of seismic isolated structures

Near-field ground motions include large pulses that may greatly amplify the dynamic response of long period structures, particularly if structures deform in the inelastic range. In recent years several seismologists have doubted that base-isolated structures are vulnerable to large pulse-like ground motions generated at near-fault locations.

Makris and Chang (2000) investigated the response of isolated structures to high frequency spike and low-frequency, low-acceleration pulses, simulating the cinematic characteristics of the ground motions observed near the faults of major earthquakes. Observing that near source ground motions are particularly destructive to some structure because not of their PGA, but of their 'incremental' ground velocity, they sustained that seismic isolation could be effective against near-source ground motions provided that the appropriate energy dissipation mechanism is assured.

Makris and Chang (2000) studied the effects of supplemental damping on classical s.d.o.f. and 2-d.o.f. systems, equipped with different dissipation mechanisms, shown in Fig. 2.5: (i) Viscous Model (elliptical force-displacement loop, e.g. high damping rubber bearing and viscous fluid dampers), (ii) Rigid-Plastic Model (rectangular force-displacement loop, e.g. sliding bearings), (iii) Elastic-Plastic Model (parallelogram shaped force-displacement loop, e.g. lead-rubber bearings), (iv) Viscoplastic Model (rectangular force-displacement loop with curved horizontal branches, e.g. sliding bearings and viscous fluid dampers, elastomeric bearings and controllable fluid dampers, sliding bearings and controllable fluid dampers), (v) Elasto-Viscoplastic Model (parallelogram shaped force-displacement loop with curved horizontal branches, e.g. lead-rubber bearings and viscous dampers).

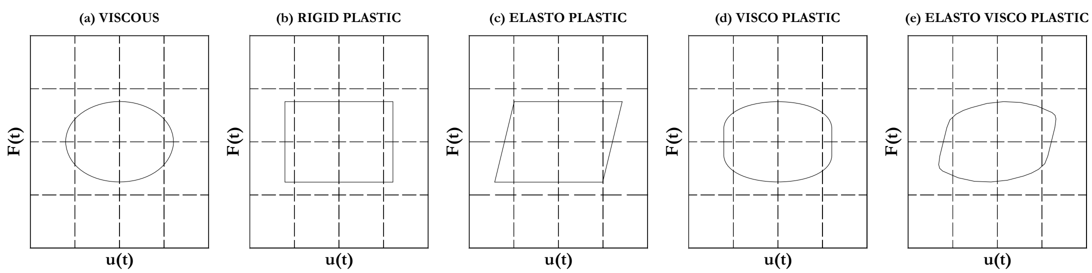

Fig. 2.5. Idealizations of energy dissipation mechanisms of practical seismic isolation systems

Makris and Chang (2000) found that structural response quantities due to the recorded motions resemble the structural response quantities due to trigonometric pulse-type motions only when the isolation period reaches high values (i.e., T_I=3 sec or more). The response of structures with relatively low isolation periods (i.e., T_I<2.0 sec) is substantially affected by the high frequency that overrides the long-duration pulse. Therefore, the concept of seismic isolation is beneficial even for motions that contain long-velocity and displacement pulses. It is observed that a relatively low value of plastic (friction-type) damping removes any resonant effect that a long-duration pulse has on a long-period isolation system. According to this, there is no need for extremely long isolation periods in order to go further away from the long period pulse that dominates a near-source ground motion. The study of Makris and Chang (2000) showed that under seismic excitation of relatively long durations, the response of a structure depends more on the amount of energy dissipated per cycle than on the nature of the dissipative force: consequently, rigid-plastic behaviour results to nearly the same response reduction as elastic-plastic behaviour with the same yield (or friction) force. They concluded that a combination of relatively low values of plastic (friction) and viscous damping results in an attractive design since displacements are substantially reduced without increasing appreciably base shear and superstructure accelerations.

2.4 PROPERTY MODIFICATION FACTORS OF SEISMIC ISOLATION BEARINGS

Typically, the nominal value of a specific property of a device applies for specific conditions and relevant state of loading. The properties of seismic isolation bearings vary due to the effects of wear, ageing, temperature, history and nature of loading, etc. The concept of property modification factors has been introduced by Constantinou *et al.*(1999), in order to quantify the effect of different phenomena on the nominal properties of an isolator: bounding values for different properties of isolators are evaluated based on statistical analysis of the variability of the properties during experimental test and the likelihood of occurrence of relevant events.

$$P_{max} = \lambda_{max} P_n \qquad P_{min} = \lambda_{min} P_n$$
$$\lambda_{max(min)} = \prod \lambda_{i,max(min)} \tag{2.14}$$

Where each $\lambda_{I,max(min)}$ is larger (smaller) or equal to unity and is associated with a different aspect of the isolation system, such as wear, contamination, ageing, history of loading (scragging), cumulative travel (wear), temperature, velocity, normal pressure, etc. EC8 provisions require that, in addition to the set of nominal Design Properties (DP) derived from the Prototype Tests, two sets of design properties of the isolating system shall be properly established, Upper bound design properties (UBDP), and Lower bound design properties (LBDP). AASTHO provisions are similar.

Studying the factors influencing the real behaviour of isolators, and their relative importance in the global seismic response of structures, may be carried out at different levels of complexity: the first level consist in evaluating the range of variability of a given property by multiplying its nominal value by a Property Modification Factor (PMF), affecting strictly the bearing property (equation (2.14)). The second level consists in the phenomenological evaluation (scrutinising test results), of the range variability of a specific property, then in the analysis of the effective importance that this variability of the isolator has on the global response of isolated structures. In this way, property variations that do not affect the structural response are not acconted for. In both cases, a careful evaluation of the relative likehood of occurrence of the different varying conditions influencing the variation range of the property is needed, in order to avoid excessive conservatism due to the simultaneously appliance of all those conditions, based on the statistical analysis of the property variation with time and the joint probability of occurrence.

2.4.1 Variation of the coefficient of friction

The basic dry friction theory is based on three assumptions, validated experimentally under specific conditions: (i) the total frictional force that can be developed is independent of the apparent contact area; (ii) the total frictional force developable is proportional to the total normal force acting across the interface; (iii) in case of slow sliding velocities, the total frictional force is independent of the velocity; (iv) immediately before slippage, the friction is higher then during sliding (breakaway friction force).

The last two observations are particularly important in case of seismic motion, when the movement crosses all the stages from its activation thru high velocities, and the variation of the coefficient of friction with the operating conditions of the interface might be relevant.

Several authors studied the variation of the coefficient of friction (e.g. Bondonet and Filiatrault, 1997, Constantinou *et al.*, 1999). Results from test performed on sheet-type PTFE-steel interfaces by Bondonet and Filiatrault (1997) are reported. Tests were done varying the bearing pressure (5, 15, 30, 45 MPa), the frequency of the sinusoidal input (0.02, 0.2, 1.0, 2.0, 5.0 Hz) and the displacement (±10 mm, ±70mm), for a maximum sliding velocity of 0.82 m/s, corresponding to a maximum acceleration of 1.03 g. Three types of Teflon were tested: unfilled PTFE, glass-filled PTFE, carbon-filled PTFE. The test results are shown in Fig. 2.6 to Fig. 2.8. From these and other (Tsai, 1997) experimental tests on teflon-metal interfaces it is observed that:

- the differences between the static and the stedy state coefficient of friction are small at low excitation frequencies, while increasing the excitation frequency a significant transient response is recorded;
- the initial (static) coefficient of friction increases from a minimum to a maximum as the velocity increases, while the dynamic coefficient of friction grows as the velocity increases for low velocities, then, past a critical velocity, it starts to decrease to a final coefficient that can be even smaller then the minimum dynamic coefficient.
- either of the two coefficients decrese at the increasing of the confining pressure.
- the reciprocal quasi-static friction coefficient is linearly proportional to the normal pressure;

- the resultant friction force has the same action line of the displacement increment in the opposite direction, and depends on both the instantaneous velocity and the normal pressure (Fig. 2.12).
- the amplification factor (i.e. the increment of the dynamic friction force with respect to the quasi-static force and at the same applied normal pressure), is a simple function of the sliding velocity, and approach to a constant value after sliding velocity overcome a certain value.
- the quasi static friction force is independent from the normal pressure history.

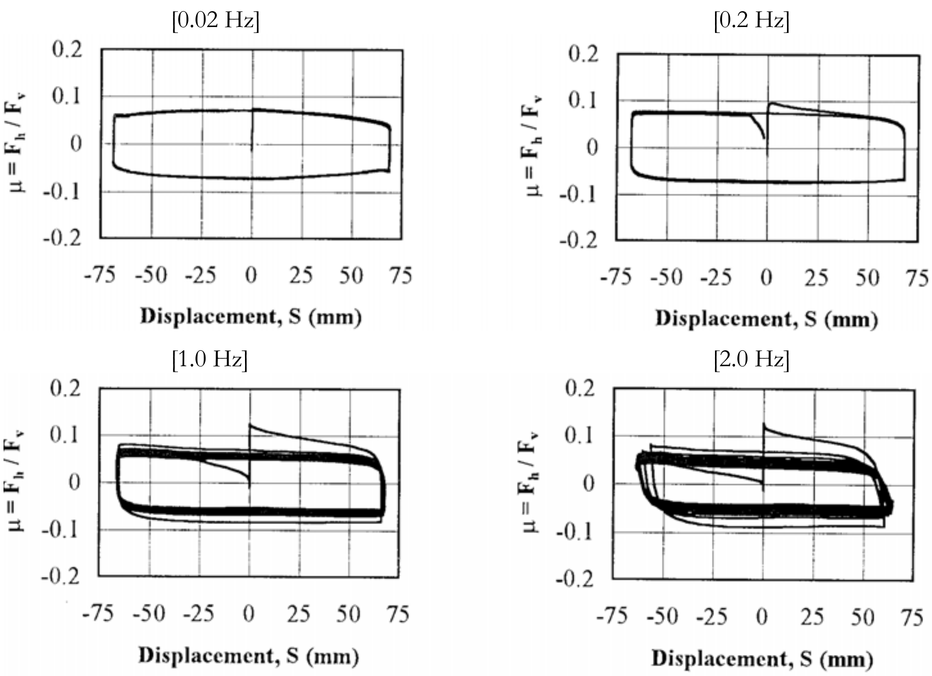

Fig. 2.6. Frictional response of unfilled Teflon-steel interface (confining pressure of 30MPa) at different load frequencies (Bondonet and Filiatrault, 1997)

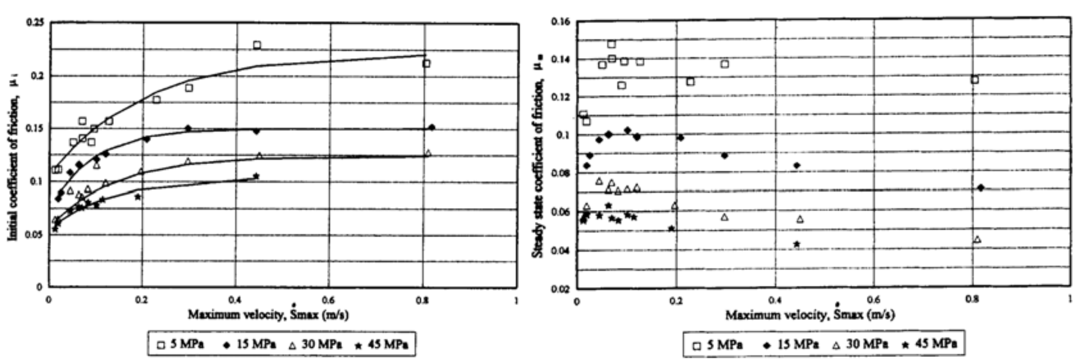

Fig. 2.7. Variations of initial (left) and steady state (right) coefficients of friction with absolute maximum velocity (Bondonet and Filiatrault, 1997)

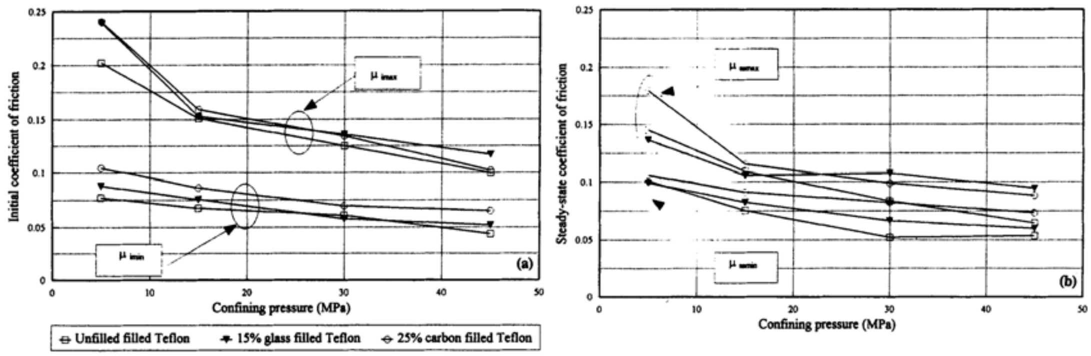

Fig. 2.8. Variations of initial (left) and steady state (right) coefficients of friction with the confining pressure (Bondonet and Filiatrault, 1997)

The friction coefficient results depending on the load dwell (time of loading), cumulative movement (travel) and wear, roughness of the stainless steel, contamination (presence of debris at the interface) and lubrication. Detailed description of these effects, relatively less important, is found in Constantinou *et al.* (1999).

2.4.1.1 Pressure and velocity dependent behaviour

Constantinou *et al.* (1999), after a thorough review of the theory of friction, concluded that the shear strength s at the interface to a first approximation is a linear function of the actual pressure p, of the kind $s_0+\alpha p$. As a result, the friction coefficient, is given by equation (2.15), where A_0 is the apparent contact area (very close to the real contact area for those kind of interfaces) and N is the normal load. Considering that α is very small compared to the other terms, the inverse of the coefficient of friction is found to be a linear function of the bearing pressure, systematically consistent with experimental results (Fig. 2.9).

$$\mu = \frac{A_0 s_0}{N} + \alpha \qquad (2.15)$$

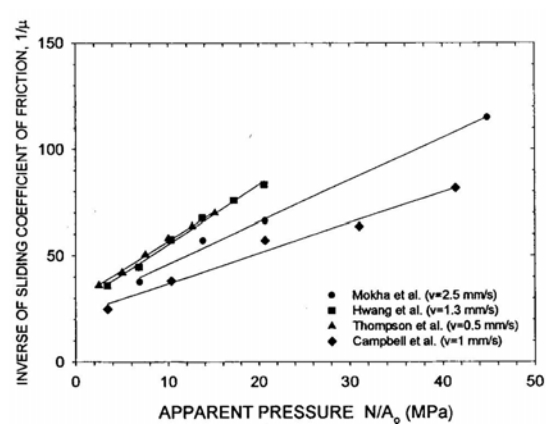

Fig. 2.9. Dependence of 1/μ on Sliding Pressure (Constantinou et al., 1999)

Fig. 2.10 shows the dependence of the friction coefficient on sliding velocity and bearing pressure for clean, unlubricated interfaces at normal ambient temperature. The sliding value of the friction coefficient is characterized by a minimum value f_{min} progressively increasing with velocity, attaining a constant value f_{max} for high velocities. The increment respect to f_{min} is approximately 5-6 times of f_{min} at speeds of interest in seismic applications (above 0.5 m/s). Under these conditions there is a considerable heating at the interface, that might even result in a local melting of the PTFE, causing a further reduction in the friction coefficient, as discussed in the following section.

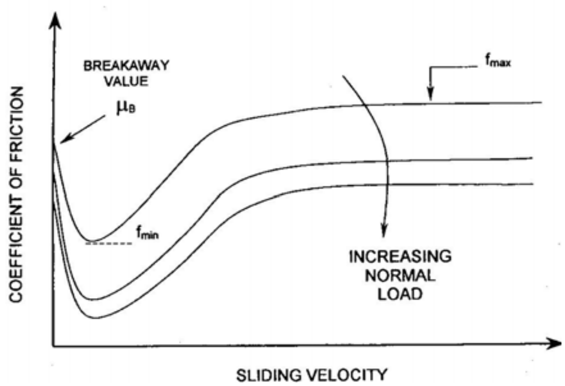

Fig. 2.10. Friction coefficient of PTFE-Polished Stainless Steel Interface at varying velocity and normal load

In general, for a fixed value of the apparent pressure, the sliding coefficient of friction can be described by equation (2.16) (Mokha *et al.*, 1988, Constantinuou *et al.*, 1990 and 1993), where a = 20-30 s/m for unfilled PTFE, and a > 100 s/m for PTFE composite. Equation (2.16) is plotted in Fig. 2.11, showing the evident effects of the ratio f_{max}/f_{min}.

$$\frac{\mu}{f_{max}} = 1 - \left(1 - \frac{f_{min}}{f_{max}}\right)\exp(-av) \qquad (2.16)$$

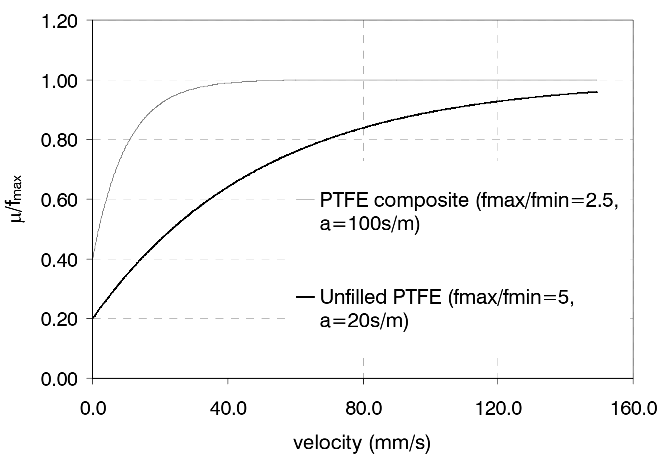

Fig. 2.11. Effect of parameter a and of the ratio f_{max}/f_{min}

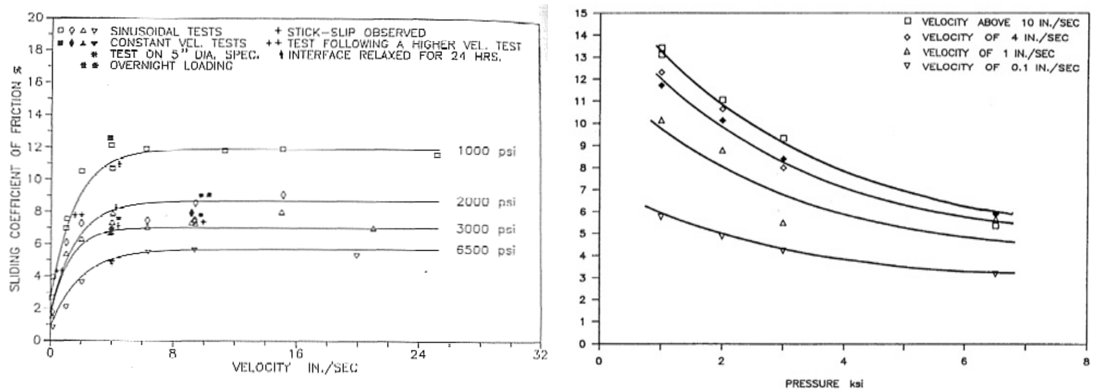

Fig. 2.12. Effect of velocity and pressure on μ of unfilled Teflon (right), and on f_{max} of Glass-filled Teflon (Constantinou et al., 1999)

Fig. 2.13 presents the normalized experimental data at different displacement capacities d_d and normal pressure N of the bearing, in order to give an idea of the trends: it can be seen, in the zoom of Fig. 2.14, that in the low velocity range the formula proposed by Constantinou fits very well experimental data. The calculation of the coefficient of friction is based on the thickness of the first loop at zero displacement.

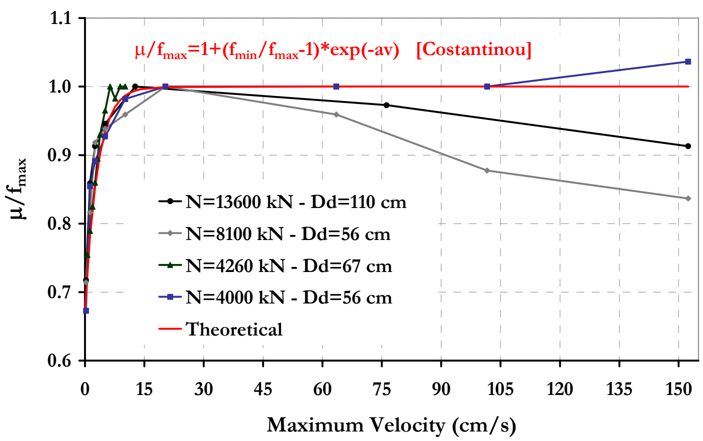

Fig. 2.13. Normalised friction coefficient-velocity dependence: theoretical vs experimental at different bearing pressures and design displacements (on the courtesy of G. Benzoni)

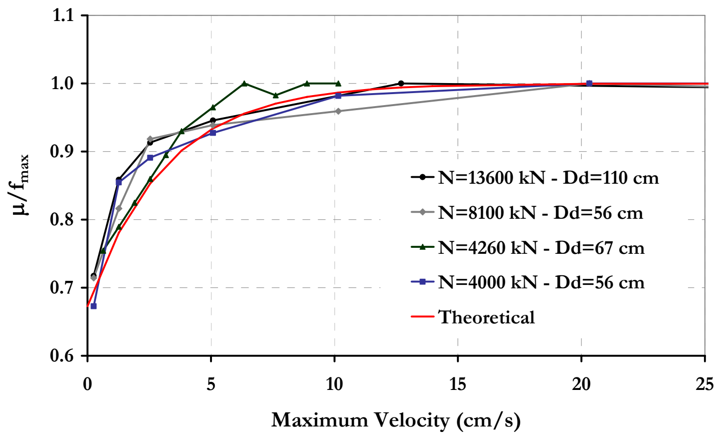

Fig. 2.14. Normalised friction coefficient-velocity dependence: theoretical vs experimental for different bearing pressures and design displacements: zoom in the small velocities range (on the courtesy of G. Benzoni)

2.4.1.2 Temperature effects

Constantinou *et al.* (1999) presented a theory to calculate the temperature rise at the contact surface and at small depth for PTFE-stainless steel interface, in case of intermittent heat flux, i.e. when the amplitude of motion is larger then the radius of the apparent contact area: a general solution for the problem of the semi-finite body with heat flux *q(t)* at depth $x = 0$ may be deduced by applying the Duhamel's theorem (Carslaw and Jaeger, 1959) to the solution of the problem of constant heat flux:

$$T(x,t) = \frac{D^{0.5}}{\pi^{0.5}k}\int_0^t q(t-\tau)\exp\left(\frac{-x^2}{4Dt}\right)\frac{d\tau}{t^{0.5}} \qquad (2.17)$$

$$q = \mu p \dot{u} \qquad (2.18)$$

where D is the thermal diffusivity and k is the thermal conductivity of the solid; q is the generated heat flux, u is the relative displacement of the interfaces and p the apparent bearing pressure. This theory, that assumes that (i) the generated heat is totally supplied by the steel part, (ii) heat conduction in one-dimensional, (iii) heat radiation is negligible and (iv) conditions of half space prevail, was consistent with experimental results. Fig. 2.15 illustrates the effects of temperature on friction. Temperature has a dramatic effect on the breakaway and at very low velocities: about a 7-fold increase for temperature of 50°C and -40°C.

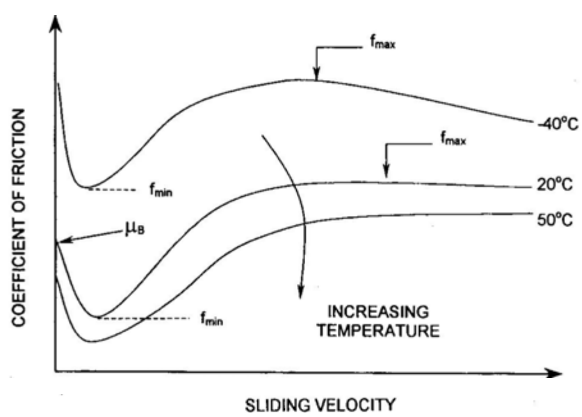

Fig. 2.15. Friction coefficient of PTFE-Polished stainless steel interface at varying velocity and temperatures

The sliding friction is known to decrease with increasing number of cycles, as a result of the heating of the interface. Fig. 2.16 shows this effect experimentally: each series is constituted by the values of the friction coefficient in three consecutive cycles on the bearings.

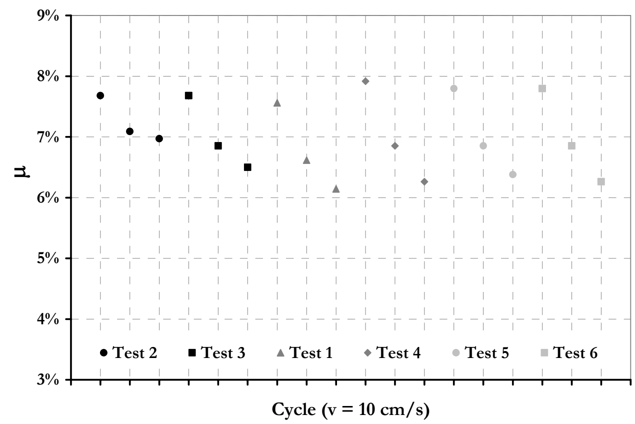

Fig. 2.16. Effect of number of cycles on the friction coefficient (on the courtesy of G. Benzoni, UCSD)

2.4.2 Representations of coulomb friction for dynamic analysis

As long as there is motion, the magnitude of friction force is constant and its direction is opposite of the sliding velocity, and whenever the sliding velocity crosses zero, the friction force suddenly changes its direction: this sudden change is the basic issue of the modelling, as it makes the system extremely non-linear. The form of the friction force is expressed by:

$$F_f = -\mu mg\, \text{Sign}[\dot{u}(t)] \qquad (2.19)$$

A satisfactory representation of the coulomb friction has been implemented through a two-phase model by a number of researchers, but in case of high frequency ground motions, detecting the exact time of the sliding velocity zero-crossing is not possible numerically.

A continouos viscoplastic friction law has been developed by several authors (Bonc, 1971; Wen, 1976; Ozdemir, 1976; Constantinou and Adnane, 1987; Graesser and Cozzarelli, 1991; Nagarajaiah *et al.*, 1993), and improved to incorporate the initial transient frictional response at high frequencies by Bondonet and Filiatrault (1997). Mostaghel and Davis (1997) proposed to replace the discontinuous friction force function with a continuous relationship, selected to be arbitrarily close to the exact discontinuous equation, in order to completely eliminate the need to keep track of stick-slip phases and their transitions. In the form they suggest, the signum function can be represented by any of the following four continuous functions, represented in Fig. 2.17 (right), controlled by the parameter values to obtain any desired level of accuracy.

$$\begin{aligned}
&f_1(\alpha_1, \dot{u}) = \text{Erf}(\alpha_1 \dot{u}) \\
&f_2(\alpha_2, \dot{u}) = \text{Tanh}(\alpha_2 \dot{u}) \\
&f_3(\alpha_3, \dot{u}) = (2/\pi)\text{ArcTan}(\alpha_3 \dot{u}) \\
&f_4(\alpha_4, \dot{u}) = \alpha_4 \dot{u} / (1 + \alpha_4 |\dot{u}|) \\
&\alpha_i > 0
\end{aligned} \qquad (2.20)$$

For practical applications, the functions in (2.20) differ from the signum function in a range of velocities very close to zero, so that when one of them is employed with the factor α_i of the order of 100 or larger, the maximum difference with the analytical solution is less than 1%. The Erf function (f_1) is shown in Fig. 2.17 (left) for different values of α_1.

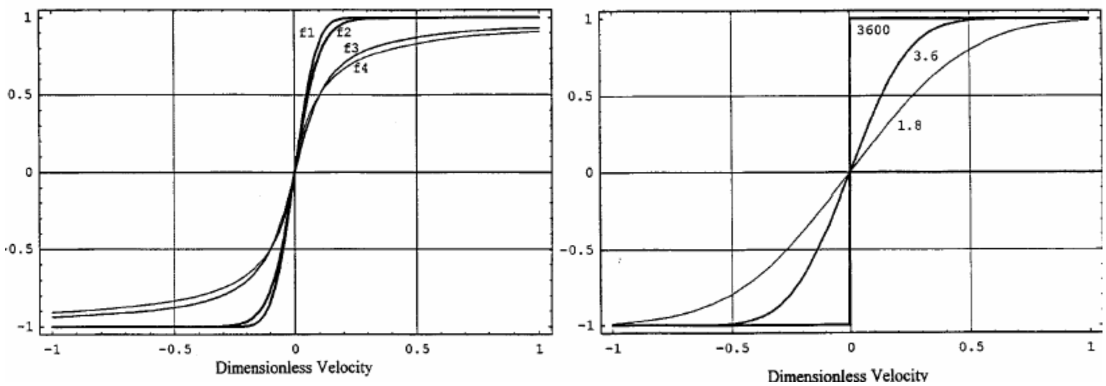

Fig. 2.17. Comparisons of the four representations of the signum function (α_i=10, i=1, 2, 3, 4) (left) and representation of the signum function by f_1 (α_1=1.8, 3.6, 3600) (right)

For the same level of accuracy, the integration time is about the same using f_3 and f_4, shorter than employng f_1 and f_2. The level of approximation can be in any case improved using larger α. It's worth to be noticed that the friction force as defined though the one of the (2.20) is applicable for small as well as for large values of the friction coefficient, and it is valid even if the friction coefficient is a function of the sliding velocity or of time.

2.5 DISSIPATING AND ISOLATING DEVICES

The reference normative framework for designing isolating/dissipating systems is:

- ENV 1998 (Eurocode 8)
- AASTHO Standard specifications for highway bridges
- AASTHO Guide specifications for seismic isolation design
- EN 1337 Structural bearings
- European Standard on Antiseismic devices (under preparation by CEN TC 340)
- Italian Ordinanza 3274, (20 March 2003)

The design properties of isolators/dissipators depend on their behaviour, which may be one or a combination of the following:

- HYSTERETIC BEHAVIOUR: the force-displacement relation of the isolator unit may be approximated by a bilinear relation (Fig. 2.18). The parameters characterising the bi-linear law are: the yield force at monotonic loading F_y, the force at zero displacement at cyclic loading F_0, the elastic stiffness at monotonic loading K_e (equal to the unloading stiffness at cyclic loading), the post elastic (tangent) stiffness K_p, the energy dissipated per cycle E_D at the design displacement d_d, (equal to the area enclosed by the actual hysteresis loop).
- VISCOUS BEHAVIOUR: the force of viscous devices is proportional to v^{α} , where v is the velocity of motion. The force is zero at the maximum displacement and therefore does not contribute to the effective stiffness of the isolating system. The force-displacement relation of a viscous device is shown in Fig. 2.18 (for sinusoidal motion), and depends on the value of the exponent α.

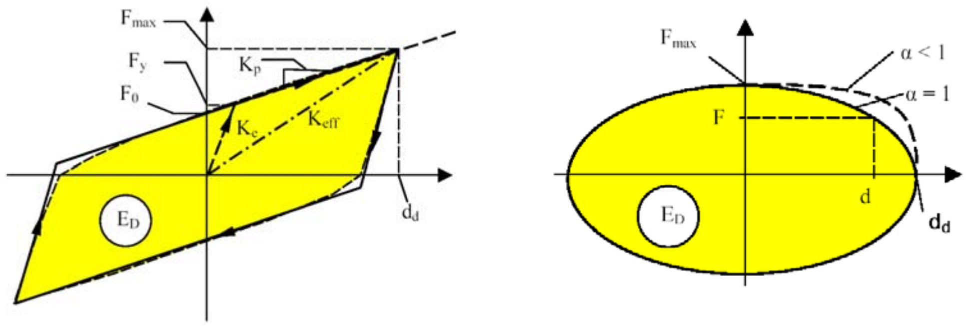

Fig. 2.18 General hysteretic behaviour (left) and viscous behaviour (right)

- FRICTION BEHAVIOUR Type 1: sliding devices, with flat sliding surface, limit the force transmitted to the superstructure to equation (2.21), where N_{sd} is the normal force on the device (Fig. 2.19, left). Due to the possible substantial permanent offset displacements, they should be used in combination with devices providing adequate restoring force.

$$F_{max} = \mu_d N_{sd} \mathrm{sign}(\dot{d}) \qquad (2.21)$$

- FRICTION BEHAVIOUR Type 2: sliding devices, with spherical sliding surface of radius R_b (e.g. Friction Pendulum Bearings), provide a restoring force proportional to the design displacement d_d (equation (2.22) and Fig. 2.19, right), and a force displacement relation given in equation (2.23), which is a small displacement approximation.

$$F_{restoring} = \frac{N_{sd}}{R_b} d_d \qquad (2.22)$$

$$F_{max} = \frac{N_{sd}}{R_b} d_d + \mu_d N_{sd} \mathrm{sign}(\dot{d}) \qquad (2.23)$$

In either of the two cases, the energy dissipated per cycle E_D at the design displacement d_d is:

$$E_D = 4\mu_d N_{sd} d_d \qquad (2.24)$$

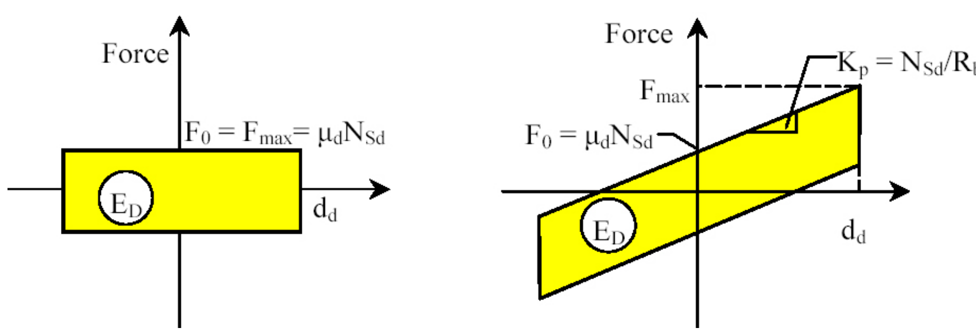

Fig. 2.19. Sliding Friction Hysteretic behaviour for Flat (left) and Curved (right) Surfaces

2.5.1 Antiseismic device typologies

This section briefly introduces different anti-seismic devices with their main hysteretic characteristics. The functions of an isolating/dissipating system are generally one or a combination of the following: (i) supporting gravity loads, (ii) providing lateral flexibility, (iii) providing restoring force, (iv) providing energy dissipation, either of hysteretic or viscous nature. According to their main characteristics, common types of antiseismic devices can be grouped in the following typologies: dampers, elastomeric isolators, sliders.

2.5.1.1 Dampers

Dampers are passive energy dissipating devices able to damp out seismic energy. They are essentially "mechanical" dampers, based on the concepts of not involving external power sources and dissipate energy as structure deforms. They can be grouped into: Metallic (Steel hysteretic)/Friction Dampers and Viscous (Hydraulic) Viscoelastic Dampers. Aside those passive devices, active and semi-active dampers have been recently developed based on the polarising properties of electro and magnetorheological fluids subjected to electric and magnetic fields.

Dampers typologies are:

- Friction Dampers: Sumitomo Devices, Pall Devices;
- Metallic Dampers: yielding steel systems, lead extrusion devices, sometimes combined with bearings to form sliders;
- Viscous and Viscoelastic Dampers: Taylor Devices;
- Lock-up Devices: shear links, sometimes combined with Hysteretic Dampers;
- Self-centring Dampers: Shape Memory Alloys, Energy Dissipation Restraints, SHAPIA Devices;
- Electro and Magnetorheological Dampers;

2.5.1.2 Elastomeric isolators and lead rubber bearings

Elastomeric isolators are laminated rubber bearings consisting of rubber layers reinforced by integrally bonded steel plates (Fig. 2.20, left). They can be either low damping or high damping bearings. Low damping elastomeric bearings have an equivalent viscous damping ratio $\xi \approx 0.05$ (±20%). Their behaviour may be approximated by that of a linear elastic element, with unscragged (§ 7.2) secant shear modulus at shear strain of 2.0, G = 1.0 MPa (±15%). High damping elastomeric bearings show a substantial hysteresis loop corresponding to an equivalent viscous damping ratio of 0.10 to 0.20. Normally, the equivalent viscous damping is a function of the displacement. The force-displacement relationship for these devices is linear, with added equivalent viscous damping. The insertion of a lead plug in an elastomeric isolator (Fig. 2.20, right) provides energy dissipation for seismic response and stiffness for static loads. The hysteretic cycle is approximated as elasto-plastic. The actual hysteresis loop is more complex: the force-displacement relationship of typical elastomeric isolation bearings is non-linear as a result of their inherent damping properties. Experimentally obtained shear force-displacement relationships for elastomeric bearings show strong non-linearities and stiffening behaviour dependent on shear strain magnitude (Fig. 2.21). In particular, large lateral displacements and axial loads on the bearings influence the critical load, the horizontal stiffness, the damping, the height and the overturning of the bearings.

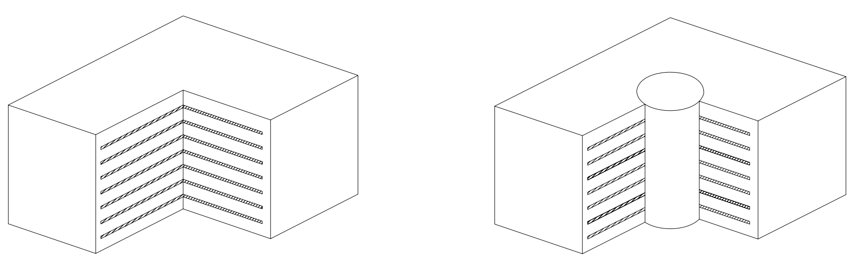

Fig. 2.20. Laminated (left) and Lead (right) Rubber Bearings

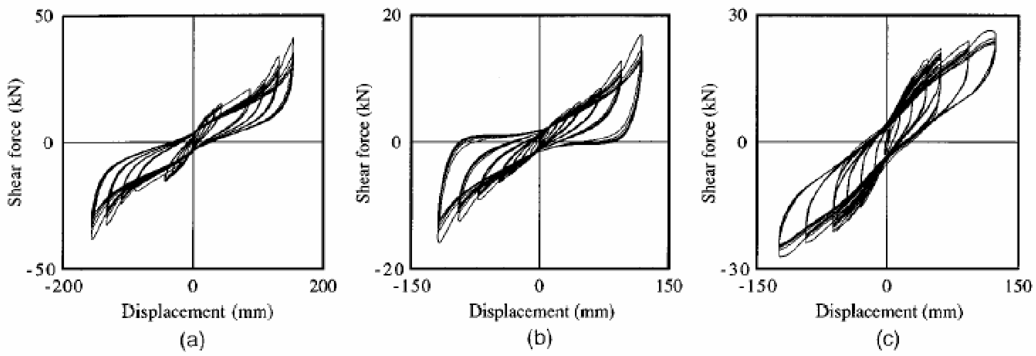

Fig. 2.21. Hysteretic loops obtained from tests of individual bearings: (a-b) high-damping; (c) lead-rubber.

2.5.1.3 Sliding devices

This class consists of sliding supports providing frictional damping forces. These devices can be either sliding bearings or friction pendulum systems. The Sliding Bearings like stainless steel – PTFE bearings are widely used in bridge design to accommodate slow thermal movements. Their approximately rectangular force-displacement loop provide very high hysteretic damping, however, the high initial stiffness may lead energy into higher modes. The Friction Pendulum System (FPS, Fig. 2.22) is an isolation system given of a built-in self-centering action, due to the concavity of its sliding surface.

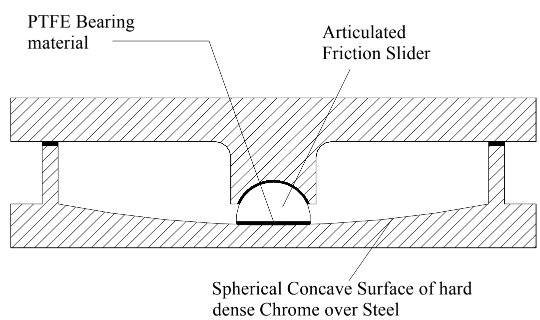

Fig. 2.22. Radial section of the FPS device

The hysteretic loop of FPS is approximately rigid plastic with post yielding hardening. The actual hysteresis loop is more complex, depending on a series of factors, the main of which is the strong dependence of their response on the axial force variation on the device. The actual constitutive law of the FPS element is an elasto-plastic type with strain hardening: the yielding shear and the post elastic stiffness depend on the axial force, resulting in a hysteresis loop extremely varying from the standard constant shape (Fig. 2.23). Other issues related to this kind of devices regard the variability in the friction coefficient properties, due to the vertical pressure, to the sliding velocity and to the temperature.

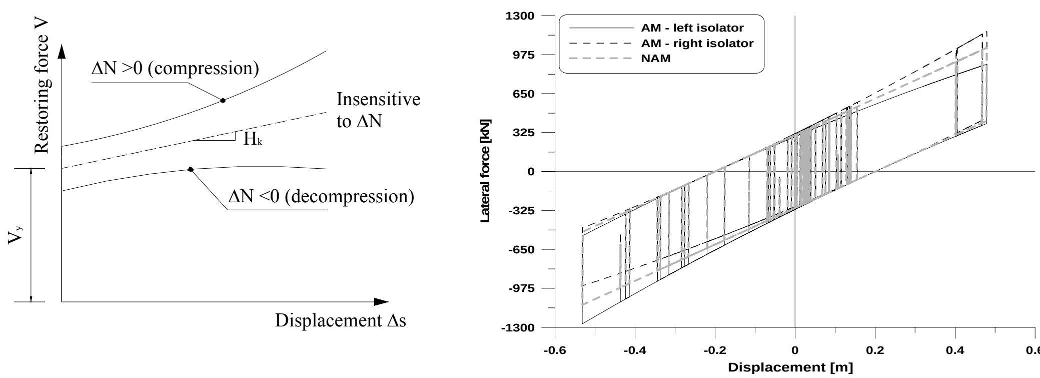

Fig. 2.23. FPS Constitutive law (left) and hysteresis loops (right): simplified and advanced models

2.5.2 Isolation/Dissipation systems issues

A number of issues are related to the employment of isolator and dissipator devices, among these:

- Advanced Modelling Issues. The illustrated representations of the global force-displacement relationships of the devices are in general a first approximation of the actual behaviour: the differences in advanced and simplified models, according to the observations on the actual behaviour illustrated in § 2.5.1, may lead to differences in the structural response whose importance has to be evaluated. Once refined models for different isolation systems are developed, it should be studied how they influence the structural response, in order to find out protection factor for different isolation systems, when a simplified model of the devices is employed. In other words, if the seismic demand on piers, or generally on the structure, increases when the refined models are used, the simpler modelling might be allowed, provided that adequate protection factors are accounted for.
- Re-centering problem. The problem of re-centring the bearing in its original position after an event that cause any kind of offset is relevant in designing the Isolation/Dissipation system. Only pure spring with zero-damping are perfectly re-centring, while energy dissipation generate residual displacements; particularly, anti-seismic devices based on friction may offset due to thermal effects or small earthquakes as long as the friction force is equilibrated by the re-centring force. On the contrary hysteretic dampers, up to yielding, act as perfect springs.
- The Heat Generation Problem. The heat generation due to the relative movement in the device might be a problem for the correct functioning or the life of the isolator/dissipator itself. Marioni (2002) analysed numerical examples of different devices, having the same characteristics in terms of period of the isolated structure, design displacement and number of cycles during the earthquake. Table 2.1 shows a comparison among the devices in terms of temperature increase per cycle: it can be easily seen that heat generation may be critical for some kind of energy dissipating anti-seismic devices, for which full scale dynamic tests are envisaged.

Table 2.1. Comparison of temperature increase per cycle for different antiseismic devices

	Thermal Capacity (kJ/kg°C)	Temperature Increase/Cycle (°C)
Flexural Hysteretic Steel Dampers	0.502 (steel)	5.33°C
LRB	0.129 (lead)	27.3°C
HRDB	0.8 (rubber)	6.4°C
Friction Device	0.502 (steel)	(temperature given by the solution of Fourier Equation, as a function of time and distance from the interface)
Viscous Dampers		thermal behaviour as a function of the pressure and the size of the damper

3. DEVICE TYPOLOGIES: METALLIC AND FRICTION DAMPERS

This kind of dampers, relatively economic, are used when a control is needed on the level of the provided force, when an increased initial structural stiffness is needed, and/or when the main concern is to reduce displacement as opposed to acceleration. Friction Dampers dissipate the seismic energy by friction developing between two solid bodies sliding relatively one to the another. Typical examples of these devices are:

- Slotted-bolted connections;
- Pall devices;
- Sumitomo Devices.

Metallic dampers take the advantage of hysteretic behavior of metals when deformed into the post-elastic range. A wide variety of different types of devices have been developed, with basic shapes cut from thick steel plates, among these:

- C/E-shaped Hysteretic Dampers;
- EDU device;
- ADAS and TADAS Elements;
- Lead Extrusion Devices;
- Torsional beams, bell dampers, steel tubes, etc;

3.1 BASIC HYSTERETIC BEHAVIOUR AND DYNAMIC RESPONSE WITH METALLIC/FRICTION DEVICES

The macroscopic model and the analysis of the dynamic response of structures equipped with metallic and friction dampers is basically the same, due to the essentially equivalent elastic-perfectly plastic behaviour exhibited by the devices (Fig. 3.1).

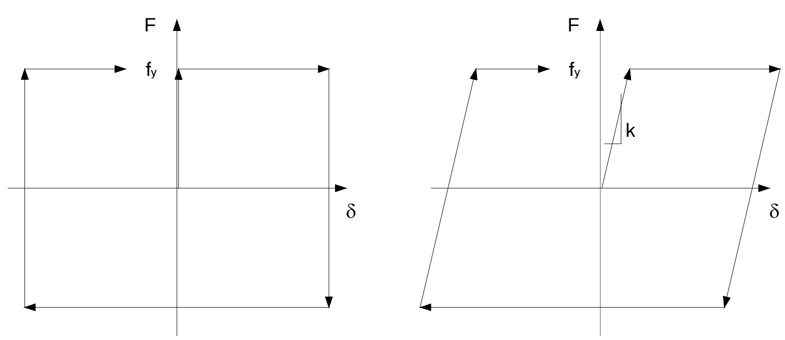

Fig. 3.1. Friction/Metallic Dampers hysteretic loops (f_y is the slip/ yield load for friction/yielding dampers)

Fig. 3.2 illustrates the Dynamic Amplification Factor (DAF) of a SDOF structure (of dynamic characteristics M, K, C), with a viscous damping of the 5%, given of a yielding damper (f_y, k) of negligible mass, subjected to sinusoidal excitation of amplitude P_0, : the DAF is strongly reduced depending on the ratios k/K and f_y/P_0. In order to understand the nature of the dynamic response of structures equipped with metallic/friction dampers, the simple system of Fig. 3.3 (left) is considered as excited by a cosinusoidal driving force. Fig. 3.3 (right) shows the decomposition of the forces as carried by the diagonal braces of a general braced subsystem. The corresponding transmitted shear is:

$$V_{si} = 2P_{yi} \cos \alpha_i \tag{3.1}$$

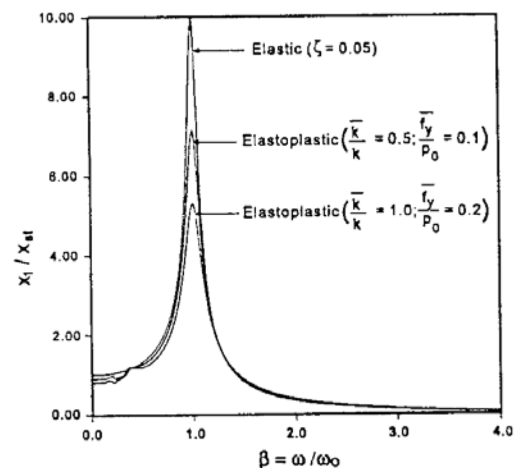

Fig. 3.2. DAF for harmonic base excitation with yielding device

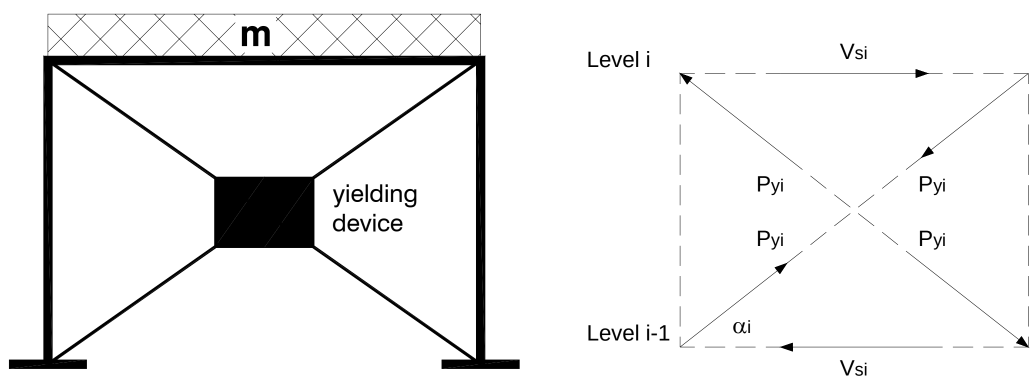

Fig. 3.3 Single Storey Friction/Metallic Damped Structure (left) and General decomposition of the braced sub-system (right)

3.1.1 Response at resonance

The condition on the brace yield load to provide bounded amplitudes at resonance (Filiatrault, 2003) is:

$$\frac{2P_y \cos \alpha}{W} > \frac{\pi}{4} \frac{a_g}{g} \tag{3.2}$$

It may be noted that not only a bounded response is not unconditionally obtained (condition (3.2)), but it also depends on the ground motion. Besides, it can be demonstrated that the resonance amplitude is minimized if the following applies:

$$\frac{2P_y \cos \alpha}{W} = \frac{\pi}{2} \frac{a_g}{g} \tag{3.3}$$

It is noted that the displacement corresponding to condition (3.3) is greater than the yield displacement, i.e. the structure at resonance is already yielded, regardless the value of the yield load. Solution for minimizing response at frequencies other then resonance cannot be found analytically, but it can be shown (Filiatrault, 2003) that the condition is of the type:

$$\frac{2P_y \cos\alpha}{W} = \frac{a_g}{g} Q\left(\frac{T_b}{T_g}; \frac{T_b}{T_u}\right) \qquad (3.4)$$

Where the multiplier of a_g/g is a function Q of the ratios of the period of the braced structure (T_b) respectively to the period of the ground motion (T_g) and to the period of the unbraced structure (T_u). It can be expected that these parameters will be important in case of a system excited by a general earthquake ground motion: generally speaking, the optimum yield load depends on the frequency and amplitude (in particular linearly proportional to this latter) of the ground motion and it is not a strictly structural property.

3.2 FRICTION DAMPERS

In the case of friction dampers, the design philosophy to enhance the structural performance is to provide a way for the structure to yield without damaging the existing structural members: seismic energy is dissipated by mean of friction, i.e. by making steel plates sliding one against the other, while bolts hold the steel plates together providing the normal component of the friction force. Sliding plates are fixed to the cross braces and then clamped together. At a given sliding load, P_y, the plates begin to slide and dissipate energy. Varying the sliding load will alter the seismic energy attracted by the structure.

Incorporating the braces adds initial lateral stiffness to the system, thus lowering the natural period of the structure and providing a margin over which the structure can shift its period if resonance is encountered: any time the current structural period attracts seismic energy enough to activate the friction dampers, the resonance phenomenon can be avoided by a period shift. When in fact at the low braced period the structure attracts large amounts of seismic energy, the structure begins to soften as the friction dampers begin to slip and dissipate energy: the reduced lateral stiffness of the structure, due to the dampers slippage, causes the desired period shift. If the braced natural period is moved far from the unbraced natural period, the structure will have a sufficient ability to soften.

3.2.1 Advantages and disadvantages of friction dampers and environmental effects

These devices possess good characteristics of structural behavior. Some of their advantages are the listed below:

- They have high capacity of energy dissipation; compared to devices based on yielding of metals, friction dissipators possess a great capability of absorbing energy. This characteristic disappear with the wearing of the sliding surfaces.
- Their behaviour is not seriously affected by the amplitude, the frequency contents or the number of cycles of the driving force.
- They have a controllable friction force (through the pre-stressing normal force).
- Frictions dissipators are not affected by fatigue effects; the materials are low maintenance or even maintenance free.
- Friction dampers perform well in various environmental conditions such as temperature.
- The damper design is straightforward and low tech: the design does not require expensive engineering design costs or testing prior to implementation.

Some potentially relevant disadvantages exhibited by Friction dissipators are:

- The energy dissipated per cycle is only proportional to the maximum displacement instead of the square of the same displacement, as in the case of viscous damping: this can be relevant for sudden pulses and for inputs stronger than those expected. Moreover, resonance peaks can not be properly cut.
- Durability is also a controversial issue, mostly due to the high sensitivity of the coefficient of friction to the conditions of the sliding surfaces.
- High frequencies can be introduced in the response, due to the frequent and sudden changes in the sticking-sliding conditions. The dynamic highly non-linear behavior of friction dissipators makes their numerical simulation very difficult. This situation has arisen some controversial issues, such as the possible introduction of high frequencies into the structural response, as well as the lack of studies of these devices when subjected to near-fault pulses.

Environmental effects might alter the frictional characteristic of the sliding interface. Critical conditions to be assessed in a design situation are:

- Localised heating of the contacting materials during slippage: on occasions, these thermal effects may alter the frictional response by causing material softening or by promoting oxidation. However, for the type of sliding systems typically encountered with friction dampers, system response will be barely sensitive to the relatively small variations in ambient temperature.
- Atmospheric moisture and contaminants: physic-chemical processes may be triggered by atmospheric moisture of contaminants, occurring at the material interfaces. These processes may change the physical and chemical character of the surfaces, thus significantly affecting the frictional response.
- Formation of oxide layers or scale on the exposed surfaces.
- Crevice corrosion (cathodic/anodic effect between exposed and inaccessible regions) and Bimetallic corrosion: in aggressive environments, corrosion may be a problem. It is necessary to rely on physical testing to determine the extent of corrosion expected in a given situation and to find out the potential effects on the frictional characteristics of a sliding system.

3.2.2 Numerical simulation of friction dissipators

The dynamic behavior of friction dissipators is closely related to the contact theory since there are friction forces generated by sliding surfaces. Basically, the numerical simulation of friction dampers is based on the rectangular relationship friction force-displacement (Fig. 3.1, left). The way of modeling Coulomb friction and advanced modeling of the property modification factors of the coefficient of friction were also discussed in §2.4. In order to carry out the numerical simulation of structures equipped with friction dampers, some computer programs have been written specifically with this purpose while others use commercial software packages such as DRAIN-2D, DRAIN-TABS, SADSAP, SAP2000NL or ADINA. Basically, the existing models fall into one of these two categories:

- Models where the dynamic behaviour of the friction dissipators is described by the contact analysis and plasticity theory. Usually the equations of motion are solved by using Lagrange multipliers or penalty methods (e.g. ADINA). This approach can be accurate but it is costly in terms of computational effort.
- Simpler models where elasto-plastic laws for the friction dissipators are implemented in finite element models of the whole structure (DRAIN-2D, DRAINTABS, SADSAP, SAP2000NL). These models have been developed to simulate, approximately, the perfectly plastic shape of the hysteretic loops using an elastic-plastic hysteretic model and considering for the initial stiffness any big value to approach an 'ideal' vertical branch. This approach might lack of accuracy.

3.2.3 Friction damper typologies: slotted-bolted connections

The simplest form of friction dampers are the Slotted-bolted Connections introduced at the end of conventional bracing members (Fig. 3.4). It is important to ensure that the slippage of the device occurs before the compressed braces buckle or yield. Each connection incorporates a symmetric shear splice with slotted holes in the connecting plates extending from the bracing member: the slot length has to accommodate the maximum slip anticipated from the design earthquake. Disc spring washer can be used in the bolting assembly to accommodate the possible variation in the plate thickness due to the wear at the contact surfaces and to the temperature rise resulting from friction heating. Tests results performed by Pall *et al*. (1980) and Tremblay and Stiemer (1993) show that sliding connections can exhibit a very high energy dissipation capability under extreme loading conditions, provided that appropriate materials and bolt clamping forces are used.

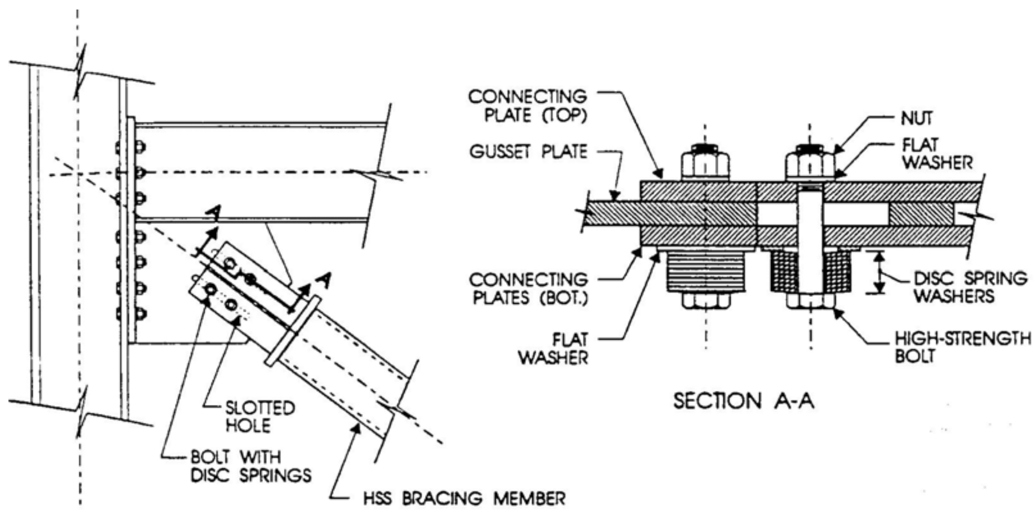

Fig. 3.4. Slotted Bolted Connection Assemblage (Tremblay and Stiemer, 1993)

3.2.3.1 Detailing aspects

Bracing members shall be selected in order to minimize cost and optimize the building performance. It is important in the detailing of the brace to avoid the that yielding of the sliding surfaces. It is possible (Fig. 3.5) to incorporate four or even six large diameter bolts in the oversized slots. Using these large diameter bolts will allow the total clamping force to be safely applied. These bolts will have to spread the clamping force over a sufficient area to ensure that localized compressions do not inhibit the sliding of the plates. Should this retrofit proposal be selected in terms of performance and cost, this is an important aspect to address.

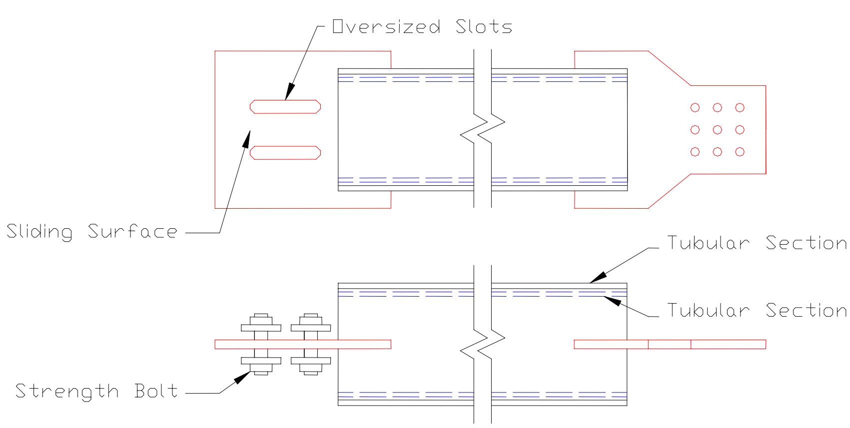

Fig. 3.5. Bracing Details

3.2.4 Friction damper typologies: Pall devices

The Pall Device consists of diagonal brace elements with a friction interface at their intersection, connected together by horizontal and vertical link elements (Fig. 3.6, left). These link arms ensure that when the load applied to the device via the braces initiate the slip on the tension diagonal, then the compression diagonal will also slip of an equal amount in the opposite direction (Fig. 3.6, right). The normal force on the sliding interface, responsible for the friction resistance, is achieved through a bolt at the intersection of the diagonal arms. Utilization of this type of geometric deformation in the cross bracing of a building frame (or in multi-bent bridge pier or deck) is a way to permit substantial controlled energy dissipation (Tyler, 1983), as shown by the typical hysteretic loop of a Pall Device in Fig. 3.7.

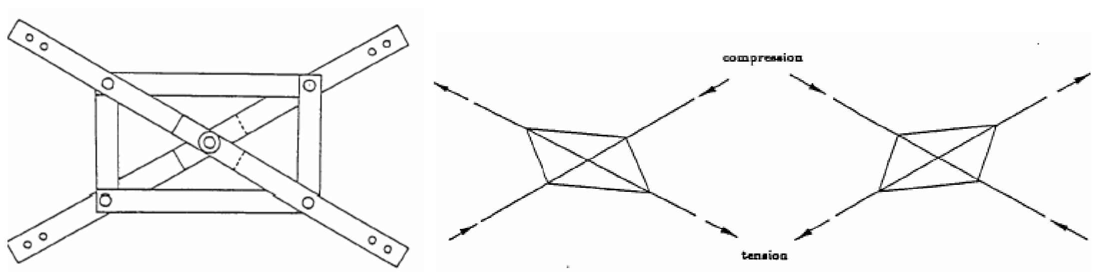

Fig. 3.6. Pall Friction Damper: Device and Deformed Configurations

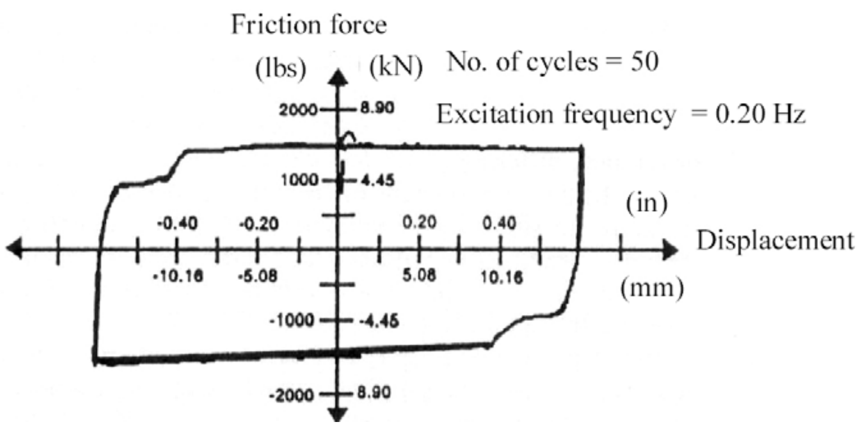

Fig. 3.7. Hysteretic loop of a Pall Friction Device

3.2.5 Friction damper typologies: Sumitomo devices

The Sumitomo Device was designed and developed by Sumitomo Metal Industries, Ltd., Japan, originally as a shock absorber in railway rolling stock. It is a cylindrical device with friction pads that slide directly on the inner surface of the steel casing of the device (Fig. 3.8). The friction devices might be attached to the underside of the floor beams and connected to chevron brace assemblages. The Sumitomo dampers exhibited outstanding behavior: their hysteretic behavior is extremely regular and repeatable (Fig. 3.9). The devices show almost no variation in slip load during earthquake motion; their force-displacement response is known to be quite independent of loading frequency, amplitude, number of loading cycles, and temperature.

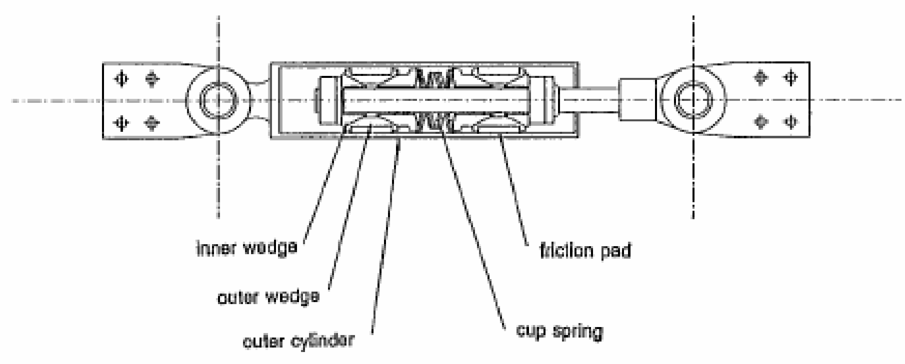

Fig. 3.8. Sectional view of the Sumitomo friction damper

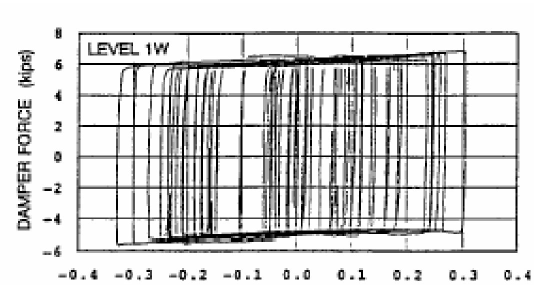

Fig. 3.9. Typical damper hysteresis loops (Aiken et al., 1993)

3.3 STEEL HYSTERETIC DAMPERS

Hysteretic dampers originated in New Zealand in the early 1970's, and were first used in the U.S. in the early 1980's. Hysteretic dampers dissipate energy by flexural, shear or extensional deformation of the metal in the inelastic range. Typically, mild steel plates with triangular or hourglass shapes are used. These devices are able to sustain repeated cycles of stable yielding, avoiding premature failure. Further, they are reliable, maintenance free, not sensitive to temperature variations and not subjected to ageing. In continuous span bridges, they may be located either in one position (e.g. one abutment) to allow free movements of the bridge (in this case they must be designed for very large forces), or distributed in several locations to allow thermal movements of the structure (normally associated to hydraulic shock transmission units). The steel used for these devices must be characterized by a very high elongation at failure and a very low hardening, in order to grant a very high low-cycle fatigue life with negligible performance decay after many cycles. There are three types of metallic damper, according to their working principle:

- Uniform moment bending beam with transverse loading arms;
- Tapered-cantilever bending beam;
- Torsional beam with transverse loading arms;

Several devices developed in the early 1980's showed some limits: reduced capacity to resist yield cycles without breaking, characteristic degradation after first cycles with progressive reduction of the yield force up to failure, asymmetry of the load-displacement cycles with stiffness variations in tension and compression and difficulty to provide uniform response in any direction.

New devices overcoming these limits have been developed. They are based on the combination of C-shaped elementary energy dissipators. Tests on these devices have shown long cyclic life, almost no cycle deterioration before failure and very good dissipation thanks to the almost square shape of the hysteresis loops (Fig. 3.16).

These devices may constitute either the dissipative part of a seismic isolation system of the bridge deck, or they may simply act as dampers by themselves. Then they can be arranged to be a part of one-directional or multidirectional bridge bearings. The conceptual design of the single damper unit is based on optimisation criteria, i.e.:

- An optimised shape allows almost constant strain range across each section: in this way, the diffusion of plasticization is uniform over the most of the volume, and, by preventing localisation and concentration of deformation, extended low-cycle fatigue life is obtained.
- Particular design arrangements neutralise the effects of geometry changes, that otherwise can cause strain hardening or softening behaviour and/or asymmetrisation of the hysteresis cycles at large displacements: the dissipation effectiveness is improved, and large displacements and damping of response in all directions are allowed.

Design process of Hysteretic Dampers is based on the bi-linear load-deflection plot (Fig. 3.16) given by the manufacturer. Marioni (1996) suggest selecting, by trial and error, the Hysteretic Dampers such that the sum of yield forces is:

$$\begin{aligned} &\sum F_y = 0.1\ W \qquad \text{(high seismicity area)} \\ &\sum F_y = 0.07\ W \qquad \text{(low seismicity area)} \end{aligned} \tag{3.5}$$

where W is the total weight of the structure. Nonlinear analyses are always required in order to check the design displacement: if it’s too small (too large), the sum of the yield forces have to be increased (decreased), in order to rise (low) the threshold of the yielding and increase (reduce) the energy dissipated by the structure. Some more sophisticated method is further illustrated in details.

In the preliminary design of structures equipped with metallic/friction devices, particular attention might be paid to the substitution of the nonlinear system by a linear system with equivalent viscous damping. This might be done just for a very preliminary estimation of the dynamic response: because of the nonlinear nature of real yielding devices, the results obtained through the linear system with equivalent viscous damping might be non-conservative, either because the equivalent viscous damping is estimated at the maximum amplitude cycle or because the use of damping always reduces the dynamic response: nonlinear time history analyses are envisaged in order to fully asses the effect of supplemental damping devices on the structures.

3.3.1 Numerical simulation of metallic dissipators

The family of force-displacement loops for a bending-beam or twisting-beam damper can be scaled on the basis of a simple model, to give a set of stress-strain curves (Skinner *et al*., 1993). Approximate force-displacement loops for a wide range of steel-beam dampers can be obtained from the scaled stress-strain curves (Fig. 3.10, left), by means of the force and displacement scaling factors found in Skinner *et al.* (1993), depending on the damper shape and based on a simplified model of the yielding beam.

For design purposes, the curved force-displacement loops are usually approximated by bilinear hysteresis loops with an initial stiffness K_{b1}, a yielded stiffness K_{b2} and a yield force Q_y. The approximated bilinear hysteresis loop is shown in (Fig. 3.10, right): the curved loop A'B'ABA' is symmetric about the centre O, and the coordinates of the vertices A and A' are the maximum cycle displacements X_b and the maximum force S_b. The initial stiffness K_{b1} is the slope of the parallel lines AB, A'B', where B and B' are the loop intercepts on the X-axis. The yield stiffness K_{b2} is the slope of the parallel lines AC, A'C', where CC' is the line through O with slope K_{b1}.

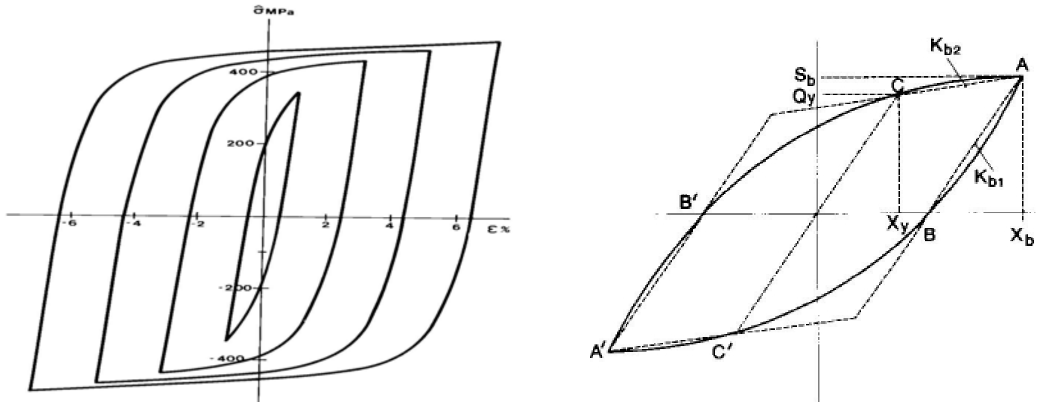

Fig. 3.10. Scaled stress-strain loops for a steel-beam damper (left) and bilinear approximation (right)

3.3.2 Hysteretic Damper Typologies: E-shaped Devices

The E-shaped Device is shown in Fig. 3.11: it can be viewed as a symmetric one storey, two-bays portal frame, hinged at the base (Fig. 3.12). The device is forced to deform anti-symmetrically in the elasto-plastic range: the legs are designed to act essentially as lever arms, deforming elastically, while the energy dissipation occurs only in the transverse beam, where the desired uniform plasticization is ensured by the acting constant moment.

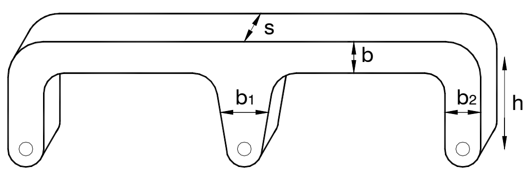

Fig. 3.11. Typical E-Shaped hysteretic damper layout

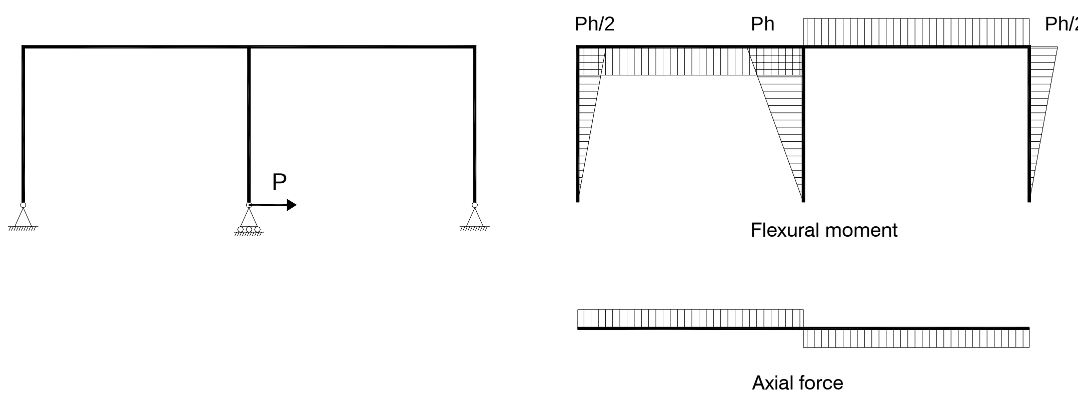

Fig. 3.12. Static Scheme of an E-shaped hysteretic damper

The fact that both moment and axial force have opposite sign in the two parts of the transverse beam allows the neutralization of the geometry changes effects and permit to avoid the progressive accumulation of axial strain, that is the main source of deterioration at increasing number of cycles in those devices in which moment alternates and axial force does not: E-shaped Hysteretic Dampers are characterized by a high repetition of hysteresis cycles (>50), very low degradation after 50 cycles and very high dissipating efficiency (>70%). Mechanical quantities characterising the device are shown in Equation (3.6), referring to the geometry in Fig. 3.11.

$$
\begin{aligned}
M_y &= \sigma_y \frac{sb^2}{6} & M_p &= \sigma_y \frac{sb^2}{4} \\
P_y &= \sigma_y \frac{sb^2}{3h} & P_p &= \sigma_y \frac{sb^2}{2h} \\
\delta_y &= 2\frac{hl}{b}\varepsilon_y\left(1+\frac{\alpha}{3}\frac{h}{l}\right) & \delta_{max} &= 2\frac{hl}{b}\varepsilon_{max}\left(1+\frac{\alpha}{2}\frac{h}{l}\frac{\varepsilon_y}{\varepsilon_{max}}\right) \cong 2\frac{hl}{b}\varepsilon_{max} \\
\alpha &= 2\left(\frac{b}{b_1}\right)^3+\left(\frac{b}{b_2}\right)^3
\end{aligned}
\tag{3.6}
$$

M_y and M_p are the yielding and plastic moments of the transverse beam, P is the corresponding transverse load and δ is the displacement at the location where P is applied. Typical values of maximum axial strain for mild steel dampers are in the range of 3% for the design earthquake and 5% for the extreme event, and generally the local ductility μl, represented by the ratio of the ultimate to yielding axial strains is around 15-20. The global displacement ductility μ and the elastic stiffness K of the device are:

$$
\mu = \frac{2}{3}\mu_l \frac{\left(1+\frac{\alpha}{2}\frac{h}{l}\frac{\varepsilon_y}{\varepsilon_{max}}\right)}{\left(1+\frac{\alpha}{3}\frac{h}{l}\right)} \cong \frac{2}{3}\mu_l \frac{1}{\left(1+\frac{\alpha}{3}\frac{h}{l}\right)}
\tag{3.7}
$$

$$
K = \frac{P_y}{\delta_y} = \frac{1}{6}E\frac{sb^3}{h^2 l}\frac{1}{\left(1+\frac{\alpha}{3}\frac{h}{l}\right)}
\tag{3.8}
$$

3.3.3 Hysteretic damper typologies: C-shaped devices and EDU device

C-shaped elements grant very high energy dissipation, very high fatigue resistance and allow the realisation of multidirectional devices (Fig. 3.13).

Fig. 3.13. C-shaped device (left) and EDU device (right)

A typical C-shaped damper has a semicircular shape (Fig. 3.13, left), with constant radius r, while depth varies in order to ensure uniform plasticization through each section. By equating the moment at a generic section of height *b(a)* to the plasticization moment of that section it is obtained:

$$b(\alpha) = b_{max}(sen\alpha)^{1/2} \qquad (3.9)$$

Where α is polar coordinate referring to the centre of the C device (Fig. 3.14). The maximum depth b_{max} is in the middle, and the minimum at the supports, where it is small enough to guarantee the shear and axial load transfer. The angular opening of the device is generally 180°, or greater when the displacement demand is particularly high. Equations (3.10) gives the yielding and plastic quantities of the device.

$$\begin{aligned} M_y &= \sigma_y \frac{sb(\alpha)^2}{6} & M_p &= \sigma_y \frac{sb(\alpha)^2}{4} \\ P_y &= \sigma_y \frac{sb_{max}^{\ 2}}{6r} & P_p &= \sigma_y \frac{sb_{max}^{\ 2}}{4r} \\ \delta_y &= 4.824 \frac{r^2}{b_{max}} \varepsilon_y & \delta_{max} &= 4.824 \frac{r^2}{b_{max}} \varepsilon_{max} \\ \mu &= \frac{2}{3}\mu_1 & K &= 0.03455E \frac{sb_{max}^3}{r^3} \end{aligned} \qquad (3.10)$$

or, when opening exceed 180°:

$$\begin{aligned} P_y &= \sigma_y \frac{sb_{max}^{\ 2}}{6} \frac{1}{r(\cos\alpha_0 + 1)} \\ b(\alpha) &= b_{max}\sqrt{\frac{\cos\alpha_0 - \cos\alpha}{\cos\alpha_0 + 1}} \\ \delta &= 4\frac{r^2}{b_{max}}\varepsilon_{max}\sqrt{\cos\alpha_0 + 1}\left[\int_{\alpha_0}^{\pi}\sqrt{\cos\alpha_0 - \cos\alpha}\, d\alpha\right] \end{aligned} \qquad (3.11)$$

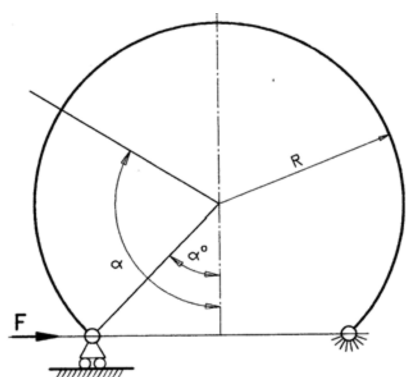

Fig. 3.14. C-shaped device static scheme

The very simple equations (3.10) and (3.11) consider only bending deformation, and, not accounting for geometry changes, are valid for very small displacements. When geometry changes are important, hardening in tension and softening in compression is expected. To avoid this effect, C-shaped devices are usually coupled in such a way to behave as E-shaped devices: compared the latters, in the C-shaped device the material is used better, as almost all plasticised.

3.3.3.1 The EDU device

The EDU Device is a multi-composed device constituted by C-shaped elementary energy dissipators (Fig. 3.13, right, Fig. 3.15), combined in order to be forced to deform anti-symmetrically, i.e. for each compressed one, another is in tension; the radial symmetry allows uniform behaviour under earthquake loading acting in any direction. This device can be coupled with hydraulic shock transmitters in parallel.

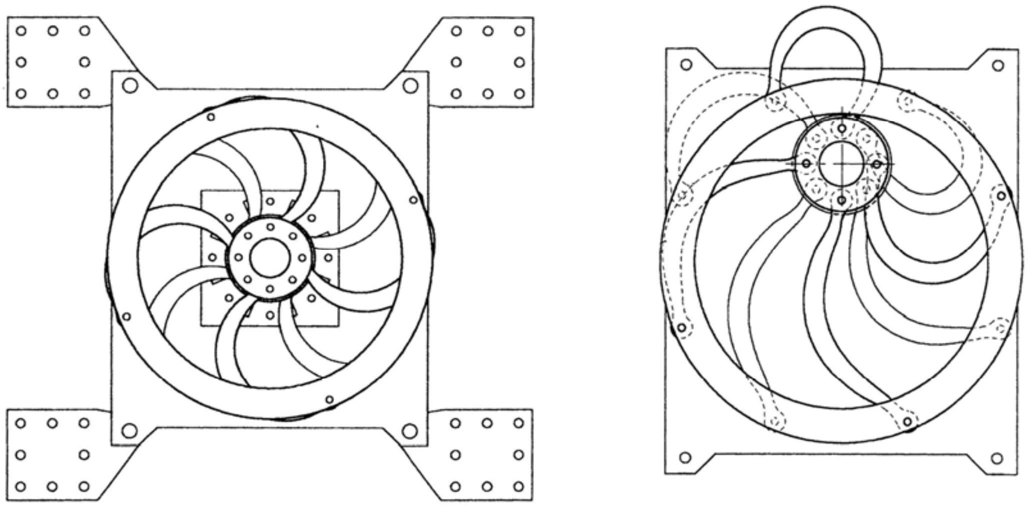

Fig. 3.15. EDU Device: device and deformed configuration

Different design requirements, different responses in longitudinal and transverse directions or unidirectional devices can be easily met by a suitable arrangement of the elementary dissipators or combining elementary dissipators with different stiffness. The EDU device has been tested by Marioni (1996) with a real earthquake of 7.4 magnitude with PGA of 0.8g: the device proved to be able of dissipating much more energy (Fig. 3.16) than any other system and fulfilled European standards for in-service conditions. It showed self-recentering properties for thermal effects and small earthquakes, and, when used in parallel with high damping rubber bearings, could fulfil any AASHTO requirement. Due to its conceptual simplicity, the EDU device has low costs.

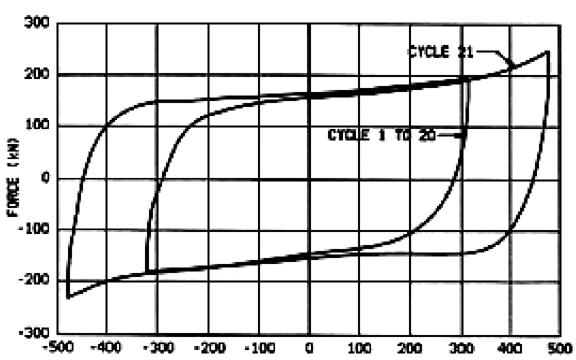

Fig. 3.16. Load deflection plot of the EDU device (Marioni, 1996)

3.3.4 Hysteretic damper typologies: ADAS and TADAS elements

The Bechtel Added Damping and Stiffness (ADAS) device is another example of a hysteretic damper. The X-plate constituting the ADAS is was developed from the triangular plate devices born in New

Zealand (Tyler 1978, Boardman, 1983) and firstly employed as piping support elements (Steimer, 1980 and 1981). ADAS elements are designed to dissipate energy through the flexural yielding deformation of mild-steel plates: they consist of multiple X-shaped mild steel plates configured in parallel between top and bottom boundary connections (Fig. 3.17). A rectangular plate, when plastically deformed in double curvature, will yield only at its ends, giving a plastic concentration undesirable both in terms of the amount of energy that can be absorbed and by its inherent lack of stability and repeatability in the plastic range: the particular advantage of an X-plate is that, when deformed in double curvature, the plate deformation is uniform across its height, and once pushed into its plastic regime, the yielding is distributed and contemporary at all sections.

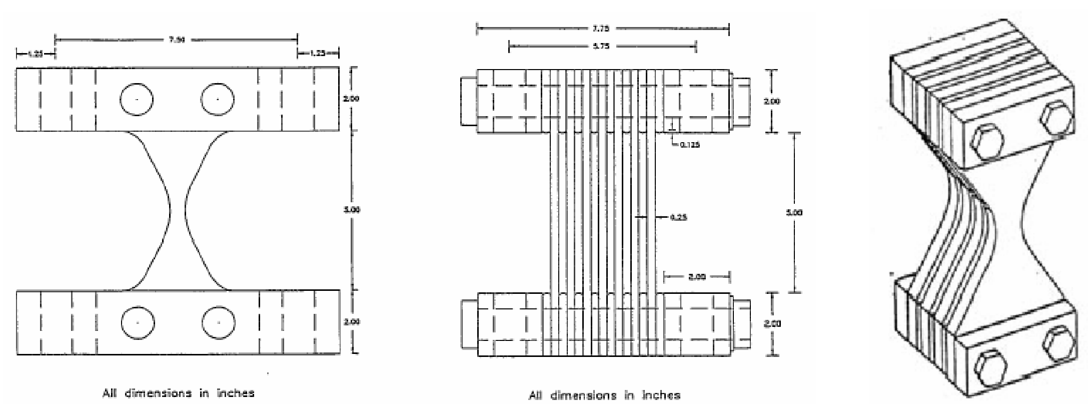

Fig. 3.17. Added Damping and Stiffness (ADAS) element

A typical hysteresis loop from one test of a 7-plate element is shown in Fig. 3.18. The primary factors characterising the ADAS element behaviour are the device elastic stiffness, the yield strength, and the yield displacement. ADAS elements are capable of sustaining more than 100 loading cycles with a displacement ductility of 3, proving stable response and no degradation; they can safely be designed for displacement ductility ranges up to about 10. Tests performed by Bergman and Goel (1987) indicated similar results.

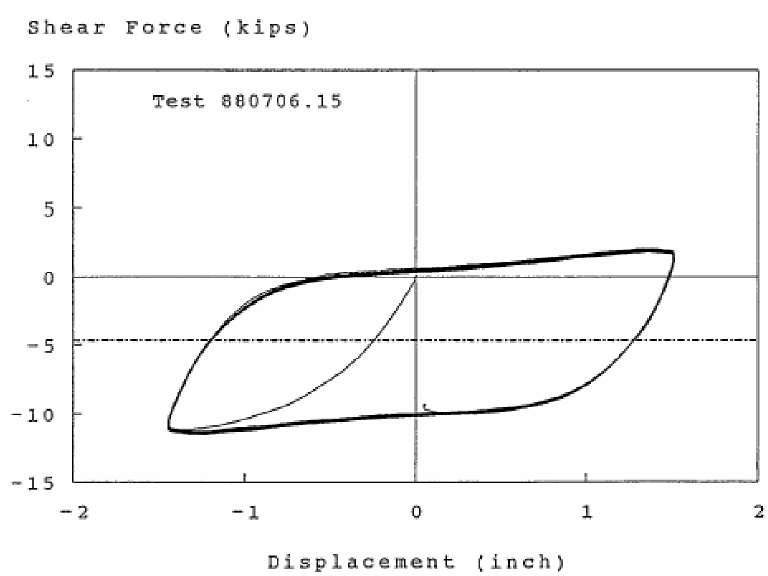

Fig. 3.18. 7-Plate ADAS element hysteretic behavior

One practical configuration for installing ADAS devices in a structure is in conjunction with a chevron brace assemblage, designed using capacity principles, based on an ADAS element strength of at least twice the device yield strength. The performance of an ADAS element is influenced by the degree of restraint at its extremities, and the design of these connection details must be aware of this factor: experimental tests indicated the importance of rigid boundary connections for successful performance of ADAS elements. Possible shortcomings with X-shape ADAS are that the stiffness of the device is very sensitive to the tightness of the bolts and generally much less than that predicted by assuming both ends fixed; moreover, the flexural behaviour might be weakened when the device is subjected to axial loads. Triangular ADAS (TADAS) devices were developed to avoid these inconveniences. TADAS elements use triangular steel plates instead of X-shape plates, with boundary conditions of welding at bottom and bolting at top (Fig. 3.19). Stiffness varies linearly along the height, as well as moment does, implying constant curvature, and avoidig curvature concentration. Experimental Load-deformation relationships do not show significant stiffness or strength degrading. The TADAS device can be modelled as bilinear elasto-plastic, and it can sustain a large number of yielding reversals (Fig. 3.20).

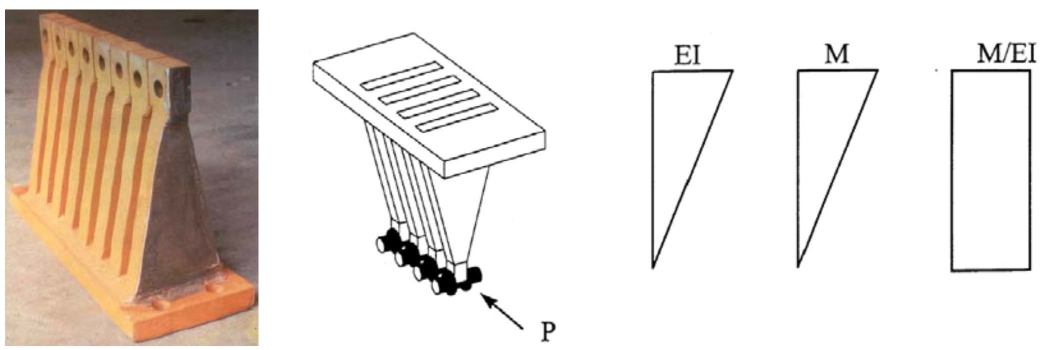

Fig. 3.19. TADAS element

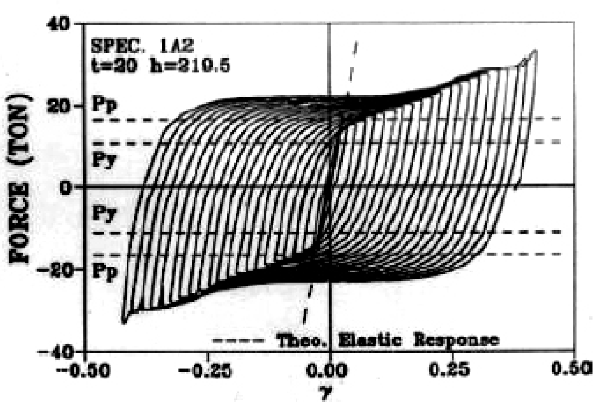

Fig. 3.20. TADAS load-deformation test results (Tsai et al.)

3.3.5 Hysteretic damper typologies: lead extrusion devices

The Lead Extrusion Dampers (LEDs) take the advantage of the extrusion of lead through orifices. Fig. 3.21 illustrates two types of lead extrusion dampers: the constricted tube, that forces the extrusion of the lead through a constricted tube, and the bulged shaft, that uses a bulged shaft through a lead cylinder. The main advantages of these devices are due to the lead properties: the hysteretic behaviour is essentially rectangular, stable and unaffected by number of load cycles (Fig. 3.22), allowing to maxime the energy dissipation, it is unaffected by any environmental factor and fatigue is not a major concern, because strain rate has a minor effect and aging effects are insignificant.

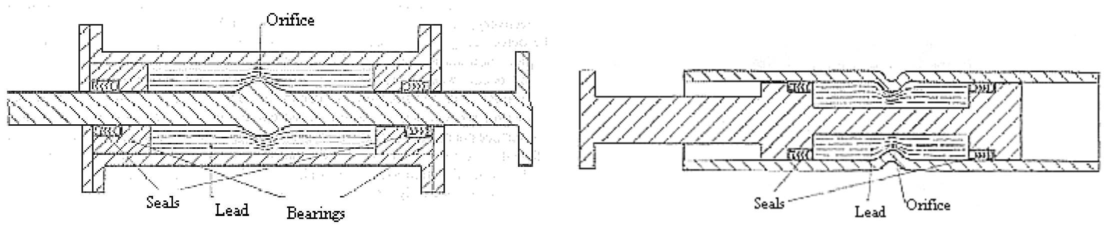

Fig. 3.21. Longitudinal section of a bulged-shaft (left) and of a constricted-tube (right) extrusion energy absorber

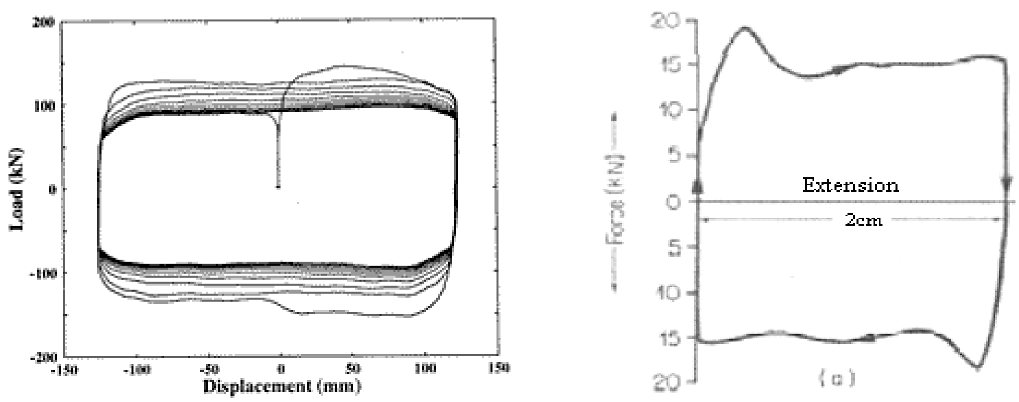

Fig. 3.22. Lead force displacement curve (left) and test results on a constricted tube absorber (right)

3.4 DESIGN CONSIDERATIONS

The design of structures equipped with metallic/friction dampers can be divided in four stages: (i) the estimation of the optimum parameters for dampers and adjacent elements by hand- calculation; (ii) the design of dampers and adjacent elements to meet the determined optimum parameters; (iii) the application of capacity design checks for all members of the structure under the expected ultimate force generated by the metallic/friction dampers; (iv) nonlinear time history analyses checks of the whole equipped structure. The design procedure illustrated hereafter was developed by Filiatrault and Cherry (1990), and can be extended to any energy dissipating system exhibiting an elastic-perfectly plastic behaviour.

3.4.1 Conceptual design: concepts of yield/slip shear and optimization criterion

Design steps for steel moment resisting frames essentially consist in: (i) selecting the dampers location; (ii) selecting the bracing members; (iii) determining the design ground motion parameters (design peak ground acceleration a_g, predominant ground period T_g); (iv) determining the optimum yield/slip load; (v) verifying the forces increased by the dampers on the other structural elements and checking the whole structure by nonlinear dynamic analyses.

The concept of the optimum yield/slip load consist in finding the optimum distribution of the slip load resulting in the optimum energy dissipation. The total dissipated seismic energy is the product of the slip/yield load and the total slip travel of each damper, summed over all the dampers. An optimum yield/slip shear distribution should be proportional to the interstorey drift arising from a first mode vibration of the structure. Due to the fact that very little benefit is achieved by using this optimum distribution as compared with the use of the simpler uniform slip shear distribution, the latter is recommended: such a distribution simplifies the design procedure and eliminates the risks of improperly distributing the dampers specified for a structure during contruction.

An approximate design equation for the total optimum base slip shear *V0* has been derived by Filiatrault and Cherry (1990) from the results of a parametric study conducted, based on the minimization of the vibration energy and considering the energy balance between the input energy and the sum of kinetic, strain, viscous and damper energy (equation (2.1)). This implies that the optimum yield/slip load does not necessary maximize total energy dissipation. The found relationships are:

$$V_0 / W = C_g a_g / g \tag{3.12}$$

$$C_g = \begin{cases} \dfrac{T_g}{T_u}\left[(-1.24n-0.31)\dfrac{T_b}{T_u}+1.04n+0.43\right] & 0 \le \dfrac{T_g}{T_u} \le 1 \\ \dfrac{T_b}{T_u}\left[(0.01n+0.02)\dfrac{T_g}{T_u}-1.25n-0.32\right]+ & \\ +\dfrac{T_g}{T_u}(0.002-0.002n)+1.04n+0.42 & \dfrac{T_g}{T_u} > 1 \end{cases} \tag{3.13}$$

In equation (3.12), *W* is the total seismic weight of the structure and n is the number of stories, *Tb* and T_u are the fundamental periods of the braced and unbraced structure respectively, and *Tg* is the predominant ground period. Equation (3.13) can be used in a graphical representation, named as Design-Slip Load Spectrum (Fig. 3.23), for any given value of *Tb/Tu*, providing a more simplified method for establishing *V0*.

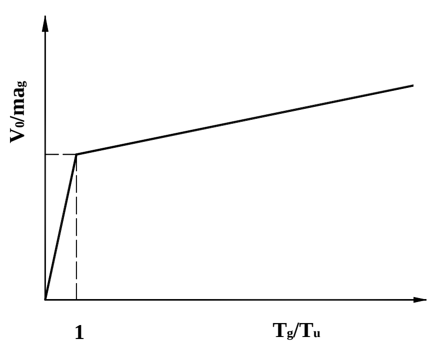

Fig. 3.23. Design-slip load spectrum

3.4.2 Choice of bracing members and design procedure

Results from the parametric study of Filiatrault and Cherry (1990) also brought to an optimal choice for the bracing members, resulting to be those having the largest possible cross-sectional area; this must be balanced with the limitations of costs and availability of material. The best response occurs in fact from small values of the ratio between the braced and unbraced periods, which correspond to large diagonal cross-braces. It is recommend, when possible, a ratio T_b/T_u smaller than 0.4. The following preliminary design steps are suggested (Filiatrault, 2003):

- STEP 1: calculate the fundamental period of the unbraced structure, T_u.
- STEP 2: choose sections for diagonal cross bracing such that T_b/T_u <0.40, if economically possible and feasible on the structural point of view (e.g. softening phenomena may impose the choice of a specific value of T_b).

- STEP 3: estimate the peak ground acceleration, a_g, and predominant ground period, T_g; the maximum peak ground acceleration for which this design procedure is recommended is a_g =0.4g.
- STEP 4: verify that the following non-dimensional ratios fall within the limits in equations (3.14) and (3.15). Maybe the non-dimensional ratios will not all within recommended values; however, this procedure is not expected to provide immediately the optimum solution, in case these limits are not verified: in this case the initial design is used only as a starting point, and the optimum solution is found through nonlinear dynamic analyses.

$$0.20 \le \frac{T_b}{T_u} \le 0.80 \qquad 0.50 \le \frac{T_g}{T_u} \le 20 \tag{3.14}$$

$$0.005 \le \frac{a_g}{g} \le 0.40 \qquad n \le 10 \tag{3.15}$$

- STEP 5: construct the appropriate design slip-load spectrum, and estimate the total slip shear V_0;
- STEP 6: distribute V_0 uniformly among the floors of the structure;
- STEP 7: distribute the slip shear of each floor amongst the number j of friction dampers per floor:

$$\sum_j P_{y,ij} 2\cos\theta_{ij} = V_{s(i)} \tag{3.16}$$

- STEP 8: Estimate the tensile-yield load of the cross braces and verify that these cross braces do not slip for wind effect (Filiatrault, 2003) and do not yield before slippage occurs.

It should be noted that this design procedure assumes the friction dampers will fully dissipate the seismic energy. Although the design procedure should theoretically find the optimum solution of slip load, the optimum solution is not always immediately attained, especially when not all the non-dimensional parameters match the recommended values. All of these factors combine to produce a solution that may result in a design of the proper magnitude, but probably not the ideal solution. Therefore, after obtaining the preliminary analysis results, intermediate analyses are required to improve the solution for the given design records.

4. DEVICE TYPOLOGIES: VISCOUS AND VISCOELASTIC DAMPERS

4.1 VISCOUS DAMPERS

Linear devices produce damping forces proportional to the velocity of the damper deformation, greatly attenuating the higher-mode seismic response, that is only relatively reduced by high isolator damping. Hydraulic dampers (Marioni, 1999 and 2002) utilise viscosity properties of a fluid to improve structural resistance against the earthquake. They are generally used as shock transmitters, able to allow slow movements (in service conditions) without valuable resistance, and stiffly react to dynamic actions.

It should be possible to develop effective velocity dampers, of the adequate linearity, by using the properties of high-viscosity silicone liquids: a double-acting piston drives the silicon fluid cyclically through a parallel set of tubular orifices (Fig. 4.1), giving high fluid shears and hence the required velocity-damping forces. By using a sufficient working volume of silicon to limit the temperature rise to 40°C during a design-level earthquake, the corresponding reduction in damper force is limited to about 25%. Shortcomings are the increasing of silicon volume with temperature (10%/100°C) and its tendency to cavitate under negative pressure.

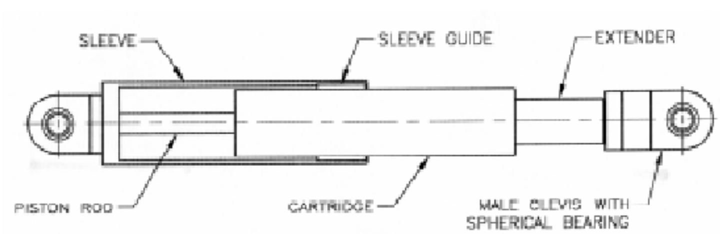

Fig. 4.1. Typical fluid viscous damper

The force generated by the device can be described by the following:

$$F = CV^{\alpha} + A \qquad (4.1)$$

where F is the force applied to the piston, V is the piston velocity, C, A and α are constants depending on the fluid and circuit properties; α may range between 0.1 and 2, according to the type of valves. Force-displacements plot for devices with different values of α subject to sinusoidal input are elliptical-shaped. Fig. 4.2 illustrates the dependence of the force on the velocity, for different values of α. In case of low α the dissipated energy per cycle is maximised. When energy dissipation is required, $\alpha \leq 2$ is preferred in order to increase the hysteretic area; in this case they are called Viscous Dampers (VD), for which a reference value of α is generally 0.1. The parameter α higher than 2 is preferred when the difference of force at low and high velocities shall be maximised, in order to react stiffly as soon as the velocity increases, while allowing slow movements due to thermal variations, creep and shrinkage, and becoming rigid in case of dynamic actions (braking force and earthquake), or when energy dissipation is not required; in this case they are called Shock Transmission Devices (STD) or Hydraulic Couplers.

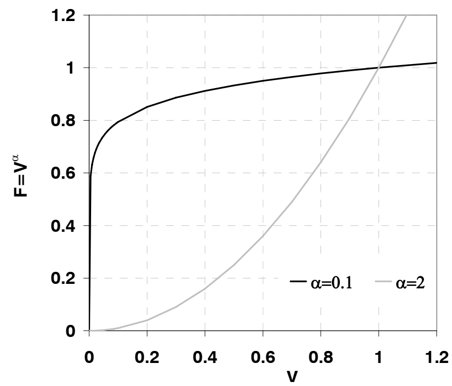

Fig. 4.2. Force-velocity type dependence for different values of the parameter α

In the design process for viscous dampers the nonlinear analysis of the structures is always required. Marioni (1996) suggests to select, by trial and error, the Viscous Dampers such that the sum of the constant *C* is:

$$\begin{aligned} &\sum C = 0.1\,\mathrm{W} \qquad \text{(high seismicity area)} \\ &\sum C = 0.07\,\mathrm{W} \qquad \text{(low seismicity area)} \end{aligned} \tag{4.2}$$

where W is the total weight of the structure. Then non linear analyses are needed to check the design displacement S_D; if it's too small (too large), the sum of the constants *C* has to be increased (decreased), in order to rise (low) the threshold of the yielding and reduce (increase) the energy dissipated by the structure. Some more sophisticated method is further illustrated in details.

4.1.1 Basic hysteretic behaviour of viscous dampers

In order to understand the nature of the viscous dampers dynamic response, a pure Viscous Element (Fig. 4.3, left) subjected to a time-varying relative axial displacement history $x(t) = X_0 \sin(\omega t)$ is studied; *X0* is the relative amplitude between the two ends of the element. Assuming the axial force induced in the element as linearly proportional to the relative velocity between its extremities (equation (4.3)), the force-displacement relationship is easily found in equation (4.4):

$$F = C\dot{x} \tag{4.3}$$

$$\frac{F}{X_0 C\omega} = \pm\sqrt{1-\left(\frac{x}{X_0}\right)^2} \tag{4.4}$$

Equation (4.4) describes an elliptical loop (Fig. 4.3, right), in which the amplitude of the maximum force induced in the element is linearly proportional to the damping, to the displacement amplitude and to the excitation frequency: this is a reason why in MDOF systems, each mode has an assigned viscous damping. It is worth to note that during seismic excitation, the frequency continuously varies, and in the same way the amplitude of hysteresis loops, i.e. the energy dissipated per cycle (E_D) through viscous damping, as evident in equation (4.5).

$$E_D = \int_0^{2\pi/\omega} F(t)x\,dt = \pi C\omega X_0^2 \tag{4.5}$$

An important characteristic of linear viscous dampers is that, differently from e.g. friction dampers, the acceleration of the damper is out of phase with the floor acceleration, which is limited in this way. On the other hand, the proportionality of the viscous damper force to displacement implies that virtually there is no limit to the damper force itself, that is virtually unbounded, while e.g. in friction dampers it is limited by the damper yielding treshold.

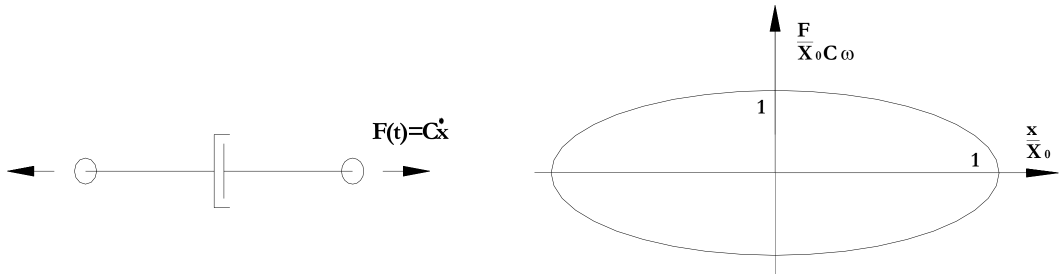

Fig. 4.3: Dashpot model (left) and cyclic response (right) of a pure viscous element

Non linear viscous devices with α<1 provide a limit for the increase of the force with displacements. Considering a pure Viscous Element subjected to a time-varying relative axial displacement history $x(t)= X_0 sin(\omega t)$, and assuming that induced axial force in the element is of the type of equation (4.6), the energy dissipated per cycle is shown in equation (4.7), (loops shown in Fig. 4.4).

$$F = C\,\mathrm{sign}(\dot{x})|\dot{x}|^{\alpha} \tag{4.6}$$

$$E_D = \int_0^{2\pi/\omega} F(t)x\,dt = 2\sqrt{\pi}C\omega(X_0)^{\alpha+1}\omega^{\alpha}\frac{\Gamma(1+\alpha/2)}{\Gamma(3/2+\alpha/2)} \tag{4.7}$$

In the practical range of velocities and exponential coefficient (0.2 to 1), the ratio of the gamma functions in equation (4.7) is close to unity, and the ratio between the nonlinear damping constant and the damping constant of an equivalent dissipating linear system can be approximated as in equation (4.8), by equating the energy dissipated per cycle. Consistent units must be used as equation (4.8) is not dimensionally homogeneous.

$$\frac{C_{NL}}{C_L} \cong \frac{\sqrt{\pi}}{2}(\omega X_0)^{1-\alpha} \tag{4.8}$$

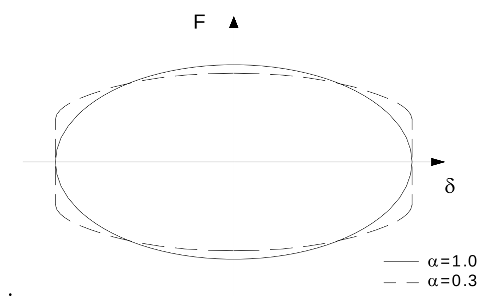

Fig. 4.4. Hysteresis loop of a viscous damper with different values of α

4.1.2 Viscous damper typologies: the Taylor device

The Taylor device is a fluid damper incorporating a stainless steel piston with a bronze orifice head and an accumulator; the device is filled with silicon oil (Fig. 4.5). The force generated by the fluid inertial damper is due to the pressure differential across the piston head. Due to the fluid compressibility, the volume reduction following the flow develops a restoring spring-like force, generally prevented by the use of an accumulator: test results indicate a cut off frequency of 4Hz (depending on the design of the accumulator, Filiatrault, 2003), under which no stiffness is produced. This means that higher modes, with frequencies larger then the cut-off treshold, might be affected by the elastic component. The damping constant of the device is not importantly affected by the temperature. Analytical results also showed that modelling these dampers as simple linear viscous elements yields predicted responses in good agreement with experimental results; the purely viscous nature is evident in Fig. 4.6.

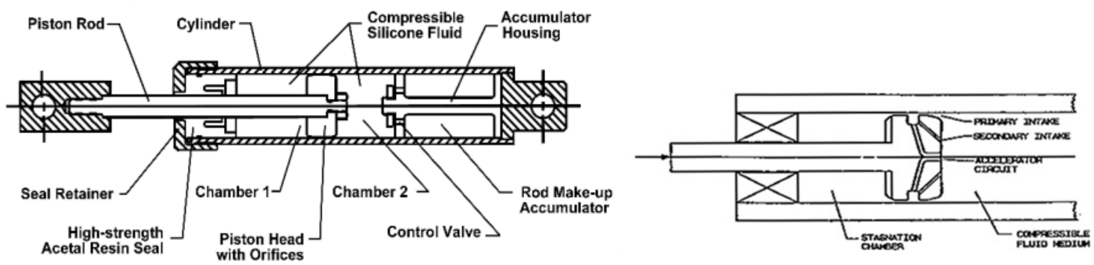

Fig. 4.5. The Taylor device (left) and detail of the fluid control orifice (right)

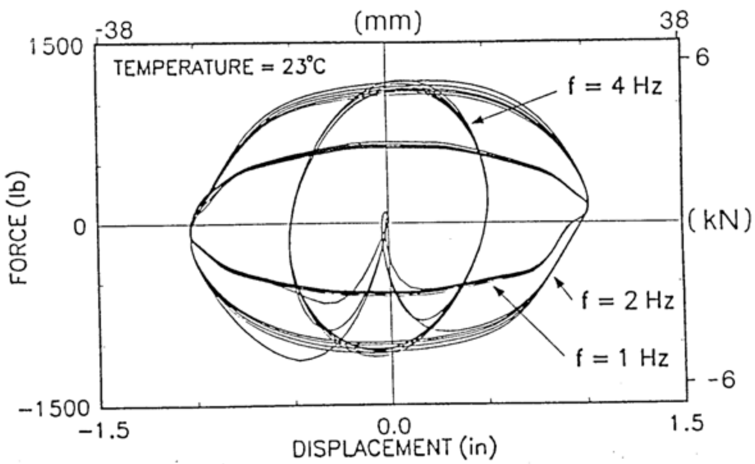

Fig. 4.6. Experimental hysteresis loop of a Taylor fluid damper at various frequencies and temperatures (Constantinou et al. 1993)

Fig. 4.7. The Taylor device: San Francisco Civic Center dampers

4.1.3 Design procedure of structures equipped with linear viscous dampers

The following design procedure is based on the addresses of Filiatrault (2003).

- STEP 1: the structural properties of the original building (without dampers) are evaluated, together with the seismic response in its existing condition, by means of dynamic analyses;
- STEP 2: the desired damping ratio is evaluated;

In order to get the preliminary distribution of the damping constant, the desired damping ratio in the fundamental mode is determined by studying the performance of the original building and with different damping ratios by means of nonlinear analyses on a simplified model of the structure under the design earthquake. Physically, a maximum damping ratio of about 35% of critical can be achieved with currently available viscous dampers. It might happen that no remarkable improvement in the building performance is evident after a threshold of the damping ratio: this may be due to the effect of specific characteristics inherent to the structure (e.g. soft story mechanisms at some level). Alternatively, to further simplify the preliminary design process, the desired damping ratio is evaluated through the design response spectra at various damping.

- STEP 3: the desired and possible damper locations in the structure are selected;

To determine the preliminary damping constant for each linear viscous damper C_L, the *method of fictitious springs* is suggested by Filiatrault (2003): it consists in replacing the viscous dampers in the undamped structure by fictitious elastic springs carrying the same maximum forces as the viscous dampers, assuming first mode harmonic motion of the structure. For the desired damping ratio in the first mode, the fundamental period $\overline{\overline{T}}_1$ of the building braced by equivalent fictitious springs is determined by following expression:

$$\overline{\overline{T}}_1 = \frac{T_1}{\sqrt{2\xi_1 + 1}} \tag{4.9}$$

where, T_1 is the fundamental period of the original structure. The ratio of the horizontal component of the fictitious spring in each floor is same as the distribution of the unbraced floor stiffness. The required fictitious spring in each floor is calculated and placed at the locations where the viscous damper devices will be introduced. Via dynamic analyses, the corresponding period in the first mode is computed. According to the relation between fictitious spring stiffness and the fundamental period, the exact stiffness for the fictitious spring in first floor is determined from following equation:

$$\frac{\overline{K}_{tj}}{\overline{K}_{ti}} = \frac{(\overline{w}_{tj})^2 - w_1^2}{(\overline{w}_{ti})^2 - w_1^2} \tag{4.10}$$

in which, $\overline{K}_{ti}$ and $\overline{K}_{tj}$ are the fictitious spring stiffness in the ith and jth trials, $\overline{w}_{ti}$ and $\overline{w}_{tj}$ are the corresponding frequencies of the first mode in each trial, and w_1 is the first mode frequency of the unbraced structure. Based on the distribution of the fictitious springs, one has to confirm with the modal analysis that the fundamental period of the such equipped structure is close enough to the period of the building with the selected damping ratio in the first mode. The preliminary damping constant in each floor is determined by the following equation:

$$C_L = \frac{K_{sj} T_1}{2\pi} \tag{4.11}$$

- STEP 4: a trial and error procedure is used to evaluate the damping constant C for each damper, usually by means of time-history analyses or modal analysis with elevated viscous damping ratios. The maximum force in the damper is required to manufacture the device.

In case of nonlinear viscous dampers, the exponential coefficient α has to be selected. Once linear damping constants are established with the procedure illustrated above, an initial estimate of nonlinear damping constants can be obtained with equation (4.8). For this purpose, the excitation frequency of the original structure can be taken as the fundamental frequency of the original structure without dampers and X_0 can be assumed as the displacement in the dampers corresponding to a desired performance drift level.

According to the preliminary distribution of damping constants, dynamic analyses are conducted to obtain the optimum distribution of the damping constants. When specific collapse mechanisms (e.g. soft storey) occur, it might be necessary to modify the damping constant distribution. First the best building performance is determined with the selected total damping constant; to evaluate the optimum scenario, a performance based index might be used and the redistribution factors for the damping constants are determined, based on the damage state. Then the building performance is verified: additional amount of damping might be necessary at some locations until the optimum final design on the damping distribution is determined.

- STEP 5: Cross Brace Design; in the final design stage, the chevron braces connected to the viscous damping device are designed. According to the damping forces obtained from the dynamic analyses, the sections of the diagonal braces at each location are chosen.

The modelling of the viscous damper device with the cross braces might be carried out as shown in Fig. 4.8. A fictitious frame element only providing the bending stiffness is introduced between the nodes used by the damping element.

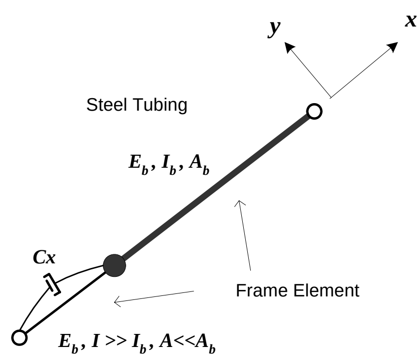

Fig. 4.8. Modeling of viscous damper and cross braces

- STEP 6: Final Design Check.

The energy balance of the retrofitted structure has to be checked. Compared with the results of unretrofitted structure, the total input energy might be either increased or reduced. Most of the energy is dissipated by the viscous damper rather than the strain energy, whilst in the original structure, the energy is mainly dissipated by the strain energy: the structural damage is thus reduced after the viscous cross-braced solution is applied. An example of energy balance showing the amount of energy dissipated by viscous mechanisms in a retrofitted structure is shown in Fig. 4.9.

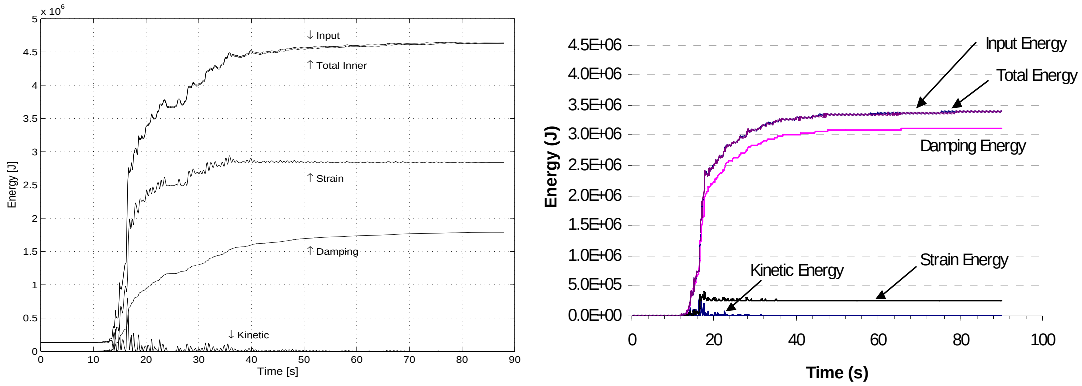

Fig. 4.9. Example of Energy balance of a structure equipped with VD, before (left) and after (right) the retrofit

Peak accelerations also have to be checked, as they might be on occasions increased after the retrofit: the solution may be accepted provided that they are maintained under desired or code tolerance levels. For the application of the proposed viscous cross-braced retrofit solution, the required capacity on the foundation needs to be as well verified, in terms of demand in base shear and overturning moment before and after the retrofit.

4.1.3.1 Implementation of fluid dampers: fabrication and detailing issues

Fluid dampers mounted in a structure are essentially a "bolt-in" item, of a relatively compact size. If used as part of a structural bracing system, the fluid dampers usually will have a smaller cross-sectional envelope than a conventional steel brace. A brief discussion on the implementation of fliud dampers is provided in terms of fabrication issues (Size vs. Cost) and detailing (Attachments and Brace Styles).

If a given structure requires a specific amount of total macroscopic damping, this latter needs to be divided among the number of dampers. The end result is a maximum force and damping function for each individual damper. The question arises if the engineer should select a large number of small dampers, or a lesser number of large dampers. The structural engineer normally starts out with multiple dampers of the same size, distributed uniformly throughout the structure. The resulting design consists in many dampers in the relatively small force range of 5 tonnes to 25 tonnes output. If the structure is small enough to require less than 32 pieces of this size, than this will probably be the most effective size, since quantities smaller than 32 pieces tend to become costly, due to set-up, engineering, and test charges being amortized over a small quantity. The next step is to reduce the number of dampers by using the next larger size, and continuing this process until the quantity of dampers goes below 32 pieces, or the force rating of the damper goes over 300 tonnes, or finally the structure begins behaving less efficiently because the dampers are not appropriately distributed. Currently available damper sizes from manufacturers range from 5 to 800 tonnes of force output. In terms of relative cost, the least expensive sizes on a force basis are usually in the range of 100-250 tonnes. In most cases, dampers larger than 600 tonnes output are used only on large bridges. Also dampers larger than 250 tonnes tend to become costly, due to a problem of general lack of available high-strength steel in the very large sizes, requiring special orders to the steel mill.

There are three ways to setup dampers into a building or bridge structure (Fig. 4.10):

- Base isolation dampers have clevises and spherical bearings at each end. These long stroke dampers are connected to the foundation and to the building frame respectively, using mounting pins. The mounting pins for base isolation dampers must be oriented vertically, to allow proper articulation during out of plane motion.
- Dampers for chevron bracing systems have clevises and spherical bearings at each end. Connections are similar to base isolation dampers, except that the mounting pins are usually

oriented horizontally. The typical plus or minus 5° rotation angle of a spherical bearing will accommodate out of plane motion for the relatively small drifts encountered with this type of installation.

- Dampers for diagonal bracing systems have a clevis with spherical bearing at one end, and a mounting plate at the opposite end. The mounting plate attaches to a brace extender.

Maintenance is not required for a properly designed and manufactured fluid damper used for seismic and wind damping in structures. Usually, visual inspection of the dampers should occur after a major seismic or wind storm event. In the event of seismic overload, the damper mounting pins may bend or shear. After a major seismic event, some structures may require an enhanced inspection, according to regional code requirements. In some cases, regulations may require that a few dampers be randomly removed from the structure, and subjected to testing in order to verify the damping output.

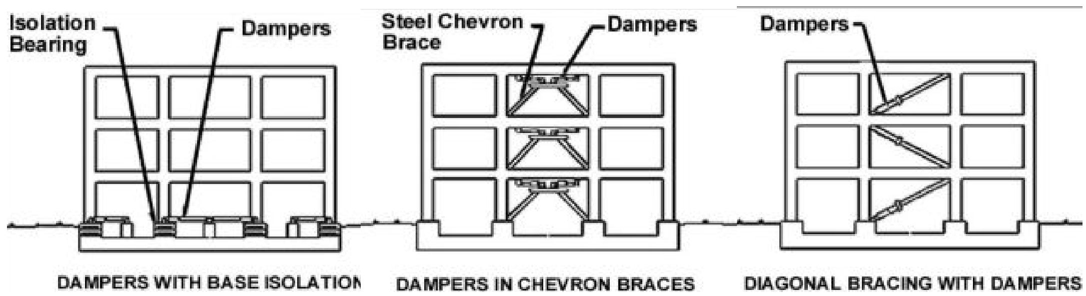

Fig. 4.10. Basic mounting attachment styles

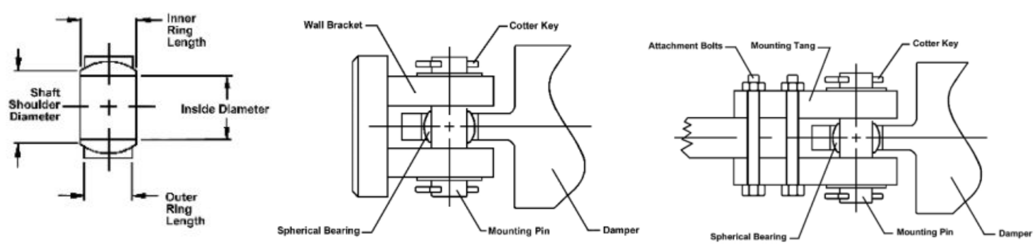

Fig. 4.11. Spherical bearing (left) and schematic of a completed attachment (center and right)

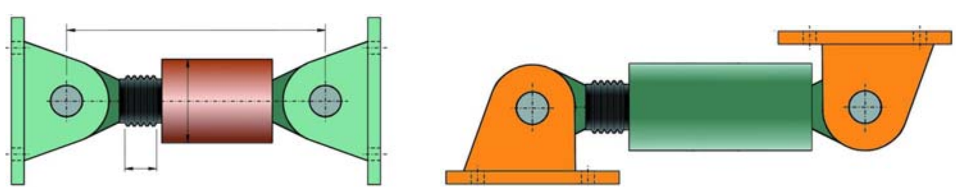

Fig. 4.12. Typical fixing detail for installation between abutment and bridge (left) and between top of pier and bridge (right)

4.1.4 Effects of supplemental viscous damping on asymmetric-plan systems

The combined effects of irregularities in plan (curves, changes of direction) an 12q23d in the pier height layout of irregular bridges lead to an asymmetric distribution of the centres of mass and of stiffness, possibly affecting the seismic response of the system: particularly, irregular bridges with flexible decks constitute torsionally-very-flexible systems. Goel (1998) studied the influences of plan asymmetry on the seismic responses of simple one-storey systems, equipped with supplemental fluid linearly-elastic viscous dampers.

Referring to Fig. 4.13, the effect of the location of the Supplemental Damping Centre (CSD) with respect to the centres of Mass and Stiffness (CM and CR) of the system is investigated, togheter with the effect of the planwise distribution of dampers with respect to the CSD. Other significant parameters are ratio of the two and the Supplemental Damping ratio. The peak deformations at the flexible and stiff edges of the system measure the effects of the asymmetry, being indicative of the deformation demands at the ends of a deck span, and of the spacing required to avoid pounding between adjacent girders.

Goel (1998) showed that edge deformations in asymmetric-plan systems can be reduced by a factor of up to about three by proper selection of the supplemental damping parameters alone (particularly of the plan-wise distribution of the supplemental damping), without any redistribution (often unfeasible) of stiffness and/or mass properties of the system. In particular, they observed that: (i) for the same amount of supplemental damping, an asymmetric distribution led to a higher reduction in edge deformations as compared to a symmetric distribution; (ii) the large reduction in edge deformations occur when the CSD is as far away as physically possible from the CM; the CSD should be on the opposite side of the CR to obtain a reduction in the flexible edge deformation; (iii) the largest reduction in edge deformations is obtained when the supplemental damping is distributed as far away from the CSD as possible; (iv) a near optimal reduction may be obtained by using as few dampers as possible in the direction under consideration and locating the outermost dampers at the two edges (to calibrate the CSD eccentricity at least equal to the structural eccentricity), and by putting other dampers in the perpendicular direction, spreading them respect the CSD without influencing its position; (v) the effects of the plan-wise distribution of supplemental damping are much more significant for strongly coupled and torsionally-very-flexible asymmetric-plan systems (with a ratio lower than the unity between the torsional and the transverse vibration frequencies).

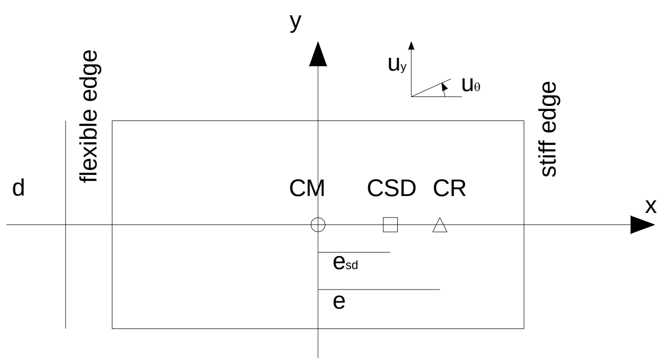

Fig. 4.13. Plan view of the one-storey system

4.2 SHOCK TRANSMISSION DEVICES

Shock Transmission Devices (STD) can closely approximate the ideal parameters such that low velocity displacements are allowed with negligible resistance, withstanding high seismic loads with minimal deformation: they have an α value approaching 2. The oil filled cylinder is divided into two chambers by a piston and fixed to the structure normally through spherical hinges (allowing rotations up to ±3° in all directions), in such a way that the relative movement of the structure causes the piston to move inside the cylinder, allowing the oil flow from one chamber to the other through a hydraulic circuit. The oil flow through the circuit is practically independent of the external temperature: the constant performance level of the device is provided thanks to a design based on a turbulent oil flow practically independent from the viscosity of the fluid and therefore from its temperature. When the device dimensions are very large (it can reach 870mm of diameter and 2900mm of length in exceptional cases) an external hydraulic circuit and an external accumulator are preferred to the internal ones employed in smaller devices, to allow easy access, to avoid any interference between the flexural bending of the device due to own weight and to the behaviour of the circuit, and to avoid overpressure in the cylinder due to the oil thermal expansion.

4.3 VISCOELASTIC DAMPERS

Typical Viscoelastic dampers are constituted by copolymers or glassy substances; they are generally incorporated in bracing members and dissipate energy through shear deformations of the Viscoelastic material (Fig. 4.14).

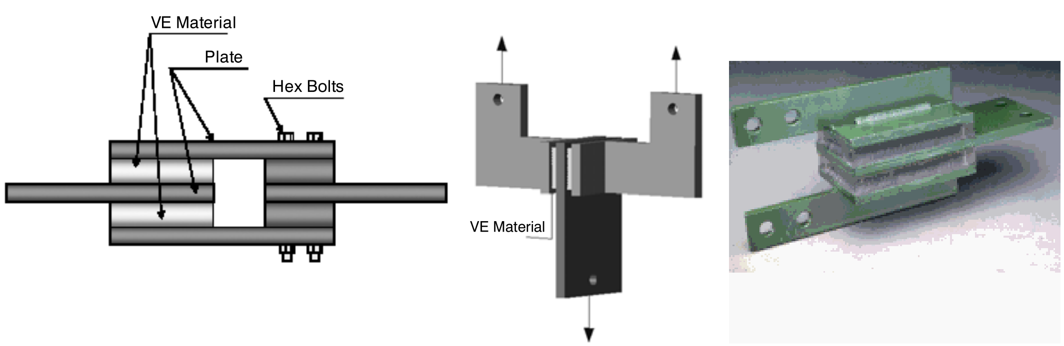

Fig. 4.14. VE damper part of a bracing member: typical scheme (front and 3D views) and picture

4.3.1 Viscoelastic dampers typologies

Fig. 4.15 and Fig. 4.16 show some typical working schemes of the Viscoelastic dampers.

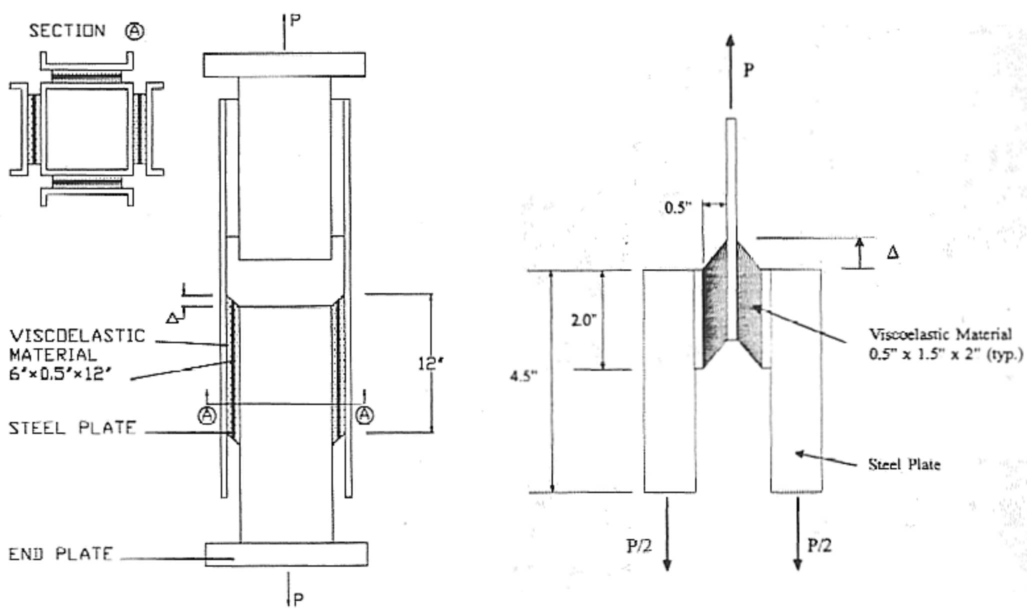

Fig. 4.15: Examples of viscoelastic dampers

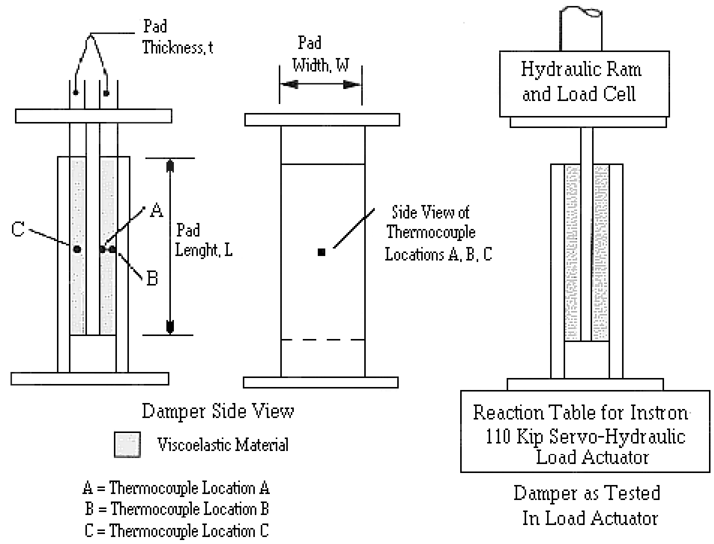

Fig. 4.16: Examples of Viscoelastic Dampers

4.3.2 Basic hysteretic behaviour of viscoelastic dampers

In order to understand the nature of the viscoelastic dampers dynamic response, the Kelvin Solid model in Fig. 4.17 is used to represent the device: G_E and G_C represent respectively the instantaneous elastic response and the shear viscous damping constant exhibited by the viscoelastic material. Assuming that the Viscoelastic material has unit height h and unit area A, its viscous and elastic shear stiffnesses are shown in equation (4.12). The solution for an excitation of the kind of $x(t) = X_0 sin(\omega t)$ is found in equation (4.13), which describes an elliptical shaped loop (Fig. 4.17) inclined with respect to the principal axis of a quantity corresponding to the instantaneous elastic stiffness: the response can be easily viewed as the sum of a linear elastic component and a viscous elliptical component: still maximum force does not occur at maximum displacement, and optimum phasing can be obtained by adjusting the material properties $\overline{K}$ and $\overline{C}$. The energy dissipated per cycle is easily shown to be given by equation (4.5), with C replaced by $\overline{C}$: this can be also deduced observing that the elastic component does not contribute to the energy dissipation. The equivalent viscous damping ratio of the element is shown in equation (4.14), where $\overline{\omega}$ is the oscillating circular frequency of the element.

$$\overline{K} = \frac{G_E A}{h} \quad ; \quad \overline{C} = \frac{G_C A}{h} \tag{4.12}$$

$$\frac{F}{X_0 \overline{C}\omega} = \frac{\overline{K}}{\overline{C}\omega}\left(\frac{x}{X_0}\right) \pm \sqrt{1 - \left(\frac{x}{X_0}\right)^2} \tag{4.13}$$

$$\begin{aligned} \overline{\zeta} &= \overline{C} / 2\overline{\omega} m = G_C \overline{\omega} / 2G_E = \eta / 2 \\ \overline{K} &= \overline{C}\,\overline{\omega} / \eta \end{aligned} \tag{4.14}$$

In viscoelasticity, the Shear Storage Modulus G_E is a measure of the energy stored recovered per cycle, the Shear Loss Modulus $G_C\overline{\omega}$ is a measure of the energy dissipated per cycle, and the ratio of the two is called *Loss Factor* η (that can be taken as 1.35, (Singh and Moreschi, 2001)). Their actual values can be experimentally obtained from displacement-controlled sinusoidal tests at various excitation frequencies, as they are respectively the effective stiffness of the loop and the damping coefficient of the energy dissipated per cycle. These moduli are function of the excitation frequency, the ambient temperature, the shear strain level and the variation of the internal temperature within the material during operation. Chang *et al.* (1993) investigated the dynamic cyclic shear response of different types of Viscoelastic materials. They found that both G_E and $G_C\bar{\omega}$ decrease with an increase of the ambient temperature, but η remains fairly constant. Moreover, damper properties are fairly independent of strain at strain level below 20% for different temperatures and frequencies.

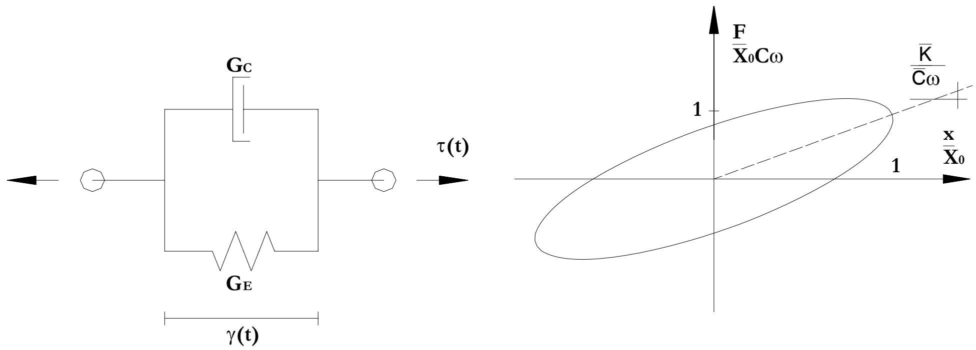

Fig. 4.17: Kelvin solid model (left) and hysteresis loop of harmonically excited viscoelastic damper (right)

4.3.3 Dynamic analysis of viscoelastic dampers equipped structures

Consider the system in Fig. 4.18. The axial force in the bracing element F_B, corresponding to the shear force in the Viscoelastic material, is shown in equation (4.15). The corresponding horizontal component is obtained multiplying it by $\cos\theta$, and considering the displacement compatibility between the frame displacement x and the brace axial deformation Δ ($\Delta = x \cos\theta$). The resulting Standard Equation of Motion for the SDOF is obtained in (4.16), where c and k are the characteristics of the unbraced structure: it can be easily seen that this is the Standard Equation of Motion of a SDOF system with modified damping and stiffness characteristics, according to the parameters of the Viscoelastic material.

$$F_B(t) = \bar{K}\Delta(t) + \bar{C}\dot{\Delta}(t) \tag{4.15}$$

$$m\ddot{x}(t) + (c + \bar{C}\cos^2\theta)\dot{x}(t) + (k + \bar{K}\cos^2\theta)x(t) = -m\ddot{x}_g(t) \tag{4.16}$$

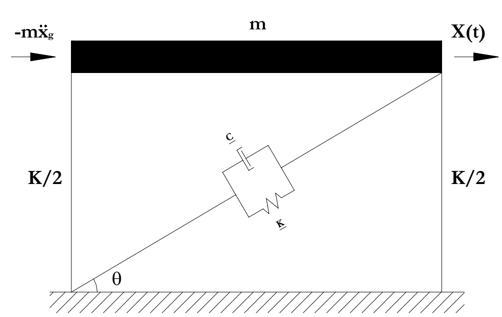

Fig. 4.18: Single storey structure equipped with viscoelastic dampers

In order to extend the analysis to MDOF systems, some simplifying assumption is made: (i) the original damping matrix of the structure is neglected, due to the much higher contribution of the added dampers; (ii) the damping matrix of added dampers $\underline{\underline{\bar{C}}}$ is assumed to have the same orthogonality properties as the original mass and stiffness matrices of the structure. Uncoupling modes with the modal superposition method, it is obtained:

$$
\begin{aligned}
& M_i \ddot{u}_i + \bar{C}_i \dot{u}_i + \bar{\bar{K}}_i u_i = P_i(t) \\
& M_i = \underline{A}_{(i)}^T \underline{\underline{M}}\,\underline{A}_{(i)} \qquad \bar{C}_i = \underline{A}_{(i)}^T \underline{\underline{\bar{C}}}\,\underline{A}_{(i)} = \frac{\eta_i \bar{K}_i}{\bar{\bar{\omega}}_i} \\
& \bar{\bar{K}}_i = \underline{A}_{(i)}^T \left[\underline{\underline{k}} + \underline{\underline{\bar{K}}}\right] \underline{A}_{(i)} \qquad \bar{K}_i = \underline{A}_{(i)}^T \left[\underline{\underline{\bar{K}}}\right] \underline{A}_{(i)}
\end{aligned}
\tag{4.17}
$$

The modal response is obtained in equation (4.18), where the ith damping ratio is expressed as (4.19). The symbols $^{-}$ and $^{=}$ stay respectively for the contribution of added dampers only and for the contribution of both added dampers and original structure. Alternatively, nonlinear time history analyses are performed, and each Viscoelastic damper is modelled with its own properties, assumed to be constant.

$$
u_i(t) = \frac{1}{M_i \bar{\bar{\omega}}_{di}} \int P_i(t) \exp\left(\bar{\bar{\zeta}}_i \bar{\bar{\omega}}_i (t-\tau)\right) \sin\left(\bar{\bar{\omega}}_{di} (t-\tau)\right) d\tau
\tag{4.18}
$$

$$
\bar{\bar{\zeta}}_i = \frac{\eta_i}{2}\left(1 - \frac{\omega_i^2}{\bar{\bar{\omega}}_i^2}\right)
\tag{4.19}
$$

4.3.4 Critical damping of structures with elastically supported viscoelastic dampers

When an overall structural system can be modelled by a Voigt-type model (i.e. a system of a spring and a dashpot in parallel), the governing equation of vibration is reduced to a second-order differential equation. In the case that the effect of the damper support stiffness is not negligible (as in the system of Fig. 4.19, the governing equation of vibration is reduced to a third-order differential equation, for which the conventional method for second-order differential equations of definition of the critical damping cannot be applied.

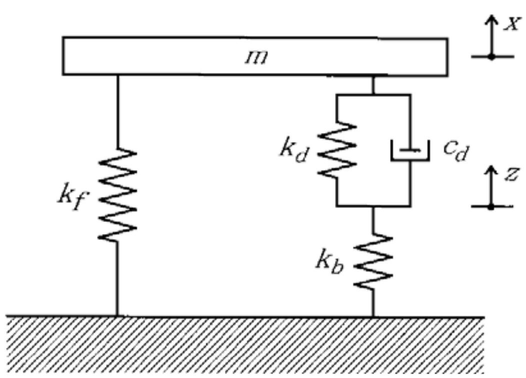

Fig. 4.19. SDOF system with an elastically supported visco-elastic damper

The critical damping and characteristics of the third order differential equations have been investigated in detail by Lee *et al.*, (2002): they obtained the third-order differential equation (4.20), where *m* and k_f denote the structural mass stiffness, k_d and c_d the visco-elastic damper stiffness and damping coefficient, k_b the stiffness of the visco-elastic damper support; x and z denote the displacement of the mass m and that of the connecting point between the visco-elastic damper and the support member (Fig. 4.19). In order to provide the critical damping coefficients bounding underdamped vibration and overdamped vibration, the discriminant of the cubic Equation must be equal to zero: a quadratic expression of c_d^2 is obtained, and for it to have positive roots (critical damping coefficient) its discriminant has to be positive, as well as the sum of the two roots, yielding to the condition (4.21).

$$
\begin{aligned}
&m\dddot{x} + \frac{m}{c_d}(k_b + k_d)\ddot{x} + (k_b + k_f)\dot{x} + \frac{1}{c_d}(k_f k_b + k_d k_b + k_d k_f)x = 0 \\
&A = k_b + k_d \quad B = k_b + k_f \quad C = k_f k_b + k_d k_b + k_d k_f \\
&m\lambda^3 + \frac{mA}{c_d}\lambda^2 + B\lambda + \frac{C}{c_d} = 0
\end{aligned}
\tag{4.20}
$$

$$
AB - 9C \geq 0 \tag{4.21}
$$

As evident in Fig. 4.20 (left), in which discriminant function is illustrated, two critical damping coefficients are individuated. Provided that the condition (4.21) on model stiffness parameters is satisfied, it is worth to notice that two critical damping coefficients exist: the finite region of overdamped vibration is finite and between these two critical damping coefficients, in contrast to that (semi-infinite) for second-order differential equations. Lee *et al.*, (2002) analysed simple numerical examples, considering the following cases: (i) Case 1: underdamped vibration ($c_d < c_{crit1}$); (ii) Case 2: overdamped vibration ($c_{crit1} < c_d < c_{crit2}$); (iii) Case 3: combination of underdamped vibration and overdamped vibration ($c_{crit2} < c_d$). Results of these cases are shown in Fig. 4.20 (right): in the last case, a small vibration component is superposed to an overdamped vibration, i.e. the smaller critical damping coefficient is the practically meaningful one, allowing to define the critical damping ratio as the ratio of a damping coefficient c_d to the smaller critical damping coefficient c_{crit1}. Lee *et al.*, (2002) expect this formulation to be applicable to other similar systems governed by third-order differential equations.

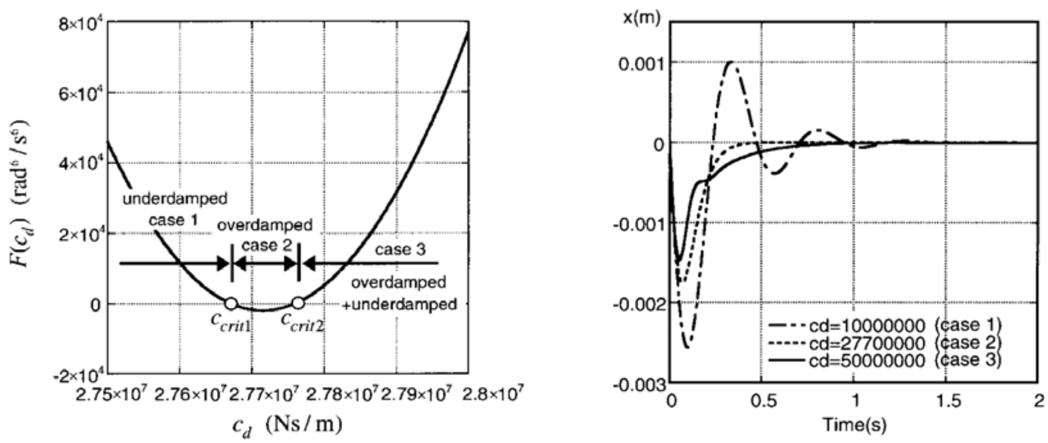

Fig. 4.20. Discriminant function of the third-order differential equation (left) and time histories of free vibration of the three analysed numerical models with different damping coefficients (right)

4.3.5 Design procedure of structures with viscoelastic dampers

The design procedure, suggested by Filiatrault (2003) for structures equipped with viscoelastic dampers follows:

- STEP 1-2-3: same as for viscous dampers (§4.1.3);
- STEP 4: the damper $\overline{K}$ and η are selected on the base of available viscoelastic material and of the geometry of the damper. A trial and error procedure follows, as starting point the added stiffness at the j^th storey may be chosen proportional to its unretrofitted counterpart, i.e. applying relationship (4.22). The damper thickness is chosen such that the maximum shear strain in the material is lower than the ultimate value (equation (4.23)). For a viscous material with known G_E and G_C at the design frequency and temperature, the damper is sized according to the (4.24).

$$\zeta = \frac{\eta \overline{K}}{2\left(k_j + \overline{K}\right)} \tag{4.22}$$

$$h \geq \Delta_d / \gamma_{ult} \tag{4.23}$$

$$A = \frac{\overline{K} h}{G_E} \tag{4.24}$$

- STEP 5: the damping ratio for each mode is evaluated through the (4.19). Alternatively, $\overline{C}$ for each damper can be obtained from the:

$$\overline{C} = \frac{G_E A}{h} \tag{4.25}$$

- STEP 6: a dynamic analysis is performed to evaluate the response of the retrofitted structure.

4.4 A METHOD TO DETERMINE THE OPTIMAL AMOUNT AND LOCALISATION OF DAMPERS

In order to determine the optimal amount of viscous and visco-elastic damping and the best placement of dampers in the structure, required to achieve a desired level of response reduction, Singh and Moreschi (2001) proposed a gradient-based method. The latter consists in minimising a response-dependent performance function $\underline{R}(\underline{c})$ of the added damping coefficients c_i at the ith degree of freedom, obtained by considering a stochastic description of the input motion. If linear visco-elastic devices are added, their contribution is included in the stiffness matrix of the structure.

The solution is searched under the condition of equation (4.26), where C_T is the total amount of damping coefficient values to be distributed in the structure. Since the constraints given by (4.26) are linear in the design variables c_i, the Rosen's gradient projection method is suggested, as an effective yet simple technique for the numerical solution of the optimization problem. The optimization algorithm is based on the following general iterative scheme of equation (4.27), where k is the iteration number, β_k is the step size and s_k is the search direction.

$$\begin{aligned} &\min\left(f\left[\underline{R}(\underline{c})\right]\right) \\ &\text{subjected to} \quad \sum c_i - C_T = 0 \quad , \quad 0 \leq c_i \leq c_{i\_max} \end{aligned} \tag{4.26}$$

$$\underline{c}_{k+1} = \underline{c}_k + \beta_k \underline{s}_k \tag{4.27}$$

The basic assumption of the gradient projection technique is that the search direction is confined in the subspace defined by the active constraints: the direction is found in such a way that it is forced to be normal to the constraint gradient, to approach the minimum of the function in the direction of the steepest descent. The problem can be divided in two basic parts: after the search direction s_k has been determined, the maximum permissible step size β_k along s_k is determined such that no constraints are violated.

The performance function can be defined as a vector of response quantities, e.g. in terms of their root-mean-square values, normalised with respect to the corresponding response quantities of the original structure(without supplemental damping devices). To include the representation of more structural response quantities in the optimization process, a composite performance function could be defined as a weighted contribution of different performance indices.

To obtain the gradients of the performance function, the rates of change of the root-mean-square values of the response quantities are evaluated with respect to the design variables c_i. If the structural system behaves nonlinearly, this is carried out numerically, whilst in linear cases the gradients can be defined more conveniently in terms of the gradients of the modal quantities of the structural systems, by means of a response spectrum approach. The sensitivities of the design variables are defined in terms of their partial derivatives with respect to the problem parameters, and can be used to estimate the total amount of damping needed to obtain a desired performance.

Not knowing a priori the amount of damping required to achieve the desired reduction in the response, an initial choice for the total damping C_T has to be made: e.g. this total damping is first distributed uniformly at different locations. If the prescribed reduction level could not be achieved with the chosen amount of damping C_T, it must be increased of the estimated needed ΔC_T; then a new optimization problem is solved, with the equality constraint set to the new value C_T, up to convergence to the desired response reduction.

The above design is addressed to be not a globally optimal, but rather an improvement over an arbitrarily selected distribution. If the globally optimal solution is desired, then several randomly selected initial guesses for the distribution may be used. It might be of interest to know the cross-effectiveness of a design obtained for different performance objectives. Singh and Moreschi (2001) found that the sensitivity of the optimal design with respect to the changes in the ground motion intensity parameter do not seem to be high.

5. DEVICE TYPOLOGIES: SELF-CENTERING DAMPERS

Generally dampers do not limit the residual displacements of the structure after a seismic event. Some recently developed damper system incorporate re-centering capabilities, characterised by the so-called flag-shaped hysteretic loop. The main advantage of the self-centring behaviour consists in reducing permanent offsets when the structure deforms inelastically. A number of different devices have been developed, among these:

- Shape Memory Alloys Dampers (SMA),
- Energy Dissipating Restrain (EDR);
- The Friction Spring Seismic Dampers;
- The Post-Tensioned Energy Dissipating (PTED) steel connections;

5.1 SELF-CENTERING DAMPER TYPOLOGIES: SHAPE MEMORY ALLOYS DAMPERS

Shape-Memory Alloys (SMAs) have the capacity to undergo large strains and subsequently to recover their initial configuration. The basis for this behavior is that, rather than deforming in the usual manner of metals, shape-memory alloys undergo transformations from the austenitic to the martensitic crystal phase (Hodgson, 1988). Sasaki (1989) studied the suitability of Nitinol for energy dissipation under seismic-type loading, and investigated flexural, torsional, shear, and axial modes of deformation. Graesser (1991) and Witting (1992) have continued the studies of shape memory alloys for energy dissipation applications in structures. A Nitinol energy dissipator has the particular advantages of being mechanically very simple and reliable.

Currently, there is no reference normative for the design of SMA, even if guidelines were developed recently by the MANSIDE Consortium (1998).

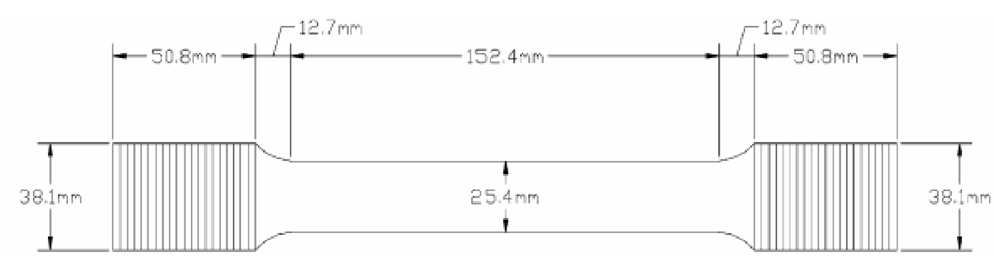

Fig. 5.1. Example of Nitinol SMA restrainer bar

The use of the SMA restrainers in multi-span simply supported bridges at the hinges and abutments can provide an effective alternative to conventional restrainer systems: the SMA restrainers can be designed to provide sufficient stiffness and damping to limit the relative hinge displacement. The SMA restrainers may be connected from pier cap to the bottom flange of the girder beam in a manner similar to typical cable restrainers, as shown in Fig. 5.2. The restrainers are typically used in a tension-only manner, with a thermal gap to limit the engaging of the restrainer during thermal cycles. If adequate lateral bracing could be provided, the restrainers can be made to act in both tension and compression.

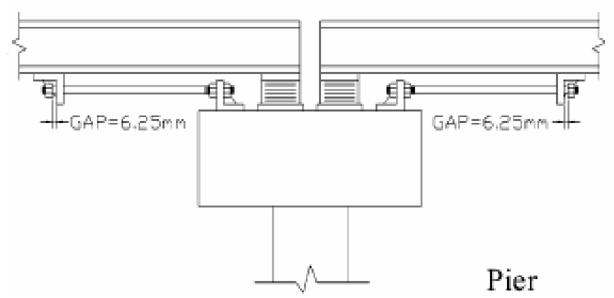

Fig. 5.2. Configuration of shape memory alloy restrainer bar used in multi-span simply supported bridges

DesRoches and Delemont (2002) investigated the effectiveness of the SMA restrainer bars in bridges through an analytical study of a multi-span simply supported bridge. The results showed that the SMA restrainers reduce relative hinge displacements at the abutment much more effectively than conventional steel cable restrainers. The large elastic strain range of the SMA devices allows them to undergo large deformations while remaining elastic and due to their superelastic properties, they are able to maintain their effective stiffness for repeated cycles, differently from conventional restrainer cables once yielded. In addition, the superelastic properties of the SMA restrainers results in energy dissipation at the hinges.

Finally, evaluation of the multi-span simply supported bridge subjected to near-field ground motion showed that the SMA restrainer bars are extremely effective for limiting the response of bridge decks to near-field ground motion: the large pulses from the near-field record produced early yielding in conventional cable restrainers, thus reducing their effectiveness and resulting in large relative hinge displacements for the remainder of the response history. The SMA restrainer is able to resist repeated large cycles of deformation while remaining elastic. In addition, the increased stiffness of the SMA restrainers at large strains provides additional protection from unseating as the relative hinge opening approaches the critical value.

5.1.1 Macroscopic hysteretic behaviour of the SMA

The shape memory effect in metals was first observed in the 1930s. In 1962, researchers at the Naval Ordinance Laboratory observed the phenomenon in Nickel-Titanium (NiTi, or Nitinol). Shape memory alloys are a class of alloys that display several unique characteristics, including Young's modulus-temperature relations, shape memory effects, and high damping characteristics. Mechanical properties of SMA devices are re-centering, energy dissipation and fatigue resistance.

SMAs are binary or ternary metallic alloys that can be found in two different phases, Austenite and Martensite, capable of experiencing thermo-elastic solid transformations; each phase is stable at different thermo-mechanical states. Austenitic structure has a higher degree of symmetry and is stable at higher temperatures and lower stresses, while martensitic structure is generally met at lower temperatures and higher stresses. For some SMAs, such as Nitinol (NiTi SMA), the phase change can be stress-induced at room temperature if the alloy has the appropriate formulation and treatment. The most peculiarities of SMA are: (i) the *memory effect*, i.e. the aptitude to recover the initial shape by heating; (ii) the *superelasticity*, i.e. the aptitude to recover the initial shape as soon as the external action is removed. The stress-induced shape memory property is based on a stress-induced Martensite formation.

The real behavior is affected by the rate at which the loads are applied and the variations of temperature of the sample. Phase transformations occur at a relatively constant stress within a finite length deformation range beyond which the initial stiffness is, at least approximately, recovered. The austenitic phase of the material is stable before the application of stress. However, at a critical stress level the martensite becomes stable, yielding and showing a stress plateau, as shown in Fig. 5.3 and (5.4). Since the martensite is only stable because of the applied stress, the austenite structure again becomes stable during unloading, and the original undeformed shape is recovered. Fig. 5.3 illustrates the theoretical behavior of Nitinol as it is loaded in tension allowing the full volume of the Nitinol to effectively dissipate energy; the key characteristic is that if the strain is less than ε_{el} there is no permanent deformation. NiTi SMAs demonstrate a high level of energy dissipation and a superelastic hysteresis. Another very useful characteristic of superelastic NiTi SMAs is that they harden after conversion to stress-induced Martensite, at approximately 6–8% of strain level.

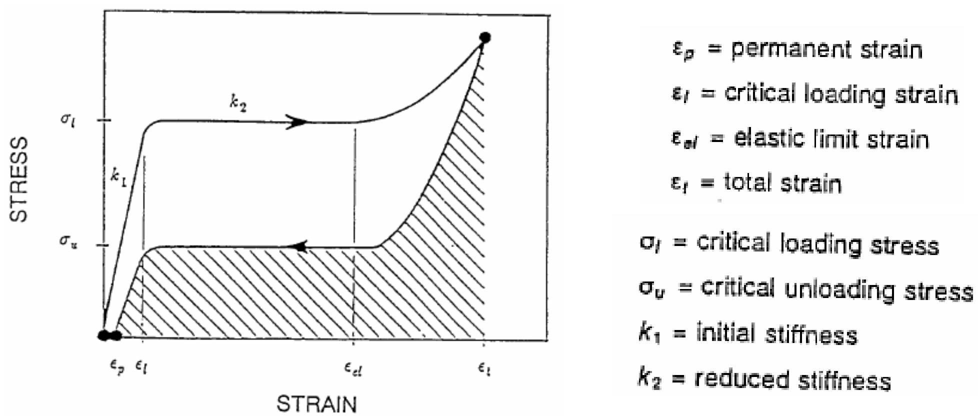

Fig. 5.3. Stress–strain relationship for superelastic shape memory alloys

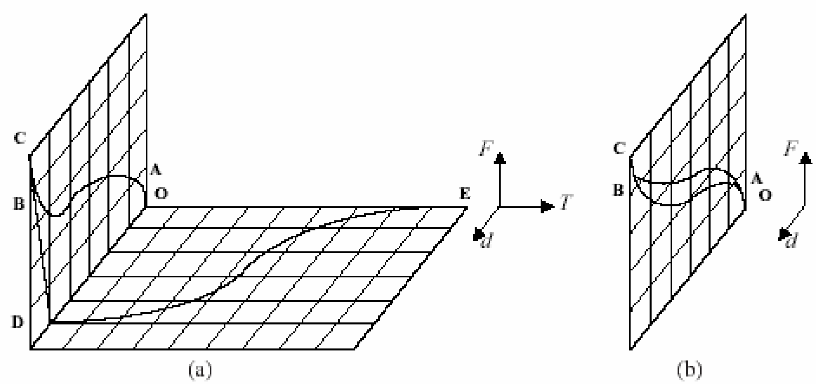

Fig. 5.4. Typical behaviour of an SMA element: shape memory effect (a) and superelasticity (b)

Nitinol shape memory alloys possess several useful characteristics for use as restrainers in bridges, as shown in Table 5.1, where they are compared to typical structural steel properties, such as: large elastic strain range, hysteretic damping, highly reliable energy dissipation (based on a repeatable solid state phase transformation), strain hardening at strains above 6%, excellent low- and high-cycle fatigue properties, and excellent corrosion resistance.

Table 5.1. Comparison of NiTi SMA properties with typical structural steel

Property	Ni–Ti shape memory alloy	Steel
Recoverable elongation	8%	0.2%
Young's modulus	8.7E4 MPa (Austenite), 1.4–2.8E4 MPa (Martensite)	2.07×10^5 MPa
Yield strength	200–700 MPa (Austenite), 70–140 MPa (Martensite)	248–517 MPa
Ultimate tensile strength	900 MPa (fully annealed), 2000 MPa (work hardened)	448–827 MPa
Elongation at failure	25–50% (fully annealed), 5–10% (work hardened)	20%
Corrosion performance	Excellent (similar to stainless steel)	Fair

5.1.1.1 Experimental test on shape memory alloy dampers

The stress–strain curve of the NiTi damper under tension cyclic loading is shown in Fig. 5.5 (DesRoches and Delmont, 2002). In this case the specimens were loaded at increasing strains ranging from 0.5 to 8.0% strain: the damper has a loading plateau stress of approximately 450 MPa, with strain hardening of approximately 7%. The residual strain increases with increasing total strain deformations. For total strains less than 4%, the residual deformation is less than 0.25%. After a total strain of 8%, the bar showed approximately 1% residual strain. The 1% residual strain value indicates that slip began to contribute to the overall deformation. Although the loading plateau remains constant, the unloading plateau decreased as the total deformation increased: this important effect results in significantly more energy dissipation for larger strain values. Finally, the specimen began to significantly strain harden after approximately 5–6% strain, with a stiffness that is approximately 45% of its initial stiffness. Other tests were conducted by Aiken *et al*. (1993), and are shown in Fig. 5.6 and Fig. 5.7: when preloaded, Nitinol demonstrated the special ability to "yield" repeatedly without loosing its preload.

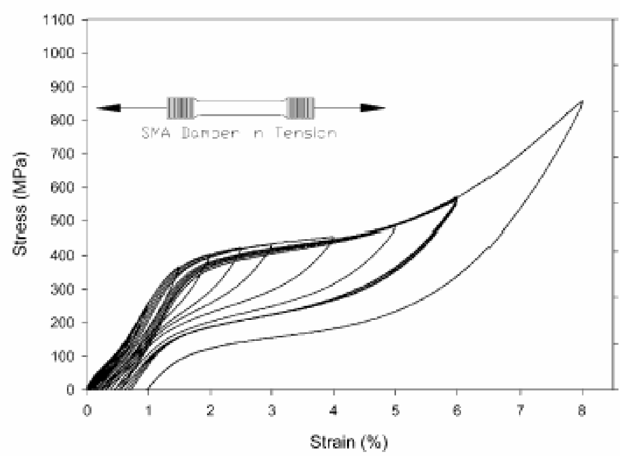

Fig. 5.5. Stress–strain curve from tension test of SMA restrainer bar (DesRoches and Delmont, 2002)

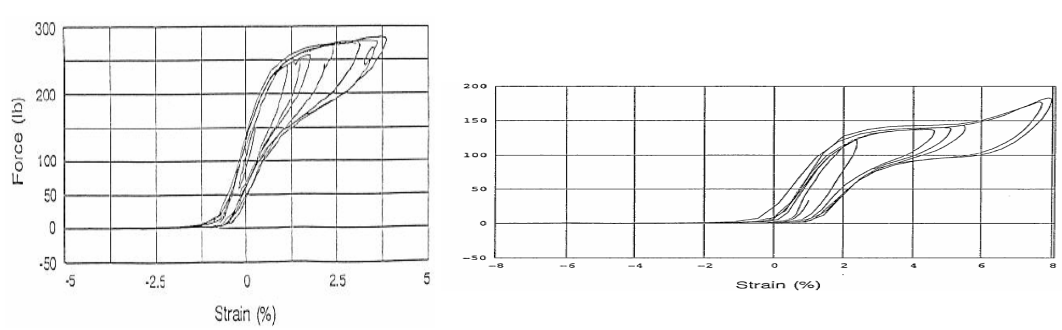

Fig. 5.6. Nitinol Moderate-Strain (up) and High-Strain (down) Hysteresis Behavior

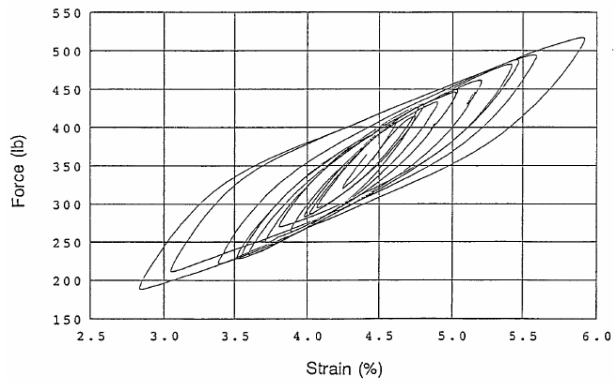

Fig. 5.7. Nitinol hysteresis behavior with pre-strain applied

5.1.2 Analytical models of SMA restrainer

The SMA restrainers can be modeled by means of tension-only multi-linear elements representing the force-displacement relationship of the SMA, including the yield plateau and unloading plateau. As previously mentioned, the unloading stress and residual deformation depends on the total deformation. In the study of DesRoches and Delemont (2002), the residual deformation is taken as zero, and the unloading stress is kept constant (Fig. 5.8), based on the average value over the strain range tested: parametric studies conducted showed that small variations in the parameters used in the analytical model for the residual deformation and the unloading stress have a negligible effect on the response.

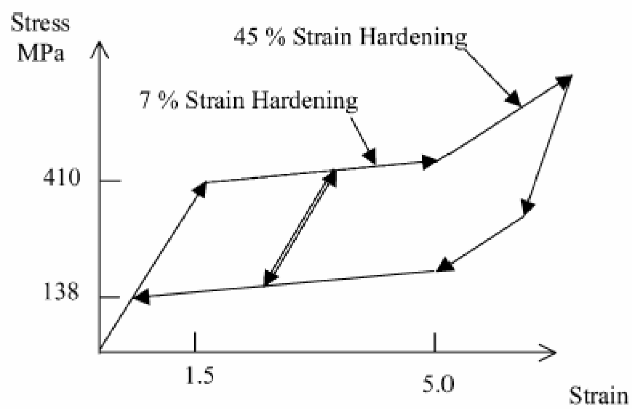

Fig. 5.8. Analytical model of SMA restrainer

Other analitycal models for SMAs can be found in the Liang–Rogers (1990) model and the Ivshin–Pence (1994) model. The former (Fig. 5.9, left) provides a sharp transition at the start and at the end of the transformation phases, therefore resembling the classical elastic–plastic behaviour; in this case, the only differences between steel and SMA braces are restricted to those properties possessed by the SMA materials: the recovery of the initial stiffness at the end of the transformation phase during loading, which implies the possibility to perform drift control and the pseudo-elasticity upon unloading, which is responsible for the re-centring capabilities of the SMA devices. The latter model (Fig. 5.9, right) is actually more accurate.

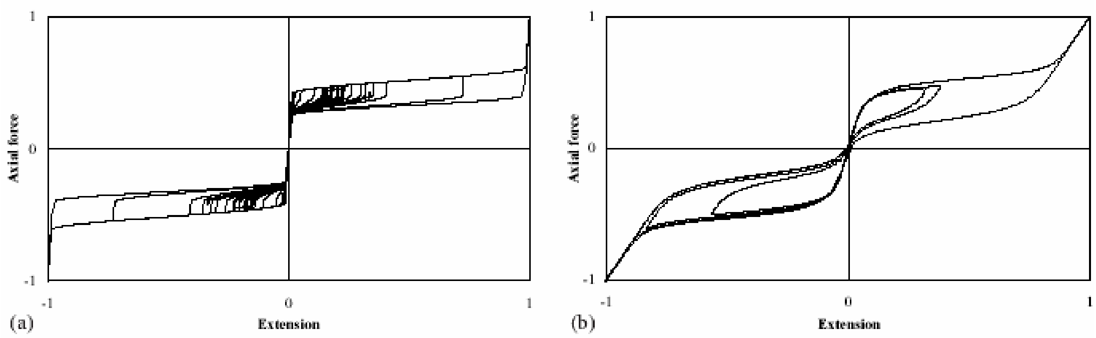

Fig. 5.9. Constitutive models for SMA finite elements: (a) Liang–Rogers and (b) Ivshin–Pence

5.2 SELF-CENTERING DAMPER TYPOLOGIES: THE ENERGY DISSIPATING RESTRAINT

Fluor Daniel, Inc., has developed and tested a type of friction device, called Energy Dissipating Restraint (EDR), originally used as a seismic restraint for the support of piping systems in nuclear power plants. The mechanism of the EDR consists of sliding friction wedges with a stop located at the end of the range of motion. A complete detail for this device can be seen in Fig. 5.10. The main components of the device are the internal spring, the steel compression wedges, the Bronze friction wedges sliding on a steel barrel, the stops at both ends of the internal spring, and the external cylinder. Full description of the EDR mechanical behavior and detailed diagrams of the device are given by Nims (1993).

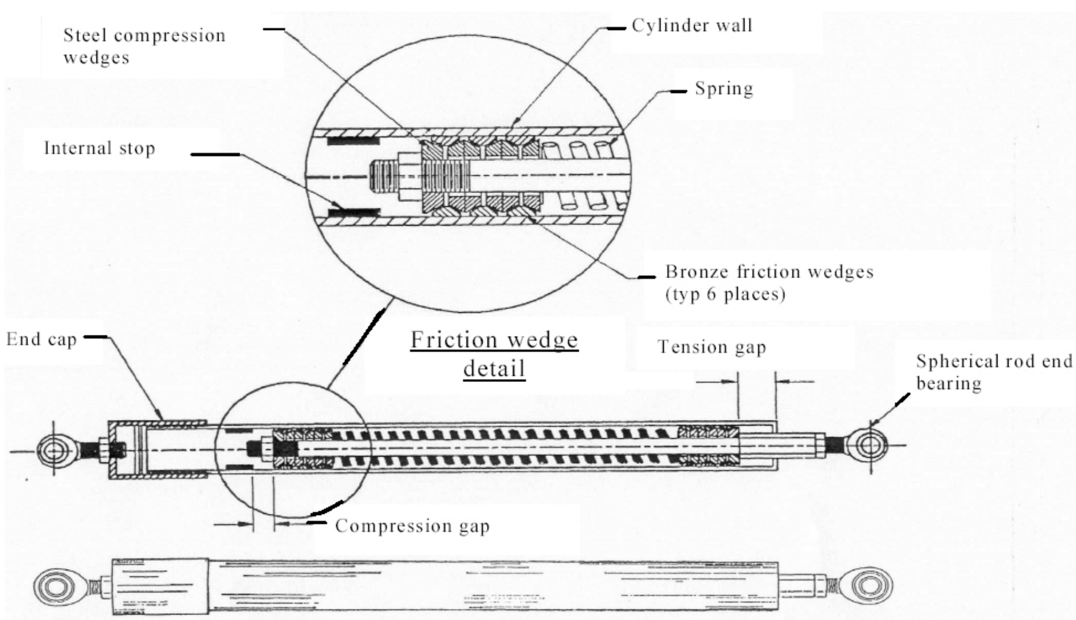

Fig. 5.10. External and internal views of the EDR (Nims et al., 1993)

Characteristic features of the device are its self-centring capability and the developed frictional force proportional to the displacement. In operation, the compressive force in the spring acting on the compression and friction wedges causes a normal force on the cylinder wall. This normal force is proportional to the force in the spring. The normal force and the coefficient of friction between the bronze friction wedges and the steel cylinder wall determine the slip force in the device.

In the EDR, two types of behavior are combined: linear stiffness and friction. Different combinations in between are possible, developing several different types of hysteresis loops, in dependence on the spring constant of the core, the initial slip load, the configuration of the core, and the gap size. Two typical hysteresis loops for different adjustments of the device are shown in Fig. 5.11. The most interesting behaviour consists in possessing fat "S-shaped" loops and self-centring properties. The friction force dissipating the energy is proportional to the displacement and the internal preload of the EDR. The proportionality between the dissipated energy and the displacement makes the EDR effective at low levels of seismic excitation or for wind loads while also being effective at high seismic levels.

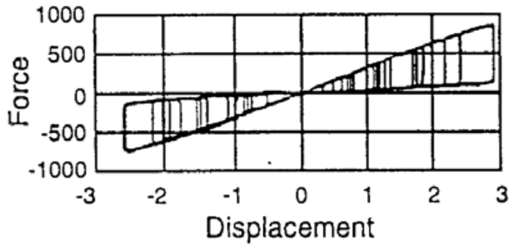

Fig. 5.11. Hysteresis loop shapes (lb-in units, Richter et al., 1990) for EDR tested with different adjustments: left: no gap, no preload; right: no gap, some preload

5.3 SELF-CENTERING DAMPER TYPOLOGIES: THE FRICTION SPRING SEISMIC DAMPER

The SHAPIA seismic damper, also known as Friction Spring Damper, uses a ring spring to dissipate earthquake-induced energy (Kar and Rainer 1995, 1996; Kar *et al.* 1996). A section through a typical ring spring assembly (Fig. 5.12) consists of outer and inner rings with tapered mating surfaces. As the spring column is loaded in compression, the axial displacement is accompanied by sliding of the rings on the conical friction surfaces: the outer rings are subjected to circumferential tension (hoop stress), and the inner rings experience compression.

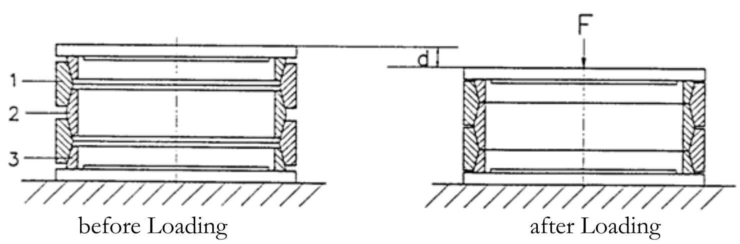

Fig. 5.12. Friction spring details. 1—outer ring; 2—inner ring; 3—inner half ring

At the time of assembly and fabrication of the damper, special lubricant is applied at the tapered surfaces and at the external surfaces of the ring stack as a unique treatment for lifelong operation. The damper housing is virtually hermetically sealed to prevent any access of contaminants and to preserve and protect the lubricant. Some pre-compression by means of a centrally located tie-bar may be needed to align the rings axially as a column stack. The fabrication and assembly details are designed to ensure that the friction springs themselves are always in axial compression whenever the damper unit is subjected to either tension or compression. Fig. 5.13 shows a diagrammatic view of the prototype unit. The spring stack is retained at its ends by the flanges of a pair of cups. The damper carries no external load.

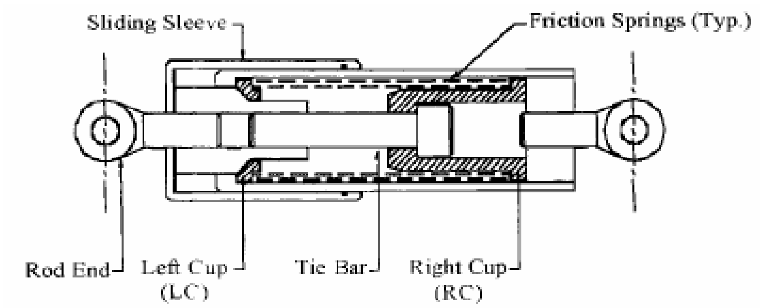

Fig. 5.13. Diagrammatic view of seismic damper

During the process of loading and unloading, it offers spring effects together with damping. It is also strongly self-centering, provided that no plastic deformations have occurred: the ring springs are designed to remain elastic during a seismic event so that no repair or replacement should be required, and the structure should thus be protected against aftershocks and future earthquakes. This friction-based seismic damper is designed to display a symmetrical flag-shaped hysteresis diagram stable and repeatable (Fig. 5.14). Five different physical parameters define the hysteretic behaviour of the SHAPIA damper (Fig. 5.14): an elastic stiffness K_0, a loading slip stiffness $r_L K_0$, an unloading slip stiffness $r_U K_0$, a slip force F_s, and a residual re-centring force F_c. The maximum forces reached upon loading F_{maxL} and unloading F_{maxU} are also shown.

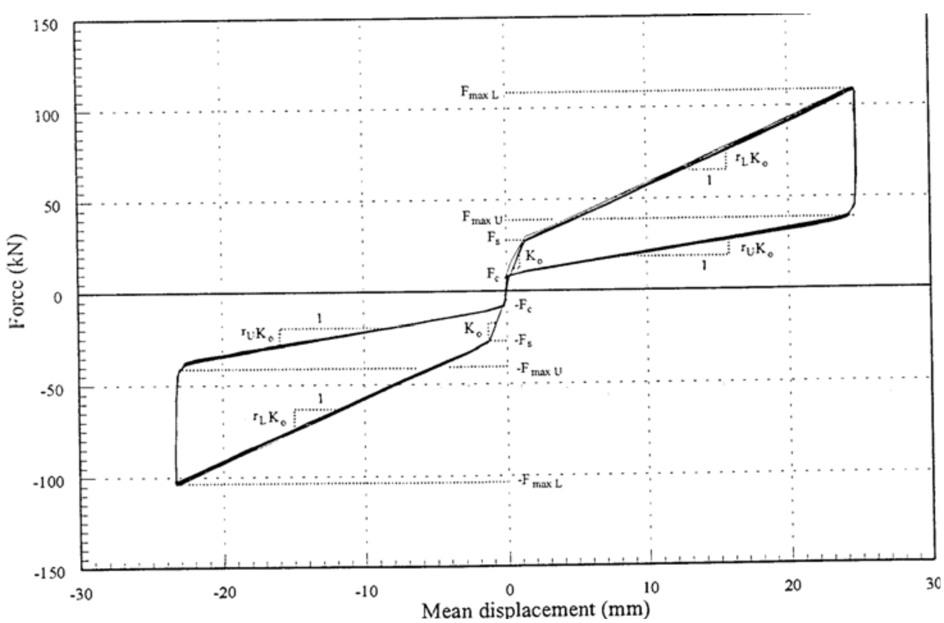

Fig. 5.14. Experimental force-displacement hysteresis loops of seismic damper

5.3.1.1 Experimental studies on SHAPIA dampers

Filiatrault *et al.* (2000) evaluated the performance of a 200-kN capacity prototype of the SHAPIA damping system under simulated earthquake ground motions. The values of parameters characterising the tested damper are listed in Table 5.2. They found:

- In both the characterization tests and the earthquake simulation tests, the force-displacement hysteresis loops of the damper are repeatable, stable, and identical in tension-compression. The energy dissipating and the re-centring characteristics of the damper were demonstrated. The energy dissipation capacity of the damper was found to increase with the imposed displacement.

- The behavior of the damper is nearly identical for all frequencies (considered range: 0.05–2.0 Hz). All intermediate loading and unloading of the damper occur in a predictable manner, within the backbone curve of the force-displacement hysteresis loops.

Table 5.2. Physical parameters defining hysteretic behavior of seismic damper prototype tested

Parameter (1)	Numerical values (2)
Elastic stiffness K_o	23.2 kN/mm
Loading slip stiffness $r_L K_o$	3.48 kN/mm
Unloading slip stiffness $r_U K_o$	1.39 kN/mm
Slip force F_s	28 kN
Residual recentering force F_c	9 kN

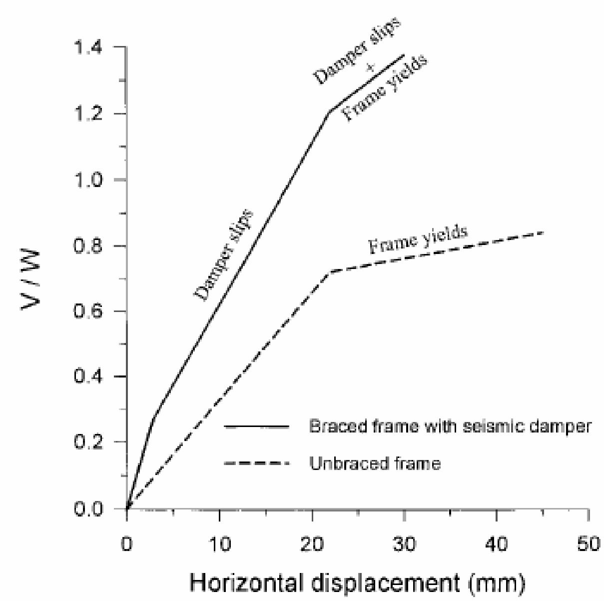

Fig. 5.15. Pushover analysis of unbraced frame and braced frame with seismic damper

- The degradation of the damper is minimal. The energy dissipated per cycle in the durability test decreased by less than 4% from the first to the twentieth cycle of loading.
- In the shake table tests, the damper was effective in reducing lateral displacements.
- The seismic damper dissipated an amount of the energy fed into the structure sufficient to protect the structure from undergoing severe inelastic deformations in both tests.

5.4 SELF-CENTERING DAMPER TYPOLOGIES: THE POST-TENSIONED ENERGY DISSIPATING STEEL CONNECTIONS

Moment-resisting connections using post-tensioning concepts were developed for precast concrete construction and recently extended to steel Moment Resisting Frames: Christopoulos *et al.* (2002) demonstrated that the performance of these connections is excellent under simulated seismic loading, due to their capacity of ensuring small residual drifts through self-centring capabilities, even when significant transient inelastic deformations occurred during the seismic response.

The post-tensioned energy dissipating (PTED) connection incorporates high strength steel post-tensioned bars designed to remain elastic, and confined energy-dissipating bars designed to yield both in tension and in compression. Fig. 5.16 illustrates the implementation of the PTED steel connection on a steel frame, together with its deformed configuration. Fig. 5.17 shows a moment-rotation relationship obtained experimentally from a large scale PTED connection (Christopoulos *et al.*, 2002), in which the self-centring capacity and energy dissipation characteristics are evident.

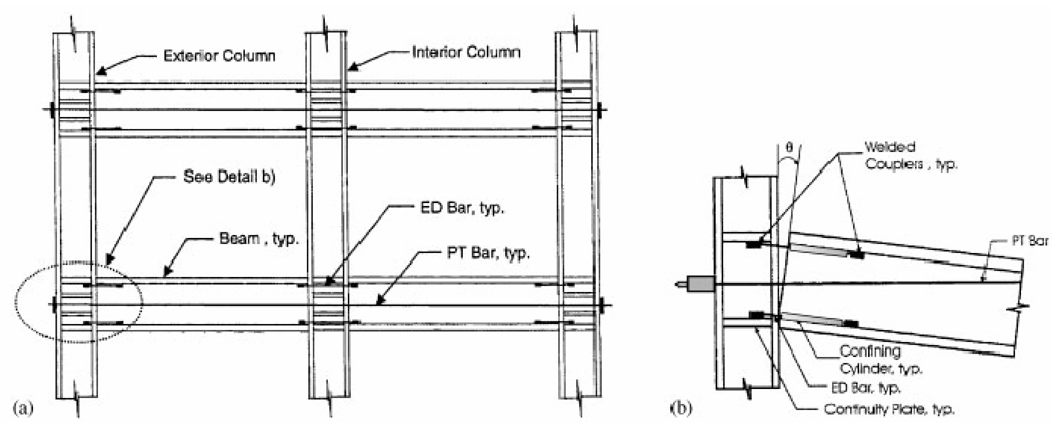

Fig. 5.16. PTED steel connection: (a) steel frame with PTED connections; (b) deformed configuration of exterior PTED connection.

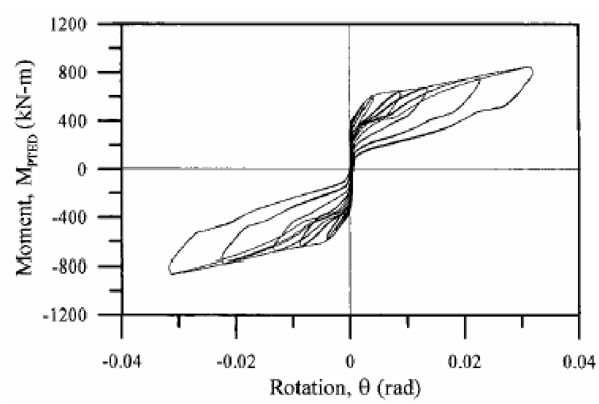

Fig. 5.17. Experimental moment–rotation curve of PTED connection

Fig. 5.18 shows an idealization of the flag-shaped hysteretic behaviour of a PTED connection: the overall response of the connection can be decomposed into the non-linear elastic contribution from the PT bars and the bilinear elasto-plastic hysteretic contribution provided by the ED bars. The same kind of flag-shaped behaviour can be achieved using specialized energy dissipating dampers or material (such as shape memory structural dampers or friction spring dampers). Fig. 5.19 shows the idealized hysteretic force–displacement relationship of a system incorporating PTED connections. Two independent response parameters α and β are associated to the hysteretic model of the device: α is the post-yielding stiffness ratio, ranging from 0.02 to 0.35, and β reflects the energy dissipation capacity of the system, ranging from 0.0 (piecewise non-linear elastic system) to 1.0 (maximum to ensure self-centering capability). Fig. 5.20 shows the qualitative force–deflection relationships of flag-shaped hysteretic systems for different values of α and β.

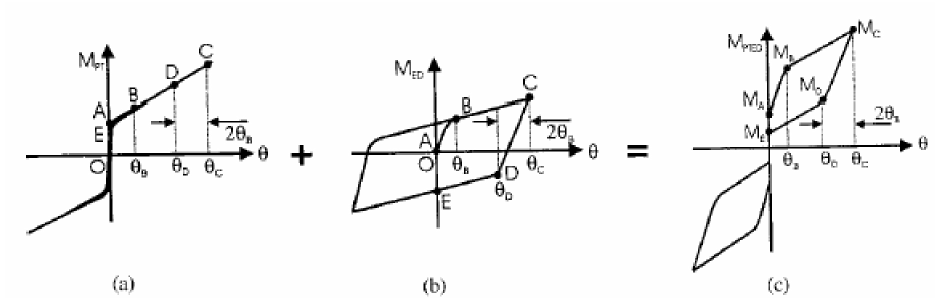

Fig. 5.18. Idealized hysteretic behaviour of the PTED connection: (a) contribution of PT Bars; (b) contribution of ED bars; and (c) moment–rotation relationship of PTED connections

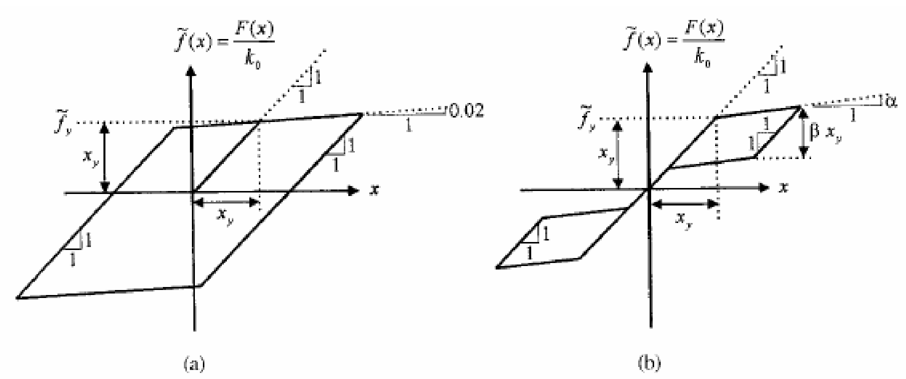

Fig. 5.19. Idealized pseudo force–displacement relationships: (a) system with welded connections; and (b) system with PTED connections

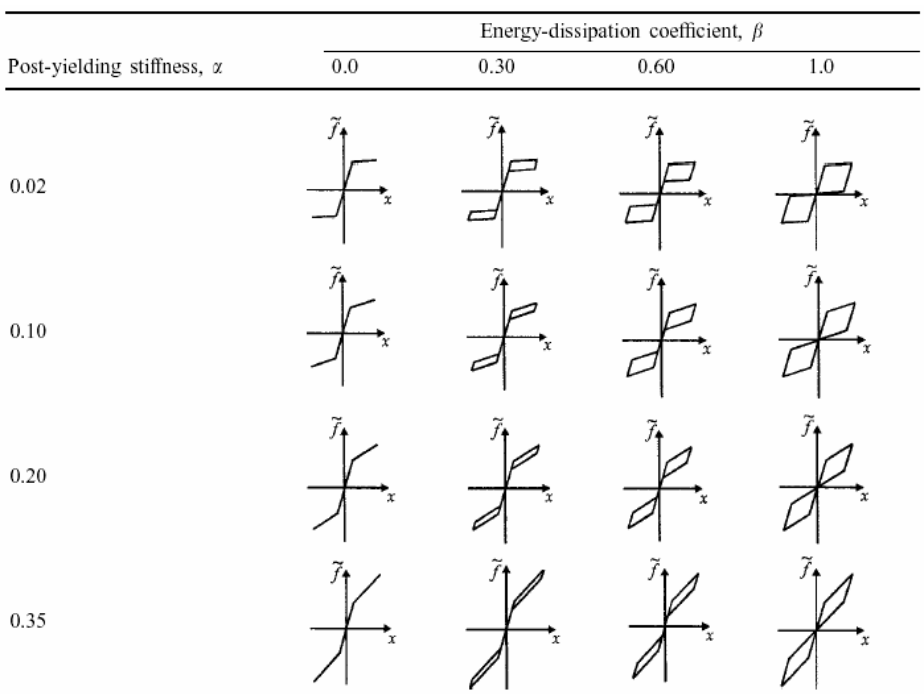

Fig. 5.20. Qualitative force–deflection relationships of flag-shaped hysteretic systems for different values of α and β

5.4.1 Parametric studies on PTFE connections

Christopoulos *et al*. (2002) investigated the seismic response of SDOF systems incorporating a bilinear elasto-plastic hysteretic model or a flag-shaped hysteretic model. The independent parameters α and β, defining respectively the post-yielding and the energy-dissipation of the flag-shaped hysteretic model, allow for flexibility in tailoring the response of this type of SDOF system: the comprehensive parametric study determined the influence of these parameters on displacement ductility, absolute acceleration, absorbed energy and residual drifts. It was observed that:

- The reduced displacement ductility in system with short initial period (T0≤1.0) and low strength levels (i.e. the largest displacement ductility systems) is most effectively achieved by increasing α rather than β. For long period and high strength systems is the opposite: increasing β rather than α is more effective. Beside, the seismic response of flag-shaped hysteretic systems was qualitatively similar to the elasto-plastic hysteretic systems.
- With respect to the absolute acceleration, the flag-shaped hysteretic system produces higher values than the comparable elasto-plastic one, particularly for low strength systems with large values of α, whilts nearly insensitive to β.
- The absorbed energy increases for low period/low strength systems. Insensitive to α, it doubles when β changes from 0 to 1, indicating a higher amount of hysteretic damping but also large cumulative inelastic excursions. The energy absorbed by the flag-shaped hysteretic system is obviously less then the comparable elasto-plastic one, but the damage is concentrated in the replaceable energy-dissipating bars of the PTED connections.
- Thanks to the self-centering capacity, there are no residual drifts, always present in the elasto-plastic systems.

5.5 A FLAG SHAPED HYSTERETIC MODEL FOR RE-CENTRING DAMPERS

The last three presented dampers can be represented by an unique flag shaped hysteresis loop, with a number of characterizing parameters suitable to the single specific shapes. The general model is shown in Fig. 5.21, and numerically translated in relationships (5.1) to (5.3): equation (5.1) represent the loading branches, i.e. when $x_i > x_{i-1}$. and equation (5.2) represent the unloading path, i.e. when $x_i < x_{i-1}$. Fig. 5.22 and Fig. 5.23 show the general model fitted to the illustrated Self-Centering Dampers by setting some of the seven parameters to predetermined values, according to equations (5.4) to (5.11). Appropriate conditions for the loading/unloading paths have to be set, as well as for the friction transient phase change, either by means of a step function (sign-type) or a continuous function as discussed in § 2.4.2.

$$\begin{aligned} &F = Kd && 0 < d < d_1 \\ &F = F_1 + K_1(d - d_1) && d_1 < d < d_2 \end{aligned} \qquad (5.1)$$

$$\begin{aligned} &F = F_2 + K_3(d - d_2) && d_3 < d < d_2 \\ &F = F_0 + +K_2(d - D_0) && D_0 < d < d_3 \\ &F = K_0 d && 0 < d < D_0 \end{aligned} \qquad (5.2)$$

$$\begin{aligned} &K_0 = F_0 / D_0 \\ &d_1 = F_1 / K \\ &d_2 = d_1 + (F_2 - F_1) / K_1 \\ &d_2 = (F_0 + K_3 d_2 - F_2 - K_2 D_0)/(K_3 - K_2) \end{aligned} \qquad (5.3)$$

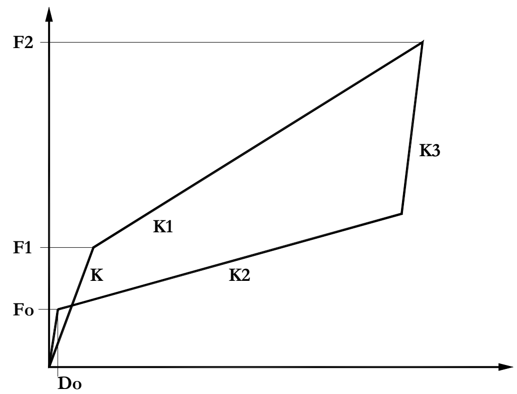

Fig. 5.21. Flag shape general hysteresis model for SC dampers

EDR in trapezoidal configuration: **K=K3=∞; D0=0**

Load: $F = F_1 + K_1(d - d_1) \qquad 0 < d \le d_2$ *(5.4)*

Unload: $F = F_0 + +K_2(d - D_0) \qquad 0 < d < d_2$ *(5.5)*

EDR in triangular configuration: K=K3=∞; D0=0; F0=F1=0

Load: $F = K_1 d \qquad 0 < d < d_2$ *(5.6)*

Unload: $F = K_2 d \qquad 0 < d < d_2$ *(5.7)*

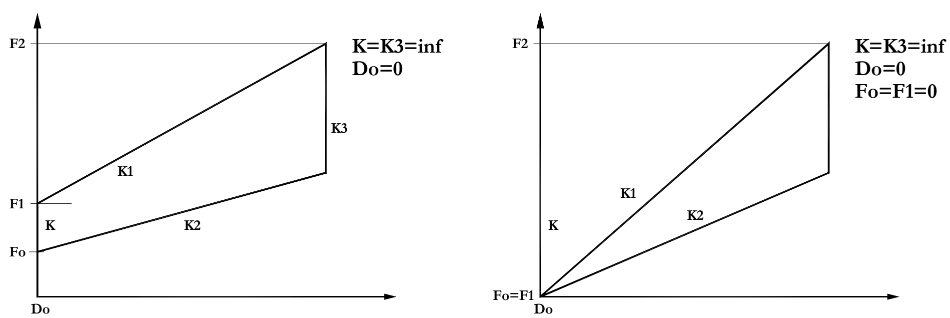

Fig. 5.22. General model in EDR configurations

SHAPIA damper: **K3=∞; D0=0**

Load: $$\begin{aligned} F &= Kd & 0 < d < d_1 \\ F &= F_1 + K_1(d - d_1) & d_1 < d < d_2 \end{aligned}$$ *(5.8)*

Unload: $F = F_0 + +K_2 d \qquad 0 < d < d_2$ *(5.9)*

PTED connection: **K=K3; D0=F0/K; K1=K2**

Load: $$\begin{aligned} F &= Kd & 0 < d < d_1 \\ F &= F_1 + K_1(d - d_1) & d_1 < d < d_2 \end{aligned}$$ *(5.10)*

$$\begin{aligned} & F = F_2 + K(d - d_2) && d_3 < d < d_2 \\ \text{Unload:}\quad & F = F_0 + +K_2(d - D_0) && D_0 < d < d_3 \\ & F = Kd && 0 < d < D_0 \end{aligned} \tag{5.11}$$

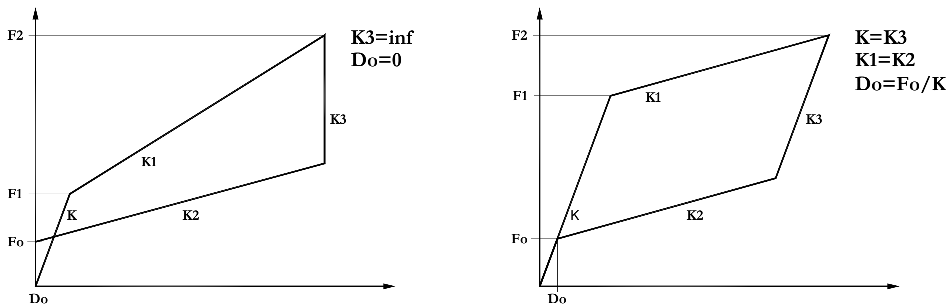

Fig. 5.23. General model in SHAPIA configuration and PTED configuration

6. DEVICE TYPOLOGIES: ELECTRO AND MAGNETORHEOLOGICAL DAMPERS

In recent years, manufacturers have shown an increased interest in MR devices. For instance, the Lord Corporation has been developing MR fluid and manufacturing MR truck seat dampers for a number of years now. Recently, the military has shown interest in using MR dampers to control gun recoil on Naval gun turrets and field artillery. Another area of study that has incorporated MR dampers is the stabilization of structures during earthquakes.

Magnetorheological Dampers (DMPs) typically consist of hydraulic cylinders containing micron-sized magnetically polarizable particles suspended within a fluid. With a strong magnetic field, the particles polarize and offer an increased resistance to flow. By varying the magnetic field, the mechanical behaviour of the MRD can be modulated: MR fluids can be changed from a viscous fluid to a yielding solid within millisecond and the resulting damping force can be considerably large with a low-power supply. Electrorheological Dampers (ERDs) are the electric analogue ones. ER fluid contains micro-sized dielectric particles and its behaviour can be controlled by subjecting the fluid to an electric field. Magnetorheological fluids are an alternative solution to Electrorheological ones when very compact devices are needed, as the rheological behaviour is similar to the ER-fluids but with higher yield stress. In the case of steady fully developed flow, the shear resistance of MR/ER fluids may be modelled as having a friction component augmented by a Newtonian viscosity component. MR/ER Dampers can be placed between the chevron brace and the rigid diaphragm or beam.

6.1 SEISMIC RESPONSE AND CONTROL STRATEGIES WITH MR/ERDS

MR and ER dampers can be either employed as passive and semi-active devices or as active control devices. Control strategies based on semi-active devices combines the reliability of passive systems maintaining the versatility of active devices operating on battery power only. A semi-active control device does not input mechanical energy into the controlled structural system, but it can be controlled to optimally reduce the system response. Command signals are calculated based on the desirable control forces and input into an actuator, and different control force strategies (e.g. Xu *et al.*, 2000; Ribakov and Gluck, 2002) based on the optimal control force or displacement can be used to tailor the force required for enhancing the structural behaviour at every time instant of the occurring earthquake.

The damper force due to the yielding shear stress in fluids can be controlled through the change in the applied electric or magnetic field. The concept of the clipped Optimal Force Control is the following: when the j^{th} damper is providing the desirable optimal force, the voltage applied to the damper should remain at the current value; if the magnitude of the force produced by the j^{th} damper is smaller than the magnitude of the desired optimal force, and the two forces have the same sign, the voltage applied to the damper has to be increased; otherwise it has to be set to zero. An example of Control Force Strategy is the istantaneous optimal control with velocity and acceleration feedback (VAF), developed by Ribakov and Gluck (2002): an analysis of the structural response at discrete time steps during an earthquake yields the optimal forces required to the MR dampers for each time increment. Consequently, the magnetic field in the dampers is set to develop damping forces equal to those obtained by the optimization procedure.

The optimal displacement vector cannot be directly controlled, thus the damper force is tailored such that the measured displacement vector traces the optimal displacement vector as close as possible. The concept of the Optimal Displacement Control is the following: when the j^{th} damper displacement is approaching the desirable optimal value, the friction force in the damper should be set to its minimum value so as to let the damper reach its optimal displacement as soon as possible. When the j^{th} damper moves in opposite direction to the optimal displacement, the friction force in the damper should be set to its maximum value (or to the j^{th} damper force if smaller, to avoid the sticking condition) so as to prevent the damper motion away from the optimal target at most.

Xu *et al.* (2000) studied the effectiveness of the semi-active dampers in reducing seismic response of structures. They compared five structural typologies: unbraced, ordinarily braced, passive off MR/ERD (magnetic/electric field constant set at minimum yielding shear stress level), passive on MR/ERD (magnetic/ electric field constant set at maximum yielding shear stress level), semi-active control. The most effective strategy in reducing displacement respect to the unbraced structure is the semiactive, followed by the passive off, because the passive off dampers can dissipate vibration energy as viscous dampers. They observed that the performance of the dampers is strongly dependent on the choice of the damper parameters, i.e. the Newtonian viscosity η and the maximum yielding shear stress τ_{ymax}. They found that for a given structure and a given ground motion, there is the optimal value of η and τ_{ymax}, by which the maximum seismic response reduction can be achieved, independently of the employed control strategy. Then, there is a range for the yielding stress out of which the performance reduction deteriorate untill a certain value. Moreover, they showed that the seismic responses of buildings can be well controlled by smart ER dampers, and that maximum base shear can be strongly reduced. Nevertheless, the performance of smart damper with control strategy was found depending on the earthquake intensity, as the maximum yielding shear stress optimal value actually varies with the maximum PGA, and on the stiffness ratio of brace to structure, depending on the fraction of force (to which the energy dissipation capacity is related) that the braces allow the damper to develop.

Ribakov and Gluck (2002) studied a base isolation system using controllable MR dampers, composed of sliding isolators and controllable fluid dampers employing MR fluid activated selectively within a given range of the base displacements. The basic idea of the selective control strategy is that dampers are activated and the control forces are applied to the structure to keep base displacements within allowed limits. They compared different strategies for seismic protection of structures, such as FPS, active tendons controlling a fixed base structure, and base isolated structure continuously and selectively controlled by semi-active MRDs; with the selectively controlled MRDs, the response is globally reduced. Comparing selective to continuous strategies (in which control forces are activated only when the drift exceeds a specifc threshold of the isolator capacity or applied at each time instant, respectively), they found a comparable reduction in the seismic response with same magnitude of the applied maximum control forces, thus requiring a significantly smaller amount of energy for the dampers activation: regular commercial available batteries may supply the low accumulted energy required by them, making their control independent of external sources of energy.

6.1.1 Neural network emulation of inverse dynamics of MR dampers

When the relation between the command signals and the actuator forces is linear or can be explicitly established, the calculation of command signal is not an issue; otherwise it is likely that the command signals cannot be calculated beforehand and some additional feedback algorithms might be needed to produce the desired control forces. Via the neural network techniques, well known for their ability to approximate arbitrary functions, Chang and Zhou (2002) explored the possibility of developing an inverse dynamic model of the MR dampers that estimates the damper voltage required to produce the desirable control force.

Fig. 6.1 shows the control strategy for a structure controlled through a MR damper under earthquake ground acceleration: the control algorithm calculates a desirable control force f_d based on response and/or excitation. The desirable control force and the structural response are passed into an MR constraint filter, which ensures that the desirable control force is realizable by the MR damper before passing into the Neural Network model. If the desirable control force is not realisable, the voltage is set at the maximum or minimum when the desirable control force is larger or smaller than the allowable; if the desirable control force is realizable, the force and the structural response (a few time steps of structural displacements at the location where the damper is attached, damper forces, and command voltages) are passed into the Neural Network model, used to emulate the inverse dynamics of MR damper.

The emulation of the inverse dynamics of the MR damper can be regarded as an identification problem for a complex and unknown nonlinear system: the Neural Network estimation is basically a nonlinear mapping between the inputs and the outputs data used to train the Neural Network model itself. In general, the forces generated by the MR damper can follow those calculated from the optimal control algorithm quite well, within the damper capacity. The output for the inverse model is the command voltage to be supplied to the MR damper, in order to produce the desirable control force under the current response condition. This voltage is input into the MR damper supplying the force f acting on the structure. Such an active operation do not always offer significant performance improvement over using the damper passively.

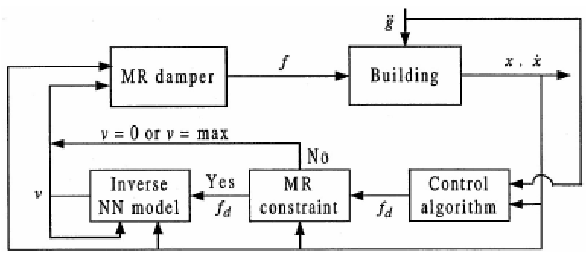

Fig. 6.1. Semiactive neural network control strategy

6.2 MAGNETORHEOLOGICAL DAMPERS

Magnetorheological (MR) fluid is composed of oil and varying percentages of iron particles coated with an anti-coagulant material. When unactivated, MR fluid behaves as ordinary oil, while if exposed to a magnetic field, the micron-size iron particles dispersed throughout the fluid align themselves along magnetic flux lines. This reordering of iron particles can be visualized as a large number of microscopic spherical beads threaded onto a very thin string. Once aligned in this fashion, the iron particles resist being moved out of their respective flux lines and act as a barrier to fluid flow.

MR fluid can be used in three different ways, referred to as squeeze mode, shear mode, and valve mode. A device that uses squeeze mode has a thin film (on the order of 0.5 mm) of MR fluid sandwiched between paramagnetic pole surfaces as shown in Fig. 6.2 (left). An MR fluid device is said to operate in shear mode when a thin layer (≈ 0.1 to 0.4 mm) of MR fluid is sandwiched between two paramagnetic moving surfaces. Shear mode (Fig. 6.2, center) is useful primarily for dampers not required to produce large forces and for clutches and brakes. The last mode of MR damper operation, valve mode (Fig. 6.2, right), is the most widely used: the MR fluid is used to impede the flow of MR fluid from one reservoir to another.

When MR fluid is used in the valve mode, the areas where the MR fluid is exposed to magnetic flux lines are usually referred to as “choking points” (see Fig. 6.3). Varying the magnetic field strength has the effect of changing the apparent viscosity of the MR fluid. The term “apparent viscosity” is used since the carrier fluid exhibits no change in viscosity as the magnetic field strength is varied. Upon exposure to a magnetic field, the MR fluid as a whole will appear to have undergone a change in viscosity. As the magnetic field strength increases, the resistance to fluid flow at the choking points increases until the saturation point has been reached. This resistance to movement that the iron particles exhibit is what allows us to use MR fluid in electrically controlled viscous dampers.

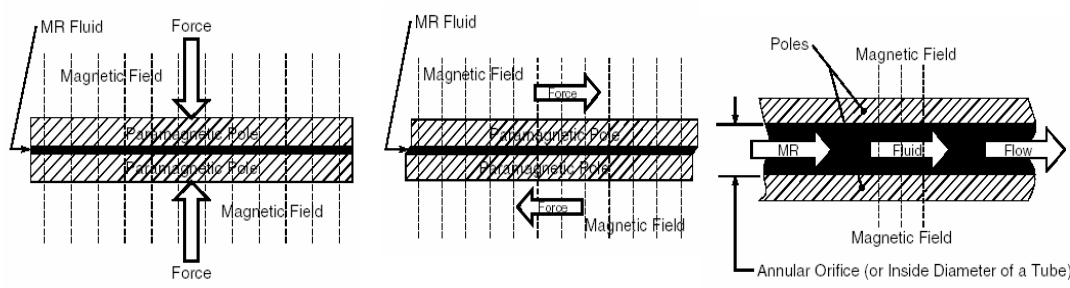

Fig. 6.2. MR fluid used in squeeze, shear and valve modes

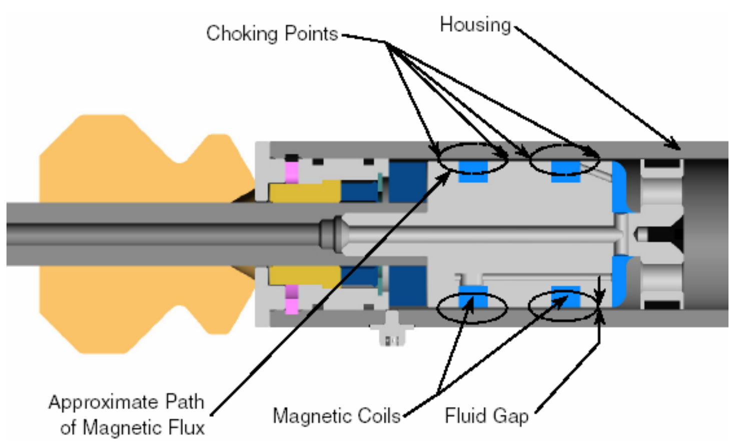

Fig. 6.3. Typical MR damper (Poynor, 2001)

6.2.1 Magnetorheological damper typologies: monotube and twin tube

A monotube MR damper (Fig. 6.4) has only one reservoir for the MR fluid. An accumulator piston is used in order to accommodate the change in volume resulting from the piston rod movement. The accumulator piston provides a barrier between the MR fluid and a compressed gas (usually nitrogen) that is used to accommodate the necessary volume changes.

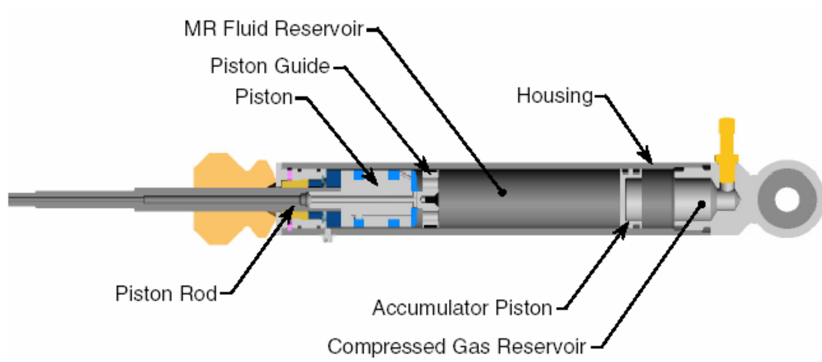

Fig. 6.4. Monotube MR damper section view (Poynor, 2001)

The twin tube MR damper has two fluid reservoirs, one inside of the other. This configuration (Fig. 6.5) has an inner and an outer housing. The inner housing guides the piston/piston rod assembly just as the housing of a monotube damper does. This inner housing is filled with MR fluid so that no air pockets exist. The outer housing partially filled with MR fluid helps to accommodate changes in volume due to piston rod movement: a valve assembly called a "foot valve" attached to the bottom of the inner housing regulates the fluid flow between the two reservoirs (Fig. 6.5, bottom).

In order for a twin-tube MR damper to function properly, the compression valve must be stiff relative to the pressure differential that exists between either sides of the piston when it is in operation. The return valve must be very unrestrictive so that as little resistance to fluid flow as possible is provided. The damper should function properly as long as the valving is set up properly, the damper is used in an upright position and the MR fluid settling is not a problem. With this type of MR damper, the latter condition is a major concern since the iron particles can settle into the valve area and prevent the damper from operating properly. All MR dampers are affected by MR fluid settling, but this problem is particularly prevalent in the twin tube variety.

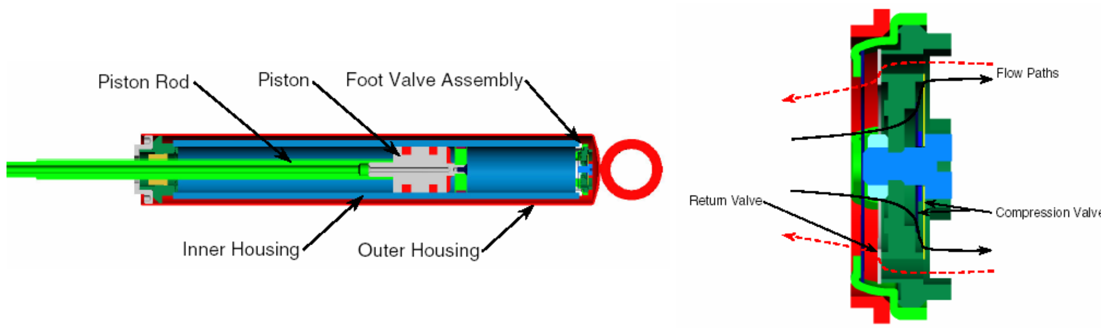

Fig. 6.5. Twin tube MR damper and detail of foot valve (Poynor, 2001)

6.2.2 Magnetorheological damper typologies: double-ended MR and MR piloted hydraulic dampers

The double-ended MR damper (Fig. 6.6, left) has piston rods of the same diameter that protrude through both ends of the damper. Since there is no change in volume as the piston rod moves, the double-ended damper does not require any accumulator. Double-ended MR dampers have been used for bicycle applications, gun recoil applications, and for stabilizing buildings during earthquakes. MR piloted hydraulic dampers (Fig. 6.6, right) are hybrid dampers in which a small MR damper controls a valve that, in turn, is used to regulate the flow of hydraulic fluid.

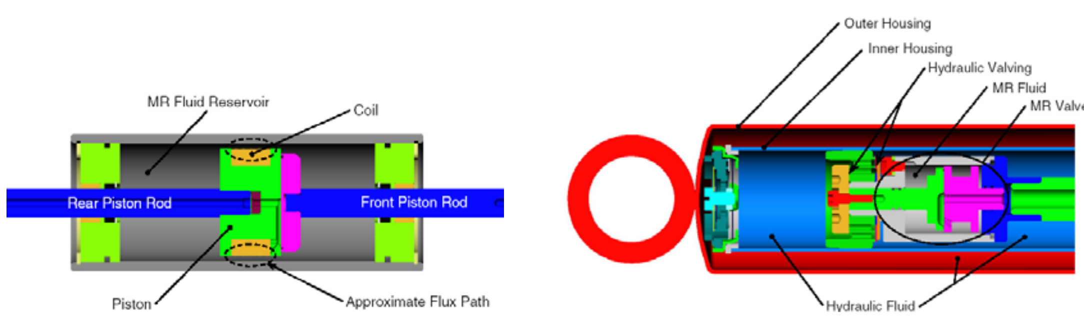

Fig. 6.6. Double-ended MR damper (left) and MR piloted hydraulic damper (right), (Poynor, 2001)

6.2.3 A magnetorheological damper model

The MR Damper hysteretic behaviour is nonlinear, and can be modelled by various hysteresys models (Bingham - in Shames and Cozzarelli, 1992; Spencer *et al.* (1997); Bouc, (1967); Wen, (1976), etc.). The well-known Bingham viscoplastic model consists of a viscous damping term in parallel with a controllable yield force, as described in equation (6.1), where C_{MR} is the damping coeffcient, $\dot{d}_{MR}$ is the velocity transferred to the damper, and F_y is the yield force related to the fluid yielding stress. The yield force is controllable by sending a voltage signal to the electromagnets in the MR damper. Experimental measures of the force in a MR damper (Spencer *et al.*, 1997) showed that although the force-displacement behaviour appears to be reasonably modelled, the behaviour of the damper is not captured, especially for velocities close to zero.

$$F_{MR} = C_{MR}\dot{d}_{MR} + F_y \mathrm{sign}(\dot{d}_{MR}) \tag{6.1}$$

The Bouc-Wen model shown in Fig. 6.7 (left) predicts accurately the force-displacement behaviour in the damper, but the nonlinear force-velocity response does not roll-off the region where the acceleration and velocity have opposite signs and the magnitude of velocities is small. Spencer *et al.* (1997) proposed a phenomenological model of the damper, shown in Fig. 6.7 (right), adapted to fluctuating magnetic fields, ruled by equations (6.2), where x , f , and y are respectively the displacement, the force and an internal pseudodisplacement of the MR damper; u is the output of a first-order filter, and v is the command voltage sent to the current driver. In this model, k_1 is the accumulator stiffness, c_0 and c_1 is the viscous damping coefficients observed at large and low velocities, respectively; k_0 controls the stiffness at large velocities; and x_0 is the initial displacement of spring k_1 associated with the nominal damper force due to the accumulator; γ, β and A are hysteresis parameters for the yield element; and α is the evolutionary coefficient. Values for the parameters proposed by Spencer *et al.*, (1997) are listed in Table 6.1.

$$\begin{gathered}
f = c_1\dot{y} + k_1(x - x_0) \\
\dot{y} = \frac{1}{(c_0 + c_1)}[\alpha z + c_0\dot{x} + k_0(x - y)] \\
\dot{z} = -\gamma|\dot{x} - \dot{y}|z|z|^{n-1} - \beta(\dot{x} - \dot{y})|z|^n + A(\dot{x} - \dot{y}) \\
\alpha = \alpha_a + \alpha_b u \qquad c_0 = c_{0_a} + c_{0_b} u \\
c_1 = c_{1_a} + c_{1_b} u \qquad \dot{u} = -\eta(u - v)
\end{gathered} \tag{6.2}$$

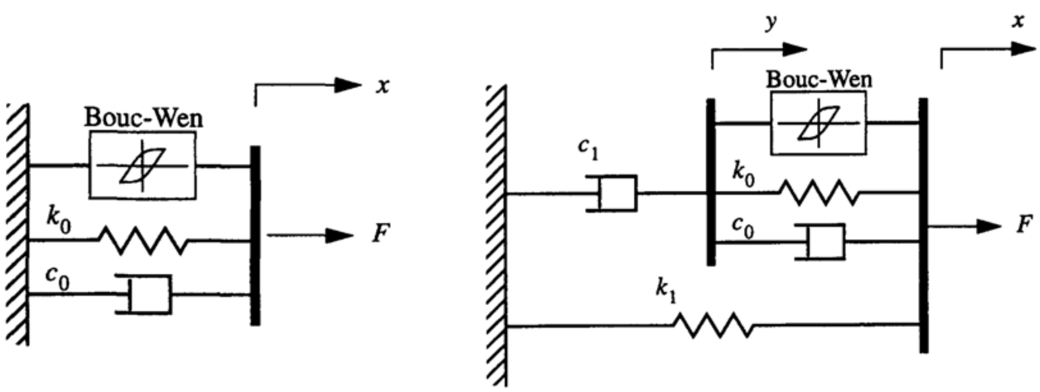

Fig. 6.7. Bouc–Wen model and mechanical model of the MR damper

Table 6.1. Parameters for the model of an MR damper (Spencer et al., 1997)

Parameter	Value	Parameter	Value
c_{0a}	21.0 Ns/cm	α_a	140 N/cm
c_{0b}	3.5 Ns/cmV	α_b	695 N/cmV
k_0	46.9 N/cm	γ	363 cm^{-2}
c_{1a}	283 Ns/cm	β	363 cm^{-2}
c_{1b}	2.95 Ns/cmV	A	301
k_1	5.0 N/cm	n	2
x_0	14.3 cm	η	190 Hz

Based on the existing upper limit for the evolutionary variable (Spencer, 1986), Chang and Zhou (2002) individuated an approximated simple form for the force in the damper (equation (6.3)): substituting the maximum and minimum voltage, a range is found of forces realizable by the MR Damper.

$$f_u \cong \frac{c_{1a} + c_{1b}v}{c_{0a} + c_{1a} + (c_{0b} + c_{1b}v)v}\left[(\alpha_a + \alpha_b v)z_u + (c_{0a} + c_{0b}v)\dot{x}\right] \quad (6.3)$$

6.3 ELECTRO-INDUCTIVE DEVICES

Principles of operation of the electro-inductive devices are: (i) the generation of electrical power from seismic vibration as a primary energy source for the device mechanical input (passive and semi-active devices); (ii) the regulation of the sign and of the amount of the instantaneous power flow exchanged between earthquake and device in order to achieve a real time control of the vibration modes of the structure to be protected (active devices).

Two possible working schemes, shown in Fig. 6.8, have been investigated by Marioni (2002): a linear dissipator basically composed by two plates with permanent magnets and an inner plate of conductive non magnetic material moving between the previous two; and a rotating system where the linear earthquake motion is converted into a rotational one through a screw: the advantage of this solution is the possibility of amplifying the relative velocity by a suitable selection of the ratio between linear and rotational motion. Advantages of these devices are low maintenance, no ageing effects, no limitations on life cycles, low scattering of the response and no temperature sensitivity. Passive energy dissipating systems have inherent limitations such as they are generally tuned to the first vibration mode, while active ER dampers can be effective over a much wider range of frequencies.

The electro-inductive dissipators can be compared to the viscous dampers, due to their capability of providing both viscous and friction-type forces. The damping force developed by ER Damper depends on physical properties of the used fluid, on the pattern of flow in the damper and on its size. When an electric field is applied, the behaviour of the ER fluid is nearly viscoplastic, and the shear stress in it has to exceed the developed 'yield' stress to initiate flow. This mechanism is responsible for their controllable viscoplastic behaviour. The force produced by a linear fluid viscous device, is proportional to the velocity of the piston in the fluid, up to a limiting frequency, beyond which the device becomes viscoelastic; the resulting damping force $f_{ER}(t)$ in the ER damper is given in equation (6.4), where C_d is the viscous characteristic of the viscous ERD, x is the displacement at the damper location and F is the controllable yield force.

$$f_{ER}(t) = C_d \dot{x}(t) + F\text{sign}\left[\dot{x}(t)\right] \quad (6.4)$$

Fig. 6.8. ER Dampers: linear (left) and rotating (right) working schemes (Marioni, 2002)

6.3.1 Viscous and adjustable friction-type forces for electrorheological dampers

Makris *at Al.* (1996) showed that under long-period rapid pulses, viscous dissipation combined with controllable friction-type dissipation can reduce substantially structural displacements demands by keeping accelerations at low levels. ER dampers can supply the friction force needed at the beginning of the shaking through their capability of developing rigid visco-plastic behaviour, but they are able to avoid residual drifts by removing friction forces at some point of the shaking. ER dampers can operate as passive devices in absence of power, providing optimum response with a minimum amount of power supplied with a battery, being relatively inexpensive when compared to hydraulic dampers with mechanically controlled orificing.

Most ER dampers in the past involved shear flow. Fig. 6.9 shows an ER damper designer by Makris *et al.* (1996). The damper consists of an outer cylinder and a double-ended piston rod that pushes the ER-fluid through a stationary annular duct. The electric field is created perpendicular to the fluid flow across the bypass.

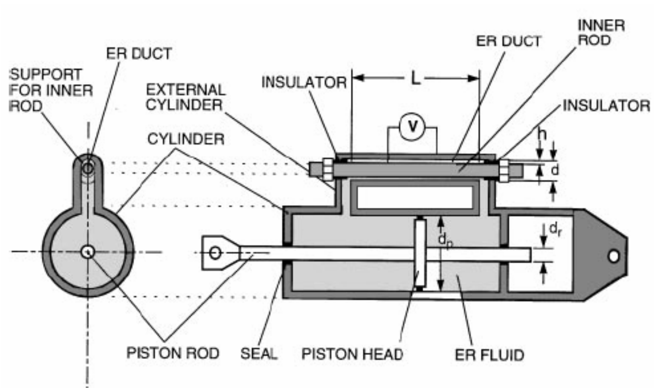

Fig. 6.9. Schematic of the ER Damper

Advantages of this kind of ER-dampers are that: (i) there are no moving parts within the damper besides the piston; (ii) it is a compact device that can produce relatively large forces; (iii) the ER damper yield forces can provide significant rigidity and, once exceeded, substantial energy dissipation; (iv) once the power fails, or during seismic events where viscous damping alone is sufficient to mitigate the response, the damper operates as a passive device providing a reasonable damping amount; (v) it can be positioned in any direction, because the ER material is nested within a very thin ring and apparently the surface tension that develops on the fluid eliminated the settling problem. In order to take advantage of the unique rigid-viscoplastic behaviour of ER Dampers, in which the electric field in the ER-damper can be activated in milliseconds, a simple mechanism that will announce the arrival of the strong seismic pulse is needed, like a sensor in the vicinity of the structure.

The Hagen Poiseuille flow that develops within the damper is responsible for the development of large forces across the piston head. The bypass consists of the inner rod (electrode) and the outer cylinder (ground). The shear stress that develops across the bypass is given by equation (6.5), where Δp is the pressure drop across the piston head, r is the radial distance from centre line of the ER duct, and L is the length of the duct (Fig. 6.10). This stress distribution is independent of the flowing material and can be seen as the stress demand across the duct to maintain equilibrium. If $h<<d$, the solution for the Poisseuille flow tends to that for flow between parallel plates, and if the fluid is Newtonian, with zero-shear-rate viscosity, η_0, the pressure drop due to viscous stresses under steady flow (in case of no field, i.e. E=0) is given in equation (6.6), where A_p is the piston head area, Q is the flow rate through the ER-duct, d is the diameter of the ER-duct, h is the width of the gap and n is the number of bypasses.

$$\tau_{xr}(r) = \Delta p \frac{r}{L} \tag{6.5}$$

$$\begin{gathered} \Delta p_v = \frac{1}{n} \frac{12\eta_0 LQ}{\pi d h^3}; \\ Q = A_p \dot{u}(t) \end{gathered} \tag{6.6}$$

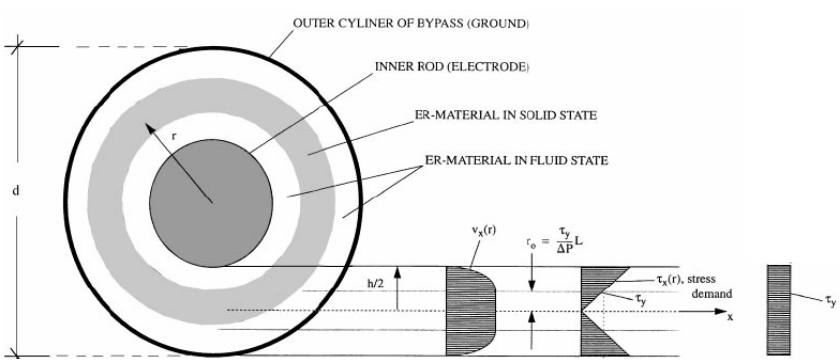

Fig. 6.10. Stress and velocity profiles of the yielding ER-fluid across the annular duct

When electric field is applied the behaviour of the ER-fluid is viscoplastic and the shear stress has to exceed the finite yield stress to initiate flow. The yield stress represents the capacity of the material to exist in a solid state. If the stress demand in equation (6.5) exceed the yield capacity of the ER material, then the ER material adjacent to the walls will yield and flow. For a rigid-viscoplastic material the velocity profiles across these fluidized rings is parabolic, whereas across the remaining solid core-ring is constant. As the pressure drop increases, more material yields. The pressure drop under viscoplastic flow is given in equations (6.7), reaching asymptotically expression (6.8) with increasing flow rate; this second equation is valid everywhere except for the zero-velocity limit, where the factor 3, in the second term is 2.

$$\Delta p = \frac{1}{n}\frac{12\eta_0 LQ}{\pi dh^3}\frac{1}{1-3\dfrac{\tau_y L}{\Delta ph}+4\left(\dfrac{\tau_y L}{\Delta ph}\right)^3} \tag{6.7}$$

$$\Delta p(t) \rightarrow \frac{P(t)}{A_p} = \frac{1}{n}\frac{12\eta_0 LA_p}{\pi dh^3}\dot{u}(t) + 3\frac{\tau_y L}{h}\mathrm{sign}[\dot{u}(t)] \tag{6.8}$$

Fig. 6.11 shows recorded (left) and predicted (right) force–displacement loops with (solid line) and without (dashed line) electric field. As the piston velocity increases, viscous effects dominate over plastic effects and the fraction of the force that can be controlled reduces. The predicted response is computed with relationship (6.9), where P_y is a permanent friction force acting on the damper seals: the resulting piston force is a function of the piston velocity, the mechanical properties of the ER-material and the geometric characteristics of the damper.

$$P(t) = \Delta p(t)A_p + P_y \mathrm{sign}[\dot{u}(t)] \tag{6.9}$$

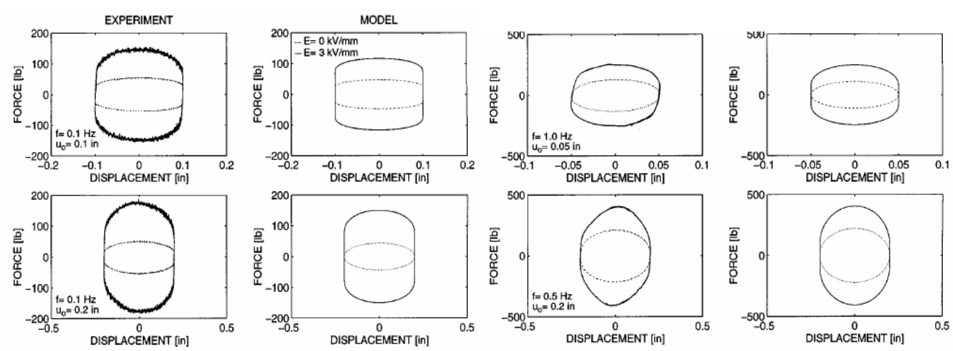

Fig. 6.11. Comparison of recorded and predicted force-displacement loops of the electrorheological damper with (solid line) and without (dashed line) electric field.

In order for the ER-damper to be effective, the viscous and plastic components have to be comparable. For a cylindrical piston, equation (6.8) yields to the relation between the plastic damping ratio and viscous damping ratio:

$$\frac{\varepsilon}{\xi} = \frac{\pi j \tau_y dh^2 \omega_0}{2\eta_0 A_p V_p \omega_p} \tag{6.10}$$

This equation relates the ratio of plastic to viscous damping with the material properties of the ER fluid to be used, the dimensions of the damper and the parameters of the earthquake pulse; knowing the desired values of ε and ξ (see § 0), the cylinder diameter *d* can be determined. The higher the yield stress of the fluid, the smaller the diameter of duct needed to achieve the same ratio.

When ER Dampers are incorporated within the frame of a flexible structure the design piston velocities are relatively low (7-25 cm/sec), and the design of the damper shown in Fig. 6.9 is appropriate. The number of bypasses has to increase with increasing piston velocity, in order to keep the flow rate at low values. When the ER Dampers are placed within the isolation system of the structure the design piston velocities are of the order of 100 cm/sec or higher. For this application, Makris *et al.* (1996) proposed a different design, shown in Fig. 6.12. A damper with a diameter of 30-40 cm can be easily accommodated in a isolation system, since the clearance of the isolation space is dictated from the height of the bearing. An attractive feature of the design of the ER-damper shown in

Fig. 6.12 is that the ER duct has a large contact area with the environment , allowing a better cooling of the device, useful also in other applications (e.g. wind), where dampers are expected to operate for long time intervals. Current available ER Dampers can deliver the level of friction type forces needed even for large design velocities (i.e. 100 cm/s).

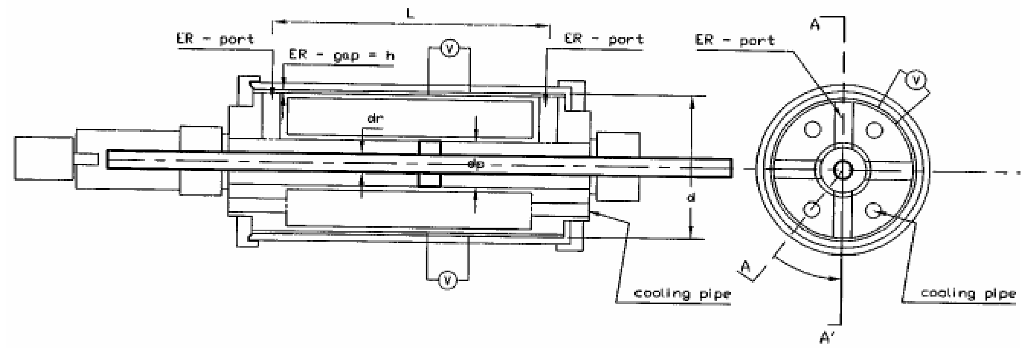

Fig. 6.12. Schematic of the new ER-damper, able to operate under high design velocities, adequate for seismic isolation systems. Section A–A is projected in line A–A

In case of ER Dampers, Ribakov and Gluck (1999) address a procedure in which viscous properties of the ER devices are selected using passive control theory, and active control theory is then used to find the optimal control forces, practically obtained by varying the applied electric field at every time step. The electric field in each device at every time step is varied such that the forces produced in the dissipating devices are equal to those obtained by the optimization procedure: when the optimal force is less than the viscous part, no electric field is needed, and when the optimal force overcome it, then the value of the electric field produces in the ERD a supplemental force equal to the needed increment. The numerical investigation (Ribakov and Gluck, 1999) showed differences in displacement reduction between passive viscous and active ER controlled structures ranging between 55 and 65%, without increases in peaks of velocity and acceleration.

Makris *et al.* (1996), present the solution of the equation of motion of a SDOF with combined viscous and Coulomb-friction damping subjected to a sinusoidal excitation (in equation (6.11)): the solution of this non linear equation results in stops with finite duration. The displacement history solution is given, in terms of general initial conditions U_0 and $\dot{U}_0$ at the beginning of each subinterval (so putting together over each subinterval it is possible to construct the entire time history of the transient motion). Velocity and acceleration derive through direct differentiation of displacement.

6.3.2 Effects on rigidity-plasticity, viscosity of ER dampers with near-field ground motion

Adjusting the type of dissipation mechanism allows protecting a structure from totally different motions that might be generated from the same earthquake only some kilometer apart. Makris (1997) studied the effects of near-source earthquake motions on one- or two-span isolated bridges equipped with energy friction-type dissipators: considering dampers exhibiting a behaviour ranging from rigid-plastic to purely viscous, in order to avoid the permanent displacements coming from large friction forces, those latters can be relaxed at some instant during the free vibration of the structure, while using viscous mechanisms to damp free vibrations.

The motion of a SDOF is considered, representing a stiff superstructure resting on an isolation system (e.g. a one- or two-span isolated bridge oscillating along its longitudinal direction), ruled by relationships (6.11), where P is the damping force resulting from the isolation system, ξ is the viscous damping ratio and F the friction-type force.

$$\ddot{u}(t)+\omega_0^2 u(t)+\frac{P(t)}{m}=-a_g(t)$$
$$P(t)=2\xi\omega_0\dot{u}(t)+F\text{sign}[\dot{u}(t)] \tag{6.11}$$

Under harmonic excitation with frequency ω_p and velocity-response amplitude V, the energy dissipated per cycle with displacement amplitude U, when the dissipation is purely viscous and purely due to friction forces are shown in equation (6.12). The plastic damping ratio is defined as the ratio of the friction force to the induced acceleration force, as given in equation (6.13), where j is a parameter characterising the pulse type, j=1 for type B pulse and j=2 for type A pulse (Makris and Chang, 2000). Sliding occurs when $\varepsilon<1$. The relationship (6.14) is obtained when the energies dissipated by friction and by viscous forces are the same and in case of steady-state conditions. Considering pulse excitations, steady-state conditions do not prevail, and Makris (1997) observed that when ω_p is close to the natural frequency (say $0.6<\beta<1.2$) the ratio jV/V_p approximes the unity, thus leading to equation (6.15).

$$E_v=2\pi\xi m\omega_0 VU \qquad E_p=4FU \tag{6.12}$$

$$\varepsilon=j\frac{F}{m\omega_p V_p} \tag{6.13}$$

$$\varepsilon=j\frac{\pi}{2}\frac{\xi}{\beta}\frac{V}{V_p} \qquad \beta=\frac{\omega_p}{\omega_0} \tag{6.14}$$

$$\varepsilon\cong\frac{\pi}{2}\frac{\xi}{\beta} \tag{6.15}$$

Effect on low and high isolation systems have been investigated by Makris (1997). Fig. 6.13 report results for low-periods SDOF systems (T_0 = 0.625 sec) subjected to the pulse type-A, with different combinations of friction-type and added viscous damping: (i) the Light solid line represents the case of pure viscous damping (ξ=0.234; ε=0); the Heavy solid line is the case of viscous damping combined with friction-type damping (ξ=0.234; ε=0.50); the Heavy dashed line is obtained with same parameters (ξ=0.234; ε=0.50), but removing the friction forces (i.e. ε=0) during free vibrations; the Light dashed line is obtained with other settings of pure viscous damping (ξ=0.434, and ε=0).

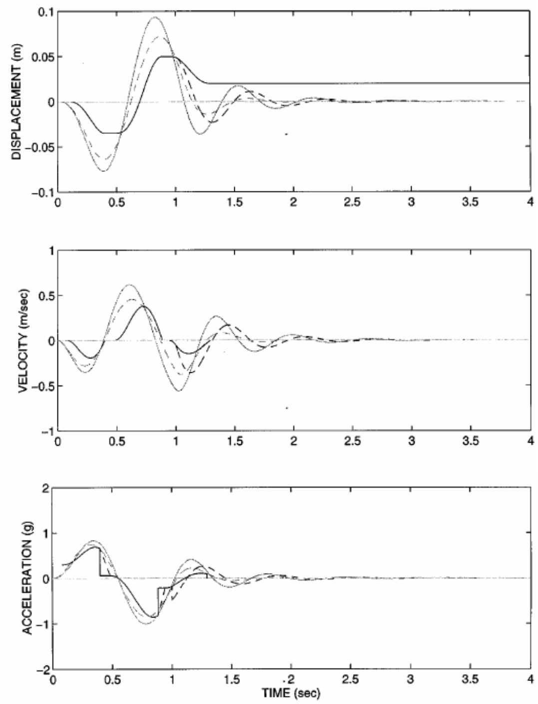

Fig. 6.13. Computed response of low-periods SDOF systems subjected to the pulse type-A, combining differently friction-type and added viscous damping

Two systems in which the same amount of additional damping is provided with added viscous or friction type damping (Heavy solid vs Light dashed line) are compared: the additional plastic damping ratio with ε=0.50 corresponds to an additional viscous-damping-ratio value of 0.2 (equation (6.15)); despite the large amount of viscous damping, neither the bearing displacements nor velocities reduce. Moreover, both dissipative configurations result in substantial base shears, which shows that supplemental damping reduces displacements at the expense of developing substantial base shears. For these rapid, long period motions, viscous damping alone has little effect in reducing the response, whereas, friction-type damping can substantially reduce displacements and velocities without increasing accelerations. On the other hand, viscous damping alone is beneficial for high-frequency motions with sharp accelerations.

Fig. 6.14 report results for long-periods SDOF systems (with T_0=2.25s) combining differently friction-type and added viscous damping, subjected to the pulse excitation of type-B: (i) the Light solid line represents the case of pure viscous damping (ξ=0.15; ε=0.0); (ii) the Heavy solid line is obtained combining viscous damping and friction-type damping (ξ=0.15; ε=0.4); (iii) the Light dashed line is another case of pure viscous damping (ξ=0.4; ε=0.0); (iv) the Heavy dashed line is obtained with same parameters of (ii) (ξ=0.15; ε=0.4), but removing the friction forces (i.e. ε=0) during free vibrations.

Cases (ii) and (iii) are compared, having the same amount of additional damping because the additional plastic damping ratio of ε=0.4 corresponds to an additional viscous-damping-ratio value of 0.25. Despite the large amount of viscous damping, the bearing displacements are slightly greater than the displacement obtained with friction-type damping forces: before the pulse strikes the structure, friction-type forces are activated to reduce displacements without increasing accelerations. At some point friction forces may be relaxed to allow the structure to recentre while free vibrations are damped by virtue of viscous damping.

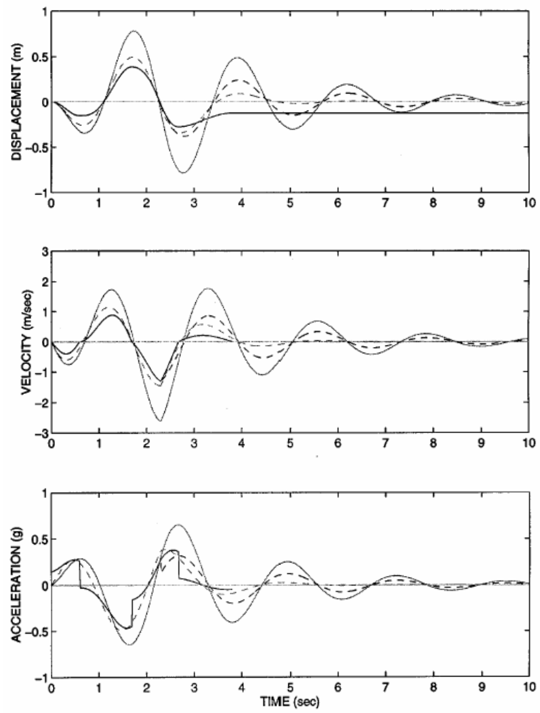

Fig. 6.14. Computed response of long-periods SDOF systems subjected to the pulse type-B, combining differently friction-type and added viscous damping.

7. DEVICE TYPOLOGIES: ELASTOMERIC ISOLATORS

An elastomeric isolation bearing consists of a number of rubber layers and steel shims, bonded in alternating layers, to produce a vertically stiff but horizontally flexible isolator. The alternating steel and rubber layers act to restrain the rubber layer from bulging laterally. This kind of bearings provide flexibility and hysteretic/viscous damping forces. They can be either low damping or high damping bearings. The insertion of a lead plug in an elastomeric isolator provides energy dissipation for seismic response and stiffness for static loads. They can be grouped in:

- Natural Rubber Bearings;
- High Damping Rubber Bearings (HDRB);
- Lead Rubber Bearings (LRB).

7.1 ELASTOMERIC ISOLATOR TYPOLOGIES: RUBBER BEARINGS AND LAMINATED RUBBER BEARINGS

Chracteristic parameters of typical Laminated Rubber Bearings (Fig. 7.1 and Fig. 7.2) are the vertical load capacity, the bearing horizontal and vertical stiffnesses, the bearing lateral period, the bearing damping and the allowable seismic displacement, as described hereafter. The bearing damping, due only to the viscous behaviour of the rubber, is in the order of 5% of critical, corresponding to a hysteretic loop rather linear (Fig. 7.4).

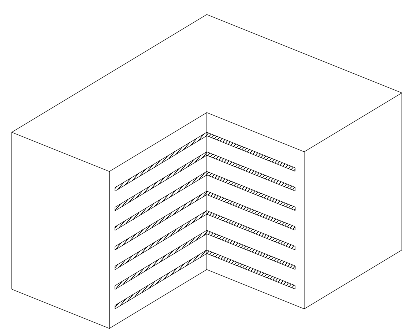

Fig. 7.1. Schematic design of a laminated natural rubber bearing

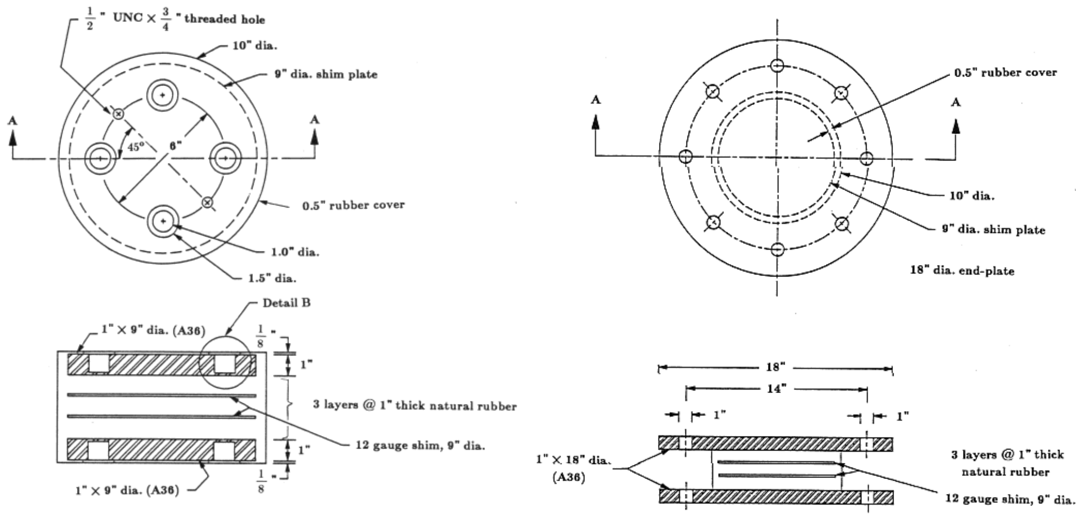

Fig. 7.2. Plan and cross section of low shape-factor rubber bearing with doweled (left) and bolted (right) end-plate connection (EERC).

7.1.1 Characterising parameters

Characterizing parameters of a natural rubber bearing are:

- The VERTICAL LOAD CAPACITY W

$$W < A' G S \gamma_W \tag{7.1}$$

$$\begin{aligned} S_{\text{Rectangular Bearing}} &= b_x b_y / 2(b_x + b_y) t_i \\ S_{\text{Circular Bearing}} &= D / 4 t_i \end{aligned} \tag{7.2}$$

In equation (7.1), γ_W is the allowable shear strain, which can be taken equal to $6S\varepsilon_z$, where ε_z is the vertical strain, when rubber is assumed to be incompressible (Skinner *et al.*, 1997); A' is the overlap of top and bottom area (A) of bearing at maximum displacement (Fig. 7.3), and it ranges from $0.4A$ to $0.7A$, but a value of 0.6 is typically used for design earthquake; G (≈1MPa), is the shear modulus of rubber; S is the bearing shape factor, i.e. the loaded to force-free area ratio of the rubber layer, generally ranging from 3 to 40. The allowable vertical stress on the gross area is in the order of 5÷10 MPa, but it is indirectly governed by limitation on the equivalent shear strain in the rubber due to different load combinations and stability requirements.

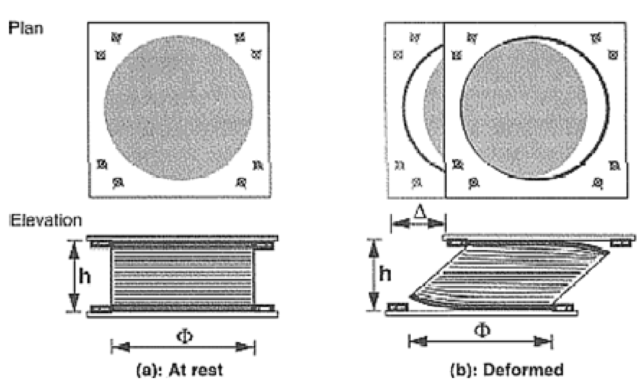

Fig. 7.3. Rubber bearing with recessed plate connection: undeformed and deformed configurations.

- BEARING HORIZONTAL STIFFNESS Kb AND LATERAL PERIOD Tb

$$K_b = GA/h \tag{7.3}$$

$$T_b = 2\pi(M/K_b)^{0.5} = 2\pi(Sh\gamma_{xz}A'/Ag)^{0.5} \tag{7.4}$$

In equations (7.3) and (7.4) h is the total rubber height, i.e. the sum of the layer thicknesses, M is the beard mass and g the acceleration of gravity. K_b is in the order of 1÷2 MN/m. The actual value of the lateral stiffness might be affected by the amount of vertical load (as evident in Fig. 7.4), depending on different factors, as discussed later (§ 7.5).

There will be some reduction in the bearing height with large displacements, partly due to flexural beam action and partly to the increased compression of the reduced A'. The resulting inverted pendulum action, under structural weight, reduce K_b, and in extreme cases also re-centering forces. The inverted pendulum forces can be reduced by increasing S up to 10÷20. This problem, accurately studied by different authors (Kikuchi and Aiken, (1997), Nagarajaiah and Ferrell, (1999), Buckle *et al.*, (2002)) will be discussed later on. T_b is in the order of 2÷3 sec. According to the second part of equation (7.4), obtained by substituting the (7.1) and (7.3), the lateral period results to be a function of the square root of bearing height to layer thickness ratio, $(h/t)^{0.5}$.

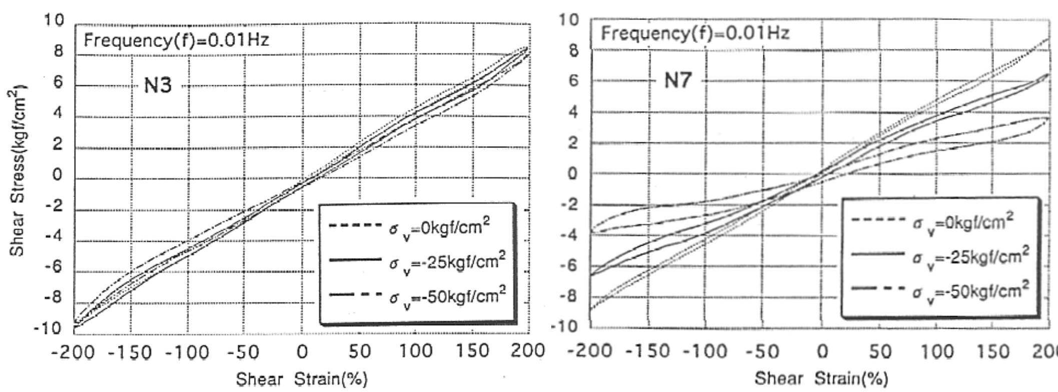

Fig. 7.4. Horizontal shear stress-strain hysteresis loop of low-shape factor natural rubber bearings (EERC), 31.5 mm (left) and 73.5 mm (right) high

- BEARING VERTICAL STIFFNESS Kv

The vertical deflection of a bearing is the sum of the deflection due to the rubber shear strain and to rubber volume change. The corresponding stiffnesses in series are described in equation (7.5) and combined in the resulting vertical stiffness of equation (7.6), where κ (≈ 2000MPa) is the rubber compression modulus. The magnitude of the global stiffness is in the order of 1000÷2000 MN/m.

$$\begin{aligned} K_{z-\text{shear strain}} &= 6GS^2A/h \\ K_{z-\text{volume change}} &= \kappa A/h \end{aligned} \tag{7.5}$$

$$K_z = 6GS^2A\kappa/(6GS^2 + \kappa)h \tag{7.6}$$

- ALLOWABLE SEISMIC DISPLACEMENT Δb

It can be limited by either the seismic shear strain γ_s or the overlapping area factor. In the first case it is given by equation (7.7). The rubber bearings must withstand the combined rubber shear strains due to structural weight and seismic displacement; for bridges, additional shear strains due to traffic loads and thermal displacements must be accounted for. The damaging effect of a given rubber strain increases with its total duration and number of cycles. The allowable limit for the seismic shear strain γ_s, depends on the amount of shear strain γ_W mobilised by the vertical load (in equation (7.1)): sustainable steady shear strain in a rubber bearing is given in equation (7.8) (Bridge Engineering standards, 1976), where ε_{tu} is the short-term failure tensile strain, ranging from 4.5 to 7.

$$\Delta_{\text{b-seismic shear strain}} = h\gamma_s \tag{7.7}$$

$$\gamma_w = 0.2\varepsilon_{tu} \tag{7.8}$$

Under combined action of uplift and end moments, the rubber undergoes to large negative pressures, possibly causing small cavities in the rubber, which grow progressively during sustained and cyclic negative pressures. The latters cause a large reduction in the axial stiffness, and even if their effect on the horizontal stiffness is reduced, they can be important in modelling the rubber bearing. It is usual to design bearings so that negative pressures do not occur, or occur with low frequencies and durations, avoiding higher negative pressures by means of proper detailings.

A limit to the displacement is provided also by the overlapping area ratio. The ratio *A'/A* depends on the shape of the bearing: for a cylindrical bearing of diameter *D* it is shown in equation (7.9), where $\theta = \Delta b/D$, and for small values of θ leads to the (7.10).

$$\left(\frac{A'}{A}\right)_{\text{Circular Bearing}} = 1 - \frac{2}{\pi}(\theta + \sin\theta\cos\theta) \tag{7.9}$$

$$:\Delta_{\text{b-Circular Bearing}} \cong 0.8D\left(1 - \frac{A'}{A}\right) \tag{7.10}$$

In case of rectangular bearings, the ratio is shown in equation (7.11); When the displacement can be in any direction, a conservative estimate of the displacement limit is obtained by equation (7.12), where b is the shortest side. When displacement is allowed only in one direction, parallel to a side B of the rectangular bearings, its value is given in equation (7.13). Allowing an overlapping are ratio of 0.6, the allowable seismic displacement is in the order of magnitude of *D/3* and *b/3*.

$$\left(\frac{A'}{A}\right)_{\text{Rectangular Bearing}} \cong 1 - \frac{\Delta_{bx}}{b_x} - \frac{\Delta_{by}}{b_y} \tag{7.11}$$

$$\Delta_{\text{b-Rectangular Bearing}} \cong 0.8b\left(1 - \frac{A'}{A}\right) \tag{7.12}$$

$$\Delta_{b-//B} = B\left(1 - \frac{A'}{A}\right) \tag{7.13}$$

Other factors in rubber bearing design may concern the long term stability and the resistance to environmental factors, such as ultraviolet and ozone. AASTHO and EC8 recommendations are reported in §7.4, maintaining respectively the same nomenclature used in the two codes.

7.2 ELASTOMERIC ISOLATOR TYPOLOGIES: HIGH DAMPING RUBBER BEARINGS

High Damping Rubber Bearings (HRDB) consist of alternate layers of rubber and steel plates of limited thickness bonded by vulcanization (Fig. 7.5). they are able to support vertical loads with limited deflection, due to very high vertical stiffness, and capable of supporting operating horizontal loads (e.g. wind), with very low displacements. Their life time is over 60 years.

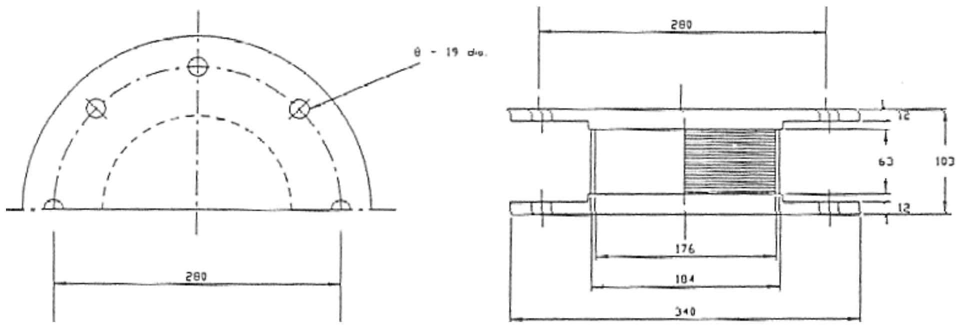

Fig. 7.5. Half plan and elevation of a typical HDRB (EERC)

HRDB can provide both period shift and energy dissipation (Fig. 7.6): the rubber compound presents damping capability, at least corresponding to 10% of equivalent viscous damping, and normally dependent on the bearing displacement. The rubber compound is designed to withstand very large shear deformations, much larger than the standard elastomeric bearings. The rubber compound stiffness is much higher (up to 4 times) for small deformations and reduces for large deformations.

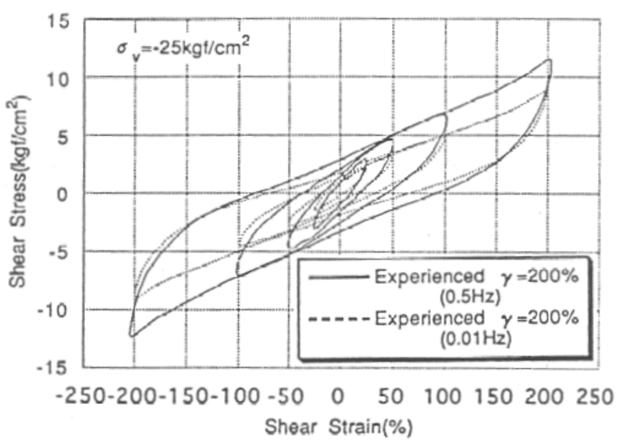

Fig. 7.6. Horizontal shear stress-strain hysteresis loop for a low shape-factor HDRB (EERC)

The fixation to the structure is based on positive connections: HRDB can transfer very large horizontal load to the structures, either by recess or dowels or by bolts. In the first case the rubber is not subjected to tensile stresses, but $\tan\gamma_{max}=1.4$ to limit bending of the steel plates vulcanised to the rubber and prevent risk of roll-over; in the latter case the maximum shear strain is achieved but the rubber has to have extremely high mechanical properties due to the high stress level it undergoes.

7.2.1.1 Rubber properties

Physical-mechanical rubber characteristics refer to CNR10018, AASHTO, BS5400, European Standards pr EN1337. A range of variability of rubber properties is provided in Table 7.1. The rubber behaviour strongly depends on amplitude and history: e.g. at a rubber strain amplitude of 50% after the first cycle of operation (the so-called 'unscragged' state) the modulus is approximately 1.5 times that for the subsequent 'scragged' cycles. Scragging occurs in elastomeric bearings that are subjected to one or more cycles of high shear deformation before testing. Scragged bearings show a significant drop of the shear stiffness in subsequent cycles. The reduction in scragged properties decrease with increasing strain amplitude. The original unscragged properties are recovered in a period of a few hours to a few days. This effect is prominent mainly in high damping and in low modulus bearings.

Table 7.1. Rubber properties (Alga Spa, 2003)

	Compound		
Characteristic	**SOFT**	**NORMAL**	**HARD**
hardness (Shore A3)	40±3	60±3	75±3
tensile strain (%)	20	20	18
tensile strenght (MPa)	750	600	500
G (MPa)	0.4	0.8	1.4
equivalent viscous damping (%)	10	10	16

7.2.2 Preliminary design for HRDB isolating systems

In preliminary design of HRDB Isolating Systems, it can be assumed that base isolators act like perfect springs and that the superstructure is a rigid mass. The mass of the structure is known, the designer has to choose:

- The structural period (normally between 2 and 3 sec) and the total stiffness of the base isolators.
- The equivalent viscous damping of the isolators (normally ranging between 10% and 16%), through which spectral response values S_a and S_d can be determined and reduced with the parameter (EC8, prEN 1998-1):

$$\eta = \sqrt{\frac{10}{5+\xi_{eq}}} \geq 0.55 \tag{7.14}$$

- The design shear strain of the rubber $\tan\gamma$: the thickness h can be determined through the relative displacement S_d.

$$h = \frac{S_d}{\tan\gamma} \tag{7.15}$$

The net rubber thickness shall be increased to allow for the movements due to temperature, creep and shrinkage. According to the EC8 provision, the total maximum displacements of each isolator unit shall be obtained by adding to the total design seismic displacements, the offset displacements potentially induced by the permanent actions, by the long-term deformations (concrete shrinkage and creep) of the superstructure and by 50% of the thermal action.

- The rubber shear modulus, through which the total area A of the isolators can be found:

$$A = \frac{K_b h}{G} \tag{7.16}$$

Now dimensions of the single unit can be determined, provided that allowable vertical pressure is 7-15 MPa (for G=0.7-1.4 MPa) or 4-10MPa (for G=0.4-0.7 MPa), and buckling is prevented. It is generally recommended to reduce the number of different isolators and to check the manufacturer availability.

7.3 ELASTOMERIC ISOLATOR TYPOLOGIES: LEAD RUBBER BEARINGS

The insertion of a lead plug in the laminated rubber bearing provides energy dissipation for seismic response and stiffness for static loads (Fig. 7.7 to Fig. 7.8), while most of the self-centering property is lost. Parameters characterising the Lead Rubber Bearing (LRB) are the yielding shear and the sustainable post-yielding shear force, respectively in equations (7.17) and (7.18), where τ_{ly} is the lead yield shear strength (≅ 10.5MPa), and G_l is the lead initial stiffness (≅ 130MPa). The yielding Shear is the total bearing shear at the lead yield displacement, i.e. approximately the lead yielding shear (the rubber contribution is very small respect to the lead contribution at this displacement), and the sustainable post-yielding shear force is the shear at the design displacement of the isolator.

$$V_y = \tau_{ly} A_l \left(+ \frac{G_r A_r}{h} \Delta_y \right) \tag{7.17}$$

$$V_d = \tau_{ly} A_l + \frac{G_r A_r}{h} \Delta_d \tag{7.18}$$

The initial elastic stiffness has been estimated from experimental results in the range of 9÷16 times the horizontal stiffness of the rubber alone. The yield strength of the isolator is proportional to the size of the lead plug, while the post yielding stiffness is proportional to the rubber bearing stiffness, with a variation of up to ±40%, but more likely within ±20%. The maximum force has an uncertainty of ±20%. This simplified bi-linear model and the real loop are compared in Fig. 7.8.

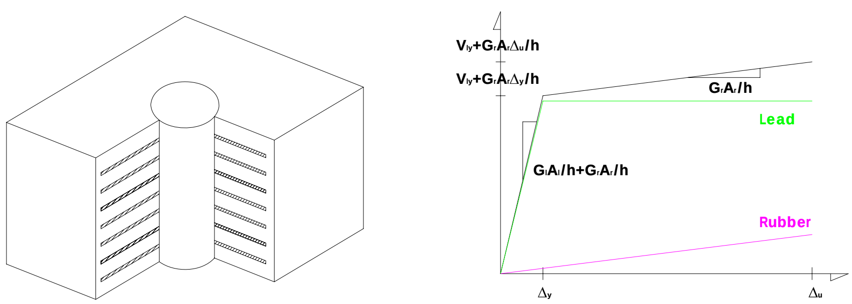

Fig. 7.7. Schematic design of a lead rubber bearing (left) and schematic bilinear constitutive law (right)

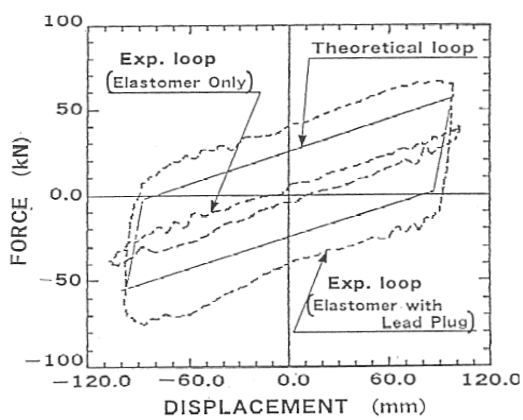

Fig. 7.8. Hysteretic loops for elastomeric bearings with and without lead plug (EERC)

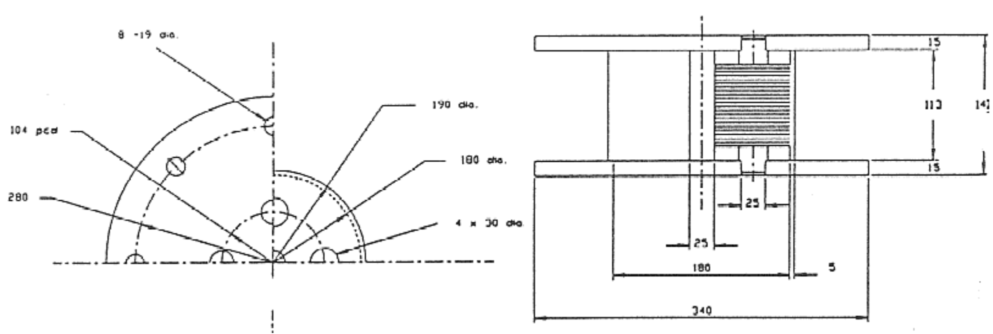

Fig. 7.9. Half plan and elevation of a typical LRB (EERC)

If bridge deck is mounted on LRBs, because of the daily temperature excursion, the bearing has to accommodate several displacements of ±3mm, without producing large forces. A relationship of the type of (7.19), in which *a* is a constant parameter, was found for the rate dependence, meaning that the rate dependence at typical seismic frequencies (1Hz) is low, iin the order of a force increment of 8% for a rate increase of a factor of 10, while for slow frequencies it is more important (a force increment of 40% for the same change of rate).

$$\tau_1 = a\dot{\gamma}^b; \qquad b = \begin{cases} 0.13 \div 0.15 & \dot{\gamma} \le 3\times 10^{-4}\,\text{Hz} \\ 0.03 \div 0.035 & \dot{\gamma} > 3\times 10^{-4}\,\text{Hz} \end{cases} \tag{7.19}$$

The LRB is not strongly dependent on fatigue and temperature excursions within -35° / +45°. The effects of vertical load on hysteresis are not relevant if the device is properly designed (e.g. S>10).

7.3.1 Preliminary design of LRB isolating systems

The preliminary design philosophy is displacement-based, thanks to the possibility of reducing the structural system to an equivalent SDOF system in which the contributions of n isolators in parallel are summed. The aim is to keep the displacement of the structure (i.e. of the isolation system, as it coincides with the level at which the maximum displacement occurs) under a specified design limit.

The following parameters have to be designed: the total rubber area A_r and lead area A_l, to be split in *n* isolators; the lead height h_l, i.e. of the isolator, that is the same for the *n* isolators. The equivalent single LRB is found comparing the two systems of one isolator, with A_r, A_l and h_l, and n isolators, with A_r/n, A_l/n and h_l, in Table 7.2, where the index *i* corresponds to the individual isolator unit.

Table 7.2. Equivalent SDOF isolator

One isolator (with Ar, Al and h)	n isolators (with Ar/n, Al/n and h each)
$K_r = G_r A_r / h_l$	$K_{ri} = G_r (A_r / n) / h_l$
$V_u = D_u \dfrac{G_r A_r}{h_l} + A_l \tau_{yl}$	$V_{ui} = D_u \dfrac{G_r (A_r / n)}{h_l} + (A_l / n)\tau_{yl} \quad \rightarrow \quad V_u = nV_{ui}$

It has to be noted that the same stiffness of the two systems can be obtained just imposing that aspect ratio A_r/h_l of the equivalent SDOF isolator be *n* times the aspect ratio of the *n* isolators. Nevertheless this would change the ultimate shear, which depends only on the lead area, and the yielding displacement, which depends only on the lead height. Therefore, the damping characteristics of the system would be altered. Preliminary design is based on the following observations:

- The mass of the structure to be isolated is known; the system is reduced to an equivalent SDOF system with the mass equal to the first modal mass M_I; the 1st mode mass factor might be eventually assumed in the order of 0.95, to be checked on the model.
- The equivalent viscous damping of the system is calculated as the equivalent viscous damping of the cycle at the maximum displacement of the system. Clearly the estimated damping results to be an upper bound, as the energy dissipated over the duration of the earthquake has contributions of high and low cycles. The spectral response value S_d can be determined and reduced with the parameter η of equation (7.14).

A very preliminary design might follow the steps listed below, assuming the post-yielding stiffness K_2 as one tenth of the initial elastic stiffness K_1:

- Choice of the isolation period T_I, normally of 2-3 sec as an initial trial value.
- $S_d(T_I)$ is obtained from the 5% damping Response Spectrum. A desired damping value is selected in order to keep the displacement below the target value Δ_d.
- The corresponding equivalent stiffness of the system is computed as:

$$K_{eq} = \frac{4\pi^2 M_I}{T_I^2} \qquad (7.20)$$

- Assuming $K_2=0.1K_1$, known displacement, yield shear V_y and post yielding stiffness are found such that the equivalent viscous damping matches the chosen damping.

This scheme is not the most efficient, as Δ_d, K_r and V_y are not independent parameters, and the design procedure may eventually result in an unfeasible isolation system due to a series of factors and limitations. The first one is that choosing an ultimate admissible displacement implies a lower bound for the rubber area size (overlapping area limit), implying a minimum K_2*h. Then, K_1 is a function of K_2, A_l and V_y. This is the reason why all the procedure is in reality a function of one parameter: the isolator height, h_l. Based on this observation, the following preliminary design is proposed by the author, as a function of T_I, h_l, and Δ_d.

- STEP 0 (Input Data): input data are the mass, the shear moduli of the rubber and of the lead, and the yield strength of the lead (Table 7.3).

Table 7.3. Preliminary design of LRB systems: input data

Mass	**G_{rubber}**	**G_{lead}**	**$\tau_{y,lead}$**
M_I	1 MPa	130 MPa	10 MPa

- STEP 1: T_I, Δ_m, ξ_{eq} are determined (Table 7.4). A first trial value of T_I is chosen, on the 5% damped Response Spectra S_a and S_d are determined; a value of ξ_{eq} is chosen, considering that the maximum displacement ηS_d shall be less than Δ_d; the equivalent elastic stiffness K_{eq} for the system is calculated. Eventually the ultimate shear capacity V_u for the system is calculated: V_d is checked to be of the same order of magnitude of V_u, nevertheless the shear demand on the system will be determined in a more advanced phase then the preliminary design, eventually through nonlinear analyses of the structure.

Table 7.4. Preliminary design of LRB systems: step 1

T_I	**S_d**	**ξ_{eq}**	**Δ_m**	**K_{eq}**	**V_u**	**S_a**	**V_d**
(chosen)	(from 5% damping spectrum)	(chosen to properly limit Δ_m)	$= g\eta S_d$	$= M(2\pi / T_I)^2$	$= K_{eq}D_u$	(from 5% damping spectrum)	$= W_1\eta S_a$

- STEP 2: A_r, h_l and h_r (effective rubber height) are found (Table 7.5). Maintaining the overlapping ratio limit of 0.6, the minimum size of the rubber for each isolator B_{ri} is derived (from relationships (7.10), (7.12) or (7.13)) (the fact that the lead plug is inside the rubber area can be neglected at this stage), and A_r is calculated. A trial value of h_l is chosen, and, considering a ratio of 0.9, h_r is estimated.

Table 7.5. Preliminary design of LRB systems: step 2

B_{ri}	**A_{ri}**	**A_r**	**h_l**	**$a=h_r/h_l$**	**h_r**

$B_{ri} = \Delta_m / 0.4$	B_{ri}^2	$A_r = nA_{ri}$	(chosen - trial parameter)	(estimate)	$= ah_1$

- STEP 3: hysteresis loop parameters are determined (Table 7.6). The stiffness of rubber K_r is estimated, and the yielding displacement Δ_y is determined as a function of known parameters (equations (7.21)). The initial system stiffness K_I is determined from the (7.22), and A_l is from the (7.23). The system yielding shear V_y can now be calculated.

$$V_{yl} = K_1\Delta_y = A_1\tau_{yl}; \qquad \frac{G_1 A_1}{h_1}\Delta_y = A_1\tau_{yl} \tag{7.21}$$

$$V_u = K_1\Delta_y + K_r(\Delta_u - \Delta_y) \tag{7.22}$$

$$K_1 = K_r + \frac{G_1 A_1}{h_1} \tag{7.23}$$

Table 7.6. Preliminary design of LRB systems: step 3

K_r	Δ_y	K_1	A_l	V_y
$\frac{G_r A_r}{h_r}$	$\frac{h_1\tau_{yl}}{G_1}$	$\frac{V_u - K_r(\Delta_m - \Delta_y)}{\Delta_y}$	$(K_1 - K_r)\frac{h_1}{G_1}$	$A_1\tau_{yl} + K_r\Delta_y$

- STEP 4: known the system hysteresis loop parameters, the actual value of equivalent viscous damping is calculated (equation (7.24) and Table 7.7).

$$\xi_{eq} = \frac{A_{loop}}{4\pi A_{elastic}} \tag{7.24}$$

Table 7.7. Preliminary design of LRB systems: step 4

a	b	c	d	ξ_{eq}
Δ_m-Δ_y	Δ_y	V_U-V_y	V_U	$2\frac{ad - ac - cb}{\pi d(a+b)} \times 100$

- STEP 5: h_l is adjusted by a trial and error procedure. The value of h_l selected in Step 2 is adjusted until $\xi_{eq(STEP5)}$ matches $\xi_{eq(STEP1)}$. In order to avoid heavy mathematical expressions arising from Step 5 to Step 1, this can be carried out by means of a simple trial and error procedure, easily achieved by setting up an electronic worksheet and changing the values of the lead height.

The only parameters governing the procedure are T_I, h_l, and admissible Δ_m (based on the overlapping area ratio), whilst each other quantity is evaluated deterministically from their values. The last step is to calculate the real maximum admissible displacement, based on the real B_{ri}, considering that overlapping areas includes the lead area; equations (7.25) refer to the case of square bearing and monodirectional displacement: this value, which does not differ very much from the ultimate displacement estimated in step 1, will be compared with the maximum displacement coming from non linear analyses on the structure in more advanced design phases.

$$\begin{gathered} B_{ri} = \sqrt{A_{li} + A_{ri}} \\ \Delta_{admissible} = 0.4B_{ri} \end{gathered} \tag{7.25}$$

7.3.1.1 Multi-stage rubber bearings

It may happen that the rubber bearings become very long and narrow in the shape, thus becoming unstable (Fig. 7.10): multi-stage rubber bearings were developed to solve this problem. The multi-stage rubber bearings consist of small rubber bearings (rubber bearing elements) located at the four corners and stacked to multi-stage with stabilizers between each layer. Thanks to this structure, they can have great displacement absorbing capacity while maintaining horizontal stiffness equal to the very long and narrow rubber bearings.

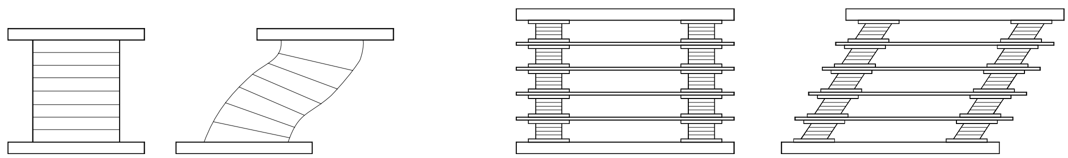

Fig. 7.10. Comparison between ordinary lamination rubber bearing and multi-stage rubber bearing

7.4 ALLOWABLE SHEAR STRAIN AND OTHER CODE RECCOMENDATIONS

7.4.1 AASTHO recommendations for the allowable shear strain

In AASTHO (2000), shear strain components for isolation design are:

- The shear strain due to compression by vertical loads γ_c (γ_W, referring to the previous nomenclature), described in equation (7.26), where *K* is the bulk modulus of the elastomer, to be taken as 2000 MPa if not measured; $\bar{k}$ is an elastomer material constant related to hardness (for values refer to Roeder, Stanton and Taylor, 1987; NCHRP Report n°298).

$$\gamma_c = \begin{cases} \dfrac{3SP}{2A_r G(1+2\bar{k}S^2)} & , \quad S \le 15 \\[2ex] \dfrac{3P(1+8G\bar{k}S^2/K)}{4G\bar{k}SA_r} & , \quad S > 15 \end{cases} \tag{7.26}$$

The allowable vertical load is indirectly governed by limitation on the equivalent shear strain in the rubber due to different load combinations and stability requirements. Creep effects on the elastomer shall be added to the instantaneous compressive deflection, when considering long term deflections (Art. 14.2.2, AASHTO 2000).

For rubber E=(3.8÷4.4)G; the compression modulus of the bearing E_b in equations (7.27) is obtained taking E=4G; for bearings with large shape factors, incompressible rubber assumption leads to overestimate the compression modulus, and the second expression of (7.26) is used, based on the empirical relation for the compression modulus given in the second equation (7.27). The shear modulus G is determined from the secant modulus between 25 and 75% shear deformation.

$$E_b = \begin{cases} 4G(1+2\bar{k}S^2) & \text{incompressible rubber} \\[2ex] \dfrac{1}{\dfrac{1}{8G\bar{k}S^2}+\dfrac{1}{K}} & \text{compressible rubber} \end{cases} \tag{7.27}$$

- The shear strain $\gamma_{s,s}$, due to imposed non seismic lateral displacement Δ_s; the shear strain $\gamma_{s,eq}$, due to earthquake-imposed lateral displacement d_t; the shear strain γ_r, due to rotation θ. The design rotation is the maximum rotation of the top surface of the bearing relative to the bottom. T_r is the total rubber height:

$$\gamma_{s,s} = \frac{\Delta_s}{T_r}\ ; \quad \gamma_{s,eq} = \frac{d_t}{T_r}\ ; \quad \gamma_r = \frac{B^2\theta}{2t_i T_r} \tag{7.28}$$

Load combinations to be checked are:

$$\begin{aligned} &\gamma_c \le 2.5 \\ &\gamma_c + \gamma_{s,s} + \gamma_r \le 5.0 \\ &\gamma_c + \gamma_{s,eq} + 0.5\gamma_r \le 5.5 \end{aligned} \tag{7.29}$$

7.4.2 EC8 recommendations for the allowable shear strain

The total design shear strain (ε_{td}) shall be determined as the sum of the following components: the shear strain due to compression ε_c, the shear strain due to the total seismic design displacement ε_s and the shear strain due to angular rotations ε_α:

$$\varepsilon_{td} = \varepsilon_c + \varepsilon_s + \varepsilon_\alpha \tag{7.30}$$

Maximum allowable values of shear strains ε_c, ε_s, and ε_{td} are given in Table 7.8. The properties of the isolator units, and hence those of the isolating system, may be affected by aging, temperature, loading history (scragging), contamination, and cumulative travel (wear). In addition to the set of nominal Design Properties (DP) derived from the Prototype Tests, two sets of design properties of the isolating system shall be properly established, Upper bound design properties (UBDP), and Lower bound design properties (LBDP). AASTHO provisions are similar.

Table 7.8. Maximum allowable values of shear strain (EC8)

Shear Strain	Maximum Value
ε_c	2.5
ε_s	2.0
ε_{td}	6.0

- The shear strain due to compression shall be determined as in equations (7.31), where G is the shear modulus of the elastomer, σ_e is the maximum effective normal stress of the bearing, given by the ratio of the maximum axial force N_{sd} on the bearings resulting from the design seismic load combination, over the minimum reduced effective area of the bearing A_r. The latter is given in equations (7.32) and (7.33), respectively for rectangular bearings with steel plate dimensions b_x and b_y (without holes) and for circular bearings with steel plate of diameter D.

$$\varepsilon_c = \frac{1.5}{S}\frac{\sigma_e}{G}\ ; \quad \sigma_e = N_{sd}/A_r \tag{7.31}$$

$$A_r = (\,b_x - d_{Edx})(b_y - d_{Edy}) \tag{7.32}$$

$$\begin{gathered} A_r = (\delta - \sin\delta)D^2/4 \\ \delta = 2\arccos(d_{Ed}/D)\ ; \quad d_{Ed} = \sqrt{(d_{Edx}^2 + d_{Edy}^2)} \end{gathered} \tag{7.33}$$

In the above equations d_{Edx} and d_{Edy} are the total relative displacements under seismic conditions, in the two principal directions, of the two bearing faces, including the design seismic displacements (with torsional effects) and the displacements due to the imposed deformations of the deck (i.e. shrinkage and creep where applicable and 50% of the design thermal effects). d_{Ed} is the total seismic design displacement, and S is the shape factor of the relevant elastomer layer.

- The shear strain due to the total seismic design displacement d_{Ed}, including torsional effects, shall be determined as in equation (7.34), where t_t is the total thickness of the elastomer.

$$\varepsilon_s = d_{Ed}/t_t \; ; \qquad t_t = \sum t_i \tag{7.34}$$

- The shear strain due to angular rotations shall be determined as in equations (7.35) and (7.36), respectively for rectangular bearings of dimensions the b_x and b_y and for circular bearings of diameter D. α_x and α_y are the angular rotations across b_x and b_y. Normally in bridges the influence of ε_α is negligible for the seismic verification.

$$\varepsilon_\alpha = (b_x^2\alpha_x + b_y^2\alpha_y)/2t_i t_t \tag{7.35}$$

$$\begin{aligned} \varepsilon_\alpha &= D^2\alpha/2t_i t_t \\ \alpha &= \sqrt{(\alpha_x^2 + \alpha_y^2)} \end{aligned} \tag{7.36}$$

7.4.3 Other EC8 recommendations: stability and fixing of bearings

In order to ensure stability to the isolator, either of the criteria in equation (7.37) must be satisfied, where b_{min} is the minimum dimension of the bearing and S_{min} is the minimum shape factor of the bearing layers.

$$\begin{aligned} b_{min}/t_t &\geq 4 \\ \sigma_e/G &\leq 2b_{min}S_{min}/3t_t \end{aligned} \tag{7.37}$$

For normal elastomeric bearings, friction may be considered to avoid the sliding of the bearing, if both criteria in relationship (7.38) are satisfied under the most adverse seismic design condition.

$$\begin{aligned} V_{Ed}/N_{Ed} &\leq k_0 + k_f/\sigma_e \\ \sigma_e &\geq 3.0 \;\; N/mm^2 \end{aligned} \tag{7.38}$$

k_0 is 0.10 for bearings with external elastomeric layer, or 0.50 for bearings with steel plates having external indentations; k_f is 0.6 for concrete and 0.2 for all other surfaces; V_{Ed} and N_{Ed} are respectively the shear and the axial force transmitted simultaneously through the bearing according to the design seismic combinations; in the first of equations (7.38), σ_e is in N/mm^2. When one of these conditions is not satisfied, or when special elastomeric bearings are used, positive means of fixing shall be provided (bolts instead of dowels), in both bearing sides, to resist the entire maximum design shear force V_{Ed}. The shear resistance of concrete under dowel action on both the supported and supporting elements should be verified using appropriate failure models.

7.5 BASIC HYSTERETIC BEHAVIOUR AND ADVANCED ANALYTICAL HYSTERESIS MODELS

The reduction of the seismic forces in the superstructure caused by the fundamental period lengthening may be accompanied by large horizontal displacements in the isolators, which, together with their lateral flexibility, may lead to significant reduction in their critical axial load.

The force-displacement relationship of typical elastomeric isolation bearings is non-linear as a result of their inherent damping properties. Experimentally obtained shear force-displacement relationships for elastomeric bearings show strong non-linearities and stiffening behaviour dependent on shear strain magnitude (Fig. 7.11 to Fig. 7.14). Tests on individual bearings revealed that beyond a certain strain level the high-damping bearings exhibit a clear stiffening behaviour, that is a material property of filled rubbers. Two analytical models, developed by Kikuchi and Aiken (1997), Nagarajaiah and K. Ferrell, (1999), and Buckle *et al.* (2002) are illustrated.

Under combined action of uplift and end moments, the rubber undergoes to large negative pressures, possibly causing small cavities in the rubber, which grow progressively during sustained and cyclic negative pressures and cause a large reduction in the axial stiffness, but little in the horizontal stiffness: this effect might be an issue in the rubber bearing modelling, but neither of the presented models accounts for it.

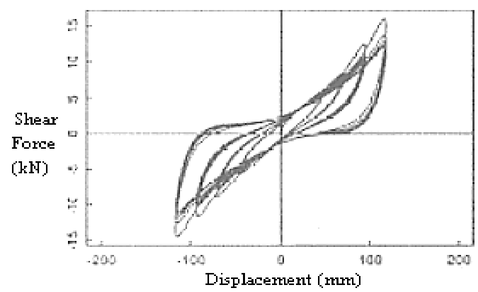

Fig. 7.11. Hysteresis loops: 100-250% shear strain sequence of a HDRB (EERC)

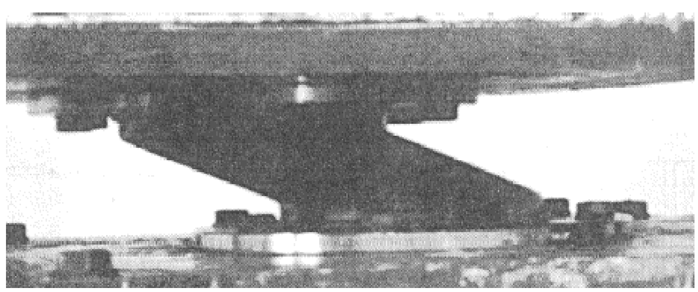

Fig. 7.12. Bearing appearance at 200% shear strain

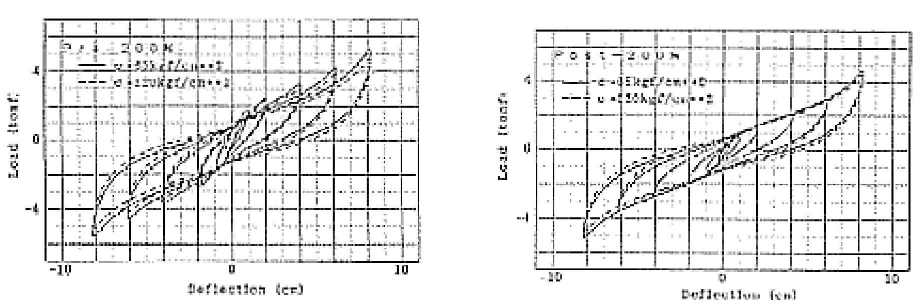

Fig. 7.13. Hysteresis loops for pre-200% (left) and post 200% (right) shear strain loading (EERC)

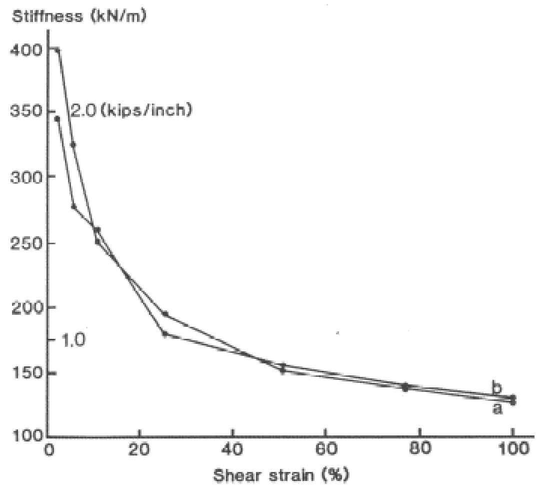

Fig. 7.14. Variation of the shear stiffnee with shear strain for bearing with different shim thickness (a=0.3 mm, b=1 mm; EERC)

7.5.1 Advanced analytical model for the shear strain-dependent nonlinearities

The analytical model proposed by Kikuchi and Aiken (1997) is able to represent the strong shear strain-dependent non-linearities of elastomeric isolation bearings. The model is basically a non linear shear spring associated to an axial linear spring. Main features of the model are:

- the force-displacement relationship is non linear, stiffening for high shear strains: the model is suitable for the high shear strain range;
- the horizontal stiffness and the damping are functions of the shear strain; the model includes the stiffness degradation due to high shear strain;
- the model is suitable for HDRB, LRB and Laminated Rubber Bearings;
- the strain rate and the axial load variation effects on the hysteresis properties of the bearing are not modelled.

The model proposed by Kikuchi and Aiken (1997), based on a modified Fujita model, defines the skeleton curve according to equation (7.39), where F_m is the peak shear force on the skeleton curve, x is the shear displacement X normalized to the peak shear displacement X_m on the skeleton curve. The parameter n specifies the stiffening, F_u is the shear force at zero displacement, a and b are obtained by matching the analytical and experimental hysteresis loop areas, and are derived in equation (7.40). The first of the (7.40) has to be solved numerically; η_{eq} is the equivalent viscous damping ratio and is evaluated from an empirical formula as a function of shear strain, based on tests on individual bearings; parameters b and c represent the nonlinear stiffening behaviour at displacements corresponding to high shear strains.

$$
\begin{aligned}
&F = F_1 + F_2 \\
&F_1 = 0.5(1-u)F_m(x + \mathrm{sign}(X)|x|^n) \\
&F_2 = \begin{cases} uF_m(1-2\exp(-a(1+x)) + b(1+x)\exp(-c(1+x)) & \dot{X} > 0 \\ -uF_m(1-2\exp(-a(1-x)) + b(1-x)\exp(-c(1-x)) & \dot{X} < 0 \end{cases} \\
&x = X/X_m \qquad u = F_u/F_m
\end{aligned}
\tag{7.39}
$$

$$\frac{1-e^{-2a}}{a}=\frac{2u-\pi\eta_{eq}}{2u}$$
$$b=c^2\left[\frac{\pi\eta_{eq}}{u}-\left\{2+\frac{2}{a}\left(e^{-2a}-1\right)\right\}\right] \tag{7.40}$$

This model easily capture the smooth transition of the hysteresis loops from the low to high shear strain levels. As can be seen in Fig. 7.15, where the equations (7.39) are shown. Model parameters are established empirically based on bearing test results. All of the parameters that control the shape of the hysteresis loop are updated using equations (7.40) when load reversal occurs from the skeleton curve.

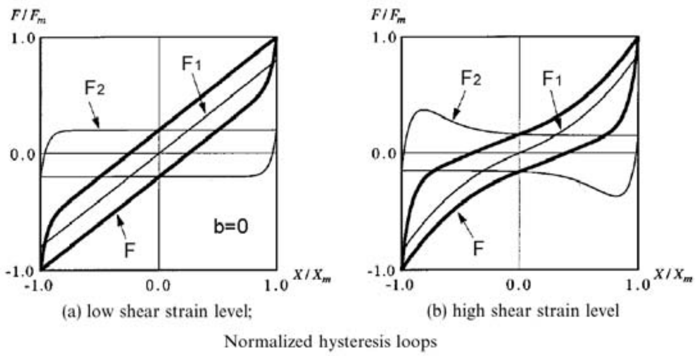

Fig. 7.15. Normalized hysteresis loops, at low and high shear strain levels respectively (Kikuchi and Aiken, 1997)

Formulae (7.39) and (7.40) model a steady-state hysteresis behaviour: a hysteresis rule for the randomly varying displacement conditions of earthquake response is further developed in (7.41), where (X_i, F_i) is the most recent point of load reversal. When the load reversal occurs in the same region (i.e. $X_i*X_{i-1}>0$), in order to avoid excessive enlargement of the hysteresis loop at load reversal in the stiffening range, equation (7.41) should be replaced by (7.42).

$$F_2=\begin{cases}F_{2i}+uF_m(2-2\exp(-a(x-x_i))+b(x-x_i)\exp(-c(x-x_i)) & \dot{X}>0\\ F_{2i}-uF_m(2-2\exp(a(x-x_i))-b(x-x_i)\exp(c(x-x_i)) & \dot{X}<0\end{cases}$$
$$F_{2i}=F_i-F_1 \qquad x_i=X_i/X_m \tag{7.41}$$

$$F_2=\begin{cases}F_{2i}+\alpha_1 uF_m(2-2\exp(-a(x-x_i))) & \dot{X}>0\\ F_{2i}-\alpha_2 uF_m(2-2\exp(a(x-x_i))) & \dot{X}<0\end{cases}$$
$$\alpha_1=\frac{2-2\exp(a(x_i-x_{i-1}))-b(x_i-x_{i-1})\exp(c(x_i-x_{i-1}))}{2-2\exp(a(x-x_i))} \tag{7.42}$$
$$\alpha_2=\frac{2-2\exp(-a(x_i-x_{i-1}))+b(x_i-x_{i-1})\exp(-c(x_i-x_{i-1}))}{2-2\exp(-a(x-x_i))}$$

Mechanical properties of elastomeric bearings are affected by load history. Experienced high shear strain degrades the subsequent stiffness in the small strain range; moreover, the stiffness gradually degrades with repeated cycling at the same displacement amplitude. Experimetally, the most significant differences are seen between the first cycle stiffness and the stiffness of subsequent cycles: two stages of effective stiffness for the skeleton curve are introduced in the model, by adding an additional force to the skeleton curve, calculated as in (7.43), where X_{max} and X_{min} are the extreme values of experienced displacement at a first-loading test, $K_{eff,i}$ is the corresponding effective shear modulus without any prior load history; K_{eff} in the skeleton curve should be obtained from a test that includes load history (i.e. from the second or later cycle). Equation (7.43) is shown in Fig. 7.16.

$$\Delta F = \begin{cases} (K_{eff,i} - K_{eff})X & X < X_{min} \quad X > X_{max} \\ 0 & X_{min} < X < X_{max} \end{cases} \tag{7.43}$$

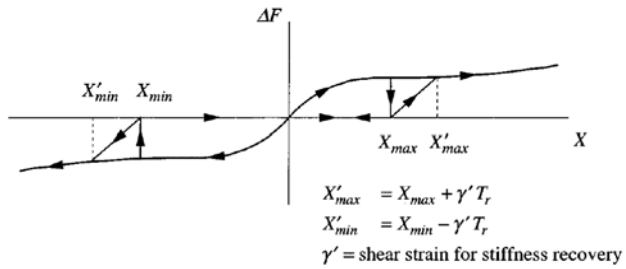

Fig. 7.16. Hysteresis rule for stiffness degradation associated with load history (Kikuchi and Aiken, 1997)

Kikuchi and Aiken verified the model on four types of elastomeric seismic isolation bearings: two types of high-damping rubber bearings, one type of lead-rubber bearing and one type of silicon rubber bearing (Fig. 7.17). Empirical formulae as functions of shear strain were identified from the test results (parameters are listed in Table 7.9) and the isolation bearings were modelled using two spring elements: a non-linear shear spring (for which the presented model is used) and a linear axial spring. Good correlation between experimental and analytical results was obtained, showing that the model can accurately predict the force-displacement relation-ship into the large strain range.

Table 7.9. Empirical parameters for HRDB A, HRDB B, LRB and Silicon rubber bearing (Kikuchi and Aiken, 1997)

High-damping A	High-damping B
$K_{eff} = 351\gamma^{-0.461}$ ($\gamma \leqslant 1.0$) (N/mm) $= 510 - 195\gamma + 34.7\gamma^2$ ($\gamma > 1.0$) $K_{eff,i} = 378\gamma^{-0.460}$ ($\gamma \leqslant 1.0$) (N/mm) $= 563 - 232\gamma + 44.6\gamma^2$ ($\gamma > 1.0$) $h_{eq} = 0.123 - 0.00876\gamma$ $u = 0.221 - 0.0344\gamma$ $n = 1.0$ ($\gamma \leqslant 2.0$) $= -1.96 + 1.48\gamma$ ($\gamma > 2.0$) a: obtained from equation (6) if $a > 15.2$, $a = 15.2$ (const.) b: obtained from equation (7) if $\gamma \leqslant 0.75$, $b = 0.0$ (const.) $c = 6.0$ (const.)	$K_{eff} = 116\gamma^{-0.295}$ ($\gamma \leqslant 1.2$) (N/mm) $= 144 - 40.4\gamma + 9.79\gamma^2$ ($\gamma > 1.2$) $K_{eff,i} = 124\gamma^{-0.282}$ ($\gamma \leqslant 1.2$) (N/mm) $= 154 - 49.7\gamma + 15.8\gamma^2$ ($\gamma > 1.2$) $h_{eq} = 0.101 - 0.0191\gamma + 0.0143\gamma^2$ $u = 0.191 - 0.0287\gamma$ $n = 1.0$ ($\gamma \leqslant 1.5$) $= 3.60 - 3.48\gamma + 1.17\gamma^2$ ($\gamma > 1.5$) a: obtained from equation (6) if $a > 13.0$, $a = 13.0$ (const.) b: obtained from equation (7) if $\gamma \leqslant 1.0$, $b = 0.0$ (const.) $c = 6.0$ (const.)
Lead-rubber	
$K_{eff} = 337\gamma^{-0.346}$ ($\gamma \leqslant 0.75$) (N/mm) $= 558 - 291\gamma + 54.1\gamma^2$ ($\gamma > 0.75$) $K_{eff,i} = 366\gamma^{-0.302}$ ($\gamma \leqslant 0.75$) (N/mm) $= 590 - 293\gamma + 51.3\gamma^2$ ($\gamma > 0.75$) $h_{eq} = 0.202 - 0.0457\gamma$ $u = 0.384 - 0.288\gamma + 0.0748\gamma^2$ $n = 1.0$ (const.) a: obtained from equation (6) if $a > 14.0$, $a = 14.0$ (const.) b: obtained from equation (7) if $\gamma \leqslant 0.25$, $b = 0.0$ (const.) $c = 4.0$ (const.)	$K_{eff} = 174\gamma^{-0.441}$ ($\gamma \leqslant 0.483$) (N/mm) $= 307 - 189\gamma + 81.3\gamma^2$ ($\gamma > 0.483$) $K_{eff,i} = 182\gamma^{-0.397}$ ($\gamma \leqslant 0.495$) (N/mm) $= 326 - 217\gamma + 92.2\gamma^2$ ($\gamma > 0.495$) $h_{eq} = 0.112 + 0.0129\gamma - 0.0138\gamma^2$ $u = 0.260 - 0.070\gamma$ $n = 1.0$ ($\gamma \leqslant 1.0$) $= 2.99 - 3.84\gamma + 1.85\gamma^2$ ($\gamma > 1.0$) a: obtained from equation (6) if $a > 12.8$, $a = 12.8$ (const.) b: obtained from equation (7) if $\gamma \leqslant 1.0$, $b = 0.0$ (const.) $c = 7.0$ (const.)

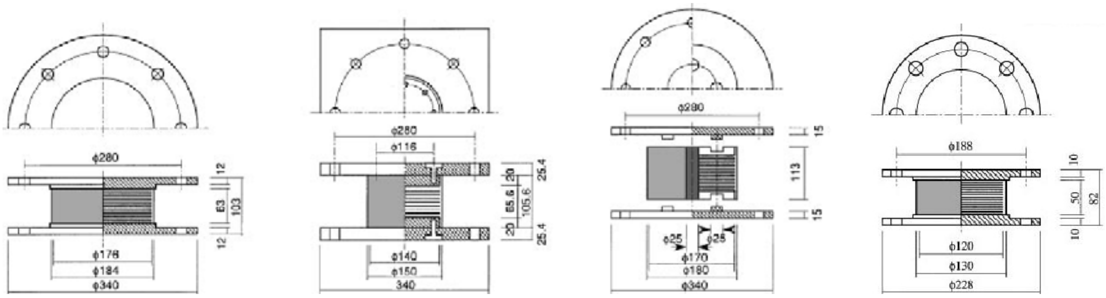

Fig. 7.17. Tested elastomeric isolation bearings, from the left: HRDB A, HRDB B, LRB, Silicon rubber bearing (Kikuchi and Aiken, 1997)

A further development of this model was carried out by Laffi (2004): based on experimental tests data on LRBs, the velocity dependence is introduced in the hysteretic behaviour of the isolator, and the scragging effect is expressed as a function of the number of cycles. Specifically, the strength degradation due to the cycling is an exponential function of the number of cycles and of the velocity.

7.5.2 Advanced analytical model of the stability

The stability of elastomeric bearings may be jeopardised due to large lateral displacements and axial loads, that are responsible for the reduction in the bearing critical load (Fig. 7.18), in the shear stiffness (Fig. 7.4 and Fig. 7.19) and in the rotational stiffness; as a consequence, the height, the damping and the overturning (in case of doweled connections) of the bearing result to be affected.

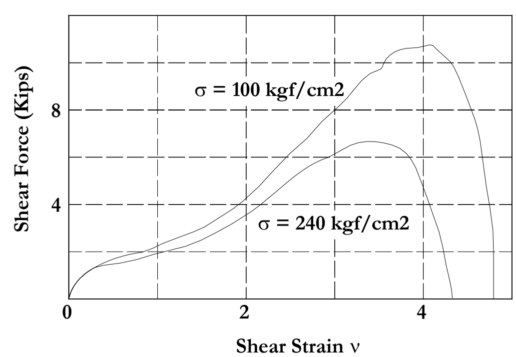

Fig. 7.18. Load-deflection relationship for the shear failure test of a HDRB (EERC)

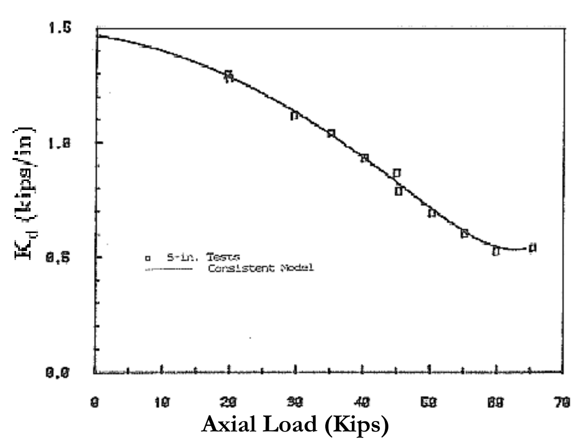

Fig. 7.19. Dynamic shear stiffness of a LRB varying the axial load (EERC)

The classical theoretical approach for the stability of rubber bearings is usually treated through Haringx's theory, based on linearity and small displacements: large displacements are accounted for by approximately reducing the value of critical load, P_{cro}, with the ratio of the effective to the actual column area at a large horizontal displacement, resulting for rectangular bearings in equation (7.44), where P_{cr} is the critical load at horizontal displacement Δ, P_{cro} is the critical load given by Haringx's theory (equation (7.49)) and B is the bearing width.

$$P_{cr} = P_{cro}[1 - \Delta / B] \qquad (7.44)$$

The inaccuracy of equation (7.44) is evident in experimental results, where unstable postbuckling behaviour is observed, with P_{cr} decreasing not linearly with increasing horizontal displacement. Moreover, the shear force–horizontal displacement curves present severe nonlinearities at increasing horizontal displacements, under constant axial load, whilst the global bearing capacity decreases at increasing axial load (Fig. 7.20).

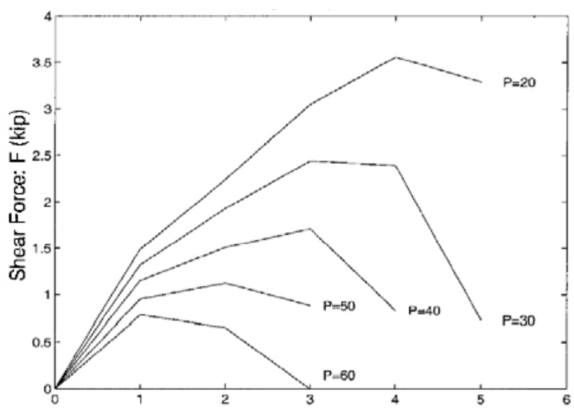

Fig. 7.20. Shear force-displacement curves as a function of the axial load

The model developed by Nagarajaiah and Ferrell, (1999), and Buckle *et al.*, (2002) consists in coupling a shear and a rotational spring, with non-linear stiffnesses. Main features of this model are that:

- the horizontal stiffness depends on the shear force, the axial load, the horizontal displacement and the shear strain;
- the rotational stiffness depends on the shear strain;
- the model predicts the reduction in the critical load with increasing horizontal displacement;
- the model includes large displacements and rotations, predicting unstable post-buckling behaviour;
- the model does not include axial flexibility of the bearing, i.e., it accounts just for the height reduction due to the horizontal displacement and axial load;
- the path dependent behaviour is not modelled;

The nonlinearities are based on the test results; the nonlinear analytical model consists of two rigid tee-shaped elements connected at mid-height by a shear spring and frictionless rollers and connected to the top and bottom plate by moment springs and frictionless hinges (Fig. 7.21). The model is 2 d.o.f.: the shear d.o.f., s, due to frictionless rollers, is resisted by a nonlinear shear spring of stiffness K_S; and the rotational d.o.f., θ, due to frictionless hinges, is resisted by nonlinear rotational springs of stiffness $K_\theta/2$, where K_θ is the rotational or tilting stiffness.

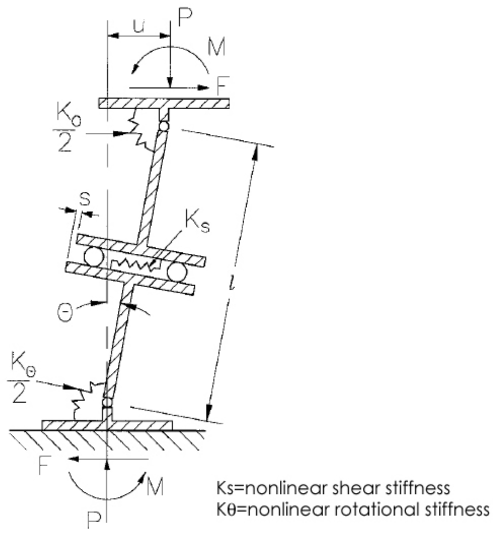

Fig. 7.21. Nonlinear analitycal model developed (Nagarajaiah and Ferrell, 1999; Buckle et al., 2002)

The model is loaded by axial load P and horizontal load F at the top of the column. The top plate is free to move vertically and horizontally; however, it is restrained in the rotational direction. The horizontal displacement, u, of the top of the column is given by equation (7.45), where ℓ is the combined height of the rubber layers and steel plates, excluding the top and bottom steel plates.

$$u = \ell\sin\theta + s\cos\theta \qquad (7.45)$$

The nonlinear horizontal stiffness of the model, K_h, is a function of the shear force and of the horizontal displacement. Both K_S and K_θ are function of s: the shear equilibrium and the rotational equilibrium are given in equations (7.46) and (7.47), where C_S and C_θ are constants, $f(s/\ell_r)$ is a function of s and ℓ_r, that is the total thickness of all the rubber layers; K_{S0} and $K_{\theta 0}$ are the shear and rotational stiffnesses at zero shear strain. These two equations constitute a nonlinear system of equations, solvable numerically in the incremental form. The height reduction h is computed with equation (7.48).

$$K_{s0}\left(1 - C_s f\left(\frac{s}{\ell_r}\right)\right)s = P\sin\theta + F\cos\theta + \frac{K_{\theta 0}C_\theta\theta^2}{2} \qquad (7.46)$$

$$K_{\theta 0}\left(1 - C_\theta\left(\frac{s}{\ell_r}\right)\right)\theta = P(\ell\sin\theta + s\cos\theta) + F(\ell\cos\theta - s\sin\theta) \qquad (7.47)$$

$$h = s\sin\theta + \ell(1 - \cos\theta) \qquad (7.48)$$

If nonlinear terms are neglected, and small angles are considered, the model reduces to the linear model of equation (7.44), for which the critical load, K_{S0}, $K_{\theta 0}$ and K_{h0} can be easily obtained, as shown in equations (7.49) to (7.51), where $(GA_s)_{eff}$ and $(EI)_{eff}$ are the effective shear and flexural rigidities, E and G are the bending and shear rubber moduli, A is the bonded rubber area, I is the moment of inertia of the bearing about the axis of bending, E_0 is the elastic rubber modulus (approximately equal to $4G$), and S is the shape factor

$$P_{cro} = \frac{(GA_s)_{eff}}{2}\left[\sqrt{1+4\frac{P_E}{(GA_s)_{eff}}} - 1\right] \tag{7.49}$$

$$P_E = \pi^2 (EI)_{eff} / \ell^2$$

$$\begin{aligned} &(GA_s)_{eff} = GA(\ell / \ell_r) \quad (EI)_{eff} = E_r I(\ell / \ell_r) \\ &E_r = E_0(1+0.742S^2) \end{aligned} \tag{7.50}$$

$$K_{\vartheta 0} = P_E \ell \qquad K_{s0} = P_s / \ell$$

$$K_{h0} = \frac{F}{u} = \frac{P_s}{\ell}\left(\frac{1-\frac{P}{P_E}-\frac{P^2}{P_E P_s}}{1+\frac{P}{P_E}+\frac{P_s}{P_E}}\right) \cong \frac{P_s}{\ell}\left(1-\frac{P^2}{P_E P_s}\right) \tag{7.51}$$

$$P_s = (GA_s)_{eff}$$

Calibrating parameters of relationships (7.47) and (7.48) by means of experimental results, lead to equations (7.52) and (7.53), where G_0=1.379MPa, C_S=0.325, α is a dimensionless constant with a value of ℓ_r, t_u is the rubber layer of unitary thickness, t_r is the rubber layer thickness and B is the bearing width.

$$G = G_0\left(1 - C_s \tanh\left(\alpha \frac{u}{\ell_r}\right)\right) \tag{7.52}$$

$$\begin{aligned} &K_s = K_{s0}\left(1 - C_s \tanh\left(\alpha \frac{s}{\ell_r}\right)\right) \qquad K_\theta = K_{\theta 0}\left(1 - C_\theta \frac{s}{\ell_r}\right) \\ &C_\theta = \alpha\left(\frac{t_u - t_r}{B}\right) \end{aligned} \tag{7.53}$$

Analytical and experimental results are in good agreement: the analytical model captures the nonlinear behaviour and axial load effects accurately, providing also useful estimates of the height reduction (subtracted of the deformation due to the bearing vertical flexibility). The critical load at a horizontal displacement equal to *B* is higher than the value of zero estimated by the linear theory (7.44).

7.6 A COMBINED ENERGY DISSIPATION SYSTEM: LEAD RUBBER DAMPERS AND OIL DAMPERS

Before concluding the section dedicated to the elastomeric bearings, an application of a combined energy dissipation system is shown. The combined system, tested by X. Lu and Q. Zhou (2002), consists of lead rubber dampers connected in parallel with oil dampers and installed in conventional frame braces. The steel brace is connected by the LRB to the upper beam, and the oil damper is connected to the brace and the upper beam (Fig. 7.1). In such a setup, the resistant forces of the two dampers in parallel are transferred to the upper beam and then to the columns, avoiding the stress concentration on columns occurring when oil dampers are directly connected to them. The working mechanism of the combined energy dissipation system is such that under lower earthquake intensity, the LRB behaves elastically and oil damper provides smaller damping force and stiffness. Under stronger earthquake the LRB develops elasto-plastic deformation, decreasing the structural stiffness, and the oil damper provides larger damping force and smaller stiffness: the seismic force on the whole structure is reduced, decreasing the response.

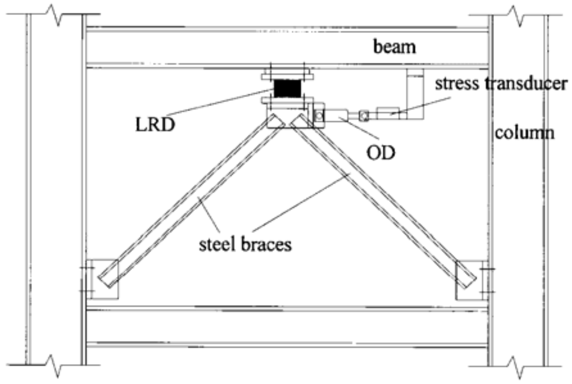

Fig. 7.22. The installation of the combined energy dissipation system in a frame

8.DEVICE TYPOLOGIES: SLIDING DEVICES

This class of devices consists of sliding supports providing frictional damping forces. Modern sliding bearings consist of a sliding interface and a rotational element needed for maintaining the full contact at the sliding interface. The rotational element may take various forms such as in the pot bearing, the spherical bearing, the disc bearing, the articulated slider in the Friction Pendulum bearing or an elastomeric bearing. The type of material at the slider interface may be:

- Unlubricated PTFE: unlubricated interfaces of highly polished austenitic stainless steel in contact with PTFE (Teflon) or similar composites (as those used in FPS bearings);
- Lubricated PTFE: lubricated interfaces of highly polished austenitic stainless steel in contact with unfilled PTFE; lubrication is applied by grease stored in dimples;
- Bimetallic interfaces: interfaces stainless steel in contact with bronze or similar metals impregnated with a lubricant such as lead, PTFE or graphite.

8.1 SLIDING BEARINGS

Stainless steel – PTFE bearings are widely used in bridge design to accommodate slow thermal movements. The friction coefficient of PTFE on steel is 0.02÷0.03 (unlubricated and lubricated PTFE respectively) for very slow slip rates. For typical seismic velocities and typical pressure for bridge bearings, it ranges around 0.10÷0.15, depending on lubrication.

In a system isolated with a set of PTFE bearings, the first isolation period arises from the substructure only and is typically very short, leading energy into higher modes, while the second isolator period tends to infinity and provides no centring force to resist displacements. Their approximately rectangular force-displacement loop gives very high hysteretic damping, and they are generally coupled with other centring devices like rubber bearings or steel dampers. In the latter case all the load is carried by the PTFE bearing and the friction coefficient should be kept as low as possible, while centring force and additional damping are provided by the dampers. In the former case they can be mounted in parallel, thus sharing the vertical load, or they can be mounted in series to provide flexibility at force levels lower than the bearing sliding forces; part of the vertical load is sustained by the rubber. Modelling of these kind of sliders is close to that of friction devices illustrated in chapter 2.

8.2 THE FRICTION PENDULUM SYSTEM

The Frictional Pendulum System (FPS) is a sliding recentering device based on the principle of the sliding pendulum motion. It consists of two sliding plates, one of which with a spherical stainless steel surface, connected by a lentil-shaped articulated slider covered by a Teflon-based high bearing capacity composite material (Fig. 8.1, left). The slider is generally locked on a vertical stud with a special hollowed end which allows free rotation of the slider and a perfect contact with the sliding surface at all times (Fig. 8.1, right). During the ground shaking, the slider moves on the spherical surface lifting the structure and dissipating energy by friction between the spherical surface and the slider (as evident in Fig. 8.2), essentially resulting in a pensulum motion with period given in equation (8.1), where F_V is the total weight on the device and R_0 is radius of the spherical stainless steel surface. Considering a system with mass M, the system stiffness K is easily obtained in equation (8.2).

$$T = 2\pi\sqrt{\frac{R_0}{g}} \tag{8.1}$$

$$T = 2\pi\sqrt{\frac{M}{K}} = 2\pi\sqrt{\frac{F_V}{gK}}$$
$$\frac{F_V}{gK} = \frac{R_0}{g} \qquad \Rightarrow \qquad K = \frac{F_V}{R_0} \tag{8.2}$$

Detailed descriptions of the basic principles of the FPS devices can be found in literature of relatively recent works (Almazan *et al.*, 2002, Wang *et al.*, 1998; Tsai, 1997).

One of the most relevant features of the FPS is that residual displacements are reduced due to the self-centering action induced by the concave spherical surface. Typically a FPS device may provide equivalent dynamic periods of vibration within the range from 2 to 5 seconds and displacement capacities greater than 1 m.

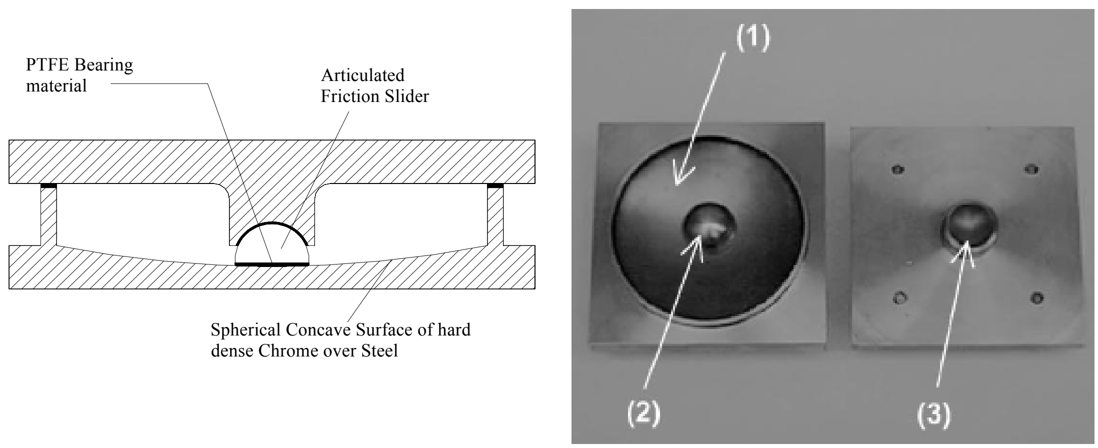

Fig. 8.1. Radial section of the FPS device (left) and components of a typical FPS (right): (1) spherical surface, (2) slider, and (3) stud

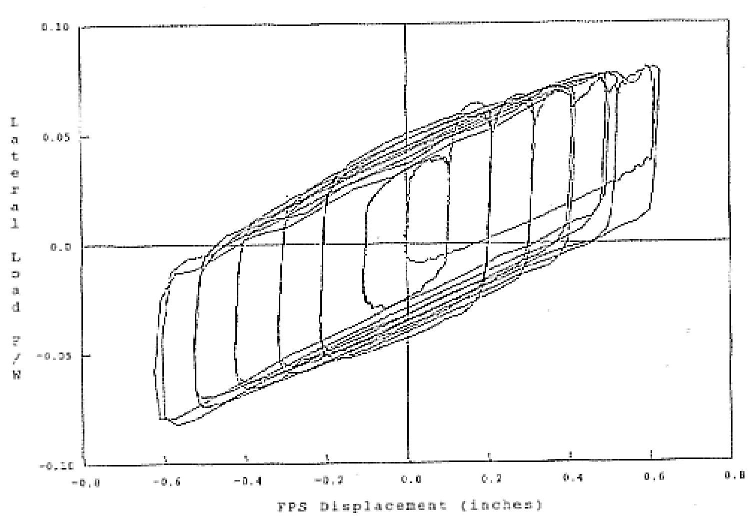

Fig. 8.2. Hysteretic response on an FPS under constant normal pressure

The device can be either mounted in an upward or downward position (Fig. 8.3), conceptually equivalent in terms of isolation effect, but different for the design implications on the superstructure and the foundation system: in the downward position, the *P-Δ* effect is transmitted to the portion of the structure below the isolation system, usually the foundation; if the FPS is positioned upward, the same *P-Δ* effect is transmitted to the resisting elements of the superstructure.

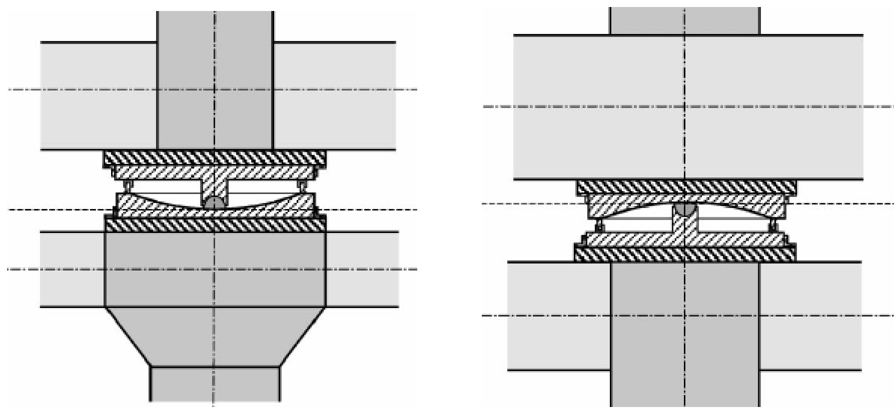

Fig. 8.3. FPS bearing in downward (left) and upward (right) position

FPS bearings are used in the retrofit of earthquake damaged bridges (e.g. Priestley and Calvi, 2002) or in the design of new bridge structures. Wang *et al.* (1998) investigated numerically the feasibility of using friction pendulum bearings for seismic isolation of bridges. They found that, at hard-soil sites, responses of the FPS isolated bridges without constraint can be drastically reduced with acceptable bearing displacements, while at soft-soil sites, responses of the isolated bridge can be amplified and the bearings displace excessively, if the bridge superstructure is entirely unconstrained. They suggested of providing a displacement constraint at one of the abutments, increasing abutment's loading as a trade-off: under this configuration, the isolated bridge performed consistently well during various earthquakes, regardless of the site conditions.

8.2.1 Basic hysteretic behaviour

The resulting isolator force consists of two main components, namely, the restoring force due to the tangent component of the self-weight, always contributing to the restoring mechanism, and the frictional force always opposing the sliding, thus contributing or resisting the restoring force depending on the direction of motion. The peculiarity of the FPS is the association of the concave sliding surface to a friction-type response: the consequent coupling between the lateral and vertical motions may produce large deformations in the isolators, but it is not considered in the small deformation theory of the most theoretical formulations, because generally small-deformations hypothesis is accurate enough for estimating global building response quantities, such as storey and isolators deformations, or storey shears and torques. The exact force–deformation constitutive relationship of the isolator may be carried out at different levels of complexity.

Considering the most general 3D system in Fig. 8.4 (left), the force-deformation constitutive law can be expressed as in equation (8.3), where $\underline{F}=(F_x, F_y)$ is the horizontal restoring force of the isolator, N is the normal contact force, $q=\{q_h,z_b\}^T$ is the vector of bearing total displacements ($q_h=\{x_b,y_b\}^T$), assuming the cinematic constraint of the spherical surface in determining $z_b=g(x_b, y_b)$. It has to be noticed that the radius of curvature ρ of the sliding surface does not need to be constant (a variable frequency pendulum isolator, namely VFPI, has been proposed by Pranesh and Sinha, 2000). N may continuously vary due to vertical motion and lateral-vertical coupling between the vertical and horizontal motions of the FPS.

$$\underline{F} = \underline{F}_{\rho} + \underline{F}_{\mu} = \frac{N}{\rho}\underline{q}_h + \mu N \left(\frac{\dot{\underline{q}}_h}{\left\| \dot{\underline{q}} \right\|} \right) \tag{8.3}$$

During the sliding phase, the total reaction *R* at the sliding surface is always located on the surface of the friction cone, changing direction continuously according to the isolator path; since the angle between the normal to the surface and the reaction *R* is *ϕ=tan-1μ*, when the angle between the resultant external force and the normal to the surface is larger than *ϕ*, the sliding velocity magnitude increases, while when it becomes smaller, the isolator velocity decreases until the sticking condition and the consequently fixed-base motion of the system. In the sticking range *R* is required to maintain equilibrium with the external resultant. The sticking condition is for the general case:

$$\left\| \underline{R} - N\underline{\hat{n}} \right\| < \mu N \quad N = \underline{R} \cdot \underline{\hat{n}} \tag{8.4}$$

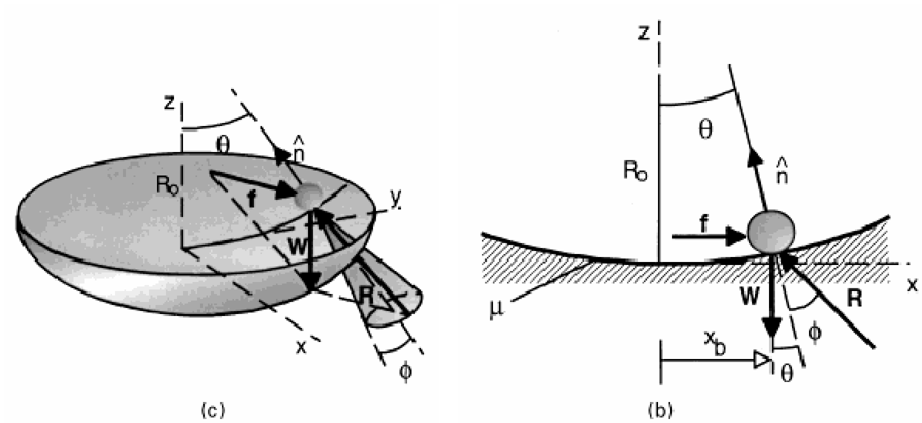

Fig. 8.4. FPS equilibrium diagrams in the 3-D (left) and 2-D (rght) models

Considering the planar system 2D in Fig. 8.4 (right), the simplest form of the constitutive law is the well-known force–deformation relationship of the FPS system in one dimension and small deformations, resulting from the horizontal equilibrium of the isolator:

$$F = \frac{F_v}{R_0} x + \mathrm{sign}(\dot{x})\mu F_v \tag{8.5}$$

The total acting vertical force F_V can be identified with the weight *W*. The two parameters characterizing the friction pendulum system behaviour are the friction coefficient and the post-yielding stiffness: these properties are influenced by temperature, velocity, bearing pressure and wearing state. Simplifications in the modeling of the FPS constitutive law lead to an essentially constant, regular, parallelogram shaped hysteresis loop: specifically those simplifications consists in the small angle approximations, in neglecting the friction at the interface of the socket of the slider, in neglecting the non-punctual transfer mechanisms of the forces and in neglecting axial force variations when considerable. If the small displacements approximation is overcome, the vertical and horizontal equilibrium equations lead to:

$$\theta = \arcsin\left(\frac{x}{R_0} \right) \tag{8.6}$$

$$N = \frac{F_v}{\cos\theta - .\mathrm{sign}(\dot{x})\mu} \tag{8.7}$$

$$F = F_v \operatorname{tg}\theta + \operatorname{sign}(\dot{x})\mu \frac{N}{\cos\theta} \tag{8.8}$$

The dependence of the friction coefficient on the sliding velocity, bearing pressure and temperature was already discussed elsewhere (2.4.1). Actually, also the stiffness of the device seems to be affected by the sliding velocity and the bearing pressure (Fig. 8.5 to Fig. 8.7): the dependence on velocity appear to be of the same kind of the friction coefficient. Experimental measures of the actual device stiffness record an increase of it up to the 10% of its theoretical value. The reason of this still need further investigation.

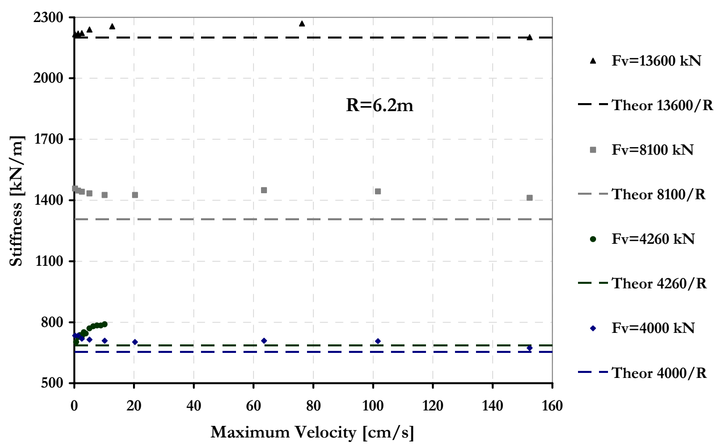

Fig. 8.5. Test results on FPS, variation of the stiffness device with the sliding velocity

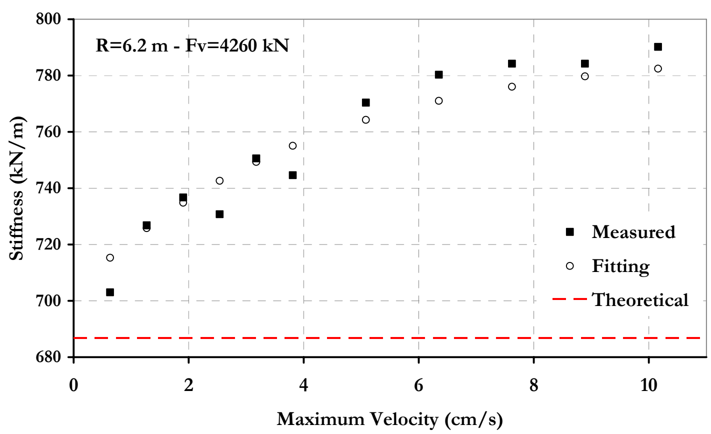

Fig. 8.6. Test results on FPS, variation of the stiffness device with the sliding velocity (small velocities range)

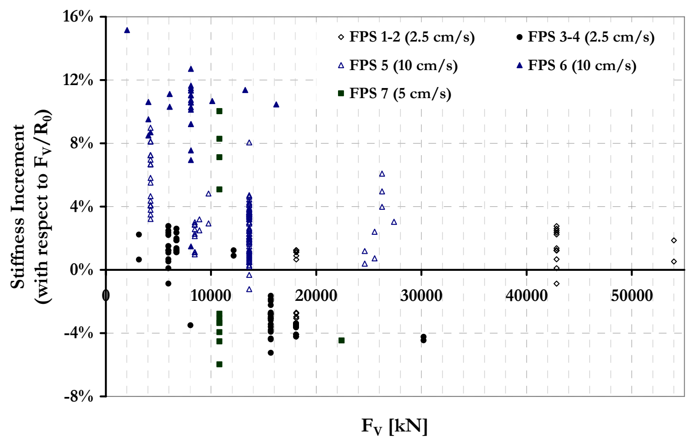

Fig. 8.7. Test results on FPS, variation of the stiffness device with the bearing pressure

One of the factors affecting the evaluation of the FPS stiffness is the consideration of the non-punctual transfer mechanisms of the forces. The concept is briefly illustrated in the free-body diagram of Fig. 8.8: the center of application of the resisting forces, i.e. the point where translational equilibrium is carried out, does not coincide with the center of the articulated slider, as it is usually considered. The equilibrium equations (8.7) and (8.8) should refer to θ_2 (Fig. 8.8, right), while equation (8.6) refers to the slider position $x(\theta)$. The fact that the two angles slightly differ, causes an increasing in the device stiffness whose importance has to be evaluated.

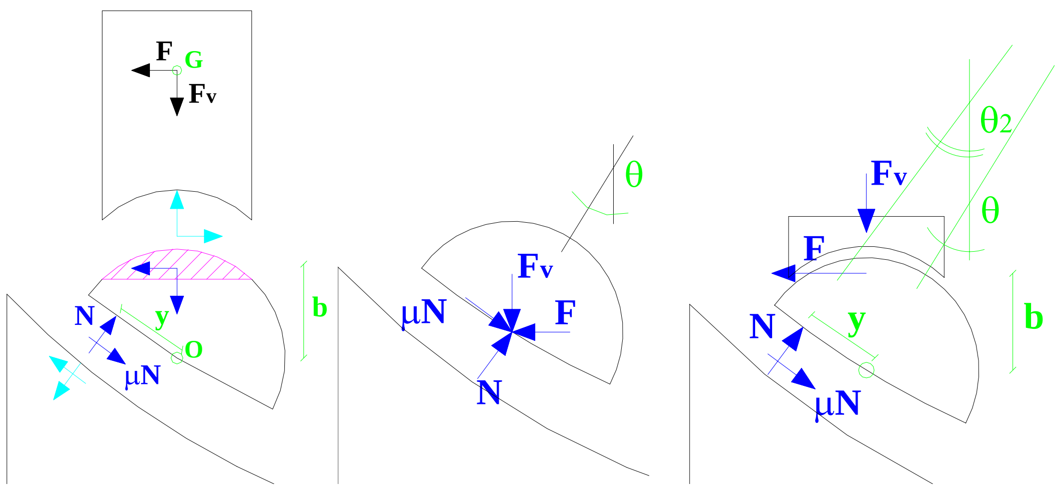

Fig. 8.8. Force transfer mechanism in the FPS: free-body diagram (left), punctual transfer mechanism approximation (center), non-punctual transfer mechanism modelisation (right)

The real behaviour of the isolator is then nonlinear and sensitive to the axial load variations: the constitutive law is characterized by a variable yield point and a post-elastic stiffness dependent on the acting axial force, and resulting in a nonlinear post-elastic branch. An accurate model of these characteristics can be found in Calvi *et al.* (2004): Fig. 8.9 shows the responses of two isolators sensitive to the axial force variations, one subjected to an increasing compression and the other to a decreasing axial load, and a third FPS insensitive to the axial force variations.

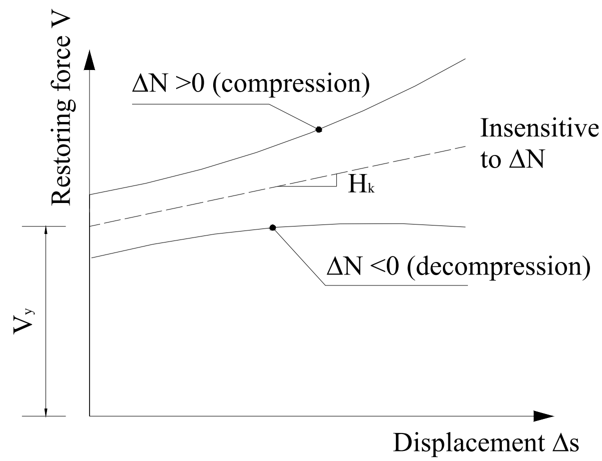

Fig. 8.9. Constitutive laws of models sensitive and insensitive models of the FPS

8.2.2 Modelling issues of the friction pendulum system

Earlier studies developed simplified analytical models capable of representing the predominantly bilinear FPS behaviour: test results were well correlated with global analytical results. Most of the theoretical formulations were carried out considering small-deformations, however, due to recent seismic event observations, the large-deformations and the associated P-Δ effects have been addressed as a possible issue in the isolators design. For these reasons, large-deformations models should be used in the design of FPS isolated structures, for which is particularly important the consideration of the axial force in the isolators as it can induce accidental torsion effects not accounted for in the current design procedures.

Almazan *et al*. (1998) studied the influence of the accuracy of the modelling, by analysisng two simple structures with FPS models, with increasing degrees of complexity: from a simplified model neglecting vertical response of the system, assuming small deformations and constant normal force equal to the weight above the isolator, to an exact structural model considering the coupling lateral and vertical motion response of the system, assuming large deformations but no uplift. Comparing models, they observed that: (i) the predicted global response quantities, such as isolators and structural deformations, from the different structural models are very similar, with an overestimation of the simpler model; (ii) larger discrepancies are observed base shears, dependently on the degree of correlation between the vertical and horizontal motion components: with a small correlation, a simple structural model can still be used within a low error; (iii) the inclusion of the vertical component of the ground motion leads to structural peak base shear and normal contact force values significantly larger; (iv) the influence of bi-directional motion is relevant in the response of rigid structures, and decrease steadily with increasing period. In general, the most relevant effect is the inclusion of the vertical ground motion as well as the lateral-vertical coupling induced by the spherical sliding.

8.2.2.1 Analytical model for the teflon-metal interface and of the local bending effects

A finite element formulation involving local bending moment effects for the FPS isolator has been developed by Tsai (1997), through a two-node element, whose point 2 is at the centre of the upper part and point 1 at the centre of the lower part of the sliding surface (Fig. 8.10, left). In 3D cases the total forces acting on point 2 of the isolator are shown in Fig. 8.10 (right), while Fig. 8.11 illustrates forces acting in the *F*-*W* plane and the local bending effects of *W* and *F* respect to the node 1 of the model.

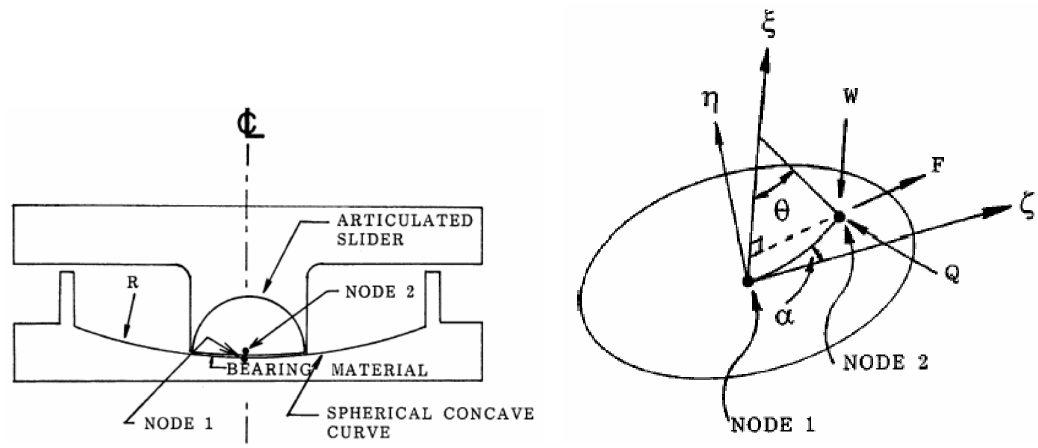

Fig. 8.10. Forces acting at nodal point 2

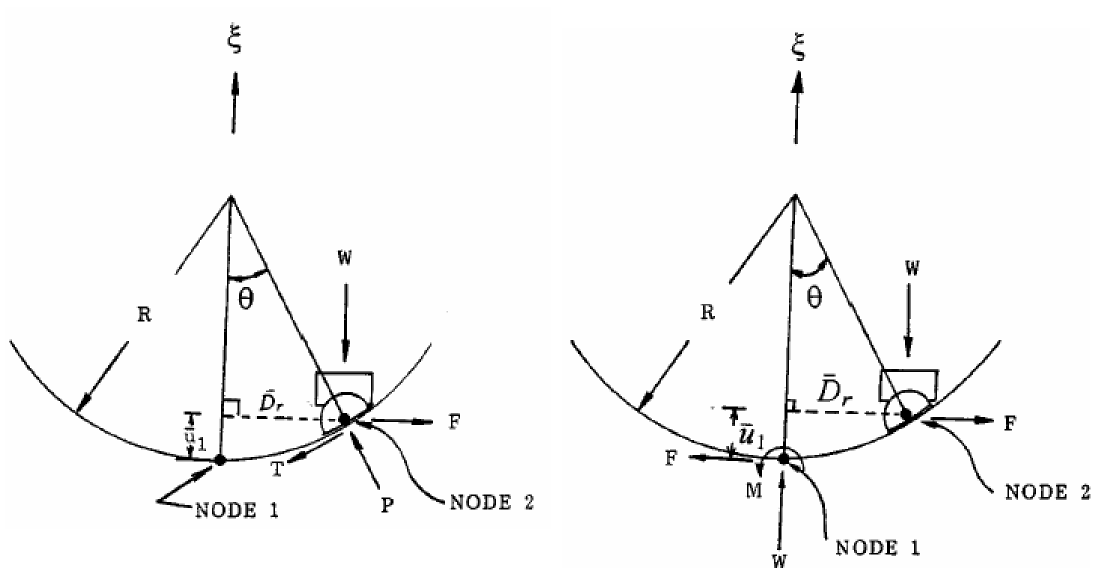

Fig. 8.11. Forces acting in F–W plane and local bending moment effect for base isolator

To simulate accurately the behaviour of the teflon-metal interface, including the effects of axial forces and velocities, Tsai (1997) used an analytical model based on visco-plasticity theory adopting an exponential function for representing the dependence of the friction force on the velocity. Numerical simulations on multi-storey structures have shown that nonlinear local bending moment effects are substantially important for base-isolated structures and that axial force variations on the isolators are of significant importance for the friction force calculation.

8.2.2.2 Modelling of the axial force variation influence

Dezza (2001), Ceresa (2002) and Calvi *et al.* (2004) developed and tested an analytical model of FPS, that takes into account the effect of the axial force variations on the isolators: the actual behaviour of the isolator has been found to be of relevance in terms of the general response quantities of the bridge structures. The formulation models both the yielding shear and the post-elastic stiffness of FPS as a function of the acting axial force, resulting in hysteretic loops characterized by non-linear post-elastic branch, as evident in Fig. 8.9. The model of the isolator has been implemented by means of a three-dimentional 2-joint finite element (Fig. 8.12), characterized by cylindrical symmetry. Presently, the simulation does not include possible uplift of the deck, allowing the isolator to be in tension. This may result in an increase of compression on the other isolator on the top of the same pier and in an increased bending moment and shear.

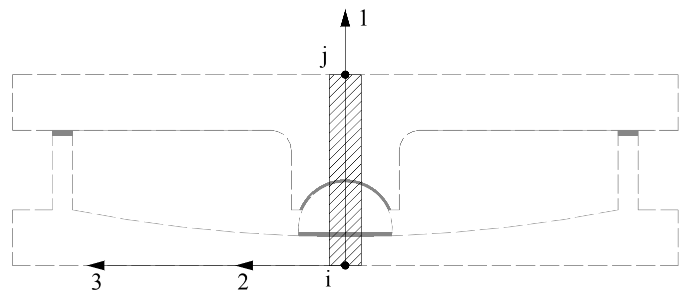

Fig. 8.12. Finite element representation of the FPS device (Calvi et al., 2004)

8.2.2.3 A physical model for the FPS uplifting

To include possible uplift and impact, Almazan *et al*. (1998) defined a physical model for the FPS, including an uniaxial gap element between isolator and sliding surface. A restitution coefficient accounts for the energy loss during the impact in the isolators in which the uplift occurs; advantage of this model is that N is computed easily: the force developed in the vertical gap element is the vertical component of R acting on the slider, whose direction is known. The only requirement is an adaptive time step at the impact instances to attain sufficient accuracy. Normal contact forces during an earthquake may vary in the mean form 1/5 to 2 the axial load due to gravitational loads, up to 5 if uplift occurs due to overturning of the structure and vertical input. The resultant vertical impact of the slider and the spherical surface leads to two effects: column base shears may increase due to increase in normal force at the isolators interface; this in fact results in the instantaneous stop of the slider from sliding and in the transmission of significantly larger shear forces to the supported columns.

Although local effects such as variation in the normal contact forces, large deformations and uplift seems not to affect considerably the global system response, Almazan *et al*. (1998; 2002) recommend to consider them in the isolation modelling and design to compute local responses such as the superstructure deformations and the normal isolator forces, expecially for near-field earthquake with strong initial acceleration pulse and for statistically correlated horizontal and vertical expected ground motion components.

REFERENCES

A

I.D. Aiken, D.K. Nims, A.S. Whittaker, J.M. Kelly, (1993), "Testing of Passive Energy Dissipation Systems", Earthquake Spectra, Vol 9(3)

Alga Spa, 2003, Algasism HRDB, manufacturer instructions

AASHTO-83, 1988, "Guide Specifications for Seismic Design of Highway Bridges", American Association of State Highway and Transportation Officials, Washington, D.C.

J.L. Almazan, J.C. De la Llera, J.A. Inuaudi, (1998), "Modelling aspects of structures isolated with the Frictional pendulum system", EE&SD, 27, pp. 845–867

J.L. Almazan, J.C. De la Llera, (2002), "Analytical model of structures with frictional Pendulum isolators", EE&SD, 31, pp. 305–332

J. W. Asher *et al.*, (1996), "Seismic isolation design of the San Bernardino County Medical Center Replacement Project", Journal of Structural Design of Tall Buildings. 5, pp 265–279.

J. Azevedo, R. Bento, (1996), "Design criteria for buildings subjected to pounding", 11th WCEE, Acapulco, Mexico, 23–28 June 1996, paper No. 1063.

B

D.M. Bergman, S.C. Goel, (1987), „Evaluation of cyclic testing of steel plate devices for added damping and stiffness", Report UMCE 87-10, Civil Engineering Department, University of Michigan, Ann Arbor, MI.

A. Bersofsky, C. Casarotti, C.S. Lee, M. Schoettler, (2003), "Seismic Retrofit of a Six Story Moment Resisting Steel Frame", Research Project for the SE 223 Advanced Seismic Design of Structures.

G. Bondonet, A. Filiatrault, (1997), "Frictional Response of PTFE Sliding Bearings at hogh frequencies", Journal of Bridge Engineering, ASCE, 2(4), 139-148.

R. Bouc, (1967), "Forced vibration of mechanical systems with hysteresis", Proceedings of the 4th Conference on Non-Linear Oscillations

S. Bruno, C. Valente, (2002), "Comparative response analysis of conventional and innovative seismic protection strategies", Earthquake Engineering and Structural Dynamics; 31:1067-1092.

I. Buckle, S. Nagarajaiah, K. Ferrell, (2002), "Stability of Elastomeric Isolation Bearings: Experimental Study", Journal of Earthquake Engineering, 128:3-11.

C

G.M. Calvi, D. Bolognini, P. Ceresa, C. Casarotti, F. Auricchio, (2004), "Effects of axial force variation on the seismic response of bridges isolated with friction pendulum systems" Jour. of Earthquake Engng., accepted for publication

G.M. Calvi, (2004), "Recent experience and innovative approaches in design and assessment of bridges", Keynote Lecture, 13th WCEE, Vancouver, B.C., Canada August 1-6, 2004 (to be published)

Ceresa, P. (2002) "Effetti di variazioni di azione assiale sulla risposta sismica di ponti isolati"- Tesi di Laurea, Università degli Studi di Pavia.

C. Chang, M. ASCE, L. Zhou, (2002), "Neural network emulation of inverse dynamics for a magnetorheological damper", Journal of Earthquake Engineering, 2:231-239.

K.C. Chang, M.L. Lai, T.T. Soong, D.S. Hao and Y:C: Yeh, (1993), WSeismic behaviour and design guidelines for steel frame structures with added viscoelastic dampers", Report No NCEER 93-0009, National Center for Earthquake Engineering Research, Buffalo, NY.

V. Ciampi, A. Marioni, (1989), "New types of energy dissipating devices for seismic protection of bridges"

C. Christopoulos, A. Filiatrault, B. Folz, (2002), "Seismic response of self-centering hysteretic SDOF systems", Earthquake Engineering and Structural Dynamics, 31, pp.1131-1150.

C. Christopoulos, A. Filiatrault A, C.M. Uang, B. Folz, (2002), "Post-tensioned energy dissipating connections for moment resisting steel frames", Journal of Structural Engineering, ASCE.

CEN, 2002, "Eurocode 8: Design of structures for earthquake resistance - Part 2: Bridges", PrEN 1998-2: 2003, Draft 2 April 2002, Comité Europeen de Normalization, Brussels, Belgium.

M.C. Constantinou, P. Tsopelas, A. Kasalanati, E. Wolff, (1999), "Property Modification Factors for Seismic Isolation Bearings", Technical Rep. No. MCEER-99-0012, Multidisciplinary Center for Earthquake Engineering Research, State Univ. of New York at Buffalo, Buffalo, N.Y.

M.C. Constantinou, M.D. Symans, P. Tsopelas, (1993), "Fluid viscous dampers in applications of seismic energy dissipation nad seismic isolation", ATC17-1 on Seismic Isolation, Passive Energy Dissipation and Active Control, 2, 581-591.

E. Cosenza, G. Manfredi, (1997), "The improvement of the seismic-resistant design for existing and new structures using damage criteria", in Seismic Design Methodologies for the Next Generation of Codes, Fajfar P, Krawinkler H. (eds). Balkema: Rotterdam.

D/ E/F

R. DesRoches, M. Delemont, (2002), "Seismic retrofit of simply supported bridges using shape memory alloys", Engineering Structures 24, pp 325–332

E. Dezza, (2001), "Previsione del comportamento sismico di ponti a travata continua in C.A. mediante parametri di regolarità"- Tesi di Laurea, Università degli Studi di Pavia.

EERC, Earthquake Engineering Research Center, , The Berkeley Earthquake Protective Systems Group and the PROSYS Online Database, from URL:http://nisee.berkeley.edu/prosys/applications.html", University of California at Berkeley

P. Fajfar, T. Vidic, (1994), "Consistent inelastic design spectra: hysteretic and input energy", Earthquake Engineering and Structural Dynamics, 23, pp 523-532.

fib TG 7.2, (2003), "Displacement-based seismic design of reinforced concrete structures", fib Bulletin 25, Lausanne, 2003

A. Filiatrault, S. Cherry, (1990), "Seismic Design Spectra for Friction Damped Structures", ASCE Journal of Structural Engineering, 116(5), pp. 1334-1355.

A. Filiatrault, R. Tremblay, R. Kar, (2000), "Performance evaluation of friction spring seismic damper", Journal of Structural Engineering, 126 (4), pp. 491-499

A. Filiatrault, (2002), "Retrofit of a steel moment frame by passive damping systems in near-field seismic environment", 2nd International Rose School Seminar , Pavia - 08 June 2002

A. Filiatrault, (2003), "SE 223 Advanced Seismic Design of Structures Class Notes", UCSD.

G/ H/I/J

R.K. Goel, (1998), "Effects of supplemental viscous damping on seismic response of asymmetric-plan systems", Earthquake Engineering and Structural Dynamics, 27:125-141

E.J. Graesser, F.A. Cozzarelli, (1991), "Shape-memory alloys as new materials for aseismic isolation", Journal of Engineering Mechanics. Vol. 117, no. 11, pp. 2590-2608.

Gulkan, P. and M. Sozen, Inelastic Response of Reinforced Concrete Structures, ACI Journal, Vol. 71, 1974, 604-610.

D.E. Hodgson, (1988), "Usiing Shape Memory Alloys". Sunnyvale, CA: Shape Memory Applications, Inc.

Y. Ivshin, T. Pence, (1994), "A thermo-mechanical model for a one-variant shape memory material", Journal of Intelligent Materials, Systems and Structures, 5, pp.455–473.

R. Jankowski, K. Wilde, Y. Fujino, (1998), "Pounding of superstructure segments in isolated elevated bridge during qearthquakes", Earthquake Engineering and Structural Dynamics, 27:487-502.

K

R. Kar, J.H. Rainer, (1996), "New damper for seismic control of structures", Proc., 1st Struct. Spec. Conf., Canadian Society of Civil Engineering, Edmonton, Alta., Canada, 835–842.

R. Kar, J.H. Rainer, A.C. Lefrançois, (1996), "Dynamic properties of a circuit breaker with friction-based seismic dampers", Earthquake Spectra, 12(2), pp. 297–314.

K. Kawashima, T. Sato, (1996), "Relative displacement response spectrum and its application", Proceedings of 11th WCEE, Acapulco, Mexico, 1996; paper no. 1103.

J.M. Kelly, (1990), "Base Isolation: Linear Theory and Design", Earthquake Spectra, 6-2, pp 223-244

J.M. Kelly, (1999), "the role of damping in seismic isolation", Earthquake Engineering and Structural Dynamics, 28, pp 3-20

J. M. Kelly, (1996), "Earthquake-Resistant Design with Rubber", 2nd edn, Springer, London.

M. Kikuchi, I.D. Aiken, (1997), "An Analitical hysteresis model for elastomeric seismic isolation bearings", Earthquake Engineering and Structural Dynamics, 26:215-231.

L

T. Laffi, (2004), Tesi di Laurea, Facoltà di Ingegneria, Università degli Studi di Bologna

L.H. Lee, S.W. Han, Y.H. Oh, (1999), "Determination of Ductility factor considering different hysteretic models", Earthquake Engineering and Structural Dynamics; 28:957-977.

L.H. Lee, I. Takewaki, K. Uetani, K. Inoue, (2002), "SHORT COMMUNICATION - Critical damping of structures with elastically supported visco-elastic dampers", Earthquake Engineering and Structural Dynamics, 31:481-486.

C. Liang, C.A. Rogers, (1990), "One-dimensional thermo-mechanical constitutive relations for shape memory materials", Journal of Intelligent Materials, Systems and Structures, 1, pp. 207–234.

X. Lu, Q. Zhou, (2002), "Dynamic analysis method of a combined energy dissipation system and its experimental verification", Earthquake Engineering and Structural Dynamics, 31:1251-1265.

M

N. Makris, (1997), "Rigidity-plasticity-viscosity: can electrorheological dampers protect base-isolated structures from near-field ground motions?", Earthquake Engineering and Structural Dynamics, 26:571-591.

N. Makris, S. A. Burton, D. Hill and M. Jordan, (1996), "Analysis and design of an electrorheological damper for seismic protection of structures', Journal of Engineering Mechanics, ASCE 122, pp. 1003–1011.

N. Makris, S. Chang, (2000), "Effect of viscous, viscoplastic and friction damping on the response of seismic isolated structures", Earthquake Engineering and Structural Dynamics

G. Manfredi, (2001), "Evaluation of Seismic Energy Demand", Earthquake Engineering and Structural Dynamics

A. Marioni, (1996), "development of a new type of hysteretic damper for the seismic protection of bridges", IV World Congress on Joint Sealing and Bearing Systems for Concrete Structures, Sacramento, USA - 29 Sept-2 Oct-1996.

MANSIDE Consortium, (1998), "Guidelines for the passive seismic protection of structures using shape memory alloy based devices", Report of the Brite/Euram Project BE95-2168

A. Marioni, (1998), "The use of high damping rubber bearings for the protection of the structures from the seismic risk", Jornadas Portuguesas de Engenharia de Estruturas, Lisboa, LNEC - 25/28 Nov-1998.

A. Marioni, (1999), "The use of hydraulic dampers for the protection of the structures from the seismic risk: an outstanding example", International Post-Smirt Conference Seminar on Seismic Isolation, Passive Energy Dissipation and Active Control of Vibration of Structures, Cheju, Korea – 23/25 Aug-1999.

A. Marioni, Rose School Conference, (22 January 2002), "The use of anti-seismic devices for the protection of the structures from the seismic risk", Pavia

N. Mostaghel, T. Davis, (1997), "Representations of Coulomb Friction for Dynamic Analysis", Earthquake Engineering and Structural Dynamics, 30:1511-1538.

N/O/P

S. Nagarajaiah, K. Ferrell, (1999), "Stability of Elastomeric Seismic Isolation Bearings", Journal of Earthquake Engineering, 125:946-954.

N.M. Newmark, W.J. Hall, (1973), "Procedures and criteria for earthquake resistant design", Building Research Series No. 46, National Bureau of Standards, U.S. Dept. of Commerce, Washington, pp. 209-236.

D.K. Nims, P.J. Richter, R.E. Bachman, (1993), "The Use of the Energy Dissipating Restraint for Seismic Hazard Mitigation" Earthquake Spectra, Special Issue, Vol. 9, No.3, EERI.

A.S. Pall, C. Marsh, P. Fazio, (1980), "Friction joints for seismic control of large panel structures", Journal of Prestressed Concrete Institute, 25(6), 38-61.

M. Pranesh, Ravi Sinha, (2000), "VFPI: an isolation device for aseismic design", Earthquake Engineering and Structural Dynamics 29, pp. 603-627

M.J.N. Priestley, G.M. Calvi, (2002), "Strategies for repair and seismic upgrading of Bolu Viaduct 1, Turkey", Journal of Earthquake Engineering.. Vol. 6, no. Special Issue 1, pp. 157-184

M.J.N. Priestley and G.M. Calvi, (2003), "Direct displacement-based seismic design of concrete bridges", ACI International Conference on Seismic Bridge Design and Retrofit, La Jolla, 2003

T.C. Pan, G. Yang, (1996), "Nonlinear analysis of base-isolated MDOF structures", 11th WCEE, Acapulco, Mexico, 23–28 June 1996, paper No. 1534.

J. C. Poynor, (2001), "Innovative Design for Magneto-Rheological Dampers," M.S. Thesis, Virginia Polytechnic Institute and State University, Blacksburg, Virginia.

Q/R/ S

Y. Ribakov, J. Gluck, (1999), "Active control of MDOF structures with supplemental ER fluid dampers", Earthquake Engineering and Structural Dynamics, 28:143-156.

Y. Ribakov, J. Gluck, (2002), "Selective Controlled Base Isolation System With Mrds", Earthquake Engineering and Structural Dynamics, 31:1301-1324.

P.J. Richter, D.K. Nims, J.M. Kelly, R.M. Kallenbach, (1990), "The EDR – Energy Dissipating Restraint, a new device for mitigation of seismic effects", Proceedings of the 1990 Structural Engineers Association of California (SEAOC) Convention, Lake Tahoe, CA.

A. Ruangrassamee, K. Kawashima, (2001), "Relative displacement response spectra with pounding effect", Earthquake Engineering and Structural Dynamics,

I.H. Shames, F.A. Cozzarelli, (1992), "Elastic and Inelastic Stress Analysis", Prentice-Hall: Englewood Cliffs, NJ, pp.120-122.

Shibata, A., and M. Sozen, "Substitute Structure Method for Seismic Design in Reinforced Concrete", Journal of the Structural Division, ASCE, Vol. 102, No.12, 3548–3566

M.P. Singh, L.M. Moreschi, (2001), "Optimal seismic response control with dampers", Earthquake Engineering and Structural Dynamics, 30:553-572

B.F. Jr Spencer, S.J. Dyke, M.K. Sain, J.D. Carlson, (1997), "Phenomenological model for magnetorheological dampers", ASCE Journal of Engineering Mechanics, 123(3), pp. 230-238

R.I. Skinner, W.H. Robinson, G.H. McVerry, (1993), "An introduction to seismic isolation", Wiley

T/U/V

D.P. Taylor, "History, design, and applications of fluid dampers in structural engineering", URL http://www.taylordevices.com/tayd.htm

R.Tremblay, S.F. Stiemer, (1993), "Energy dissipation through friction bolted connections in concentrically braced steel frames", ATC 17-1 Seminar on Seismic Isolation, passive energy dissipation and active control, Vol 2, 557-568.

C. S. Tsai, (1997), "Finite element formulations for friction Pendulum seismic isolation bearings", International Jour. for Num. Methods in Engng, vol. 40, pp. 29–49

Tyler, R.G., 1978. "Tapered Steel Cantilever Energy Absorbers," Bull. N.Z. Nat. Soc. For Earthquake Eng., Vol. 11, No. 4.

C.M. Uang, V.V. Bertero, (1990), "Evaluation of seismic energy in structures", Earthquake Engineering and Structural Dynamics, 19, pp 77-90

X/ Y/W/ Z

URL: http://nisee.berkeley.edu/prosys/applications.html

Y.L. Xu, W.L. Qu, J.M. Ko, (2000), "Seismic response control of frame structures using Magnetorheological/ Electrorheological dampers", Earthquake Engineering and Structural Dynamics, 29:557-575

Y. Wang, L.L. Chung, W.H. Liao, (1998), "Seismic response analysis of bridges isolated with friction pendulum bearings", Earthquake Engineering and Structural Dynamics, 27, 1069–109

Y.K. Wen, (1975), "Approximate method for nonlinear random vibration", Journal of Engineering Mechanics. Vol. 101, no. EM4, pp. 389-401.

Y.K. Wen, (1976), "Method for random vibration of hysteretic systems", ASCE Journal of Engineering Mechanics, 102(2), PP. 249-263

Annex A: STRUCTURAL IMPLEMENTATIONS ON BRIDGES

Worldwide Implementations of I/D systems on bridges are listed below.

Table A. 1. Structural implementation of I/D devices on bridges in Europe

Structure	Location	New/ Retrofit	Year	Damper Type	Reference/Notes
Viana do Castelo	Portugal		1989	Hydraulic Shock Transmitter, Hydraulic dissipator (FIP)	
Portimao	Portugal		1990	Hydraulic dissipator (FIP)	
Rio Guadiana	Portugal		1991	Elastomeric elastic device (FIP)	
Pont de Socorridos	Portugal		1992	Hydraulic ST	
Linda Velha	P6 No2/A - Portugal		1992	Hydraulic ST (FIP)	
Main Bridge	Second Severn Crossing (England)		1993	Hydraulic ST, elastomeric bearing (FIP)	
Nantua	Sapra A40 - France		1993	Hydraulic ST	
Nayrolles	Sapra A40 - France		1993	Elasto-plastic yielding steel devices (FIP)	
Knot of Odivelas	IC22 - Portugal		1994	Hydraulic ST (FIP)	
Riberia da Seica	Portugal		1994	Hydraulic ST, elastomeric bearing (FIP)	
Knot of Odivelas	IC22 - Portugal		1995	Hydraulic ST (FIP)	
Amoreira	Via rapida Camara-lobos - Portugal		1995	Hydraulic ST (FIP)	
Main Bridge	East Link across Storebaelt - Denmark		1995	Hydraulic ST (FIP)	
Tagus	2nd crossing of the Tagus river - Portugal		1996	Hydraulic ST, Elasto-plastic isolator (FIP)	

Table A. 2. Structural implementation of I/D devices on bridges in North America

Structure	Location	New/ Retrofit	Year	Damper Type	Reference/ Notes
Dog River Bridge	Mobile Co. (AL - USA)		1992	LRB	Isol. design selected to take advantage of force distr. and low maint. features.
Deas Slough	Richmond (Hwy. 99 over Deas Slough)		1990	LRB	Isol. design focused on redistr. of lateral forces away from the

Bridge	(BC - USA)				fixed pier to make it possible to accomplish the seismic upgrade by repl. the bearings.
Burrard Bridge Main Spans	Vancouver (Burrard St. over False Cr.) (BC - USA)		1990	LRB	Isol. reduced seismic force demand by a factor of 4 to levels within the capacity of the existing substructures.
Queensborough Bridge	New Westminster (over N. arm of Fraser River) (BC - USA)		1994	LRB	Seismic forces reduced by a factor of 1.5; force distribution favors end piers.
Roberts Park Overhead	Vancouver (Deltaport Extension over BC Rail tracks) (BC)	N	1996	LRB	Seismic forces reduced by a factor of 4, eliminating vertical overload of piles due to seismic overturning of single-column hammerhead piers.
Granville Bridge	Vancouver, Canada (BC)	R	1996	Elasto-plastic devices (crescent moon and spindle).	
White River Bridge	Yukon, Canada (YU)	-	1997	FPS	-
Sierra Pt. Overhead	S. San Francisco (U.S. 101 over S.P. Railroad) (CA)	R	1985	LRB	3'-dia. 25'-tall cols were protected by reducing elastic seismic forces to within their elastic capacity.
Santa Ana River Bridge	Riverside (10'-dia. steel water pipe over the Santa Ana River) (CA)	R	1986	LRB	Repl. of vulnerable steel bearings reduced elastic forces to w/in the elastic capacity of existing conc. wall piers and certain truss members that were overstressed.
Eel River Bridge	Rio Dell (U.S. 101 over Eel River) (CA)	R	1987	LRB	Repl. of steel bearings provided protection for the nonductile wall piers.
Main Yard Vehicle Access Bridge	Long Beach (former RR bridge over Long Beach Freeway) (CA)	R	1987	LRB	Repl. of steel bearings eliminated the potential for shear failure in the cols. of the 2-col. bent w/ infill wall; forces on the tall abutments also reduced.
All-American Canal Bridge	Winterhaven, Imperial Co. (I-8 over All-American Canal) (CA)	R	1988	LRB	Use of isol. on the superstr. replacement eliminated the need to repl. the cols. and found. or strengthen them underwater.
Carlson Boulevard Bridge New,	Richmond (part of 23rd St. Grade Separation Project) (CA)	N	1992	LRB	Isol. design reduced the elastic force coeff. to 0.45 (factor of 3 from peak) - a design advantage for the wall abutments.
Olympic Boulevard Separation New,	Walnut Creek (part of the 24/680 Reconstruction Project) (CA)	N	1993	LRB	Isol. design reduced seismic forces by factor of over 6 & saved 38% in cost of found., str. will be moved to perm. align. at

					end of reconstr. project.
Alemany Interchange	I-280/U.S. 101 Interchange, San Francisco (CA)	R	1994	LRB	Complex retrofit; isol. bearings used at certain bents to obtain specific force-deflection characteristics.
Route 242/I-680 Separation	Concord (Rte. 242 SB over I-680) (CA)	R	1994	LRB	Isol. most economical of 3 viable retrofit solutions; steel rocker bearings replaced.
Bayshore Boulevard Overcrossing	San Francisco (Bayshore Blvd. over U.S. 101) (CA)	R	1994	LRB	Isolation most economical for complex geometry; isolator bearings placed under strengthened diaphragms due to restricted space under girders.
1st Street over Figuero	Los Angeles (CA)	R	1995	LRB	Seismic forces reduced by 6, eliminating need to strengthen substructure or foundations.
Colfax Avenue over L.A. River	Los Angeles (CA)	R	1995	LRB	Seismic forces reduced by 4, eliminating need to strengthen substructures and foundations and minimizing required strengthening of truss members.
3-Mile Slough	CA	R	1997	LRB	-
Rio Vista	CA	R	1997	LRB	-
Rio Mondo Bridge	CA	R	1997	FPS	-
American River Bridge City of Folsom	CA	N	1997	FPS	-
GGB North Viaduct	CA	R	1998	LRB	-
Benicia-Martinez Bridge	San Francisco (CA)	R	1998	FPS	-
Coronado Bridge	San Diego (CA)	R	1998	HDR	-
Saugatuck River Bridge	Westport (I-95 over Saugatuck R.) (CT)	R	1994	LRB	New, widened superstr. repl. old simple spans as proposed by contr., cost of removing lead paint from existing superstr. prohibitive; isol. and force-redistr. design enabled use of existing piers and foundations.
Lake Saltonstall Bridge	E. Haven & Branford (I-95 over Lake Saltonstall) (CT)	N	1995	LRB	Repl. existing narrow pre-stressed I-girder bridge in stages; isol. design most economical for new str.
Sexton Creek Bridge	Alexander Co. (IL Rte. 3 over Sexton Creek) (IL)	N	1990	LRB	Overall seismic force input reduced by factor of 3; the isol. design redistr. much of the lat. seismic and nonseismic forces from wall piers and piled foundations to abutments.
Cache River	Alexander Co. (IL Rte. 3 over Cache R.	R	1991	LRB	Superstr. repl.; Seismic isol./force-redistr. design

Bridge	Diversion Channel) (IL)				enabled re-use of existing pier
Route 161 Bridge	St. Clair Co. (IL Rte. 161 over Dutch Hollow Rd., CSX RR & Schoenberger Cr.) (IL)	N	1991	LRB	Isol. reduced overall seismic forces and mitigated disparity in pier stiffnesses by redistr. lat. forces
Poplar Street East Approach, Bridge #082-0005	E. St. Louis (carrying I-55/70/64 over RR yard to Poplar St. Br. across Mississippi R.	R	1992	LRB	Isol. as seismic upgrade was implemented by change order to existing rehab. contract.
Chain-of-Rocks Road over FAP 310	Madison Co. (N. of I-255, I-270, FAP 310 Interchange) (IL)	N	1994	LRB	Isol. design prov. even distr. of lat. forces among substrs. & multi-direct'l resp. to lat. forces on curved superstr.; overall seismic force reduced by factor greater than 2.
Poplar Street East Approach, Roadway B	E. St. Louis (WB main line approach to Poplar St. Br. over Mississippi R.) (IL)	N	1994	LRB	Repl. existing main line str.; isol. provides serviceability demanded by this critically impt. rte. after a seismic event.
Poplar Street East Approach, Roadway C	E. St. Louis (EB main line approach to Poplar St. Br. over Mississippi R.) (IL)	N	1995	LRB	Repl. existing main line str.; isol. provides serviceability demanded by this critically impt. rte. after a seismic event.
Poplar Street Bridge	(IL- USA)	R	1995	-	Elasto-plastic isolators + hydraulic dampers.
Wabash River Bridge	Terra Haute, Vigo Co. (U.S.-40 over Wabash R=2E) (IN - USA)	N	1991	LRB	Isol. design maximized seismic protection at least cost for hammerhead wall piers and piled foundations.
US-51 over Minor Slough	Ballard Co. (KY - USA)	N	1992	LRB	Seismic forces reduced by a factor of 3.5; redistr. to minimize forces on piers.
Clays Ferry Bridge	I-75 over Kentucky R. (KY - USA)	R	1995	LRB	Widening and seismic upgrade; seismic forces reduced by factor of 2.
Main Street Bridge	Saugus (Main St. over US. Rte 1) (MA)	R	1993	LRB	Repl. badly deteriorated simple span superstr.; isol. reduced seismic forces by factor greater than 4; enabled reuse of center pier.
Neponset River Bridge	New Old Colony RR over Neponset R. between Boston and Quincy (MA- USA)	N	1994	LRB	Global design based on seismic isol.; seismic forces reduced by factor of 2.
South Boston Bypass Viaduct	S. Boston (S. Boston Bypass Rd. over Amtrak and Conrail yards, etc.) (MA- USA)	N	1994	LRB	Isol. design was most cost effective globally; serviceability after seismic event ensured for this important segment of Central Artery Project.
South Station Connector	Boston (access from Massachusetts Turnpike to South	N	1994	LRB	Isolation design, including force redistribution, simplified analysis of this complicated,

	Station Transit Center) (MA- USA)				highly irregular structure.
North Street Bridge No. K-26	Grafton (North Street over Turnpike) (MA-USA)	R	1995	LRB	Deck reconstruction and structure rehabilitation. Seismic forces reduced by a factor of approximately 3. Lateral force distribution to favor center pier.
Old Westborough Road Bridge No. K-27	Grafton (Old Westborough Road over Turnpike) (MA-USA)	R	1995	LRB	Deck reconstruction and structure rehabilitation. Seismic forces reduced by a factor of approximately 3.5. Lateral force distribution to favor piers, especially center pier.
Summer Street Bridge	Boston (over Fort Point Channel) (MA-USA)	R	1995	LRB	Historic bridge rehabilitation. Seismic forces reduced by a factor of approximately 3.5 and redistributed to favor the unreinforced stone masonry piers.
West Street over I-93	Wilmington (MA-USA)	R	1995	LRB	Force reduction from isolation enabled installation of new superstructure on existing substructures.
I-93 Mass Ave. Interchange	S. Boston (Central Artery (I-93)/Tunnel (I-90)) (MA- USA)		1996	HDR	Quantity = 743 Typical Size 5 x 20 x 25 (in)
Holyoke/South Hadley Bridge	South Hadley, MA (Reconstruct over Conn. River & Canal St.) (MA- USA)		1996	LRB, NRB	Quantity = 50, 56 Typical Size 8 x 25 x 25 (in)
NB I-170 Bridge	St. Louis (Metrolink Light Rail over NB I-170) (MO- USA)	N	1991	LRB	Isol. design facilitated distr. of longit. forces among substrs. for opt. economy while providing some seismic benefit.
Ramp 26 Bridge	St. Louis (Metrolink Light Rail over Ramp 26) (MO-USA)	N	1991	LRB	Isol. design facilitated distr. of longit. forces among substrs. for opt. economy while providing some seismic benefit.
Springdale Bridge	St. Louis (Metrolink Light Rail over Springdale Rd.) (MO- USA)	N	1991	LRB	Isol. design facilitated distr. of longit. forces among substrs. for opt. economy while providing some seismic benefit.
SB I-170/EB I-70 Bridge	St. Louis (Metrolink Light Rail over SB I-170/EB I-70) (MO-USA)	N	1991	LRB	Isol. design facilitated distr. of longit. forces among substrs. for opt. economy while providing some seismic benefit.
UMSL Garage Bridge	St. Louis (Metrolink Light Rail over access to UMSL garage) (MO- USA)	N	1991	LRB	Isol. design facilitated distr. of longit. forces among substrs. for opt. economy while providing some seismic benefit.
East Campus Drive Bridge	St. Louis (Metrolink Light Rail over E. Campus Dr.) (MO-USA)	N	1991	LRB	Isol. design facilitated distr. of longit. forces among substrs. for opt. economy while providing some seismic benefit.

Geiger Road Bridge	St. Louis (Metrolink Light Rail over Geiger Rd.) (MO-USA)	N	1991	LRB	Isol. design facilitated distr. of longit. forces among substrs. for opt. economy while providing some seismic benefit.
Hidalgo-San Rafael Distributor	Mexico (north of Mexico City) (MX-USA)	N	1995	LRB	Reduction in seismic force demand produced overall cost savings.
Relocated NH Route 85 over NH Route 101	Exeter-Stratham, Rockingham Co. (NH- USA)	N	1992	LRB	Seismic forces reduced by a factor of 4.5; then redistr. to further reduce forces on the 34' high wall abutments.
Squamscott River Bridge	Exeter (Relocated NH Rte. 101 over Squamscott R.) (NH- USA)	N	1992	LRB	Isol. and force redistr. design resulted in net savings of $160,000 (4%) in overall cost of bridge due to reduction in size of "fixed" pier and no. of piles.
Pine Hill Road over Everett Turnpike	Nashua (NH- USA)	N	1994	LRB	Overall seismic forces reduced by factor of approx. 2.5, then redistr. to favor the abutments.
Pequannock River Bridge	Morris & Passaic Co. (I-287 over Pequannock R., Paterson-Hamburg Tpk., and NY, Susquehanna & Western RR) (NJ –USA)	N	1991	LRB	Isol. design reduced overall seismic force input & mitigated disparity in pier stiffnesses by redistr. lat. forces.
Foundry Street Overpass 106.68	Newark (NJ Tpk. over Foundry St.) (NJ –USA)	R	1993	LRB	Part of NJTPA widening project, isol. chosen to guarantee serviceability of facility after a seismic event.
Wilson Avenue Overpass W105.79SO	Newark (NJ Tpk. NSO-E over Wilson Ave.) (NJ –USA)	R	1994	LRB	Part of NJTPA widening project, isol. chosen to guarantee serviceability of facility after a seismic event.
Conrail Newark Branch Overpass E106.57	Newark (NJ Tpk. NB over Conrail-Newark Branch) (NJ –USA)	R	1994	LRB	Part of NJTPA widening project, isol. chosen to guarantee serviceability of facility after a seismic event.
Wilson Avenue Overpass E105.79SO	Newark (NJ Tpk. Relocated E-NSO & W-NSO over Wilson Ave.) (NJ –USA)	R	1994	LRB	Part of NJTPA widening project, isol. chosen to guarantee serviceability of facility after a seismic event.
Relocated E-NSO Overpass W106.26A	Newark (NJ Tpk. E-NSO ramp) (NJ –USA)	N	1994	LRB	Part of NJTPA widening project, isol. chosen to guarantee serviceability of facility after a seismic event.
Berry's Creek Bridge	E. Rutherford (Rte. 3 over Berry's Cr. and NJ Transit) (NJ –USA)	R	1995	LRB	Staged constr.; new superstr. on existing substrs.; overall seismic forces reduced by factor of 3, enabling use of existing cols.
Conrail Newark Branch Overpass	Newark (NJ Tpk. Rd. NSW over Conrail-Newark	R	1995	LRB	Part of NJTPA widening project, isol. chosen to guarantee serviceability of

W106.57	Branch & access rd.) (NJ –USA)				facility after a seismic event.
Norton House Bridge	Pompton Lakes Borough and Wayne Township, Passaic County (Paterson-Hamburg Turnpike over Ramapo River) (NJ –USA)	R	1996	LRB	Seismic forces reduced by a force of approximately 2.5, enabling use of existing substructures and foundations.
Tacony-Palmyra Approaches	Palmyra, (NJ –USA)		1996	LRB	Quantity = 10 Typical Size 5 x16 dia. (in)
Rt. 4 over Kinderkamack Rd.	Hackensack,(Widening & Bridge Rehabilitation) (NJ –USA)		1996	LRB, NRB	Quantity = 24, 32 Typical Size 6 x 14 x 14, 6 x 16 x 16 (in)
Baldwin Street/Highland Avenue	Glen Ridge, NJ Bridge over Conrail (NJ –USA)		1996	LRB NRB	Quantity = 22, 44 Typical Size 7 x 10 (in)
I-80 Bridges B764E & W	Verdi, Washoe Co. (I-80 over Truckee R. and a local roadway) (NV –USA)	R	1992	LRB	Isol. and force redistr. design reduced seismic forces w/in elastic cap. of 3-col. bents and mitigated disparity in pier stiff.; simple spans tied together to make superstr. respond as diaphragm.
West Street Overpass	Harrison, Westchester Co. (West St. over I-95 New England Thwy.) (NY –USA)	R	1991	LRB	Repl. vulnerable steel bearings in 2 center spans over thrwy. traffic lanes to prevent collapse and relieve forces on center pier.
Aurora Expressway Bridge	Erie Co. (SB lanes of Rte. 400 Aurora Expy. over Cazenovia Cr.) (NY –USA)	R	1993	LRB	Seismic upgrade part of general rehab. proj.; isol. reduced forces by factor of 3; design adjusted to minimize forces on piers; to be tested by SUNY-Buffalo.
Mohawk River Bridge	Herkimer (EB and WB rdwys. of NYST over Mohawk R. and NYST Barge Canal) (NY –USA)	N	1994	LRB	Major rehab. & strengthening proj. which included seismic upgrade; isol. design avoided strengthening of cols. and foundations and will keep str. in service after a seismic event.
Moodna Creek Bridge	Orange County (NYST over Moodna Cr. at MP52.83) (NY –USA)	R	1994	LRB	Seismic upgrade; forces reduced by factor of 3.
Conrail Bridge	Herkimer (EB and WB rdwys. of NYST over Conrail, Rte. 5, etc.) (NY –USA)	N	1994	LRB	Repl. of orig. str.; isol. was most econ. overall design and will keep str. in service after a seismic event.
Clackamas Connector	Milwaukie (part of Tacoma St. Interchange) (OR –	N	1992	LRB	Isol. design resulted in $400,000 net savings (12%) due to reduct. in foundation size and will

	USA)				protect tapered single co. bents from damage in earthquake.
Hood River Bridges	Hood River, (OR – USA)		1995	NRB	Quantity = 36 Typical Size 6 x 13 x 20 (in)
Marquam Bridge	(OR –USA)	R	1995	Elasto-plastic isolators + hydraulic ST	
Hood River Bridge	Hood River, (OR – USA)	R	1996	Elasto-plastic devices (crescent moon and spindle).	
Toll Plaza Road Bridge	Montgomery Co. (Approach to toll plaza over Hwy. LR145) (PA –USA)	N	1990	LRB	Some overall seismic benefit, plus transv. thermal capability of isol. bearings on such a wide bridge was impt. consideration.
Montebella Bridge Relocation	Puerto Rico (PR – USA)		1996	LRB, NRB	Quantity = 38, 42 Typical Size 5 x 18 dia. (in)
Blackstone River Bridge	Woonsocket (Woonsocket Ind. Hwy. over Blackstone R., Providence & Worcester RR, & local rds.) (RI –USA)	N	1992	LRB	Isol. design reduced overall seismic force input & mitigated disparity in pier stiffnesses.
Providence Viaduct	Rte. I-95, Providence (RI –USA)	R	1992	LRB	2-level criteria calling for serviceability after A = 0.16g event and no collapse in A = 0.32g event; isol. was cost-effective solution and viaduct will remain in service after higher level event.
Seekonk River Bridge	Pawtuckett(I-95 over Seekonk River) (RI – USA)	R	1995	LRB	2-level criteria calling for serviceability after A = 0.16g event and no collapse in A = 0.32g event; isol. was cost-effective solution and viaduct will remain in service after higher level event. Pins and hangers rehabilitated.
I-295 to Rt. 10	Warwick/Cranston (Bridges 662 & 663) (RI –USA)		1996	LRB	Quantity = 58 Typical Size 6 x 15 dia. (in)
Chickahominy River Bridge	Hanover-Hennico County Line (US1 over Chickahominy River) (VA – USA)	N	1996	LRB	Seismic forces reduced by a factor of approximately 4. Replacement project, phased construction.
Ompompanoos uc River Bridge	Rte. 5, Norwich (VT – USA)	R	1992	LRB	Seismic forces reduced by a factor of 2.5, then redistr. to minimize forces on piers.
Cedar River Bridge	Renton (I-405 over Cedar R. and BN RR) (WA – USA)	N	1992	LRB	Isol. used for initial economy and assurance of serviceability after an earthquake.

Lacey V. Murrow Bridge, West Approach	Seattle (Approach to orig. Lake Washington Floating Br.) (WA – USA)	R	1992	LRB	Seismic isol. saved existing piers and foundations, thus avoiding need to replace the whole str.
Coldwater Creek Bridge No. 11	SR504 (Mt. St. Helens Hwy.) over Coldwater Lake Outlet (WA – USA)	N	1994	LRB	Seismic forces reduced by factor greater than 6; forces minimized at abutments.
East Creek Bridge No. 14	SR504 (Mt. St. Helens Hwy.) over East Cr. (WA – USA)	N	1994	LRB	Seismic forces reduced by greater than 6; forces minimized at abutments.
Home Bridge	Home (Key Penninsula Highway over Von Geldem Cove) (WA – USA)	N	1994	LRB	Energy-dissipation design with isolation at end piers; "hinged" at interior piers.
Duwamish River Bridge	Seattle (I-5 over Duwamish River) (WA – USA)	R	1995	LRB	Widening/retrofit project. Seismic forces reduced by a factor of 4 to levels within capacity of substructure and foundations.
Stossel Bridge	Carnation (NE Carnation Farm Road over Snoqualmie River) (WA – USA)	R	1996	LRB	Vulnerable steel rocker bearings replaced with isolators as part of overall seismic retrofit.
West Kenmore Bridge	Kenmore (Junita Drive NE over Sammemish River) (WA – USA)	R	1996	LRB	Seismic forces reduced by a factor of approximately 2=2E5, thus decreasing the scope of strengthening work required for the piers.
Bridge over County Road 3	Near Shinnston, N. of Clarksburg (new Ash Haul Rd. over Co. Rd. 3) (WV – USA)	N	1993	LRB	Designed for heavy coal-hauling vehicles; isol. design was most economical solution & ensures serviceability after seismic event.
West Fork River Bridge	Near Shinnston, N. of Clarksburg (new Ash Haul Rd. over Fork R.) (WV – USA)	N	1994	LRB	Designed for heavy coal-hauling vehicles; isol. design was most economical solution & ensures serviceability after seismic event.

Table A. 3. Structural implementation of I/D devices on bridges in Japan and Asia

Structure	Location	New/ Retrofit	Year	Damper Type	Reference/Notes
Miyagawa Bridge	Shizuoka (Japan)	N	1991	LRB	continuous steel plate girder
Uehara Bridge	Nagoya (Japan)	N	1991	LRB	continuous prestressed concrete box girder
Route #12 Interchange NBridge	Tokyo (Japan)	N	1991	LRB	continuous prestressed concrete slab

Karasaki Bridge	Fukushima (Japan)	N	1991	HDR	continuous prestressed concrete box girder
Moriguchi Route	Osaka (Japan)	N	1991	LRB	Interconnection of simply-supported girder
Moriguchi Route	Osaka (Japan)	N	1991	LRB	Interconnection of simply-supp. girder
Maruki-bashi Bridge	Iwate (Japan)	N	1992	LRB	continuous prestressed concrete box girder
Route #6	Tokyo (Japan)	N	1992	LRB	Interconnection of simply-supp. girder
Route #6	Tokyo (Japan)	N	1992	LRB	Interconnection of simply-supp. girder
Route #6	Tokyo (Japan)	N	1992	LRB	Interconnection of simply-supp. girder
Onnetoh Bridge	Hokkaido (Japan)	N	1993	LRB	continuous steel plate girder
Nagakigawa Bridge	Akita (Japan)	N	1993	LRB	continuous steel plate girder
Yama-age Bridge	Tochigi (Japan)	N	1993	HDR	continuous prestressed concrete box girder
Sakai Route	Osaka (Japan)	N	1993	LRB	Interconnection of simply-supp. girder
O-hito Viaduct	Shizuoka (Japan)	N	1994	LRB	continuous prestressed concrete slab
Hirao Bridge	Yamaguchi (Japan)	N	1994	HDR	continuous prestressed concrete box girder
Bay Shore Route	Tokyo (Japan)		1994	LRB	continuous prestressed concrete box girder
Matsunohama Bridge	Osaka (Japan)	N	1994	LRB	continuous steel box girder
Izumisano Bridge	Osaka (Japan)	N	1994	LRB	continuous steel box girder
Trans Tokyo Bay	Tokyo (Japan)		1994	HDR	continuous steel box girder
Trans Tokyo Bay	Tokyo (Japan)	N	1994	LRB	continuous steel box girder
Komatsukawa Route	Tokyo (Japan)	N	1994	LRB	Interconnection of simply-supp. girder
Komatsukawa Route	Tokyo (Japan)	N	1994	LRB	Interconnection of simply-supp. girder
Moriguchi Route	Osaka (Japan)	R	1991	LRB	Interconnection of simply-supp. girder
Moriguchi Route	Osaka (Japan)	R	1991	LRB	Interconnection of simply-supp. girder
Route #6	Tokyo (Japan)	R	1992	LRB	Interconnection of simply-supp. girder
Route #6	Tokyo (Japan)	R	1992	LRB	Interconnection of simply-supp. girder
Route #6	Tokyo (Japan)	R	1992	LRB	Interconnection of simply-supp. girder

Sakai Route	Osaka (Japan)	R	1993	LRB	Interconnection of simply-supp. girder
Chuo Expressway (Senkawa)	Tokyo (Japan)	R	1993	HDR	Interconnection of simply-supp. girder
Komatsukawa Route	Tokyo (Japan)	R	1994	LRB	Interconnection of simply-supp. girder
Komatsukawa Route	Tokyo (Japan)	R	1994	LRB	Interconnection of simply-supp. girder
Sakai Route (Nishinari)	Osaka (Japan)	R	1994	HDR	Interconnection of simply-supp. girder
Bay Shore Route (BY513)	Kanagawa (Japan)	R	1994	HDR	continuous prestressed concrete slab
Jamuna Multipurpose Bridge	Jamura - Bangladesh		1995/ 1996	Elasto-plastic yielding steel devices (FIP)	

Table A. 4. Structural implementation of I/D devices on bridges in New Zealand

Structure	Location	New/ Retrofit	Year	Damper Type	Reference/Notes
Motorway Overbridge	Dunedin (NZ)	N	-	Tapered Plate	-
Slopping Highways	Wellington (NZ)	N	-	Lead Extrusion	-
Motu	New Zealand	N	1973	Steel UBs in flexure	Steel truss
South Rangitikei	New Zealand	N	1974	10 Steel torsion bars, rocking piers	PSC box
Bolton Street	New Zealand	N	1974	Lead extrusion	Steel I beam
Aurora Terrace	New Zealand	N	1974	Lead extrusion	Steel I beam
Toetoe	New Zealand	N	1978	LRBs	Steel truss
King Edward Street	New Zealand	N	1979	Steel cantilevers	PSC box
Cromwell	New Zealand	N	1979	6 Steel flexural beams	Steel truss
Clyde	New Zealand	N	1981	LRBs	PSC U-beam
Waiotukupuna	New Zealand	N	1981	LRBs	Steel truss
Ohaaki	New Zealand	N	1981	LRBs	PSC U-beam
Maungatapu	New Zealand	N	1981	LRBs	PSC slab
Scamperdown	New Zealand	N	1982	LRBs	Steel box
Gulliver	New Zealand	N	1983	LRBs	Steel truss
Donne	New Zealand	N	1983	LRBs	Steel truss
Whangaparoa	New Zealand	N	1983	LRBs	PSC I-beam
Karakatuwhero	New Zealand	N	1983	LRBs	PSC I-beam
Devils Creek	New Zealand	N	1983	LRBs	PSC U-beam
Upper Aorere	New Zealand	N	1983	LRBs	Steel truss

Rangitaiki (Te Teko)	New Zealand	N	1983	LRBs	PSC U-beam
Ngaparika	New Zealand	N	1983	LRBs	Steel truss
Hikuwai Nos. 1 - 4	New Zealand	R	1983-84	LRBs	Steel plate girder
Oreti	New Zealand	N	1984	LRBs	PSC I-beam
Rapids	New Zealand	N	1984	LRBs	PSC I- & U-beam
Tamaki	New Zealand	N	1985	LRBs	PSC I-beam
Deep Gorge	New Zealand	N	1984	LRBs	Steel truss
Twin Tunnels	New Zealand	N	1985	LRBs	PSC I-beam
Tarawera	New Zealand	N	1985	LRBs	PSC I-beam
Moonshine	New Zealand	N	1985	LRBs	PSC U-beam
Makarika No. 2	New Zealand	R	1985	LRBs	Steel plate girder
Makatote	New Zealand	R	1986	LRBs	Steel plate girder
Kopuaroa Nos. 1 & 4	New Zealand	R	1986-87	Steel cantilever	Steel plate girder
Glen Motorway and Railway	New Zealand	N	1987	LRBs	PSC T-beam
Grafton Nos. 4 & 5	New Zealand	N	1987	LRBs	PSC T-beam
Northern Wairoa	New Zealand	N	1987	LRBs	PSC I-beam
Ruamahanga at Te Ore Ore	New Zealand	N	1987	LRBs	PSC U-beam
Maitai (Nelson)	New Zealand	N	1987	LRBs	PSC I-beam
Bannockburn	New Zealand	N	1988	Lead extrusion and LRBs	Steel truss
Hairini	New Zealand	N	-	LRBs	PSC slab
Limeworks	New Zealand	N	1989	LRBs	Steel truss
Waingawa	New Zealand	N	1990	LRBs	PSC U-beam
Mangaone	New Zealand	N	1990	LRBs	Steel truss
Porirua Ramp Overbridge	New Zealand	N	1993	LRBs	PSC double T-beam
Porirua Ramp Stream Overbridge	New Zealand	N	1993	LRBs	PSC U-beam

Table A. 5. Structural implementation of I/D devices on bridges in Italy

Bridge	**Location**	**New/ Retrofit**	**Year**	**Device Type**	**Reference/Notes**
Somplago	Udine-Tarvisio (Italy)		1974	EL (neoprene disc)	Precast segments
Savio	Tiberina E47 (Italy)		1974	OL	
Fiumerella del Noce	Calabria (Italy)		1974	OL	
Resia	Udine-Tarvisio		1981-	Long: elastom.	Box girder

Fella 2 Chiusaforte Fella 3 Sella Nevea	(Italy)	83	sleeves, Tran: elastom. discs	
Fella 1	Udine-Tarvisio (Italy)	1982	Long: EP damp. Tran: elastom. discs	Box girder
Glagno Favarinis Carnia	Udine-Tarvisio (Italy)	1982	EL (elastomer)	Box girder
Slizza 2	Udine-Tarvisio (Italy)	1983	EP	Box girder
Coccau	Udine-Tarvisio (Italy)	1983	EL (elastomer)	Box girder
Cellina	SS 251 (Italy)	1983	EL (neoprene)	Concrete beams
Bruscaia	Craco (MT) (Italy)	1983	EL (elastomer)	Box girder
Cadramazzo Fella 8 Fella 7 Fella 6 Slizza 1 Fella 4 Granuda Casello Fella 5 San Leopoldo Fella 10	Udine-Tarvisio (Italy)	1983-86	Long: elastom. sleeves, Tran: elastom. Discs	Box girder
Passerella Fella 9 Malborghetto	Udine-Tarvisio (Italy)	1983-86	OL	Steel girder
Sesia	Trafori (Italy)	1984	OL	
Scamirro	Craco (MT) (Italy)	1984	Longit: EL Transv: EL	
Pontebba	Udine-Tarvisio (Italy)	1984	EL (elastomer)	Box girder
Slizza 3 Vallone, railroad	Udine-Tarvisio (Italy)	1985	EL	Steel girders
Rivoli Bianchi	Udine-Tarvisio (Italy)	1985	Pneumatic dampers	Concrete beams
Val Freghizia Aniene	Milano-Napoli (Italy)	1985	EP (steel)	Box girder
Macchiettone Molinelle	Napoli-Bari (Italy)	1985	Long: EPs on abutments or on each span, Tran: EP on pier	PCB boxed, piers or framed RC columns

Ufita Tre Torri Vado della Ripa Lamia Paolo Omero Fabiani	Napoli-Bari (Italy)	1985-87	Long: EP devices on abutments or on each span, Tran: EP on pier	PCB boxed, piers or framed RC columns
Flumeri Brancaleone	Napoli-Bari (Italy)	1986	Long: EP devices on abutments or on each span, Tran: EP on pier	PCB boxed, piers or framed RC columns
Ballendiero Janello	Salerno-Reggio (Italy)	1986	OL	PCB
Carafone Vallonalto 1 Vallonalto 2	Napoli-Canosa (Italy)	1986	LRB	PCB
F. Freghizia 1 F. Freghizia 2	Milano-Napoli (Italy)	1986	LRB	Concrete beams
Viad. km 27,191 Viad. km 27,410 Viad. km 28,282 Viad. km 29,801 Viad. km 29,989 Viad. km 30,337 Viad. km 31,228 Viad. km 31,513	Sora-Avezzano (Italy)	1986	EL	
Corcolle 1 Corcolle 2 F. San Giuliano	Fiano-San Cesareo (Italy)	1986-87	RB + metal shock	Concrete beams
F. Capaldo La Muiatta F. Vittorio Viad. RM/PE Tevere	Fiano-San Cesareo (Italy)	1986-87	RB + metal shock	Box girders
S. Cesareo 1 Casilina Barco Fiora Ferr. RM/FI Ferr. RM/PE	Fiano-San Cesareo (Italy)	1986-87	EL (rubber discs)	Box girders/ concrete beams
S. Cesareo 2 Prenestino	Fiano-San Cesareo (Italy)	1986-87	Viscoelastic shock absorber	PCB
Coscile	Salemo-Reggio	1987	OL	PCB

Caballa	(Italy)			
Sizzine	Trafori (Italy)	1987	OL	PCB
Serra dei Lupi Cardinale	Napoli-Bari (Italy)	1987	LRB	PCB
Acqua Marcia	Milano-Napoli (Italy)	1987	Long: EP; Tran: EL	Box girders
Ceszano	F. Salerno-Nap. (Italy)	1987	EL + mechanical dissipators	
Calore	Caserta (railroad) (Italy)	1987	EL + mechanical dissipators	PCB
Platano	Potenza (Italy)	1987	EL	
Ciaramitaio	Grammichele (Italy)	1987	EL	
Viad. km. 32,383	Sora-Avezzano (Italy)	1987	EL	
Le Ville Faella Giglio Riofr Chiana San Zeno Arno Riganzi 1 Riganzi 2 Oreno Agna Ascione	Roma-Firenze Railway (Italy)	1987-89	OL	Box girder
Lontrano	Salerno-Reggio (Italy)	1988	OL	Box girders
Tagliamento	St. Pontebbana (Italy)	1988	Viscoelastic	PCB
Valle Situra Caldarone S. Nicola 1 S. Nicola 2	Roma-L'Aquila-Teramo (Italy)	1988	EL (rubber + metal shock)	Box girders
Le Grotte Biselli	Roma-L'Aquila-Teramo (Italy)	1988	OL+EL	Box girders
Grancia	SS 1 (Italy)	1988	EL	
San Mauro	F. Salerno-Nap. (Italy)	1988	EP	
Mariaccio	Roma-Napoli (Italy)	1988	EL	
Sovr. SS 11	Milano-Brescia (Italy)	1988	EL	
Gerolomini	Napoli (Italy)	1988	EL	

Viad. km. 17,009				
Viad. km. 17,303				
Viad. km. 17,593				
Viad. km. 18,344				
Viad. km. 18,649				
Viad. km. 18,954	Sora-Avezzano (Italy)	1988	EL	
Viad. km. 20,049				
Viad. km. 20,449				
Viad. km. 20,997				
Viad. km. 21,388				
Viad. km. 16,730				
Viad. km. 16,180				
Tammaro	F.Salerno-Fog. (Italy)	1988	elast. attr.	
Viadotto 7 Viadotto 4	S. Mango (Italy)	1988-90	EL	Steel girders
Morignano	A 14 (Italy)	1989	EP dampers	PCB
Lenze-Pezze	Napoli-Bari (Italy)	1989	EP	PCB
Restello Meschio	A 27 (Italy)	1989	Long: Viscoelastic Tran: EP	PCB
Pont Suaz	Aosta (Italy)	1989	EP shock absorber	PCB
Flumicello	Bologna-Firenze (Italy)	1989	OL	PCB
Temperino	Roma-L'Aquila (Italy)	1989	EP dampers	PCB
S. Onofrio	Salerno-Reggio (Italy)	1989	OL	PCB
Costaeelle Castello Cerchiara	Roma-Teramo (Italy)	1989	OL + RB	Box girders
D'Antico	Napoli-Bari (Italy)	1989	EP	PCB
Targia-Siracusa	Targia-Siracusa (Italy)	1989	EP	Concrete beams
Scrofeta Vergine	Napoli-Canosa (Italy)	1989	EP	

Lavornea	F. Salerno-Nap. (Italy)	1989	EL + mech. dissipators	
Viad. km 22,384				
Viad. km 23,397				
Viad. km 24,302				
Viad. km 25,042	Sora-Avezzano (Italy)	1989	EL	
Viad. km 25,497				
Viad. km 15,770				
Viad. km 9,330				
Scudillo	Napoli	1989	EL	
Fiume Magra	Tresana	1989	EL	
Terza corsia	Roma-Napoli	1990	LRB	Concrete beams
Santa Barbara	SS 1	1990	EP	Concrete slab
Tora	Firenze-Pisa-Livorno	1990	EP multidirec.	Steel girders
Caffaro	Salerno-Reggio	1990	OL	Concrete beams
P.O. Menia				
F. Rocca-Venafro	Avellino	1990	OL	Concrete beams
SS 206	Firenze-Pisa-Livorno	1990	EP	Steel girders
Tiasca	Trafori	1990	Elastic buffers	PCB
Vesuvio	SS 269 Vesuvio	1990	Elastic buffers	PCB
Furiano				
Malpertugio	Messina-Palermo	1990	EP	Pre-stressed concrete box girder
Inganno				
Mortaiolo	Livorno-Civitavecchio	1990	EP with OL shock absorb.	Pre-stressed concrete slabs
Collecastino	Roma-Teramo	1990	OL	
Chiovano				
Viad. Via Napoli	Sora-Avezzano	1990	EL	
Torti				
Montagna	Colle Sannita	1990	EP	
Cateni				
Passerelli				
Svincolo				
Sovrappasso	Pisa A 12	1990	EP	
Deledda				
Esero viad. 5	Cosenza	1990	EP	
Incile Arno	Pisa	1990	EL	
Colle Guardiani				
Fosso della Vite	Civitavecchia	1990	EL	
Cave di Gesso				
Peccia 2	Milano-Napoli	1990-91	EP	PCB
Formanera				

Carducci Rio Pescara Fosso Ponticelli Fosso Savone Rivolo del Lanzo S. Leonardo Petto Fiumetto	Roma-Teramo	1990-91	OL	Box girders
S. Antonio Gombetto	Rac. Goitese	1991	EP with shock absorbers	Pre-stressed concrete
Galdo 1 Galdo 2	Salerno-Reggio	1991	EP	PCB
Noncello S. Giuseppe	PN-Conigliano	1991	EP	Pre-stressed concrete
Minuto	Fondo Valle Sele	1991	OL	PCB
Savalano	Livorno-Civitavecchia	1991	EP	
Pollein e Buthier	Chatillon	1991		
Oglio	Soncino (BS)	1991	OL	
Livornese	Pisa	1991	EL	
Pian Mulino S. Rustico Mavone	Roma-L'Aquila-Teramo	1991-92	OL	Box girders
Poggio Iberna	Livorno-Civitavecchia	1991-92	OL	PCB
Lenne Svincolo 2 Svincolo 3 Lato	SS 106 Taranto	1992	EL	
Taro 1	Autostrada Cisa	1992	OL	-
Ponte nelle Alpi	Aut. Mestre-V. Veneto P. di Vedoia	1992	EP	Steel girders
Albanese	A3 SA-RC	1992	OT	-
Fragneto	SS59 Brienza	1992	EP	Steel girders
Salini Carusi	A3 SA-RC	1992	OT	
	A14 coll. Porto AN	1992	OL	
Fosso dei Mulini Pietrafitta	SS89 Gargancia	1992	OL	Concrete beams
Nocera 1 Traone	SS3 Flaminia	1992	OL	
Cannamelata	SS113 loc.	1992	OL	

Minissale	S. Agata Militello coll. A20 ME-PA loc. Calatabiano		1992	OL	
-	SS38 Stelvio		1992	ST	
S. Simone	-		1992	EP	
Tammoro	-		1992	EP	
Pecorone	-		1992	EP	
Fiumara di Gallico	A3 SA-RC		1992	ST	
Piana di Gallico	A3 SA-RC		1992	ST	
Malpasso	A20 ME-PA		1992	OL	
Sovr. SS286	A20 ME-PA		1992	OL	
Fiume Piave	-		1993	EP	
Bormida di Pallare	Aut. To-SV		1993	EL	
Fiume Panaro	-		1993	ST	
-	E45 Orte-RA		1993	EP	
No. 4	SGC Grosseto-Fano lotto 3		1993	EP	
Monteroni	SS2 Cassia		1993	EL	
Fiumetto	SS117		1994	OL	
S. Stefano	SS117		1994	OL	
-	coll. SS62 loc. S. Giustina (MS)		1994	EL	
-	A27 Mestre-BL lotto 6-bis		1994	ST	
Livenza	A28 PN-Conegliano lotto 27		1994	EP	
-	SS517 Bussentina		1994	EP	
Manubiola Taro	SS308-SS253 Ghiare-Bertorella		1994	ST	
Taro 1 Taro 2 Taro 3	SS308-SS253 Ghiare-Bertorella		1994	EL,ST	
Tarodine	SS308-SS253 Ghiare-Bertorella		1994	OL,ST	
-	A27 Mestre-BL lotto 6-bis		1994	ST	
Ponte Giulio	SS251 var. Montereale-Valcellina		1994	OL,EP	
-	SS43 Val di Non		1994	EL	
Acque Vive Bussento	SS517 Bussentina		1994	EP	

Monte Rolando sopra FS, SS47, Brenta	SS47 Valsugana	1995	OL
Bradanica		1995	ST
Rio Torto	SS517 Bussentina	1996	EP
Di Giogio Pirrera Ficuzza	A20 ME-PA Lotto 24 bis	1996	OL

EL = Elastic

EP = Elastic-plastic behavior

OL = Hydraulic dampers (EP equivalent)

OP = Hydraulic damper

SL = Sliding support

ST = Shock transmitter associated with SL RB = Rubber bearings

LRB = Lead-rubber bearings

RC = Reinforced-concrete

PCB = Pre-stressed concrete beams

Hydraulic ST = Hydraulic Shock Transmitter

UB = universal beam

PSC = prestressed concrete

Notes:

Two-way bridges have been regarded as a single bridge to define the length.

Of the more recent bridges (1985-) in Italy, typical design values are:

- yield/weight ratio: 5-28%, with a typical value of 10%
- maximum seismic displacement: +/- 30 - 150 mm, with a typical value of +/- 60 mm
- peak ground acceleration: 0.15 - 0.40g, with a typical value of 0.25g